T2R2 東京科学大学 リサーチリポジトリ
Science Tokyo Research Repository

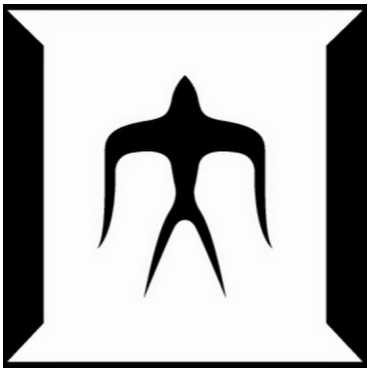
論文 / 著書情報
Article / Book Information

題目(和文)	スーパーアースにおける鉱物雲形成過程の理論的研究
Title(English)	Theoretical modeling of mineral cloud formation on super-Earths
著者(和文)	大野和正
Author(English)	Kazumasa Ohno
出典(和文)	学位:博士(理学), 学位授与機関:東京工業大学, 報告番号:甲第11381号, 授与年月日:2020年3月26日, 学位の種別:課程博士, 審査員:奥住 聡,上野 雄一郎,玄田 英典,佐藤 文衛,関根 康人
Citation(English)	Degree:Doctor (Science), Conferring organization: Tokyo Institute of Technology, Report number:甲第11381号, Conferred date:2020/3/26, Degree Type:Course doctor, Examiner:,,,,
学位種別(和文)	博士論文
Type(English)	Doctoral Thesis

Powered by T2R2 (Science Tokyo Research Repository)

Dissertation submitted for the degree of *Doctor of Science*

Theoretical modeling of mineral cloud formation on super-Earths



Kazumasa Ohno

February 12, 2020

Department of Earth and Planetary Sciences,
Tokyo Institute of Technology

Abstract

The Kepler mission have revealed that super-Earths, exoplanets whose sizes fall between Earth and Neptune, are universally present in this universe. This finding poses a fundamental question for planetary science: how were super-Earths formed? One of the valuable clues to infer the formation process is a planetary composition. Since the composition likely reflects the properties of the building blocks of a planet, the composition potentially diagnoses where and how the planet was formed.

The observation of transmission spectra of exoplanetary atmospheres open a new window to investigate the compositions of exoplanets. The atmospheric composition likely reflects not only interior composition but also the formation process; for example, a hydrogen-rich atmosphere is presumably originated from the accretion of protoplanetary disk gasses. However, recent observations have suggested that exoplanets are prone to be veiled by clouds at high altitude that make difficult to directly probe the atmosphere. In particular, the transmission spectra of super-Earths exhibit featureless spectra in most cases, suggesting the ubiquity of clouds in super-Earths.

Despite the importance of cloud, it has been highly uncertain how clouds are formed in super-Earths. Since most of previous studies prescribed cloud as a fitting parameter, the physical processes of exoplanetary cloud formation has been poorly understood to data. Because many observed exoplanets are orbiting close to central stars, their hot atmospheres yield solid mineral clouds. The intense stellar insolation also drives vigorous atmospheric circulation that may produces cloud considerably different from water clouds on our Earth. Since the cloud formation is associated to the atmospheric composition, understanding the exoplanetary cloud formation may help to constrain the atmospheric composition of cloudy super-Earths.

In this thesis, we aim to figure out mineral cloud formation on super-Earths and what we can learn from the cloudy atmospheres. We first develop a cloud microphysical model that solves vertical transport and growth of cloud particles in a self-consistent manner. The entire cloud structure is controlled by the particle size. The particle size substantially depends on the concentration of condensation nuclei and atmospheric metallicity. We find that the particle is mainly determined by the competition between particle growth and eddy transport near the cloud base. We also find that the cloud particle always grows into a size larger than a threshold determined by collision growth.The minimum size sets the upper limit of the cloud vertical extent if clouds are made of compact spheres.

Conventionally, cloud models have commonly assumed that the cloud particles are compact spheres. However, because the exoplanetary clouds are made of solid minerals, cloud particles potentially grow into non-spherical porous aggregates. We investigate how the porosity of cloud particles evolve in planetary atmospheres during the cloud formation. Using the porosity evolution model developed in planet formation community, we show that the density of cloud particles can be smaller than the material density by $\sim$ 2–3 orders of magnitude. The cloud particle ag-

gregates are compressed by gas drag once the size exceeds a threshold, which is approximately $30\ \mu\mathrm{m}$. Using our cloud microphysical model, we find that the cloud particle aggregate rarely grow into the size so large that the compression sets in. As a result, the aggregate clouds can ascend to altitude much higher than that for compact-sphere clouds.

We calculate synthetic transmission spectra to examine the composition of cloudy atmospheres from the observations. In particular, we investigate how the aggregate clouds affect the observations of the transmission spectra for the first time. The aggregate clouds obscure the spectral feature substantially. Moreover, at long wavelength, the aggregate clouds produce the spectral slope originated by the scattering properties of an aggregate. We apply the cloud and spectrum models to super-Earths GJ1214b, GJ436b, GJ3470b, HD97658b, and HAT-P-11b to constrain their atmospheric metallicity. We find that the models of high-metallicity atmospheres ($\geq 100\times$ solar abundance) better explain the transmission spectra of GJ1214b, GJ436b, and HD97658b, while the models of low-metallicity atmospheres ($\leq 10\times$solar) better explain the observations of GJ3470b and HAT-P-11b. Our results potentially indicate the presence of dichotomy of super-Earths in terms of the atmospheric metallicity.

We also investigate the interior structure of the super-Earths. Although the interior structure is sensitive to the upper boundary condition set by an atmosphere, our investigation on the transmission spectra enables us to use the reasonable atmospheric properties in the interior structure calculations. We find that the super-Earths studied in this thesis have planetary masses of 1–30% in their atmospheres, depending on ice mass fraction of planetary core. We also find that the GJ1214b, GJ436b, and HD97658b would have atmospheres too massive to explain the current atmospheric mass if in-situ formation is assumed. This potentially indicates that these super-Earths were formed at outer parts of protoplanetary disks followed by inward migration.

Contents

1 General Introduction **7**
- 1.1 Ubiquity of Super-Earths in this Universe . . . 7
- 1.2 Theory of Super-Earth Formation . . . 8
  - 1.2.1 Overview of Planet Formation . . . 8
  - 1.2.2 Current Understanding of Super-Earth Formation . . . 10
- 1.3 Transmission Spectrum of Exoplanetary Atmosphere . . . 15
- 1.4 Prevalence of Clouds in Exoplanetary Atmospheres . . . 18
  - 1.4.1 Featureless transmission spectra . . . 18
  - 1.4.2 Conventional modeling of exoplanetary clouds . . . 20
- 1.5 About this thesis . . . 23
  - 1.5.1 Purpose . . . 23
  - 1.5.2 New concept . . . 23
  - 1.5.3 Outline of this thesis . . . 24

2 Microphysical Modeling of Mineral Clouds on super-Earths **25**
- 2.1 Abstract . . . 25
- 2.2 Introduction . . . 26
- 2.3 Overview of an Adopted Microphysical Model . . . 27
- 2.4 Method . . . 29
  - 2.4.1 Outline . . . 29
  - 2.4.2 Construction of Vertical Structure . . . 30
  - 2.4.3 Transport Equations . . . 32
  - 2.4.4 Terminal Velocity of Cloud Particles . . . 33
  - 2.4.5 Microphysics of Particle Growth . . . 35
  - 2.4.6 Numerical Procedure . . . 36
- 2.5 Results of a Cloud Microphysical Model . . . 37
- 2.6 The Mechanisms Controlling Particle Size . . . 39
  - 2.6.1 Condensation Regime ($\tau_{\rm mix} < \tau_{\rm coag}, \tau_{\rm coal}$) . . . 40
  - 2.6.2 Coagulation Regime ($\tau_{\rm coag} < \tau_{\rm mix} < \tau_{\rm coal}$) . . . 41
  - 2.6.3 Coalescence Regime ($\tau_{\rm coal} < \tau_{\rm mix}$) . . . 42
- 2.7 Summary . . . 43

3 Clouds of Fluffy Aggregates: How They Form in Exoplanetary Atmospheres **45**
- 3.1 Abstract . . . 45
- 3.2 Introduction . . . 46
- 3.3 Modeling Porosity Evolution of Cloud Particles . . . 46

3.3.1 Fractal Growth . . . 47
3.3.2 Collisional Compression . . . 48
3.3.3 Gas-drag Compression . . . 49
3.3.4 A General Formula . . . 50
3.4 Application of Porosity Model to KCl Clouds in GJ1214b . . . 50
3.4.1 Analytic Estimates of Compression Threshold Sizes . . . 51
3.5 Modeling Formation of Fluffy-Aggregate Clouds . . . 53
3.5.1 Prescription of Nucleation and Condensation . . . 53
3.5.2 Aggregate Growth and Transport above the Cloud Base . . . 53
3.5.3 Numerical Procedures . . . 54
3.5.4 Vertical Distributions of Fluffy-Aggregate Clouds . . . 55
3.6 Discussion . . . 58
3.6.1 Model Caveats . . . 58
3.6.2 Comparison with Other Porosity Models . . . 60
3.7 Summary . . . 62

4 Transmission Spectra of Cloudy Atmospheres on Super-Earths 63
4.1 Abstract . . . 63
4.2 Introduction . . . 64
4.3 Methodology of Synthetic Transmission Spectrum . . . 64
4.3.1 Gas Opacity . . . 65
4.3.2 Aggregates Opacity . . . 65
4.3.3 Cloud-top Pressure . . . 67
4.4 Results of Synthetic Transmission Spectra . . . 69
4.5 Model Applications to Super-Earths . . . 72
4.5.1 Overview of Cloud Profile on Each Planet . . . 72
4.5.2 Comparisons with Observations of Super-Earths . . . 76
4.5.3 Degeneracy between Compact-Sphere and Aggregate Clouds . . . 87
4.6 Implications for Observations of JWST . . . 88
4.7 Summary . . . 90

5 Inferring Interior Structure and Formation Process of Super-Earths 92
5.1 Abstract . . . 92
5.2 Introduction . . . 93
5.3 Method . . . 93
5.4 Mass-Radius Relation of Exoplanets . . . 96
5.5 Atmospheric Mass Fraction of Super-Earths . . . 98
5.5.1 Minimum Atmospheric Mass Constrained by Atmospheric Escape . . . 100
5.6 Implications for High-Metallicity Atmospheres on Planet Formation . . . 101
5.7 Summary . . . 105

6 Summary of this Thesis 107
6.1 Microphysical modeling of mineral cloud formation . . . 107
6.2 Modeling porosity evolution of cloud particles . . . 107
6.3 Transmission spectrum of the aggregate clouds . . . 108
6.4 Atmospheres and interior structures of cloudy super-Earths . . . 108

7 Future prospect **109**
7.1 Implication for Future Observations 109
7.2 Further Model Improvements 110
7.2.1 Radiative feedback of clouds on PT profiles 110
7.2.2 Improvements of Nucleation Treatment 112
7.2.3 Multiple Mineral Clouds 113
7.2.4 Better understanding of tracer transport 115
7.2.5 Co-evolution of Size and Porosity Distributions of Cloud Particles . . . 117
7.2.6 Beyond 1D model 118
7.3 Applications of Porosity Model to Photochemical Hazes 118

A Full derivation of transmission spectrum **121**

Chapter 1

General Introduction

1.1 Ubiquity of Super-Earths in this Universe

Since the first discovery of an exoplanet 51 Pegasi b (Mayor & Queloz, 1995), nearly 4000 exoplanets[1] have been detected to date. In particular, the Kepler mission has revolutionized our understanding of the exoplanet population. Figure 1.1 exhibits the all detected exoplanets as a function of planetary mass and semi-major axis. The detected exoplanets can be classified into at least three populations. The first population is Jupiter-size planets orbiting near the central stars (semi-major axis is $a < 0.1$ AU), so-called hot Jupiters. Because of their close in orbits, many hot Jupiters have equilibrium temperature of $\geq$1000 K, significantly higher than that for Jupiter ($\sim$100 K). The second population is Jupiter-size planets orbiting far from the stars ($a > 1$ AU), called cold Jupiters. The final population is the low-mass planets with sizes between Earth and Neptune, called super-Earths.

One of the remarkable finding of the Kepler mission is the prevalence of super-Earths in this universe (e.g., Howard et al., 2012; Fressin et al., 2013; Petigura et al., 2013; Fulton et al., 2017; Fulton & Petigura, 2018). The survey of both radial velocity and transit observations suggested that about 50% of solar-type stars host super-Earths (Mayor et al., 2011; Fressin et al., 2013). Thanks to the large number of samples obtained by the Kepler mission, a planet occurrence rate, the number of planets per star, has been derived as function of planetary radius (e.g., Howard et al., 2012; Fressin et al., 2013; Petigura et al., 2013). Fressin et al. (2013) found that occurrence rates of super-Earths are significantly higher than planets larger than Neptune. Although the Kepler samples are largely composed of sun-like stars, it has been suggested that the occurrence rate of super-Earths around small M dwarfs is comparable to that for sun-like stars (Dressing & Charbonneau, 2015).

The California-Kepler Survey (Petigura et al., 2017) further improved the understanding of the population of super-Earth. The survey precisely determines the stellar properties for host stars of Kepler planets (Petigura et al., 2017), which enables us to precisely determine the planetary radius. The improvement of radius determination revealed a noticeable deficit of super-Earths with radius of 1.5–2.0$R_{\rm Earth}$ (Fulton et al., 2017; Fulton & Petigura, 2018). It has been suggested that this radius gap is originated by the atmospheric escape and thus planetary evolution after the formation (e.g., Owen & Wu, 2017; Ginzburg et al., 2018). Although above statement mainly focuses on the stellar mass of 0.85–1.2$M_{\rm sun}$, recent studies are attempting to find the radius gap around smaller stars, such as M dwarfs (Cloutier & Menou, 2019).

[1]This is according to the NASA Exoplanet Archive at 28 September, 2019.

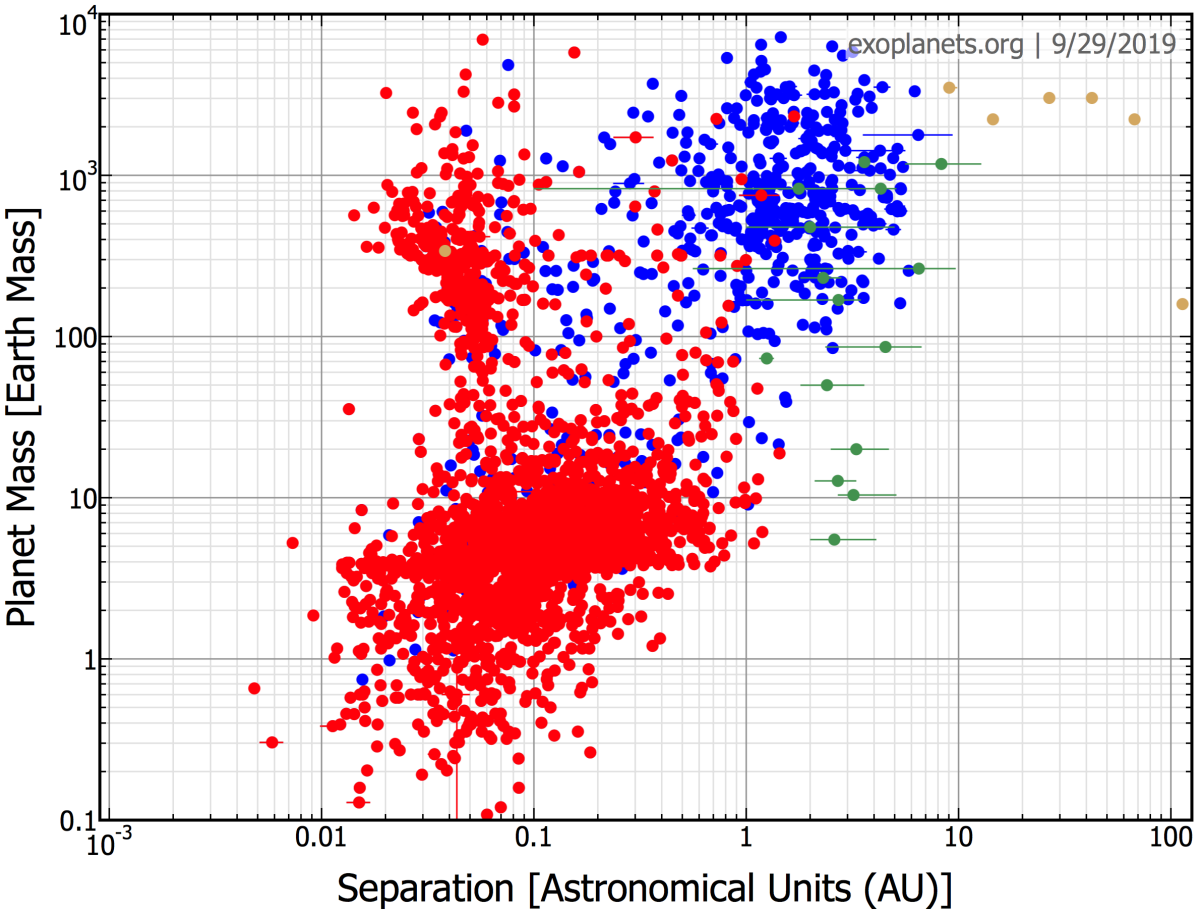


Figure 1.1: Exoplanets detected to date. The vertical and horizontal axes are planetary mass and semi-major axis. The color difference of each plot indicates difference of the detection methods, where the red, blue, green, and yellow plots denote planets detected by transit observations, radial velocity measurements, microlensing observations, and direct imaging, respectively.

Consequently, the prevalence of super-Earths in this universe is likely evident according to the current observations. On the other hand, this finding is opposite to a classical planet formation theory (Ida & Lin, 2004) that predicted the deficit of super-Earths. Thus, the prevalence of super-Earths naturally poses a fundamental question to us: how were super-Earths formed? In next section, we review the current understanding of super-Earth formation.

1.2 Theory of Super-Earth Formation

1.2.1 Overview of Planet Formation

Before introducing the current formation theory of super-Earth, we first briefly review the general outline of planet formation. It has been widely accepted that planets are formed in protoplanetary disks composed of gasses and a tiny fraction of solid particles. The first step of the planet formation is the growth of the submicron dust into km-sized planetesimals, which eventually become the building blocks of planets. This field is still under active debate because there are a number of obstacles in the planetesimal formation. For example, the dust initially grow into

large size through mutual collision [2], but the collision velocity in protoplanetary disk becomes too high to cause the sticking before planetesimals are formed (e.g., Blum & Münch, 1993). Another problem is radial drift of the dust (Adachi et al., 1976; Weidenschilling, 1977): the dust loss the angular momentum via friction with surrounding gasses, leading to be migrated to central star before planetesimals are formed (e.g., Brauer et al., 2008). A number of idea have been proposed to overcome these obstacles, such as the gravitational instability (Goldreich & Ward, 1973), streaming instability (Johansen et al., 2007), rapid growth via porosity evolution (Okuzumi et al., 2012; Kataria et al., 2013), enhanced adhesion of dust (e.g., Wada et al., 2013; Arakawa & Nakamoto, 2016; Homma et al., 2019), and local concentration near at H_2O snow line (Schoonenberg & Ormel, 2017; Hyodo et al., 2019). Although there are many obstacles in it's formation, past presence of planetesimals is presumably evident because the Solar System contains the remnant of them, namely asteroids.

Once planetesimals are formed, they grow into larger size via collision due to gravitational attraction and eventually form a protoplanet. In the classical formation theory, called planetesimal accretion hypothesis, the formed planetesimals continuously grow via mutual collision, and the building blocks of planets are mainly planetesimals (e.g., Kokubo & Ida, 1996, 1998, 2000). In this context, the planetesimals eventually grow into the total mass of a annulus with a radius of orbital distance, estimated by (Kokubo & Ida, 1998)

$$M_{\rm iso} = 2\pi a b \Sigma_{\rm s}, \tag{1.1}$$

where a is the semi-major axis, $b \approx 10a(2M_{\rm p}/3M_{\rm s})^{1/3}$ is the width of the annulus (Kokubo & Ida, 1998), $M_{\rm s}$ is the stellar mass, and $\Sigma_{\rm s}$ is the solid surface (column) mass density of the initial protoplanetary disk. If we assume the minimum mass solar nebula (MMSN), the minimum disk mass distribution to build up solar system, the solid surface density is given by (Hayashi, 1981)

$$\Sigma_{\rm s} = \left(\frac{a}{1\ {\rm AU}}\right)^{-3/2} \times \begin{cases} 7\ {\rm g\ cm^{-2}} & (a < 2.7) \\ 30\ {\rm g\ cm^{-2}} & (a > 2.7), \end{cases} \tag{1.2}$$

where the formula is split into inside and outside of the H_2O snow line. Inserting Equation (1.2) into (1.1), the isolation mass is given by

$$M_{\rm iso} \approx \left(\frac{a}{1\ {\rm AU}}\right)^{3/4} \left(\frac{M_{\rm s}}{M_{\rm sun}}\right)^{-1/2} \times \begin{cases} 0.09 M_{\rm Earth} & (a < 2.7) \\ 0.84 M_{\rm Earth} & (a > 2.7). \end{cases} \tag{1.3}$$

Equation (1.3) indicates that the planetesimal accretion form mars-mass protoplanets at ≈ 1 AU. Although the estimation of Equation (1.3) is smaller than the Earth-mass, the final assembly of terrestrial planets occurs when the depletion of disk gasses induce the orbital crossing of protoplanets (e.g., Kominami & Ida, 2002). One of the shortcoming of planetesimal accretion hypothesis is the difficulty of Jupiter formation. The planetary core gravitationally attracts the disk gasses in a runnaway fashion to be a gas giant once the core mass reaches $\sim 10 M_{\rm Earth}$, which is so-called a critical core mass (e.g., Mizuno, 1980; Stevenson, 1982; Ikoma et al., 2000). However, Equation (1.3) indicates that the isolation mass reaches only $\sim 3 M_{\rm Earth}$. Another difficulty is coming from the timescale. Assuming MMSN, the growth timescale of a protoplanet to be $\sim 10 M_{\rm Earth}$ is ~ 10 Myr at the current orbit of Jupiter (Tanaka & Ida, 1999). This is quite longer than the typical lifetime of protoplanetary disk (1–3 Myr) suggested by observations

[2] Here, the dust are stuck each other via the van der Waals force (Chokshi et al., 1993).

(Ribas et al., 2015), implying that the planetesimal accretion is too slow to form the core of gas giant at wide orbital distance. However, it is fair to mention that several idea have been also proposed to overcome the aforementioned obstacles by reducing the critical core mass, such as the rapid cooling (Movshovitz et al., 2010; Hori & Ikoma, 2010) and/or the heavy-element enrichment of protoamospheres (Hori & Ikoma, 2011; Venturini et al., 2015).

Recent studies have actively debated another growth mechanism, namely pebble accretion (e.g., Ormel & Klahr, 2010; Lambrechts & Johansen, 2012, 2014). In this scenario, the planetesimal collects the $\sim$ cm-sized pebbles drifting from outer parts of the protoplanetary disk. In contrast to the planetesimal accretion in which the protoplanet mass is limited by the local disk mass, the pebble accretion does not suffer from this limitation. Another aspect of pebble accretion is its rapid growth rate. Because pebbles are moderately coupled to ambient gasses, pebbles can efficiently accrete onto a planetesimal by losing its momentum (for detail, see review of Johansen & Lambrechts, 2017). The rapid growth via pebble accretion can reconcile the formation of solar system giant planets and a typical disk lifetime (Lambrechts & Johansen, 2012, 2014).

1.2.2 Current Understanding of Super-Earth Formation

We now focus on the formation theory of super-Earth proposed to date. Current studies of super-Earths formation usually focus on the embryo growth after the planetesimal formation. Several scenarios have been proposed to explain the nature of super-Earths so far. The scenarios can be classified into either "in-situ" formation (e.g., Hansen & Murray, 2012; Chiang & Laughlin, 2013; Lee et al., 2014; Chatterjee & Tan, 2014, 2015; Ogihara et al., 2015; Lee & Chiang, 2016; Ogihara et al., 2018; Lee, 2019; Jankovic et al., 2019) or "outside" formation followed by inward migration (e.g., Alibert et al., 2006; Terquem & Papaloizou, 2007; Rogers et al., 2011; Cossou et al., 2014; Izidoro et al., 2017; Venturini & Helled, 2017; Izidoro et al., 2019; Lambrechts et al., 2019; Bitsch et al., 2019; Liu et al., 2019). We introduce each of them in what follows (for the review, see Morbidelli & Raymond, 2016).

In-situ formation

The straightforward idea of super-Earth formation is in-situ formation through the planetesimal accretion. Since super-Earths are often observed as a multiple system (Lissauer et al., 2011), this scenario may explain the preference occurrence of multiple super-Earths. Hansen & Murray (2012) performed N-body simulations and showed that in-situ planetesimal accretion could indeed explain super-Earth formation. One of the strong advantage of the in-situ formation is that it can naturally form the rocky super-Earths. It has been known that the super-Earths with radii of $R_{\rm p} < 1.6 R_{\rm Earth}$ are dense enough to be Earth-like composition (Weiss & Marcy, 2014; Rogers, 2015). The predominant rocky composition is suggested by the radius gap (Section 1) and current atmospheric evaporation models (Owen & Wu, 2017; Ginzburg et al., 2018), although model uncertainty has been still existed. We explain more about the bulk composition of super-Earths in Section 1.2.2.

Although in-situ formation can successfully explain several properties of super-Earths suggested by observations, there are several shortcomings as well. One of the serious problem for in-situ formation scenario is the too small mass contained in the inner disk region. For example, MMSN has the mass of $3.3\ {\rm M_{Earth}}$ inside $1\ {\rm AU}$, which is a factor of 2–3 smaller than typical super-Earths. Hansen & Murray (2012) arbitrary assumed that the disk surface density is more

massive than MMSN by a factor of 5. Several theoretical studies attempted to explain the massive disk by the inward migration of solid materials from the outer disks (e.g., Chatterjee & Tan, 2014; Moriarty & Fischer, 2015). For example, Chatterjee & Tan (2014) suggests that inward migrating pebbles from the outer disks can be accumulated in the pressure maximum in close-in orbit, supplying the mass high enough to form super-Earths. Moriarty & Fischer (2015) also showed that inward migrating pebbles can be captured by planetesimals at the inner disk, depositing the sufficient mass to the inner planetesimal ring. On the other hand, the presence of massive disk is not supported by observations of millimeter thermal emission from protoplanetary disks (e.g., Andrews et al., 2009; Ansdell et al., 2016), although recent observations with ALMA suggest that estimated disk masses are often insufficient to form exoplanetary systems (Manara et al., 2018). Therefore, in order to reconcile the disk observations and massive disk, one may need to assume that the disk mass is mostly transformed into planetesimals, not responsible to the observations, before the typical age of observed disks (1–3 Myr, Ansdell et al., 2016).

Another problem is the presence of orbital migration driven by disk-planet interaction, although this is also a problem in outside formation scenario as well. Ogihara et al. (2015) showed that inward planet migration due to the disk-planet interaction is very efficient. The migration preferentially results in a orbital configuration in which the adjacent planet pairs are trapped in mean motion resonance, and planet mass steeply decreases with orbital distance. This orbital distance is inconsistent with observed orbital configurations of super-Earths (Lissauer et al., 2011). The migration timescale and direction depend on the radial gradient of disk surface density and temperature (Paardekooper et al., 2010). Recent study of Ogihara et al. (2018) suggest that the migration issue may be reconciled if magnetically driven disk wind is taken into account, which tends to reduce the surface density of inner disk (e.g., Suzuki et al., 2016).

Outside formation

Another scenario of the super-Earth formation is the formation at far from the current orbit followed by inward migration. One of the advantage of outside formation is that one does not need to assume a massive disk because an outer disk contains more mass in general. Alibert et al. (2006) simulated the time evolution of planetary interior structure and orbital radius under the circumstance of planetessimal accretion scenario. They demonstrated that close-in super-Earths can be formed via the outer formation scenario, in which initial planet core emerges even beyond the H_2O ice line. Rogers et al. (2011) applied the planetesimal accretion model of Movshovitz et al. (2010) that explicitly calculates the protoatmosphere structure and grain opacity of the atmosphere. They also calculated subsequent atmospheric mass evolution and showed that the low-density super-Earths can be formed at the current Jupiter location, although they did not explicitly calculate orbital migration and arbitrary cut off the runnaway gas accretion. (Venturini & Helled, 2017) simulated the planetary growth at 5 and 20 AU by taking into account the evolution of both mass and composition protoatmospheres. They showed that enrichment of protoatmosphere by heavy elements help to form super-Earths, although they did not explicitly calculate orbital migration. Cossou et al. (2014) performed direct N-body simulation of planetesimal accretion implemented with orbital migration. They showed that observed eccentricity and inclination distributions of super-Earths can explained by the outside formation, whereas the migration tends to produce the chain of mean motion resonance, not apparently seen in observations (Lissauer et al., 2011). Izidoro et al. (2017) also performed N-body simulations but

examine long-term dynamical evolution after the disk dissipation. They showed that the resonant chain can be broken by the dynamical instability after the disk dissipation. Izidoro et al. (2019) further performed N-body simulations of the planetesimal accretion by including the pebble accretion and showed that the difference of total pebble mass may determine whether protoplanet become a super-Earth or gas giants (for bifurcation of super-Earths and terrestrial planets, see Lambrechts et al., 2019). Bitsch et al. (2019) simulated the growth and orbital migration of protoplanets in the context of pebble accretion by taking into account the migration of H_2O snow line. They showed that ice content of super-Earth depends on the formation location of a seed protoplanet and migration history.

One of the shortcoming of this scenario is that the inward migration inevitably produces systems where adjacent planet pairs are trapped by mean motion resonance (e.g., Cossou et al., 2014; Izidoro et al., 2017). This is inconsistent with the fact that many observed planet pairs are placed near but not exactly in the mean motion resonance (Lissauer et al., 2011). However, a number of mechanisms have been proposed to break the resonance configuration, such as stochastic force from the turbulence in protoplanetry disks (Adams et al., 2008b; Rein, 2012), orbital instabilities after the disk dissipation (Izidoro et al., 2017), and the interaction with leftover planetesimals (Chatterjee & Ford, 2015).

Bulk Composition

One of the valuable information is the bulk density of planets. Because of close-in orbit, in-situ formation inevitably yields rocky super-Earths [3]. On the other hand, outside formation yields ice-rich super-Earths in certain cases, depending on the initial formation position and migration direction (Izidoro et al., 2019; Bitsch et al., 2019). Which rocky or icy material does make up super-Earths? Observed mass-radius relation offers hints to answer the question, and thus Figure 1.2 shows the exoplanet mass-radius relation. Figure 1.2 shows that the mass-radius relation of some super-Earths with radii of $< 1.6 R_{\rm Earth}$ are identical to Earth-like composition [4]. Therefore, at least, relatively small super-Earths are likely rocky planets because further deposition of ice leads to planetary radius larger than observed radius (Weiss & Marcy, 2014; Rogers, 2015)[5]. On the other hand, the composition of super-Earths larger than $\approx 1.6 R_{\rm Earth}$ is quite uncertain in Figure 1.2. For example, super-Earths with radii of $\approx 2.5 R_{\rm Earth}$ and masses of $\approx 10 M_{\rm Earth}$ are in line with the mass-radius relation of pure icy planets. However, these super-Earths can be also explained by rocky planets surrounded by tiny amount (1 wt%) of atmospheres. Because planetary atmospheres easily puff the planet radius, it is generally challenging to constrain the core composition without information on atmospheric properties (e.g., Seager et al., 2007; Adams et al., 2008a; Rogers & Seager, 2010; Valencia et al., 2013). Therefore, further information on atmospheric properties could be helpful to better constrain the planetary bulk composition.

Before moving on next subsection, we introduce the estimation of core composition from the presence of radius gap. As mentioned in Sectin 1, the California-Kepler Survey revealed the

[3] Several studies suggest that inner planets around 1 AU can accrete substantial ice because the H_2O snow line migrates to inward (Sato et al., 2016; Ida et al., 2019). The migration stems from the fact that the viscous heating is diminished with time. However, at least for solar-like stars, the snow line never migrate inside the current orbit of close-in super-Earths, ~ 0.1 AU (Oka et al., 2011).

[4] Here, Earth-like composition means Fe with mass of 32.5 wt% and silicates with mass of 67.5 wt% (Seager et al., 2007)

[5] However, even this conclusion is based on the assumption of iron contents similar to Earth-like composition. If planetary cores are allowed to be enriched by iron, we are still suffering from the degeneracy of interior structure.

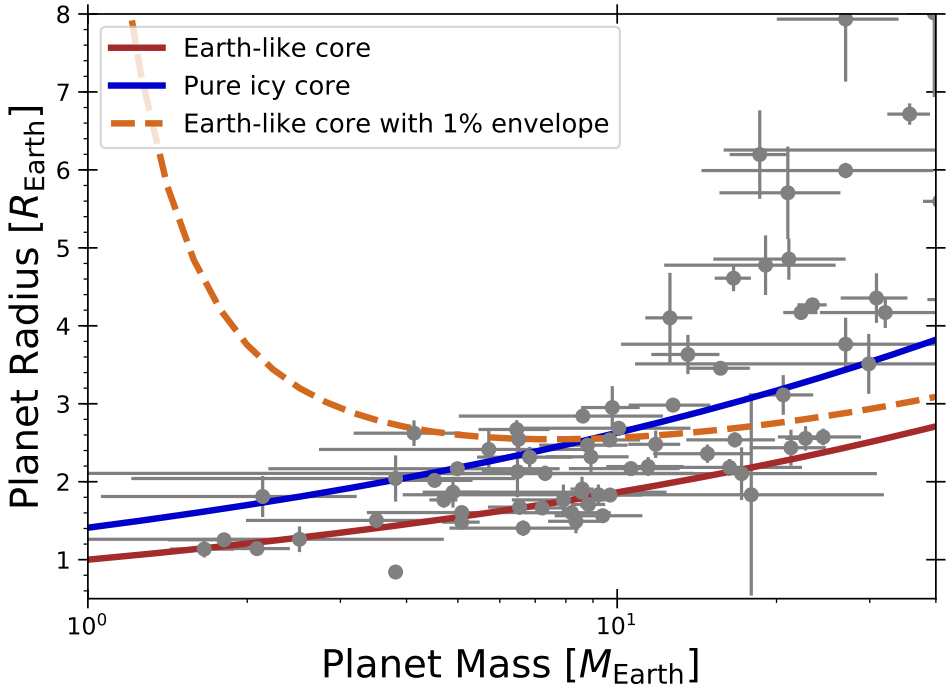


Figure 1.2: Exoplanet mass and radius determined by the radial velocity and transit observations. The mass and radius are taken from Exoplanet.eu. The brown and blue solid lines show the theoretical mass-radius relation of Earth-like core and pure icy core, taken from Zeng et al. (2019). The dashed brown line shows the mass-radius relation of rocky planets surrounded by hydrogen/helium atmospheres with masses of $\approx 0.01\times$ planetary masses, which is calculated by the model presented in Section 5 using an ideal gas EOS.

deficit of super-Earths with radius of ≈ 1.5–$2.0 R_{\rm Earth}$ (Fulton et al., 2017; Fulton & Petigura, 2018). It has been suggested that the valley is caused by atmospheric mass loss driven by high-energy stellar photons (called photoevaporation, Owen & Wu, 2017) and/or luminosity of the cooling core (called core-powered mass loss, Ginzburg et al., 2018; Gupta & Schlichting, 2019). The most recent study suggests that the position of the radius gap varies with stellar mass, which may support the photoevaporation as a predominant mechanism (Fulton & Petigura, 2018). Because the mass loss rate depends on the core density, the position of radius gap is potentially associated to the core composition. Both scenario suggest that the position of radius gap is better explained by Earth-like core rather than icy core. In the core-powered mass loss scenario, the radius gap could be explained if planet's cores are largely made of rock, and ice mass fraction is less than $\sim 20\%$ (Gupta & Schlichting, 2019). In the phoroevaportation scenario, the Earth-like core is also favored to explain the radius valley, and the dispersion of core density is relatively small (Owen & Wu, 2017).

Although the radius gap potentially provide an insight on core composition, we state some caveats of current modeling. First, above studies commonly assumed solar-composition atmospheres, and not clear how the atmospheric composition affects the results. The current photoevaporation model neglects the effect of magnetic field, but Owen & Adams (2019) showed that the effects of magnetic field may diminish the mass loss rate and reduce the core density required to explain the radius gap. Although the presence of radius gap is presumably evident, some super-

Earths are also present in the radius gap (meaning the gap is not empty, Fulton & Petigura, 2018). Fignaly, the radius gap is largely observed for sun-like stars ($M_{\rm s} = 0.85$–$1.2 M_{\rm Earth}$), and it is unclear whether low-mass stars, like M dwarfs, exhibit similar trends. Further studies would be needed to draw a more robust conclusion from the radius gap.

Atmospheric Accretion

To conclude this section, we introduce the current understanding of atmospheric formation on super-Earths. As mentioned in previous section, super-Earths with radii of $> 1.6 R_{\rm Earth}$ have low bulk density that likely suggests presence of atmospheres (e.g., Weiss & Marcy, 2014; Rogers, 2015). Lopez & Fortney (2014) showed that observed super-Earths have ~ 1–10% of total planet mass in the atmospheres if they are rocky cores surrounded by hydrogen/helium atmospheres. Hydrogen, $\rm H_2$, can be originated from either accretion of protoplanetary disk gasses onto protocore or outgassing of accreted solid [6]. Previous studies showed that outgassing can produce $\rm H_2$ with a mass of several percent at most (Elkins-Tanton & Seager, 2008; Rogers et al., 2011). Therefore, it is presumably evident that super-Earths captured substantial amount of disk gasses to form atmospheres. One of the puzzles is the modest amount of atmosphere. The classical formation theory have suggested that a planetary core captures the disk gasses in a runnaway fashion to be a gas giant once the core mass reaches $\sim 10 M_{\rm Earth}$ (e.g., Mizuno, 1980; Stevenson, 1982; Ikoma et al., 2000). How did super-Earths avoid runnaway gas accretion?

Several idea have been proposed to avoid the runnaway gas accretion on super-Earths. The most straightforward idea is that disk gasses around super-Earths may be depleted somehow. Lee et al. (2014) and Lee & Chiang (2016) suggested that the gas accretion can be halted if final assembly of super-Earths occur at inner regions of gas-depleted disks. Although the scenario might seem a fine-tuning problem, they suggest that it can be a natural consequence since the orbital crossing of protoplanet is triggered by the depletion of ambient disk gasses (Kominami & Ida, 2002). (Ginzburg & Sari, 2018) suggested that super-Earths may avoid the gas accretion by opening deep gaps in the protoplanetary disks with low viscosity. Ogihara & Hori (2018) suggested that the runnaway gas accretion could be avoided if inflow of disk gasses is regulated by weak viscous accretion.

The gas accretion is triggered by the contraction (cooling) of protoatmospehre (Lee & Chiang, 2015; Ginzburg et al., 2016), and thus heating the atmosphere and/or delaying the cooling can also inhibit the runnaway gas accretion. Lee et al. (2014) suggested that the gas accretion could be sufficiently delayed if atmospheric dust opacity is high. Lambrechts et al. (2014) showed that, though in the context of ice giant formation in solar system, intense atmospheric heating due to pebble accretion can inhibit the runnaway gas accretion on protocore of $\sim 10 M_{\rm Earth}$. Ormel et al. (2015) performed 3D hydrodynamical simulations and suggested that the protoatmosphere is continuously interchanged by ambient disk gasses, inhibiting the cooling of the protoatmosphere. Ginzburg & Sari (2017) suggested that tidal heating could inhibit the gas accretion if an initial eccentricity is the order of 0.2.

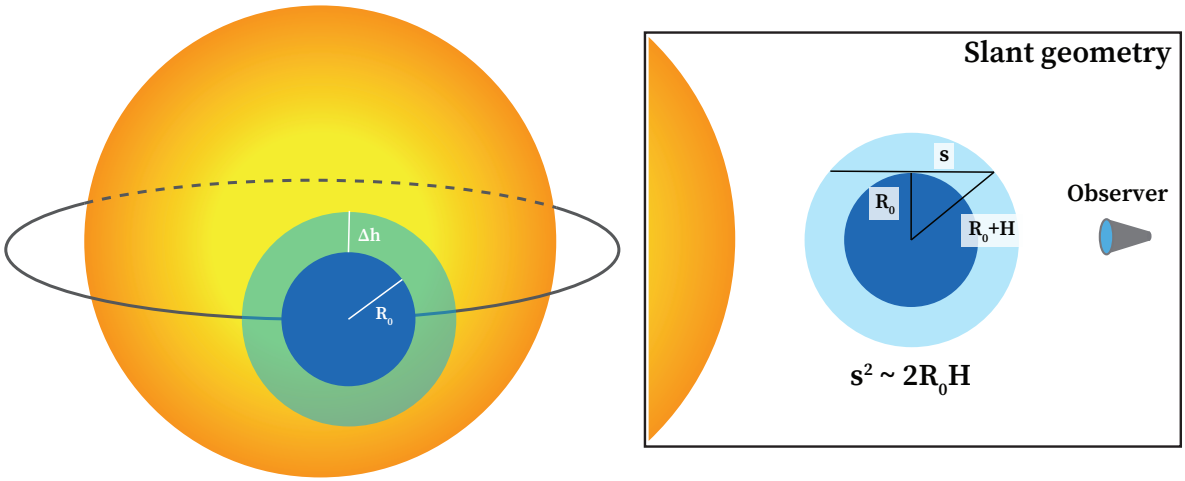


Figure 1.3: Cartoon illustrating orbital configuration of transiting exoplanets.

1.3 Transmission Spectrum of Exoplanetary Atmosphere

One of the promising ways to explore the planetary formation is an observation of exoplanetary atmospheres. If observation can distinguish whether atmosphere is hydrogen-rich or not, it helps to break the degeneracy of a planetary interior structure explained in Section 1.2.2 (e.g., Miller-Ricci et al., 2009; Miller-Ricci & Fortney, 2010). In addition, atmospheric composition itself can offer the information on past formation process. The most famous metric is atmospheric carbon-to-oxygen mass ratio (C/O). Öberg et al. (2011) suggest that atmospheric C/O potentially diagnoses the formation location because C/O of disk gasses/solids vary with orbital distance due to condensation of volatile species, such as H_2O, CO, and CO_2. Atmospheric C/O also depends on a number of factors, such as the chemical evolution of protoplanetary disk (Helling et al., 2014; Cridland et al., 2017, 2019a) and dissolution of accreted solids in protoatmospheres (e.g., Mordasini et al., 2016; Madhusudhan et al., 2014, 2017; Cridland et al., 2019b). Although the interpretation of C/O is complicated, it may offer clues to distinguish the in-situ and outside formation scenario. Another powerful metric is atmospheric metallicity—the ratio of atmospheric heavy element abundance to solar (stellar) abundance, i.e., $(N_{\rm heavy}/N_{\rm H})_{\rm atm}/(N_{\rm heavy}/N_{\rm H})_{\rm sol}$. The metallicity diagnose how much accreted solids are dissolved in protoatmospheres. For example, Fortney et al. (2013) suggest that smaller accreted solids (like pebbles) lead to the higher metallicities because they are efficiently evaporated and ablated in the atmospheres. The metallicity is also associated the mass-radius relation of exoplanets (Valencia et al., 2013, see also Section 5) and the onset of runnaway gas accretion onto protoplanet (Stevenson, 1982; Hori & Ikoma, 2011; Venturini et al., 2015, 2016). Therefore, the metallicity can be used to infer the past solid and gas accretion processes of super-Earths.

Currently, the most popular way to probe exoplanetary atmospheres is transit observations in multiple wavelength, so-called transmission spectrum (e.g., Seager & Sasselov, 2000; Brown, 2001). The basic idea of this method is that transit depth varies with observed wavelength because of the wavelength dependence of atmospheric opacity. The transmission spectroscopy has successfully detected a number of atmospheric molecules in exoplanetary atmospheres, such as Na (e.g., Charbonneau et al., 2002; Redfield et al., 2008; Sing et al., 2008; Pont et al., 2013;

[6]In this mechanism, the hydrogen is formed via oxidization of metallic iron by water.

Nikolov et al., 2014), K (e.g., Sing et al., 2015; Nikolov et al., 2015), H_2O (e.g., Tinetti et al., 2007; Swain et al., 2008; Beaulieu et al., 2010; Wakeford et al., 2013, 2018; McCullough et al., 2014; Kreidberg et al., 2015; Benneke et al., 2019a; Spake et al., 2019), and TiO (Sedaghati et al., 2017). It is evident that future observational instruments, such as the James Webb Space Telescope (JWST, planned to be launched in 2021), Twinkle space telescope (planned to be launched in 2022, Edwards et al., 2019), and ARIEL (planned to be launched in 2028, Tinetti et al., 2016, 2018), will explore exoplanetary atmospheres in more detail and extensively in the coming decade.

Several literature have introduced the theoretical basis of transmission spectroscopy with analytical argument (Lecavelier Des Etangs et al., 2008; de Wit & Seager, 2013; Bétrémieux & Swain, 2017; Heng & Kitzmann, 2017; Jordán & Espinoza, 2018). Here, we introduce a simplified analytical model to capture the basic behavior of the transmission spectrum (a more rigorous model is also presented in Appendix A). Let us consider the planets composed of a solid part with a radius of R_0 and an atmosphere with a thickness of Δh (Figure 1.3). Here, the radius R_0 points the "surface" of the planet below which is completely optically thick at any wavelength. It does not necessary mean the radius of solid core, and thus one can define the reference radius for gas giants. Supposing $\Delta h \ll R_0$, the transit depth D can be calculated as

$$D \approx \frac{\pi R_0^2 + 2\pi R_0 \Delta h}{\pi R_\mathrm{s}^2}, \tag{1.4}$$

where R_s is the stellar radius. The wavelength dependence of the transit depth is generally coming from the second term of Equation (1.4). Let us assume that the atmospheric thickness for given wavelength is determined by the height where becomes optically thick for observer. The optical depth along the line of sight of observer for a transiting planet (right panel of Figure 1.3) is called slant optical depth τ_s and approximately given by (e.g., Fortney, 2005; Heng & Kitzmann, 2017)

$$\tau_\mathrm{s} \approx \rho_\mathrm{g} \kappa \sqrt{2\pi R_\mathrm{p} H}, \tag{1.5}$$

where ρ_g is the atmospheric density, κ is the atmospheric opacity, R_p is the planet radius, and H is the pressure scale height defined by

$$H = \frac{k_\mathrm{B} T}{m_\mathrm{g} g} \sim 360 \text{ km} \left(\frac{T}{1000 \text{ K}}\right) \left(\frac{m_\mathrm{g}}{2.3 \text{ amu}}\right)^{-1} \left(\frac{g}{10 \text{ m s}^{-1}}\right)^{-1}. \tag{1.6}$$

where k_B is the Boltzmann constant, T is the temperature, m_g is the mean mass of atmospheric particles, and g is the surface gravity. The rigorous derivation of Equation (1.5) from basic a equation is presented in Appendix A (Equation A.9), but it is geometrically clear that the slant length scale is an order of $\sim \sqrt{R_\mathrm{p} H}$ (right panel of Figure 1.3). Invoking the ideal gas law, the atmospheric density is associated to the atmospheric pressure P as

$$P = \rho_\mathrm{g} g H. \tag{1.7}$$

Inserting this equation and $\tau_\mathrm{s} = 1$ into Equation (1.5), the pressure level where becomes optically thick is estimated as

$$P = \frac{g}{\kappa} \sqrt{\frac{H}{2\pi R_\mathrm{p}}}. \tag{1.8}$$

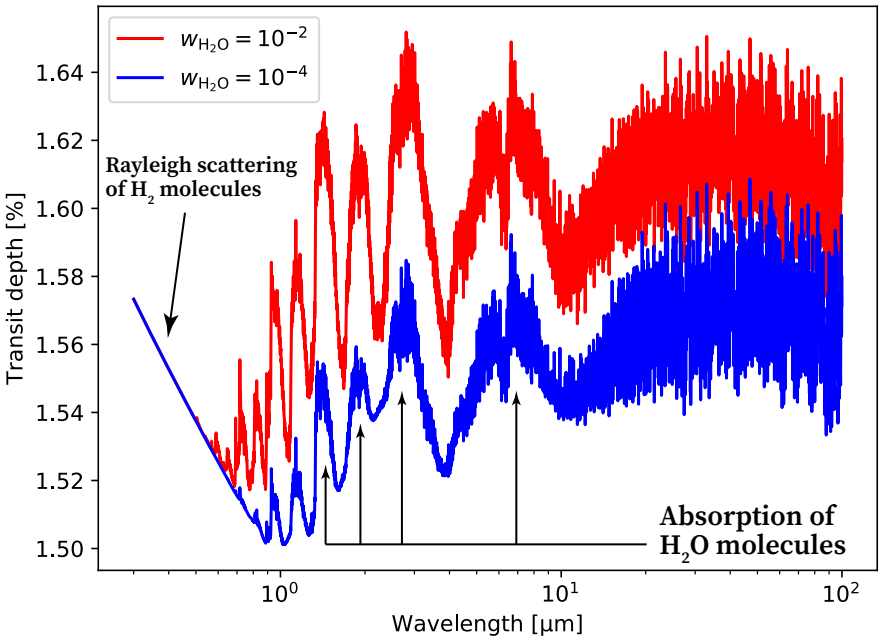


Figure 1.4: An example of synthetic transmission spectrum. The vertical and horizontal axes are transit depth and wavelength. I assume an atmosphere composed of $w_{\rm H_2} = 0.74$, $w_{\rm He} = 0.25$, and $w_{\rm H_2O} = 0.01$ (red) or $w_{\rm H_2O} = 0.0001$ (blue), where $w_{\rm i}$ is the volume mixing ratio of each molecule. Other system parameters are set to $R_{\rm s} = 0.8 R_{\rm sun}$, $R_0 = 1.2 R_{\rm jup}$, $P_0 = 10$ bar, $g = 10$ m s^{-1}, and $T = 1500$ K, as a diagnosis of a hot Jupiter. The synthetic spectra are computed by open-source radiative transfer code, petitRADTRANS (Mollière et al., 2019).

To link the pressure level to the atmospheric thickness, one needs an additional relation, which is given by the hydrostatic balance,

$$P = P_0 \exp\left(-\frac{r - R_0}{H}\right) = P_0 \exp\left(-\frac{\Delta h}{H}\right), \tag{1.9}$$

where $P_0 = P(R_0)$. Equating Equations (1.8) and (1.9), we find

$$\Delta h = H \log\left(\frac{P_0 \kappa}{g}\sqrt{\frac{2\pi R_{\rm p}}{H}}\right) = H \log \tau_0, \tag{1.10}$$

where $\tau_0 = \tau_{\rm s}(R_0)$. Thus, the transit depth is given by

$$D \approx \left(\frac{R_0}{R_{\rm s}}\right)^2 + \frac{2 R_0 H}{R_{\rm s}^2} \log \tau_0, \tag{1.11}$$

Equation (1.11) involves the several important behavior of the transmission spectroscopy. First, the degree of atmospheric signature, represented by the second term in Equation (1.11), is scaled by the atmospheric scale height, H. Second, the degree also depends on the logarithmic abundance of absorbing molecules because $\kappa = q_{\rm i}\sigma_{\rm i}/m_{\rm i}$, where $q_{\rm i}$, $\sigma_{\rm i}$, and $m_{\rm i}$ are the mass mixing ratio, extinction cross section, and the mass of i-th particles, respectively.

Figure 1.4 shows an example of a transmission spectrum of a hypothetical hot Jupiter, computed by open-source radiative transfer code, petitRADTRANS (Mollière et al., 2019). One can

see that the transit depth steeply increases at specific wavelength, which is caused by absorption of H_2O molecules in the atmosphere. The variation is approximately ~ 300 ppm and higher for higher mixing ratio of H_2O molecules. Current and near future instruments can achieve a observational noise floor of 20–50 ppm (Greene et al., 2016; Batalha et al., 2017), thus it is possible to measure these tiny variations and constrain the abundance of gas molecules. In addition, Figure 1.4 shows the continuous increase of transit depth toward short wavelength at $\lambda < 0.7$ μm. This spectral slope is owing to the Rayleigh scattering caused by hydrogen molecules. Supposing $\kappa = \kappa_0 \lambda^\alpha$, the gradient of transit depth is calculated as

$$\frac{dD}{d\log\lambda} = \frac{2R_0 H}{R_s^2}\alpha. \tag{1.12}$$

Equation (1.12) demonstrates that the gradient of the spectral slope is proportional to $H\alpha$. Specifically, the atmospheric extinction in visible wavelength is largely dominated by the Rayleigh scattering of atmospheric molecules, whose opacity is proportional to λ^{-4} (Liou, 2002). This spectral slope caused by the Rayleigh scattering, so-called the Rayleigh slope, is corresponding to $\alpha = -4$. Thus, if the atmosphere is cloud free, measuring the spectral slope might enable us to constrain H and thus atmospheric thickness, offering a hint to break the degeneracy of the interior composition.

1.4 Prevalence of Clouds in Exoplanetary Atmospheres

1.4.1 Featureless transmission spectra

One of serious obstacles in the atmospheric observations is the presence of clouds. This was first suggested by Charbonneau et al. (2002) who reported a transmission spectrum with molecular features weaker than a theoretical prediction, which we call "featureless" spectra, for a hot Jupiter HD209458b. Later, a number of observational studies similarly reported the featureless spectra for various exoplanets (e.g., Sing et al., 2008; Bean et al., 2010; Pont et al., 2013; Crossfield et al., 2013; Kreidberg et al., 2014; Nikolov et al., 2015; Kreidberg et al., 2018; Knutson et al., 2014a,b; Sing et al., 2016; Crossfield & Kreidberg, 2017; Libby-Roberts et al., 2019). Although this is reported by observations of the transmission spectra, other observational methods also suggest the presence of clouds. For example, the survey of phase curve observations[7] found that some exoplanets show light curves likely originated by scattered light from clouds (e.g., Demory et al., 2013a; Angerhausen et al., 2015; Shporer & Hu, 2015; Armstrong et al., 2016). These observations have suggested that clouds are ubiquitously present in the exoplanetary atmospheres.

Let us see the impacts of clouds in the transmission spectrum. Classically, for interpretations of featureless spectra, the exoplanet community has prescribed the effects of clouds by including a gray cloud top at specific altitude (e.g., Howe & Burrows, 2012). Here, the cloud top is defined as an altitude where a cloud becomes optically thick along the line of sight of the observer. Figure 1.5 shows the spectra of cloud-free atmospheres and atmospheres with gray cloud tops. One can see that variation of transit depth caused by H_2O absorption is largely diminished if the gray cloud top is included. This is because, if the cloud is present, transmitted star light cannot pass

[7]The phase curve is an variation of emergent flux from an exoplanet during one planet orbit. This can probe the horizontal temperature and albedo profiles (for a review, see Parmentier & Crossfield, 2018).

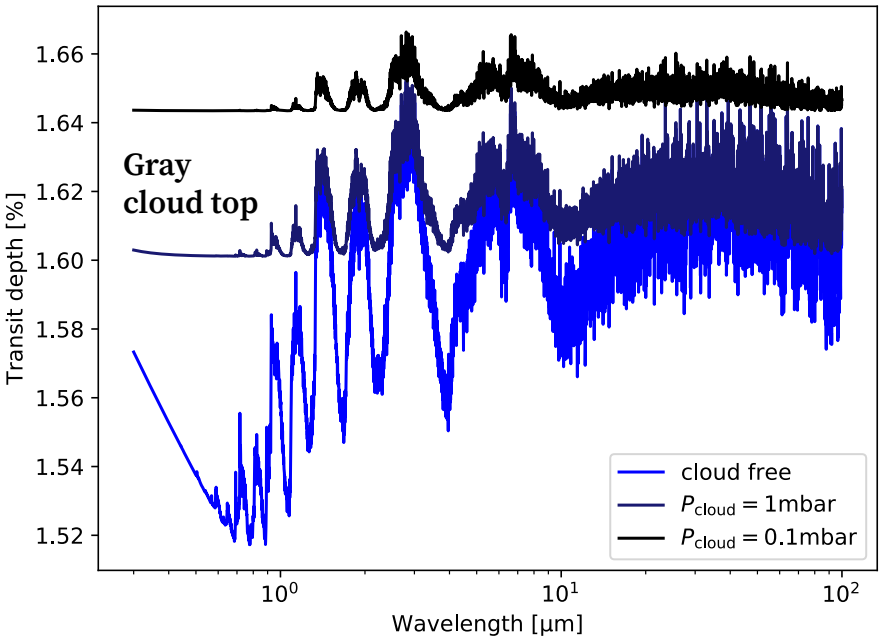


Figure 1.5: Same as Figure 1.4, but including gray cloud top. H_2O mixing ratio of $w_{H_2O} = 0.01$ is assumed for the all spectra. The blue, navy, and black lines show the spectra with cloud-free atmosphere, gray cloud top at $P = 1$ mbar, and at 0.1 mbar, respectively. The spectra are computed by the petitRADTRANS.

through deep atmospheres, and thus transit depth does not decrease even at wavelength in which H_2O opacity is very small. In other words, the prescribed cloud acts as an effective surface of the planet. The higher altitude the cloud top exists, the weaker molecular feature is. Eventually, the cloud makes a transmission spectrum close to a flat line, called a flat spectrum.

Recent observations have suggested that super-Earths are prone to exhibit the featureless or flat spectra (e.g., Bean et al., 2010; Crossfield et al., 2013; Kreidberg et al., 2014, 2018; Knutson et al., 2014a,b; Crossfield & Kreidberg, 2017; Benneke et al., 2019a; Chachan et al., 2019; Libby-Roberts et al., 2019). In general, the effects of cloud is degenerated with the atmospheric scale height, H, because small H similarly leads to a weak spectral signature (see Equation (1.11)). However, for a well-studied super-Earth GJ1214b, Kreidberg et al. (2014) showed that it is hard to explain the observed featureless spectra even if the atmospheric mean molecular weight is so high that the scale height is very small. This strongly suggest that GJ1214b possesses opaque clouds at an extremely high altitude, say $P \sim 10^{-5}$ bar in pressure. Although GJ1214b is the most extreme case, other super-Earths also exhibit featureless spectra. The amplitude of transit radius originated by H_2O absorption is approximately $\approx 6.7H$[8](Crossfield & Kreidberg,

[8]This can be understood as follows. Transit radius is given by $R_{\rm p} = R_0 + H \log\left(P_0 \kappa \sqrt{2\pi R_{\rm p}/H}/g\right)$ according to Equation (1.10). The amplitude of transit radius is evaluated as

$$\Delta R_{\rm p} = H \log\left(\kappa_{\rm high}/\kappa_{\rm low}\right), \tag{1.13}$$

where $\kappa_{\rm high}$ and $\kappa_{\rm low}$ are molecular opacity inside and outside the absorption band. Since the opacity varies with wavelength by ~ 3 orders of magnitude for H_2O (examples can be found in Public opacity database for exoplanetary atmospheres), the amplitude is equivalent to $\sim 7H$.

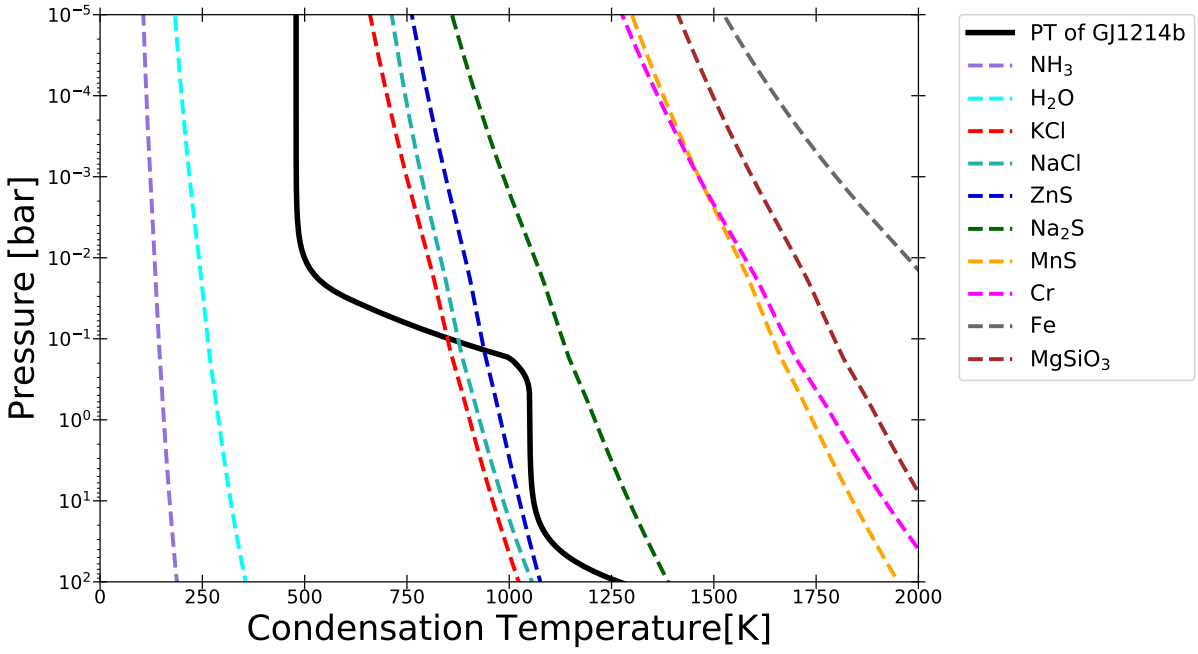


Figure 1.6: Condensation temperature of predominant mineral clouds. The pressure-temperature (PT) profile of GJ1214b calculated by an analytical model of Guillot (2010) is also shown as a black line for comparison. To calculate the condensation temperature, we use the vapor pressure of each species listed in Yau & Rogers (1989) for H_2O, Ackerman & Marley (2001) for NH_3, Fe, $MgSiO_3$, Morley et al. (2012) for KCl, ZnS, Na_2S, MnS, Cr, and Ewing & Stern (1974) for NaCl. The abundance of each molecule is calculated by the method of Morley et al. (2012), where we assume the atmospheric metallicity of $100\times$ solar abundance.

2017). Nevertheless, Crossfield & Kreidberg (2017) showed that, under the assumption of solar-composition atmospheres, the observed amplitude is usually smaller than the atmospheric scale height in the transmission spectra of super-Earths observed by the Hubble space telescope. This implies that cloud-free solar composition atmospheres are ruled out for many super-Earths, and either cloudy atmospheres or metal-rich atmospheres with small H are needed to explain the observations.

1.4.2 Conventional modeling of exoplanetary clouds

Several studies have investigated the formation of exoplanetary clouds. There are at least two candidates that produce featureless spectra introduced in Section 1.4.1, namely condensation clouds and photochemically-produced aerosols. We first define nomenclature used in this thesis since "cloud" and "haze" are often used as different meaning in different studies. In this thesis, we refer "cloud" to aerosols formed via condensation of vapor (as in terrestrial clouds) and "haze" to the aerosols formed via photochemistry of hydrocarbon molecules [9]. We will focus on condensation clouds in this thesis.

Clouds are formed via phase transition of vapor to liquid or solid particles. It has been well know that, in the terrestrial atmosphere, water vapor form clouds via adiabatic cooling. What

[9]Note that photochemical haze is not necessary made of hydrocarbon molecules. In the relatively cool environment, sulfur molecules can also form sulfide hazes via photochemistry.

composition does make up exoplanetary clouds? Since majority of exoplanets are orbiting close to central stars, the atmosphere is too hot to form water clouds, except for several exoplanets orbiting in habitable zones. Instead, it has been suggested that the high atmospheric temperature yields clouds made of condensed solid minerals, called mineral clouds (e.g., Miller-Ricci Kempton et al., 2012; Morley et al., 2013; Lee et al., 2018). The presence of mineral clouds have been suggested from the spectral energy distributions of brown dwarfs (e.g., Burgasser et al., 2002; Saumon & Marley, 2008). Figure 1.6 shows the condensation temperature of several mineral clouds. The condensation temperature is defined as a temperature above which a material is vaporized and calculated by solving

$$q_{\rm i} P = P_{\rm s}(T), \tag{1.14}$$

where $q_{\rm i}$ is the volume mixing ratio of condensing material of species i and $P_{\rm s}$ is the saturation vapor pressure. Figure 1.6 shows that several minerals have the condensation temperature relevant to the atmospheric temperature of close-in exoplanets. For example, exoplanets with $T = 500$–1000 K potentially retain salt clouds, such as KCl, ZnS, and $\rm Na_2S$. For more hotter planets, like $T \sim 1500$ K, silicates and metallic clouds potentially form in their atmospheres. If atmospheric temperature becomes lower than the condensation temperature, one can expect that the material is condensed into clouds. Although many minerals have the condenation temperature higher than atmospheric temperature in Figure 1.6, most of them are condensed into particles at very deep atmospheres, say $P > 10$ bar in pressure. Therefore, in the case of Figure 1.6, mineral clouds responsible to atmospheric observations are KCl and ZnS, as their cloud bases [10] are placed at ~ 0.1 bar.

We note that the condensation temperature is nearly invariable for different atmospheric composition. If we assume a constant latent heat L and specific volume of gas phase much larger than that of condensed phase, the saturation vapor pressure is approximated by (e.g., Yau & Rogers, 1989; Sánchez-Lavega et al., 2004)

$$P_{\rm s} = P_{\rm v,0} \exp\left[-\frac{m_{\rm i} L}{k_{\rm B}}\left(\frac{1}{T} - \frac{1}{T_0}\right)\right], \tag{1.15}$$

where $m_{\rm i}$ is the mass of a condensing molecule. Equation (1.15) is derived from the Clausius-Crapeyron equation and indicates that the vapor pressure exponentially decreases with decreasing the temperature. Combining Equation (1.14) and (1.15), the condensation temperature is estimated as

$$T_{\rm cond} = T_0 \left[1 + \frac{k_{\rm B} T_0}{m_{\rm i} L} \log\left(\frac{P_{\rm v,0}}{q_{\rm i} P}\right)\right]^{-1}. \tag{1.16}$$

Equation (1.16) demonstrates that the condensation temperature only logarithmically increases with increasing the mixing ratio $q_{\rm i}$ and pressure P. This explains the basic trend of Figure 1.6.

To assess the effects of clouds on observations, one must specify the cloud vertical structure above the cloud base; however, this has been highly uncertain to date. Conventionally, most of previous studies have prescribed cloud effects as a merely fitting parameter, such as gray optically thick layer and additional opacity with arbitrarily form (e.g., Howe & Burrows, 2012). This approach has an advantage in retrieval framework (e.g., Benneke & Seager, 2013; MacDonald & Madhusudhan, 2017) to efficiently search what cloud properties are needed to explain the observations. However, this method seriously lacks physical motivations and cannot assess

[10] Cloud base is defined as the height where atmospheric temperature is identical to the condenastion temperature.

what atmospheric properties, such as composition and dynamics, leads to the retrieved cloud properties. In addition, the method tends to suffer from the degeneracy between cloud height and atmospheric metallicity (e.g., Kreidberg et al., 2014; Knutson et al., 2014a).

As another approach, some previous studies tried to calculate the cloud vertical structure using a theoretical model. The most popular model in current exoplanet community is presumably that proposed by Ackerman & Marley (2001). This model calculates the vertical mass distributions of clouds assuming the balance between gravitational settling and upward transport via eddy diffusion. The basic equation is given by

$$-K_{\rm z}\frac{\partial(q_{\rm v}+q_{\rm c})}{\partial z}-f_{\rm sed}w_{*}q_{\rm c}=0, \tag{1.17}$$

where $K_{\rm z}$ is the eddy diffusion coefficient, $q_{\rm v}$ is the mass mixing ratio of condensing vapor, $q_{\rm c}$ is the mass mixing ratio of cloud particles, $w_{*}=K_{\rm z}/H$ is the vertical velocity scale, and $f_{\rm sed}$ is the sedimentation parameter defined as the ratio of mass-weighted particle settling velocity to w_{*}. In practice, the vapor mass mixing ratio at upper cold atmospheres is extremely low because the vapor pressure exponentially decreases with decreasing temperature. Thus, $q_{\rm c}\gg q_{\rm v}$ above at the cloud base. Then, Equation (1.17) is solved as

$$q_{\rm c}=q_{\rm c,0}\left(\frac{P}{P_0}\right)^{f_{\rm sed}}. \tag{1.18}$$

Therefore, the model of Ackerman & Marley (2001) effectively approximates the vertical mass distribution as a power-law function of pressure. Meanwhile, the effective particle radius is determined through the relation of

$$f_{\rm sed}w_{*}=\frac{\int_0^\infty v_{\rm t}m_{\rm c}f(r)dr}{\int_0^\infty m_{\rm c}f(r)dr}, \tag{1.19}$$

where $m_{\rm c}$ is the mass of a cloud particle, $v_{\rm t}$ is the particle settling velocity, and $f(r)dr$ is the number density of cloud particles with radii between r and $r+dr$. The size distribution is usually assumed as a lognormal distribution (Ackerman & Marley, 2001). Thus, the model can calculate the vertical size and mass distributions by a single parameter, $f_{\rm sed}$. Morley et al. (2013, 2015, 2017) for the first time applied this model to KCl and ZnS clouds on super-Earths GJ1214b and GJ436b to explain their featureless spectra. Gao et al. (2017a) used the model to estimate the KCl and ZnS clouds on a warm gas giant Gamma Cephei Ab, though their focus is effects of sulfur hazes on reflected light spectra. MacDonald et al. (2018) applied the model to $\rm H_2O$ and $\rm NH_3$ clouds on cold exo-Jupiters to calculate planetary reflected light spectrum. Most recently, Lines et al. (2019) incorporated the model to a general circulation model (GCM) to study the 3D cloud distributions. Mai & Line (2019) also incorporated the model to retrieval model of the CHIMERA (Line et al., 2013) as a retrieved cloud parameter.

Although the model of Ackerman & Marley (2001) has been extensively used, there are several shortcoming in the model. The most serious shortcoming is the lack of physical motivations to determine $f_{\rm sed}$, leading to large uncertainty in the predicted cloud structure. Previous studies changed $f_{\rm sed}$ as a free parameter (e.g., Morley et al., 2015); however, this obscures whether assumed $f_{\rm sed}$ is physically feasible. Even if feasible, one cannot known what physical processes are going on in the atmosphere to achieve the assumed $f_{\rm sed}$. The parameter $f_{\rm sed}$ is controlled by the settling velocity and thus the sizes of cloud particle, which are controlled by microphysics of

particle growth. In order to predict physically motivated cloud structure, one needs to calculate how the cloud particles are growing and transported in the atmosphere.

A few studies applied a cloud microphysical model to predict the cloud structure in exoplanetary atmospheres. The model developed by Helling et al. (2008) and subsequent studies are probably the most sophisticated microphysical models to date. The model takes into account the nucleation of cloud particles, particle growth via chemical surface reactions of numerous species, and gravitational settling. However, even this model involves several shortcomings. First, the model relies on the classical homogeneous nucleation theory, for which calculated nucleation rate tends to deviate from laboratory and numerical experiments by several orders of magnitude (e.g., Ford, 1997; Lee et al., 2018). Second, the model neglects collision growth of cloud particles, which plays an important role for rain and snowflake formation in terrestrial clouds (e.g., Pruppacher & Klett, 1996). Third, the model assumes that the condensing vapors are instaneously supplied at each altitude, which may lead to significant overestimation of nucleation and condensation rate in upper atmospheres [11]. Finally, the model was originally designed to calculate clouds of high-temperature condensing species, such as TiO_2 and SiO_2, formed in hot brown dwarfs (Woitke & Helling, 2003, 2004) and not applied to relatively cool super-Earths yet, for which prevalence of clouds is suggested by the transmission spectra.

1.5 About this thesis

1.5.1 Purpose

Although probing exoplanetary atmospheres potentially offers valuable information to infer the origin of super-Earths, the atmospheric observations are seriously subject to the presence of clouds. Most previous studies treat the clouds with a highly simplified manner. However, this method obscures whether the assumed cloud structure is physically feasible. Furthermore, the uncertainty of cloud properties makes it difficult to constrain the atmospheric composition.

In this thesis, we aim to establish a new framework to better constrain the atmospheric composition, especially metallicity, of cloudy super-Earths. Using the inferred atmospheric metallicity, we investigate the interior structure of cloudy super-Earths. We finally discuss what we can learn about past formation process from the atmospheric observations. The key concepts of this thesis are cloud microphysics and porosity evolution, as explained in what follows.

1.5.2 New concept

Cloud Microphysics

To overcome the shortcoming of conventional cloud modeling (Section 1.4.2), we establish a cloud microphysical model that explicitly calculates the vertical distributions of particle size and cloud mass density. This clarifies what physical processes are going on in the atmospheres and helps to break the degeneracy between cloud parameters (e.g., cloud-top height) and atmospheric composition. In this thesis, we for the first time investigate the vertical structure of mineral clouds on super-Earths using a cloud microphysical model.

[11] This shortcoming was very recently acknowledged by Woitke et al. (2019) who explicitly calculated vapor transport and consumption via dust surface reactions. They found that the assumption of the instaneous vapor supply leads to overestimate the nucleation rate, number density, and mass mixing ratio by several orders of magnitudes.

Porosity Evolution

As introduced in Section 1.4.2, close-in super-Earths likely possess clouds made of solid mineral particles. Solid aerosols are in general not necessary identical to compact spheres. Rather, they are prone to grow into non-spherical porous particles, as we can learn from the presence of snowflakes on Earth. Nevertheless, current exoplanet community has commonly assumed the cloud particle as a compact sphere. In this thesis, we establish a new framework to model how the particle porosity evolves in exoplanetary atmospheres. We further systematically examine how the porosity affects the vertical distributions of mineral clouds and resulting transmission spectra for the first time.

1.5.3 Outline of this thesis

The organization of this thesis is as follows. In chapter 2, we develop a cloud microphysical model and investigate the vertical structures of mineral clouds in warm super-Earths. We calculate the cloud structure for various atmospheric metallicity and the abundance of cloud condensation nuclei to figure out how the sizes of cloud particles are controlled by microphysical processes. This chapter is based on Ohno & Okuzumi (2017, 2018).

In chapter 3, we investigate how the porosity of mineral cloud particles evolves in exoplanetary atmospheres and influences the cloud structures. We construct the porosity evolution model applicable to atmospheric aerosols. Using a cloud microphysical model coupled with the porosity model, we show that the mineral cloud particles can grow into porous aggregates without serious compression. As a result, the porosity evolution helps to the formation of high-altitude clouds suggested for several super-Earths. This chapter is based on Ohno et al. (2019), accepted for publication in the Astrophysical Journal.

In chapter 4, we examine the transmission spectrum of cloudy super-Earths. In particular, we examine how the clouds of fluffy aggregates influence the observable transmission spectra for the first time. We also calculate the cloud structures and synthetic transmission spectra of several super-Earths, namely GJ1214b, GJ436b, GJ3470b, HD97658b, and HAT-P-11b, to constrain their atmospheric compositions. The implications for future JWST observations are also provided. This chapter is partly based on Ohno et al. (2019), accepted for publication in the Astrophysical Journal.

In chapter 5, we investigate the interior structure and formation process of super-Earths based on results of atmospheric observations. We show that the super-Earths examined in Chapter 4 have the mass of $\sim$ 1–30% in their atmospheres, depending on the ice mass fraction of their core. We also discuss a formation scenario that might explain the dichotomy of the atmospheric metallicity for super-Earths.

Chapter 6 summarizes our findings and future prospect of this thesis. The future prospects partly involve the contents of Ohno & Zhang (2019a,b).

Chapter 2

Microphysical Modeling of Mineral Clouds on super-Earths

Modified from Ohno & Okuzumi (2018), The Astrophysical Journal, 859, 34
Section 2.3 is partly from Ohno & Okuzumi (2017), The Astrophysical Journal, 835, 261

2.1 Abstract

The ubiquity of clouds in the atmospheres of exoplanets, especially of super-Earths, is one of the outstanding issues for transmission spectra survey. The vertical cloud structure is controlled by the sizes of cloud particles; however, it has been poorly understood how the particle size is determined in exoplanetary atmospheres. In this chapter, we develop a cloud microphysical model to investigate the vertical distributions of particle size and mass density of mineral clouds in super-Earths. Our model takes into account the vertical transport and growth of cloud particles in a self-consistent manner, enabling us to predict physically-motivated sizes of cloud particles. We demonstrate that the vertical profiles of mineral clouds significantly vary with the concentration of cloud condensation nuclei and atmospheric metallicity. The particle growth can be demarcated into three typical regimes in terms of the concentration of condensation nuclei and abundance of condensing vapors. In particular, we found that the cloud particles always grow into the sizes larger than the threshold set by particle coagulation. Our result would help to interpret cloud properties retrieved by observations.

2.2 Introduction

Transmission spectroscopy is one of the powerful approaches to probe the composition of exoplanetary atmospheres (e.g., Seager & Sasselov, 2000; Brown, 2001). Recent surveys of transmission spectra have shown that clouds and/or hazes are ubiquitous in exoplanetary atmospheres (e.g., Bean et al., 2010; Narita et al., 2013a,b; Kreidberg et al., 2014, 2018; Knutson et al., 2014a,b; Sing et al., 2016; Crossfield & Kreidberg, 2017; Lothringer et al., 2018; Espinoza et al., 2019; Benneke et al., 2019a). A remarkable feature of the exoplanet clouds/hazes is that some of them are present at extremely high altitude. For example, the super-Earths GJ436b and GJ1214b are suggested to have an opaque cloud/haze at an altitude as high as ~ 0.01–1 mbar (Knutson et al., 2014a; Kreidberg et al., 2014). The presence of the high-altitude clouds/hazes are also suggested for many hot Jupiters (e.g., Sing et al., 2016; Barstow et al., 2017). Understanding the origin of the high-altitudes clouds is important because they potentially offer important clues on the composition and structure of the atmosphere beneath.

One promising mechanism that may form high-altitude clouds on exoplanets is condensation from vapor to particles followed by upward transport by convection or turbulent diffusion (e.g., Ackerman & Marley, 2001) as seen in terrestrial water clouds. In close-in super-Earths where the atmospheric temperature is 500–1000 K, solid minerals such as KCl and ZnS can condense and form clouds (e.g., Miller-Ricci Kempton et al., 2012). Morley et al. (2013, 2015) investigated the vertical distribution of clouds in GJ1214b using the cloud model of Ackerman & Marley (2001). They found that mineral clouds can ascend to extremely high altitude as suggested from the observation of Kreidberg et al. (2014) if a sufficiently low settling velocity for cloud particles is assumed. The particle settling velocity is controlled by various factors, such as an atmospheric density, a particle size, and an internal density. However, because Morley et al. (2013, 2015) parameterized the ratio of the settling velocity to upward velocity as a free parameter, it is unclear whether the assumed settling velocity is realistic. Charnay et al. (2015a,b) investigated the global cloud distribution in GJ1214b using a 3D global circulation model (GCM) combined with a passive tracer model introduced by Parmentier et al. (2013). They showed that the large-scale atmospheric circulation driven by the intense day-night heating contrast can loft cloud particles to altitude high enough to obscure the spectral feature if the atmospheric metallicity is higher than $> 100\times$ solar and the particle radius is ~ 0.5 μm. However, the particle size is a free parameter in their studies. Summarizing, the key factor of the high-altitude cloud formation is a size of a cloud particle particle, while it has been largely uncertain how the size is determined.

In this chapter, we develop a 1D microphysical model to better figure out how the vertical structures of mineral clouds is determined, Our microphysical model takes into account the vertical transport and growth processes of cloud particles in a self-consistent manner. The methodology can provide a physically-motivated size of cloud particles. The organization of this chapter is as follows. In Section 2.3, we introduce a brief overview of the adopted cloud microphysical model. In Section 2.4, we describe the basic equations and numerical setting. In Section 2.5, we show the results of calculations. Then, we discuss how the sizes of cloud particles are determined by microphysical processes in different regime of particle growth. In Section 2.7, we summarize this chapter.

2.3 Overview of an Adopted Microphysical Model

Before moving on methodology section, we briefly review the momentum bulk scheme adopted in this thesis. The momentum scheme was classically used in meteorology community to predict the distribution of terrestrial water clouds (e.g., Ziegler, 1985; Schoenberg Ferrier, 1994). The basic equation describing the growth and transport of cloud particle is given as the Smoluchowski equation (e.g., Seinfeld & Pandis, 2012):

$$\begin{aligned}\frac{\partial f(m)}{\partial t} &= \frac{1}{2}\int_0^{\mathrm{m}} K(m', m-m')f(m')f(m-m')dm' - f(m)\int_0^{\infty} K(m,m')f(m')dm' \\ &+\frac{\partial}{\partial z}\left[\rho_{\mathrm{g}} K_{\mathrm{z}}\frac{\partial}{\partial z}\left(\frac{f(m)}{\rho_{\mathrm{g}}}\right) - v_{\mathrm{t}} f(m)\right] - \frac{\partial}{\partial m}\left[f(m)\dot{m}\right], \end{aligned} \tag{2.1}$$

where $f(m)dm$ is the number density of cloud particles with masses between m and $m+dm$ and n_{g} is the atmospheric mass density. In the right hand, the first and second terms express the gain and loss of particles with via collision, the third term is the vertical transport via eddy diffusion and gravitational settling, and the last term is the advection in mass space due to condensation or evaporation. The basic idea of the momentum scheme is to reduce the Equation (2.1) by introducing a moment defined as

$$\mathcal{L}_{\mathrm{i}} \equiv \int_0^{\infty} m^i f(m) dm. \tag{2.2}$$

Physically, $\mathcal{L}_0 \equiv n_{\mathrm{c}}$ and $\mathcal{L}_1 \equiv \rho_{\mathrm{c}}$ are the number and mass densities of cloud particles, respectively. According to Estrada & Cuzzi (2008), the Equation (2.1) can be rewritten as

$$\begin{aligned}\frac{\partial \mathcal{L}_{\mathrm{i}}}{\partial t} &= \int_0^{\infty}\int_0^{\infty}\left[\frac{1}{2}(m+m')^i - m^i\right] K(m,m')f(m')f(m')dm'dm \\ &+\frac{\partial}{\partial z}\left[\rho_{\mathrm{g}} K_{\mathrm{z}}\frac{\partial}{\partial z}\left(\frac{\mathcal{L}_{\mathrm{i}}}{\rho_{\mathrm{g}}}\right)\right] + \int_0^{\infty} -\frac{\partial}{\partial z}[v_{\mathrm{t}} m^i f(m)] + i m^{i-1}\dot{m} f(m) dm. \end{aligned} \tag{2.3}$$

Equation (2.3) is the basic equation of the microphysical model of moment scheme. Helling et al. (2008) and subsequent studies have applied the moment scheme to calculate the cloud structure in hot substellar atmospheres. The moment scheme has been also adopted in the planet formation community to describe the growth of dust particles in protoplanetary disks (e.g., Sato et al., 2016; Okuzumi et al., 2016; Okuzumi & Tazaki, 2019) and protoatmospheres (Ormel, 2014). In this thesis, we adopt a two-moment bulk scheme that calculates the number and mass densities of cloud particles, which was also used in meteorology community (Ziegler, 1985; Schoenberg Ferrier, 1994). According to Equation (2.3), the evolution of number ($i = 0$) and mass ($i = 1$) densities are described as

$$\frac{\partial n_{\mathrm{c}}}{\partial t} = \frac{\partial}{\partial z}\left[\rho_{\mathrm{g}} K_{\mathrm{z}}\frac{\partial}{\partial z}\left(\frac{n_{\mathrm{c}}}{\rho_{\mathrm{g}}}\right) - v_{\mathrm{t},0} n_{\mathrm{c}}\right] - \frac{1}{2}\int_0^{\infty}\int_0^{\infty} K(m,m')f(m')f(m')dm'dm \tag{2.4}$$

and

$$\frac{\partial \rho_{\mathrm{c}}}{\partial t} = \frac{\partial}{\partial z}\left[\rho_{\mathrm{g}} K_{\mathrm{z}}\frac{\partial}{\partial z}\left(\frac{\rho_{\mathrm{c}}}{\rho_{\mathrm{g}}}\right) - v_{\mathrm{t},1}\rho_{\mathrm{c}}\right] + \int_0^{\infty}\dot{m} f(m) dm, \tag{2.5}$$

where we define the averaged settling velocity of

$$v_{\mathrm{t,i}} \equiv \frac{\int_0^{\infty} v_{\mathrm{t}} m^i f(m) dm}{\int_0^{\infty} m^i f(m) dm}. \tag{2.6}$$

In the right hands of Equation (2.4) and (2.5), the second terms respectively express the decrease of number density via collision growth and increase (decrease) of mass density via vapor condensation (evaporation).

To solve Equations (2.4) and (2.5), one needs to specify the shape of a size distribution $f(m)$. The moment scheme used in meteorology community adopts a variety of the size distribution, such as monodisperse, exponential, lognormal, and gamma distribution (e.g., Ziegler, 1985; Schoenberg Ferrier, 1994; Straka & Mansell, 2005). The simplest size distribution is the monodisperse distribution, given by

$$f(m) = n_{\rm c}\delta(m - m_{\rm p}), \tag{2.7}$$

where $\delta(x)$ is the Dirac delta function and $m_{\rm p}$ is the peak mass. The assumption of monodisperse distribution implies that the cloud mass is largely concentrated in particles with a mass of $m_{\rm p}$. Inserting Equation (2.7) into (2.4) and (2.5), we obtain

$$\frac{\partial n_{\rm c}}{\partial t} = \frac{\partial}{\partial z}\left[\rho_{\rm g} K_{\rm z} \frac{\partial}{\partial z}\left(\frac{n_{\rm c}}{\rho_{\rm g}}\right) - v_{\rm t}(m_{\rm p}) n_{\rm c}\right] - \frac{1}{2} K(m_{\rm p}, m_{\rm p}) n_{\rm c}^2 \tag{2.8}$$

and

$$\frac{\partial \rho_{\rm c}}{\partial t} = \frac{\partial}{\partial z}\left[\rho_{\rm g} K_{\rm z} \frac{\partial}{\partial z}\left(\frac{\rho_{\rm c}}{\rho_{\rm g}}\right) - v_{\rm t}(m_{\rm p}) \rho_{\rm c}\right] + \dot{m}(m_{\rm p}) n_{\rm c}. \tag{2.9}$$

The mean particle mass, $m_{\rm p}$, can be determined from the moment of the mass distributions (Ormel & Spaans, 2008; Sato et al., 2016),

$$m_{\rm p} \equiv \frac{\mathcal{L}_2}{\mathcal{L}_1} = \frac{m_{\rm p}^2 n_{\rm c}}{m_{\rm p} n_{\rm c}} = \frac{\rho_{\rm c}}{n_{\rm c}}. \tag{2.10}$$

One can readily solve Equations (2.8), (2.9), and (2.10) by including the source terms originated by collision and condensation growth. The explicit formula of the microphysical terms can be found in relevant literature (e.g., Yau & Rogers, 1989; Pruppacher & Klett, 1996; Seinfeld & Pandis, 2012). We will explain the adopted formula in Section 2.4.5.

Here, we show the vertical structure of terrestrial cumulus clouds calculated by our two-moment method and that retrieved by in-situ observations in Figure 2.1. The figure is taken from our previous study (Ohno & Okuzumi, 2017), where we apply the two-moment scheme to shallow convective water clouds on Earth. The cloud and rain particles were classified in terms of net vertical velocity, $w_* - v_{\rm t}$—cloud particles are transported upward, while rain particles are settling downward. The adopted model is a relatively simple one. Nevertheless, our model reasonably reproduces the profiles retrieved by observations to an order of magnitude. Notably, the vertical distributions of cloud (rain) mass density is reasonably reproduced. Since the contribution of atmospheric extinction on transit depth is only logarithmically dependent on the atmospheric opacity (Equation 1.11), the discrepancy of a factor of few would be less significant.

The discrepancy seen in Figure 2.1 may originate from the multi-dimensional nature of terrestrial clouds. For example, the model did not include the effect of the entrainment of ambient dry airs (e.g., Pruppacher & Klett, 1996). The entrainment reduces the temperature and humidity of the updraft, both of which act to suppress the condensation growth of cloud particles. The suppressed growth in turn leads to a slower decrease in the cloud number density with height. Thus, including the entrainment may further reconcile the model predictions and observations.

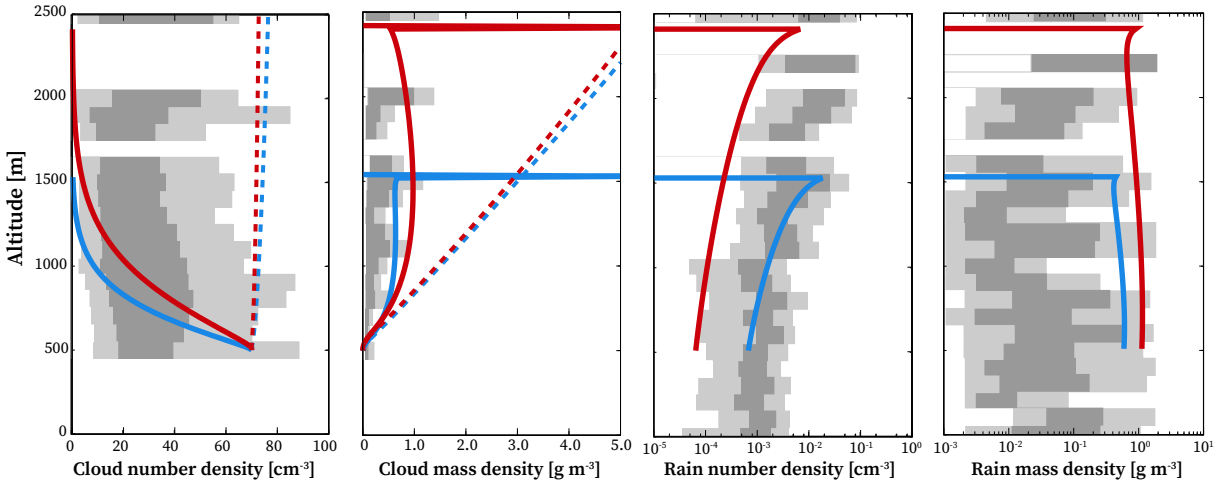


Figure 2.1: Vertical structure of trade cumulus clouds on Earth. The figure is taken from Ohno & Okuzumi (2017). From left to right, each panel shows the vertical distributions of number density of cloud particles, mass density of cloud particles, number density of rain particles, and mass density of rain particles, respectively. The red and blue lines show the profiles calculated by two-moment bulk scheme for mean vertical velocity of 0.9 and 2.0 m s^{-1}, respectively. The dotted lines show the profiles without collision growth and fail to form rain particles. The light- and dark-gray shaded areas span the 5–95% and 25–75% ranges of the in-situ observational data from the Rain in Cumulus over the Ocean (RICO) Field Campaign, taken from Figure 8 of vanZanten et al. (2011).

However, additional unknown parameters are needed to take into account the effects of the entrainment for 1D exoplanetary cloud models. Future cloud-resolving models may be able to assess the importance of the entrainment for exoplanets.

2.4 Method

2.4.1 Outline

We extend the microphysical model originally developed by Ohno & Okuzumi (2017) to predict the vertical distributions mineral clouds in exoplanetary atmospheres. The cloud model of Ohno & Okuzumi (2017) adopts a 1D Eulerian framework, and provides the vertical distributions of number (n_c) and mass (ρ_c) densities of cloud particles by taking into account the vertical transport of cloud particles due to the updraft motion and gravitational settling, and the particle growth via condensation and coalescence (see Section 2.4.3 and 2.4.5). In this study, we take into account the vertical transport of cloud particles via eddy diffusion (e.g., Ackerman & Marley, 2001). In this chapter, we suppose a hypothetical planet like GJ1214b to calculate atmospheric structures.

Following previous studies, we consider the clouds composed of solid KCl particles formed through the condensation of KCl vapor (Charnay et al., 2015a; Morley et al., 2013, 2015). KCl is expected to be the most abundant condensable material in the pressure-temperature profile on GJ1214. The initial cloud particles are assumed to form at the cloud base through the condensation of vapor onto the small nuclei that already exist in the atmosphere, the process so called

heterogeneous nucleation. On the Earth, such small nuclei, called the cloud condensation nuclei (CCNs), include sea salt, volcano ash, and dust from the land (Yau & Rogers, 1989). The amount of CCNs on exoplanets is highly uncertain as well as is their composition, and therefore we take the number density of CCNs as a free parameter. The height of the cloud base is determined from the comparison between the atmospheric temperature and condensation temperature (see Section 2.4.2). The condensation temperature is defined as the temperature at which the partial pressure of a volatile is equal to its saturation vapor pressure.

Following Ohno & Okuzumi (2017), we assume that the cloud particles have the characteristic radius $r_{\rm c}$ and corresponding mass $m_{\rm c} = (4\pi/3)\rho_{\rm int} r_{\rm c}^3$, where $\rho_{\rm int}$ is the internal density of the particles. The internal density is identical to material density for compact-sphere clouds, while varies during particle growth for aggregate clouds. Assuming the mass distribution is narrowly peaked at $m \approx m_{\rm c}$, the number and mass densities are related by $\rho_{\rm c} = m_{\rm c} n_{\rm c}$. Such frameworks are called the double-moment bulk schemes in meteorology (e.g., Ziegler, 1985; Schoenberg Ferrier, 1994) and the characteristic size method in planetary formation community (e.g., Birnstiel et al., 2012; Ormel, 2014; Sato et al., 2016). This method allows us to derive the physical understanding from calculations more clearly, and to perform the calculations with much little computational time compared to spectral bin schemes (e.g., Brauer et al., 2008) that solve the evolution of the full size distribution (see also Section 2.3).

We investigate the influences of atmospheric metallicity on the vertical profiles of clouds in super-Earths. In this thesis, the atmospheric metallicity refers to the ratio of atmospheric heavy element abundance to that of the solar atmosphere, i.e., $(N_{\rm Z}/(N_{\rm H}+N_{\rm He}))/(N_{\rm Z}/(N_{\rm H}+N_{\rm He}))_{\rm solar}$. Recent theoretical studies suggested that the atmospheres of super-Earths potentially have the metallicities higher than solar, and even higher than $100\times$ solar, depending on the properties of the building blocks of planets (Fortney et al., 2013; Venturini et al., 2016). The interior modeling also showed that GJ1214 b might have a steam atmosphere mainly composed of water vapor (Rogers & Seager, 2010; Valencia et al., 2013). Therefore, we take the atmospheric metallicity as a free parameter widely ranging from the metallicity of $1\times$ solar to water vapor atmosphere. Here, the vapor atmosphere is corresponding to the limit of the high metallicity, and the atmosphere is assumed to be made of H_2O. The metallicity difference provides the different pressure-temperature structure, total cloud mass, and eddy diffusion coefficient.

2.4.2 Construction of Vertical Structure

To determine the location of the cloud base, one must assume the pressure-temperature (PT) structure of an atmosphere. Here, we construct the PT structure using the analytical model of radiative atmosphere described by Guillot (2010) under the assumption of hydrostatic equilibrium. Guillot (2010) derived the analytical solution of global mean thermal profiles that gives good agreement with the predictions from sophisticated simulations. The stellar effective temperature, radii, semi-major axis, and planetary radii of GJ1214 b and GJ436 b are taken from the Exoplanet.eu catalog. Following Guillot (2010), the temperature in each atmospheric layer is given by

$$
\begin{aligned}
T^4 &= \frac{3T_{\rm int}^4}{4}\left[\frac{2}{3}+\tau\right] + \frac{3T_{\rm irr}^4}{4} f \\
&\quad \times \left[\frac{2}{3} + \frac{1}{\gamma\sqrt{3}} + \left(\frac{\gamma}{\sqrt{3}} - \frac{1}{\gamma\sqrt{3}}\exp\left(-\gamma\sqrt{3}\tau\right)\right)\right], \qquad (2.11)
\end{aligned}
$$

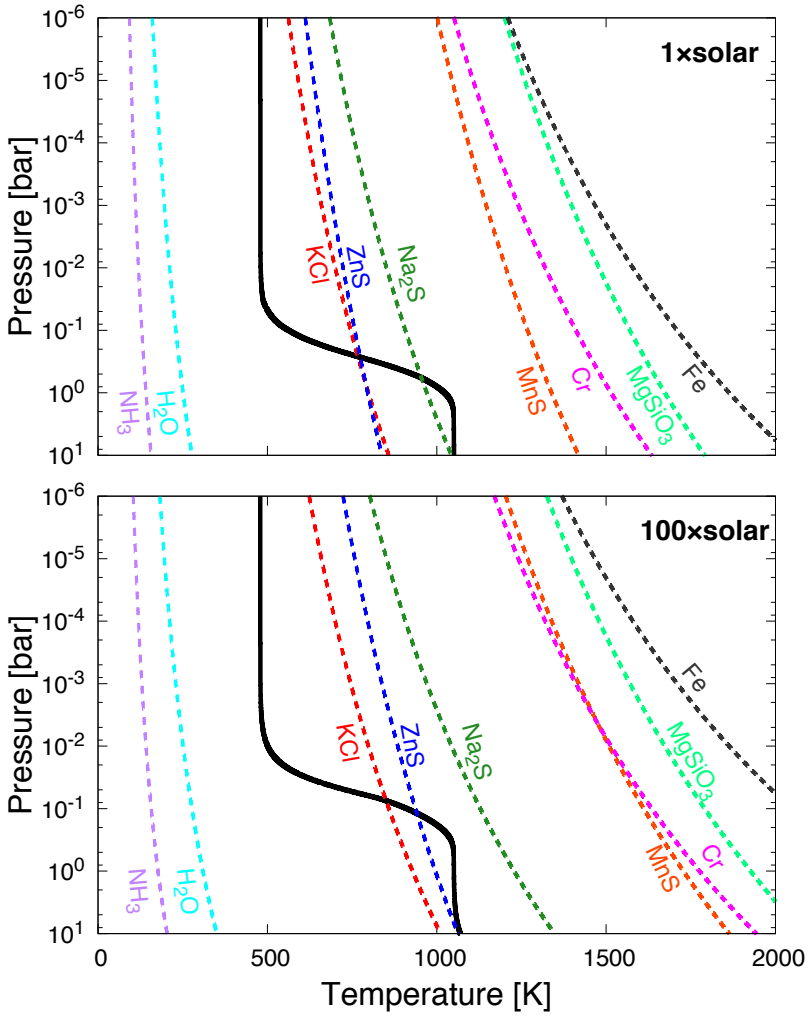


Figure 2.2: P-T profiles of GJ1214 b and the vapor pressure curves for the metallicity of $1\times$ solar (top) and $100\times$ solar (bottom) abundance, respectively. The vapor pressures used in the figures are taken from Yau & Rogers (1989); Ackerman & Marley (2001); Morley et al. (2012). The solid black lines are the P-T structure assuming the heat redistribution around the entire planet ($f = 1/4$).

where τ is the vertical infrared optical depth τ is given by

$$\tau(z) = \int_z^\infty \rho_{\rm g} \kappa_{\rm th} dz', \tag{2.12}$$

where $\kappa_{\rm th}$ is the atmospheric infrared opacity. The $f = 1/4$ is the heat redistribution factor under the assumption of the radiation redistributed around the entire planet, $T_{\rm int}$ is the intrinsic effective temperature, $T_{\rm irr}$ is the irradiation effective temperature, and the $\gamma = \kappa_{\rm v}/\kappa_{\rm th}$ is the ratio of the visible to infrared opacities, respectively. For GJ1214 b, we take $T_{\rm int} = 60$ K (Rogers & Seager, 2010) and $\gamma = 0.038$ so that reproduces the P-T structure predicted by radiative transfer models of Miller-Ricci & Fortney (2010).

We calculate τ using the fitting formula of Rosseland mean opacity of a cloud-flee atmosphere described by Freedman et al. (2014). This fitting formula is a function of atmospheric metallicity, pressure, and temperature, and valid for $P = 10^{-6}$–3×10^2 bar and $T = 75$–4000 K.

Although the opacity table for higher metallicity ($> 50\times$ solar) is not available so far, the fitting formula can provide the qualitative results for such high metallicity atmospheres. For water vapor atmosphere, we use the opacity of $50\times$ solar metallicity that yields the similar P-T structure to that for a water vapor (Miller-Ricci & Fortney, 2010) for simplify. We also neglect the opacity of cloud particles that may change the location of cloud base. We will briefly examine the possible effects of radiative feedback in Section 7.2.1.

Figure 2.2 shows the vertical P-T structures of GJ1214 b for $1\times$ and $100\times$ solar metallicity and the condensation temperature at each atmospheric layer. We predict the condensation temperature for each volatile using the saturation vapor pressure described in Yau & Rogers (1989); Ackerman & Marley (2001); Morley et al. (2012). The vapor species has a solid phase if the atmospheric temperature is lower than its condensation temperature. Therefore, for each volatile species, the cloud base is expected to be placed at the location where the P-T curve intersects the curve of condensation temperature of the species. Figure 2.2 indicates that the KCl, ZnS, and Na_2S are condensible for $1\times$ solar metallicity case, and KCl and ZnS are condensible for $100\times$ solar metallicity. Since the abundance of KCl vapor is higher than that of ZnS vapor for solar like atmosphere (Morley et al., 2012), we focus on the mineral clouds of KCl in this study. The cloud base for KCl is placed at ~ 0.4 bar for $1\times$ solar metallicity, ~ 0.1 bar for $10\times$ solar metallicity, and ~ 0.07 bar for $100\times$ solar metallicity, respectively, which is in good agreement with the prediction of previous studies (Miller-Ricci Kempton et al., 2012; Morley et al., 2013; Charnay et al., 2015a).

2.4.3 Transport Equations

We calculate the vertical distributions of the number and mass densities of cloud particles by taking into account their growth and vertical transport. The microphysics of cloud formation is complex (see e.g., Rossow, 1978; Yau & Rogers, 1989; Pruppacher & Klett, 1996; Seinfeld & Pandis, 2012). However, Ohno & Okuzumi (2017) showed that inclusion of condensation and collisional growth is enough to approximately reproduce the observations of terrestrial water clouds and Jovian ammonia clouds. Therefore, we take into account the condensation and collisional growth in this study.

Following Charnay et al. (2015a), we consider the clouds formed through the large scale atmospheric motion driven by the intense day-night heating contrast. Previous studies showed that the global averaged distributions of such clouds can be approximately reproduced by a 1D advection-diffusion model with an empirical parameterization of the eddy diffusion coefficient K_z (Parmentier et al., 2013; Charnay et al., 2015a). Hence, the master equations used here are constructed by adding the source terms expressing particle growth to the 1D advection-diffusion model:

$$\frac{\partial n_c}{\partial t} = \frac{\partial}{\partial z}\left[n_g K_z \frac{\partial}{\partial z}\left(\frac{n_c}{n_g}\right) + v_t(r) n_c\right] - \left|\frac{\partial n_c}{\partial t}\right|_{coll}, \tag{2.13}$$

$$\frac{\partial \rho_c}{\partial t} = \frac{\partial}{\partial z}\left[\rho_g K_z \frac{\partial}{\partial z}\left(\frac{\rho_c}{\rho_g}\right) + v_t(r) \rho_c\right] + \left(\frac{\partial \rho_c}{\partial t}\right)_{cond}, \tag{2.14}$$

$$\frac{\partial \rho_v}{\partial t} = \frac{\partial}{\partial z}\left[\rho_g K_z \frac{\partial}{\partial z}\left(\frac{\rho_v}{\rho_g}\right)\right] - \left(\frac{\partial \rho_c}{\partial t}\right)_{cond}, \tag{2.15}$$

where v_t is the terminal velocity of cloud particles, K_z is the eddy diffusion coefficient, and ρ_v is the vapor mass density. The terminal velocity depends on the particle size and atmospheric

Table 2.1: Model parameters for GJ1214 b

metallicity	H (km)	$q_{\rm KCl}$ (mol/mol)	K_0 ($\rm m^2\ s^{-1}$)	Δz (km)
1×solar	190	2.54×10^{-7}	7.0×10^2	20
10×solar	180	2.52×10^{-6}	2.8×10^3	20
100×solar	103	2.32×10^{-5}	3.0×10^3	10
Steam	25	2.61×10^{-4}	3.0×10^2	5

density as introduced in Section 2.4.4. Each source term, introduced in Section 2.4.5, expresses the particle growth via condensation and collision of each particle. Without these terms, the Equations (2.13)–(2.14) are reduced to the 1D transport model for fixed size particles used by Parmentier et al. (2013) and Charnay et al. (2015a).

The eddy diffusion coefficient $K_{\rm z}$ represents the strength of effective vertical mixing for cloud particles. In this study, we adopt the empirical formula of $K_{\rm z}$ proposed by Charnay et al. (2015a),

$$K_{\rm z} = K_0 \left(\frac{P}{P_0} \right)^{-2/5}, \tag{2.16}$$

where K_0 is the value of $K_{\rm z}$ at a reference pressure P_0. Charnay et al. (2015a) derived this formula from 3D GCM simulations that takes into account the transport of fixed size particles. Since they suggested that $K_{\rm z}$ is almost independent of particle size (see the figure 14 of Charnay et al., 2015a), we use Equation (2.16) for all range of particle size in our calculations. The exponent of $-2/5$ is similar to the $K_{\rm z} \propto P^{-1/3}$ predicted by mixing theory (Ackerman & Marley, 2001) and $K_{\rm z} \propto P^{-1/2}$ predicted by other GCM simulations for hot Jupiter (Parmentier et al., 2013). According to Charnay et al. (2015a), we choose the reference pressure of $P_0 = 1$ bar and take the values of K_0 as summarized in Tables 2.1. For GJ1214 b, we use the values of K_0 derived from the power-law fitting to the GCM data (see Figure 14 of Charnay et al., 2015a), which are metallicity-depenent.

2.4.4 Terminal Velocity of Cloud Particles

A terminal velocity $v_{\rm t}$ is determined by the balance between gravitational force and gas frictional force. The gas frictional force depends on the behavior of the gas flow around the settling particles, and varies with the particle size, settling velocity, and the mean free path of gas particles (e.g., Rossow, 1978; Woitke & Helling, 2003). In this study, we adopt the following formula of the terminal velocity,

$$v_{\rm t}(r_{\rm c}) = \frac{2\beta g r_{\rm c}^2 \rho_{\rm p}}{9\eta} \left[1 + \left(\frac{0.45 g r_{\rm c}^3 \rho_{\rm g} \rho_{\rm p}}{54\eta^2} \right)^{2/5} \right]^{-5/4}, \tag{2.17}$$

where η is the dynamic viscosity of the atmosphere and β is the *slip correction factor*. β accounts for the transition of gas drag behavior from viscous flow (Stokes's law) to free molecular flow (Epstein's law) around the particle, given by (Davies, 1945)

$$\beta = 1 + {\rm Kn_g}[1.257 + 0.4\exp(-1.1/{\rm Kn_g})], \tag{2.18}$$

where ${\rm Kn}_g = l/r_{\rm c}$ is the gas Knudsen number and l is the gas mean free path. Equation (2.17) without β is same as the Equation (23) in Ohno & Okuzumi (2017) that asymptotically reaches

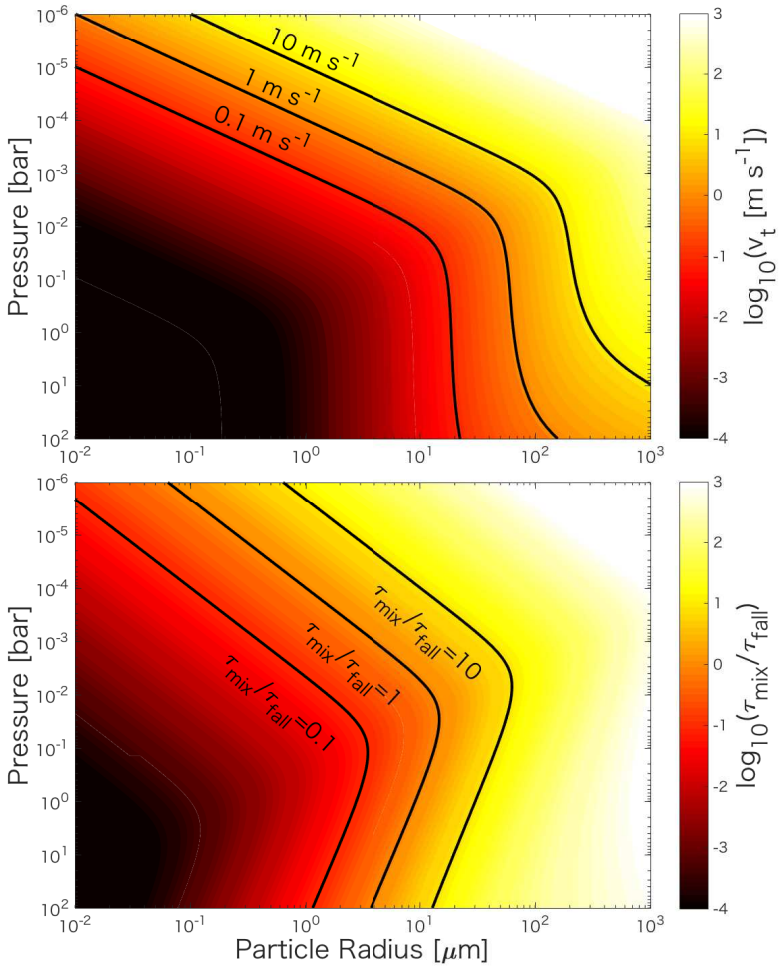


Figure 2.3: Terminal velocity of compact KCl particles (colorscale, top panel) and the ratio of the mixing timescale to the falling timescale (colorscale, bottom panel). The horizontal axis shows particle radius and the vertical axis shows atmospheric pressure, respectively. Each black contour shows the pressure and particle radius corresponding to $v_{\rm t} = 0.1$, 1, and 10 m s^{-1} for the top panel, and $\tau_{\rm mix}/\tau_{\rm fall} = 0.1$, 1, and 10 for the bottom panel, respectively. Here we assume $1\times$ solar metallicity, $K_0 = 10^3$ m^2 s^{-2}, and isothermal ($T = 500$ K) atmosphere.

the Stokes's law for a laminar flow limit, Newton's law for a turbulent flow limit, and well reproduces the intermediate regime predicted by experiment (see the Figure 7 in Ohno & Okuzumi, 2017). Top panel of Figure 2.3 shows the terminal velocity as a function of particle size and atmospheric pressure. Figure 2.3 shows the terminal velocity increases with height in the upper atmosphere because of the Epstein's law arisen from the low atmospheric density.

We also show the ratio of the mixing timescale $\tau_{\rm mix}$ to the falling timescale $\tau_{\rm fall}$ in the bottom panel of Figure 2.3. Each timescale is defined as

$$\tau_{\rm mix} = \frac{H^2}{K_{\rm z}} \tag{2.19}$$

and

$$\tau_{\rm fall} = \frac{H}{v_{\rm t}}, \tag{2.20}$$

where $H = k_{\rm B}T/m_{\rm g}$ is the pressure scale height, respectively. In Figure 2.3, the temperature, the reference eddy diffusion coefficient, and the mean molecular weight are assumed to be $T = 500$ K, $K_0 = 10^3$ m^2 s^{-1}, and $\mu_{\rm g} = 2.3$, respectively. Cloud particles ascend if $\tau_{\rm mix} \ll \tau_{\rm fall}$, and fall if $\tau_{\rm mix} \gg \tau_{\rm fall}$. Figure 2.3 indicates that the cloud particles are required to maintain their size $r0.05$ μm to ascend above 10^{-5} bar under the assumed parameters.

2.4.5 Microphysics of Particle Growth

The cloud particles ascend from the cloud base while growing through condensation of ambient saturated vapors and collision with each other. The condensation dominates the growth of small particles due to the relatively short timescale. The growth rate of $\rho_{\rm c}$ via condensation depends on the behavior of vapor molecule motion, and is expressed by (Yau & Rogers, 1989; Woitke & Helling, 2003)

$$\left(\frac{\partial \rho_{\rm c}}{\partial t}\right)_{\rm cond} = 4\pi r_{\rm c}^2 n_{\rm c}(\rho_{\rm v} - \rho_{\rm s}) \times \min\left[C_{\rm re}, \frac{D}{r_{\rm c}}\left(1 + \left(\frac{m_{\rm v}L}{k_{\rm B}T} - 1\right)\frac{LD\rho_{\rm s}}{KT}\right)^{-1}\right], \tag{2.21}$$

where $\rho_{\rm v}$ is the vapor mass density, $\rho_{\rm s}$ is the saturation vapor density, $C_{\rm re} = \sqrt{k_{\rm B}T/2\pi m_{\rm v}}$ is the relative velocity of vapor molecules, $m_{\rm v}$ is the mass of the vapor molecules, L is the specific latent heat of condensation, and D is the molecular diffusion coefficient of vapor in ambient air, respectively. The first formula in the bracket corresponds to the free molecular flow regime (Woitke & Helling, 2003) in which the vapor molecules are freely impinging onto the particles. The second formula corresponds to the diffusive regime (Yau & Rogers, 1989) in which the vapor molecules behave as continuum.

Collisional growth is induced by the relative velocity arisen from both gravitational settling and Brownian motion of particles. In thi chapter, we refer the collisional growth by gravitational settling as *coalescence* and that by Brownian motion as *coagulation*. Then the decrease in number density via collisional growth is expressed by

$$\left|\frac{\partial n_{\rm c}}{\partial t}\right|_{\rm coll} = \left|\frac{\partial n_{\rm c}}{\partial t}\right|_{\rm coag} + \left|\frac{\partial n_{\rm c}}{\partial t}\right|_{\rm coal}, \tag{2.22}$$

where $|\partial n_{\rm c}/\partial t|_{\rm coag}$ is the decrease in number density for coagulation and $|\partial n_{\rm c}/\partial t|_{\rm coal}$ is that for coalescence. The expression of $|\partial n_{\rm c}/\partial t|_{\rm coag}$ depends on particle Knudsen number ${\rm Kn_p}$ defined as

$${\rm Kn_p} = \frac{\beta}{6\eta r_{\rm c}^2}\sqrt{\frac{m_{\rm c}k_{\rm B}T}{2\pi}}, \tag{2.23}$$

The Brownian motion of particles is diffusive for ${\rm Kn_p} \ll 1$ and ballistic for ${\rm Kn_p} \gg 1$. The rate of decrease of particle number density via coagulation is given by (Seinfeld & Pandis, 2012)

$$\left|\frac{\partial n_{\rm c}}{\partial t}\right|_{\rm coag} = \begin{cases} 8\sqrt{\dfrac{\pi k_{\rm B}T}{m_{\rm c}}} r_{\rm c}^2 n_{\rm c}^2 & ({\rm Kn_p} > 1/\sqrt{2}) \\ \dfrac{4k_{\rm B}T\beta}{3\eta} n_{\rm c}^2 & ({\rm Kn_p} < 1/\sqrt{2}), \end{cases} \tag{2.24}$$

The transition takes pace at $r_c \approx 0.07$ μm under the assumptions of $T = 1000$ K, $P = 0.1$ bar, and $m_g = 2$ amu, which are equivalent to the parameters for the cloud base.

For the coalescence growth, the rate of decrease of number density $|\partial n_c/\partial t|_{coal}$ is given by (Rossow, 1978)

$$\left|\frac{\partial n_c}{\partial t}\right|_{coal} \approx 2\pi r_c^2 n_c^2 \Delta v E, \tag{2.25}$$

where Δv is the relative velocity induced by the gravitational settling, and E is the collection efficiency defined as the ratio of the effective collisional cross section to the geometric cross section (e.g., Pruppacher & Klett, 1996). For the relative velocity, Sato et al. (2016) and Krijt et al. (2016) showed that the characteristic size approach with $\Delta v = 0.5 v_t(r)$ is in good agreement with the results of spectral bin schemes, and therefore we assume $\Delta v = 0.5 v_t(r_c)$. The collection efficiency E accounts for the effect of the gas flow around the particle moving relative to the background gas, and is expressed in terms of Stokes number

$$\mathrm{Stk} = \frac{v_t(r_c)\Delta v}{g r_c}, \tag{2.26}$$

which is defined as the ratio of the stopping time $= v_t(r_c)/g$ to the crossing time $\sim r_c/\Delta v$. When $\mathrm{Stk} \ll 1$, the particles is strongly coupled to the gas flow around the another particles, and hence E behaves as $E \approx 0$ (Rossow, 1978). We evaluate E using a smoother analytic function of Guillot et al. (2014) given by

$$E = \max[0, 1 - 0.42\mathrm{Stk}^{-0.75}], \tag{2.27}$$

which vanishes at $\mathrm{Stk} < 0.3$ and approaches unity at $\mathrm{Stk} \gg 1$. If $\mathrm{Kn}_g > 1$, we assumed $E = 1$ because the influence of the gas on the particle trajectory should be weak in that region (Rossow, 1978).

2.4.6 Numerical Procedure

We numerically solve the Equations (2.13)–(2.15) until the system reaches to the steady-state profiles. The initial number density of the cloud particles at the cloud base is parameterized by the CCN number density n_{CCN}. We take the n_{CCN} as a free parameter widely ranging as 10^6–10^{15} m^{-3}. Since the composition of the CCNs in close-in super-Earths is unknown, we assume the bulk density of the CCN as that of KCl. This assumption does not affect the calculated cloud vertical profiles as long as the mass fraction of the CCNs in the cloud particles is much smaller than that of condensed vapors. Therefore, we choose the upper limit of n_{CCN} so that the total mass of CCNs does not exceed that of KCl vapor at the cloud base. We set the radii of CCNs as $r_{CCN} = 0.001$ μm, and then $n_{CCN} \approx 10^{15}$ m^{-3} corresponds to the upper limit for our calculations.

We choose the flux of a lower boundary condition so that n_c/n_g, ρ_c/ρ_g, and ρ_v/ρ_g keep the values of the cloud base. We adopt the zero-flux boundary condition at the top of the computational domain which is located at $P = 10^{-8}$ bar. The vertical coordinate z is discretized into linearly spaced bins. We use the different grid width for different atmospheric metallicity as summarized in Table 2.1. The time increment Δt is chosen at every time step so that the fractional decreases in n, ρ_c, and ρ_v do not exceed 0.5, i.e.,

$$\Delta t \leq -0.5 \times \min[(\partial \ln n/\partial t)^{-1}, (\partial \ln \rho_c/\partial t)^{-1}, (\partial \ln \rho_v/\partial t)^{-1}]. \tag{2.28}$$

However, this expression yields very small Δt because the time increment determined by condensation is much shorter than that for collisional growth and vertical transport. To avoid it, we adjust the time increment as $\Delta t \leq -0.5 \times (\partial \ln n/\partial t)^{-1}$ if $(\partial \ln \rho_{\rm c}/\partial t)^{-1} < 0.1 \times (\partial \ln n/\partial t)^{-1}$. In this case, we convert the all excess/lack of vapor from saturation value into cloud particles.

We calculate the mean molecular weight of the atmosphere assuming hydrogen-helium-water mixture in accordance with Fortney et al. (2013). Elemental abundances are taken from Lodders (2003). The mixing ratio of KCl vapor $q_{\rm KCl}$ below the cloud base is calculated assuming the number of KCl molecules is equal to that of K. For the steam atmosphere and the metallicity of $1000\times$ solar, we evaluate the mean molecular weight as that of water, and $q_{\rm KCl}$ as a ratio of K to O because the atmosphere is dominated by water rather than hydrogen for extremely metal-enriched cases. We summarize the $q_{\rm KCl}$, K_0, and H at the upper isothermal region used here in Table 2.1.

2.5 Results of a Cloud Microphysical Model

In this section, we aim to figure out physical mechanisms that control the vertical distributions of the cloud particle size. Figure 2.4 shows the calculated vertical profiles of mineral clouds in GJ1214 b. We find that the cloud particles grow only near the cloud base (left column in Figure 2.4) and stop growing in the upper atmosphere where $P \leq 10^{-3}$ bar. This occurs because the mixing timescale $\tau_{\rm mix} \propto K_{\rm z}^{-1} \propto P^{2/5}$ decreases with height, and eventually becomes shorter than the timescales of condensation, coagulation, and coalescence. The trends is also seen in the results of a contemporaneous study of Gao et al. (2018) who fully solved the evolution of particle size distribution. The final particle radius ranges from 1 to 2 μm for the metallicity of $1\times$ solar, 0.9 to 4 μm for $10\times$ solar, 1.5 to 10 μm for $100\times$ solar, and 5 to 30 μm for water vapor atmosphere, respectively. Figure 2.4 indicates that the final particle size decreases with the $n_{\rm CCN}$ and approaches a minimum value in the limit of high $n_{\rm CCN}$. In Section 2.6 we investigate how the final particle size is determined in detail. We also find that a higher metallicity leads to a larger final size, although its effect is small compared to that of CCN number density.

The cloud mass mixing ratio, defined as $\rho_{\rm c}/\rho_{\rm g}$, steeply decreases with height above the height where $\tau_{\rm fall} < \tau_{\rm mix}$. This can be understood from the transport equations. In the upper atmosphere, the source terms expressing the particle growth are negligible as mentioned above. Therefore, in a steady state, the vertical mixing of particles should balances with sedimentation,

$$-\rho_{\rm g} K_{\rm z} \frac{\partial}{\partial z}\left(\frac{\rho_{\rm c}}{\rho_{\rm g}}\right) - v_{\rm t}\rho_{\rm c} = 0. \tag{2.29}$$

When the $\tau_{\rm mix} \ll \tau_{\rm fall}$, Equation (2.29) indicates that $\rho_{\rm c}/\rho_{\rm g}$ is nearly constant for height, which is seen in the lower region of Figure 2.4. When the $\tau_{\rm mix} \gg \tau_{\rm fall}$, the mass mixing ratio decreases with height due to the particle sedimentation.

The vertical distribution of the cloud mass density also depends on the CCN number density and atmospheric metallicity (the right column of Figure 2.4). A larger CCN number density leads to a higher mass density at high altitude because the final particle size decreases with $n_{\rm CCN}$ as mentioned before. We also find that the higher atmospheric metallicity is, the higher cloud mass mixing ratio at an upper altitude is. This metallicity dependence arises because the final particle size is insensitive to the metallicity, while the cloud mass density at the cloud base is approximately proportional to the metallicity. In other words, the cloud mass mixing ratio at

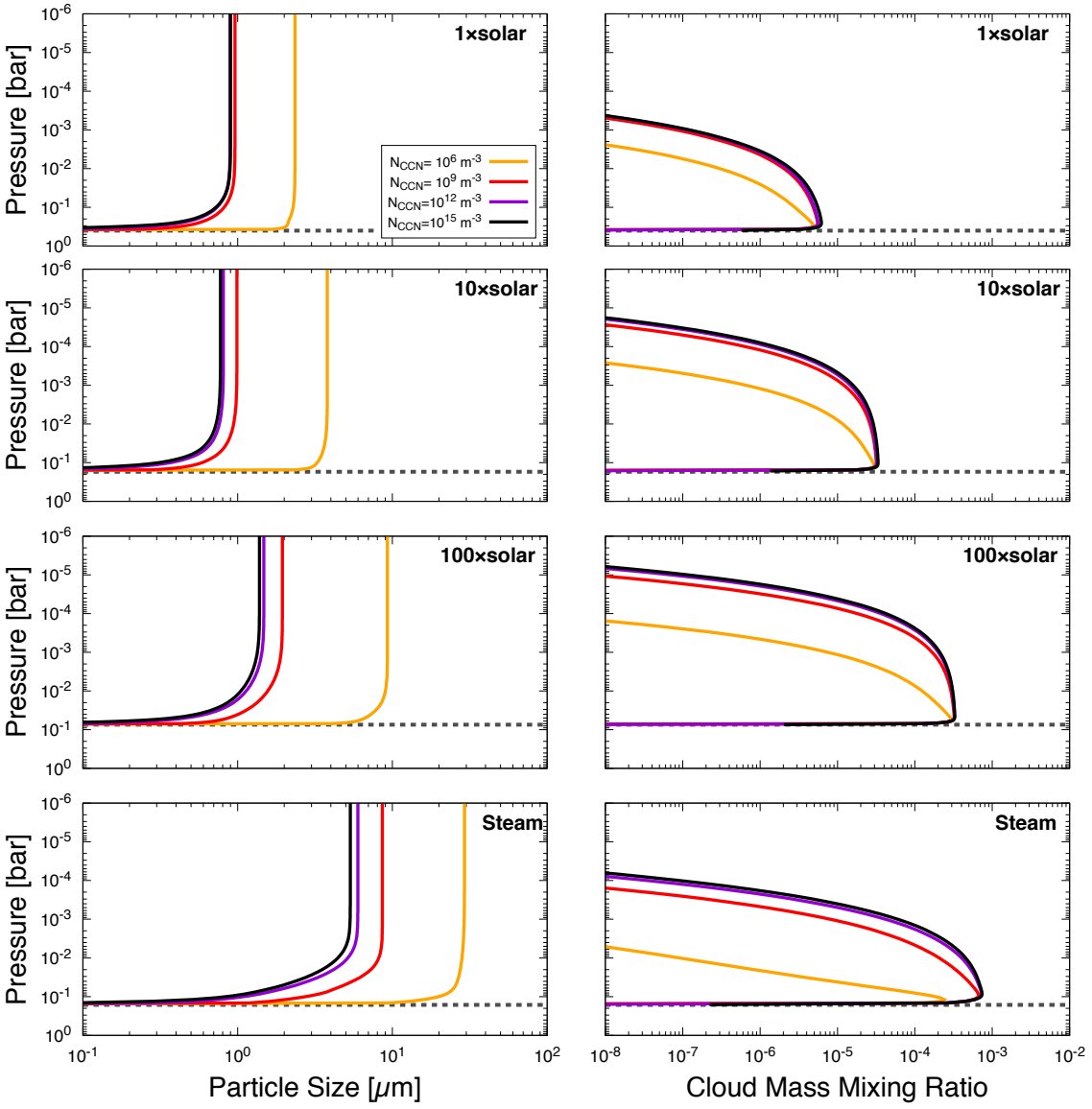


Figure 2.4: Vertical structure of the KCl cloud for different atmospheric metallicity models. The left and right columns show the vertical distributions of the particle radius and mass mixing ratio, respectively, for different values of the CCN number density $n_{\rm CCN}$. Each row, from top to bottom, is for atmospheric metallicities of $1\times$, $10\times$, $100\times$ solar, and steam atmosphere, respectively. The orange, red, purple, and black lines show the results for $n_{\rm CCN} = 10^6$, 10^9, 10^{12}, and 10^{15} m^{-3}, respectively. The gray dotted lines indicate the cloud base.

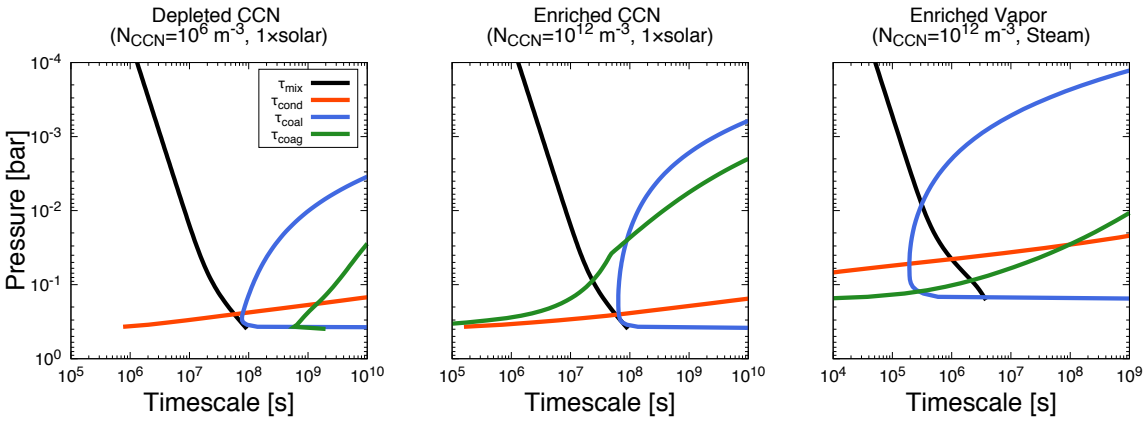


Figure 2.5: Vertical distributions of the timescales of particle growth and vertical mixing. The left, middle, and right panels show the distributions for $n_{\rm CCN} = 10^6$ and 10^{12} m^{-3} with the metallicities of $1\times$ solar, and $n_{\rm CCN} = 10^{12}$ m^{-3} with the pure steam atmosphere. The black, red, blue, and green lines show the timescales of vertical mixing, coalescence, coagulation, and condensation respectively.

an upper atmosphere reflects the abundance of condensable vapor (KCl) in a deep atmosphere. In addition, the dependence of $\tau_{\rm mix} \propto H^2$ also yields the higher cloud mass at high altitude for higher metallicity cases because the H decreases with increasing atmospheric metallicity.

2.6 The Mechanisms Controlling Particle Size

The final particle size determines how high the cloud particles can ascend. In this subsection, we discuss the mechanisms that control the final particle size. The concept introduced in this section is also applicable to the formation of aggregate clouds, as shown in later sections. Here, we introduce the timescales of condensation, coagulation, and coalescence defined as

$$\tau_{\rm cond} = \rho_{\rm c} \left| \frac{\partial \rho_{\rm c}}{\partial t} \right|^{-1}_{\rm cond}, \tag{2.30}$$

$$\tau_{\rm coag} = n_{\rm c} \left| \frac{\partial n_{\rm c}}{\partial t} \right|^{-1}_{\rm coag}, \tag{2.31}$$

$$\tau_{\rm coal} = n_{\rm c} \left| \frac{\partial n_{\rm c}}{\partial t} \right|^{-1}_{\rm coal}, \tag{2.32}$$

and the mixing timescale $\tau_{\rm mix}$ is given by Equation (2.19). Generally, cloud particles grow if $\min(\tau_{\rm cond}, \tau_{\rm coag}, \tau_{\rm coal}) \ll \tau_{\rm mix}$, and ascend without significant growth if $\min(\tau_{\rm cond}, \tau_{\rm coag}, \tau_{\rm coal}) \gg \tau_{\rm mix}$. Figure 2.5 shows the vertical distributions of the timescales of vertical mixing, condensation, coagulation, and coalescence for three cases: depleted CCNs ($n_{\rm CCN} = 10^6$ m^{-3}), enriched CCNs ($n_{\rm CCN} = 10^{12}$ m^{-3}), and enriched vapor (steam atmospheres). The mixing timescale $\tau_{\rm mix}$ decreases with height as mentioned before, whereas the growth timescales increase with height because they are inversely proportional to the density. Hence the particle growth becomes relatively less effective as the particles ascend, explaining the vertical size distribution in Figure 2.4. In following subsections, we demarcate the particle growth in three typical regimes based on timescale argument.

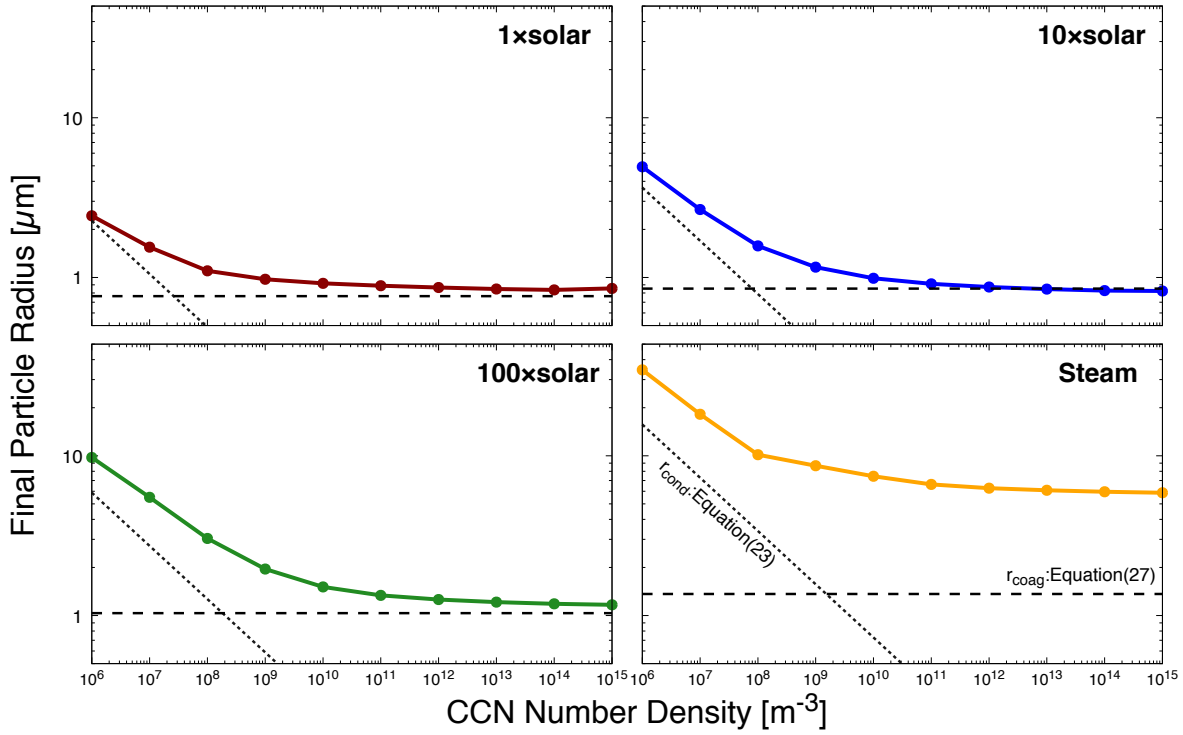


Figure 2.6: Final particle radius as a function of the CCN number density. From top to bottom, each row shows the final radius for the metallicity of $1\times$, $10\times$, $100\times$ solar, and the steam atmosphere, respectively. The dashed and dotted lines show the size determined by coagulation, $r_{\rm coag}$, predicted by Equation (2.38) and that by condensation, $r_{\rm cond}$, predicted by Equation (2.34), respectively (see Section 2.6.1 and 2.6.2).

2.6.1 Condensation Regime ($\tau_{\rm mix} < \tau_{\rm coag}, \tau_{\rm coal}$)

In the example shown in the left panel of Figure 2.5, $\tau_{\rm cond}$ is much shorter than $\tau_{\rm mix}$ and other growth timescales at the cloud base. The short $\tau_{\rm cond}$ results in the quick growth of particles near the cloud base as shown in Figure 2.4. Meanwhile, the rapid condensation also results in rapid depletion of condensing vapor. This depletion eventually terminates the condensation growth, and the total cloud mass at the cloud base is limited by the total amount of condensing vapor there, i.e., $\rho_{\rm c}(z_{\rm b}) \approx \rho_{\rm v}(z_{\rm b}) = \rho_{\rm s}(z_{\rm b})$.

If $n_{\rm CCN}$ is so small that $\min(\tau_{\rm coal}, \tau_{\rm coag}) > \tau_{\rm mix}$ at the cloud base, the particles start to ascend as soon as the condensation growth is completed (the left column in Figure 2.5). In this case, the final particle size $r_{\rm cond}$ is determined by the deposition of available vapor onto CCNs, i.e.,

$$\frac{4}{3}\pi r_{\rm cond}^3 \rho_{\rm p} n_{\rm CCN} \approx \rho_{\rm s}(z_{\rm b}), \tag{2.33}$$

and thus

$$r_{\rm cond} \approx \left[\frac{3\rho_{\rm s}(z_{\rm b})}{4\pi\rho_{\rm p} n_{\rm CCN}}\right]^{1/3}, \tag{2.34}$$

where we have assumed the initial CCN mass density is much smaller than $\rho_{\rm s}(z_{\rm b})$. Figure 2.6 shows the final particle size and $r_{\rm cond}$ for each metallicity case. As shown in Figure 2.6, the final particle size approaches $r_{\rm cond}$ for lower CCN number density. Hence, Equation (2.34) explains

why the final particle size decreases with the increasing of CCN number density. Equation (2.34) also explains the results of Gao et al. (2018), who found that the efficient homogeneous nucleation (high number density of condensation nuclei) results in small particle size.

2.6.2 Coagulation Regime ($\tau_{\rm coag} < \tau_{\rm mix} < \tau_{\rm coal}$)

Coagulation leads the further growth of cloud particles in addition to condensation if $n_{\rm CCN}$ is so high that $\tau_{\rm coag} < \tau_{\rm mix}$ at the cloud base (see middle panel of Figure 2.5). As seen in Figure 2.6, the final particle size becomes quite larger than $r_{\rm cond}$ when the CCN number density is high and thus coagulation is effective. Interestingly, Figure 2.4 also indicates that the final size eventually approaches a minimum value in the limit of high CCN number density. This implies that one can evaluate the minimum particle size regardless of uncertainty of the CCN number density.

The minimum particle size can be analytically estimated in the following way. Because the final particle size ranges as $r > 0.07$ μm in Figure 2.4, the coagulation growth falls into diffusive regime, and the $\tau_{\rm coag}$ is written by

$$\tau_{\rm coag} = \frac{3\eta}{4k_{\rm B}T\beta n_{\rm c}}. \tag{2.35}$$

Also the slip factor can be approximated as $\beta \approx \beta_\infty {\rm Kn_g}$, where $\beta_\infty = 1.657$, because the mean free path near the cloud base ($l \sim 10$ μm) is larger than the particle radius, i.e., ${\rm Kn_g} \gg 1$. Using the relation $4\pi r_{\rm c}^3 \rho_{\rm p} n_{\rm c}/3 = \rho_{\rm c}$ and $\eta = \rho_{\rm g} v_{\rm th} l/3$, where $v_{\rm th} = \sqrt{8k_{\rm B}T/\pi m_{\rm g}}$ is the mean thermal velocity, the coagulation timescale can be rewritten as

$$\begin{aligned} \tau_{\rm coag} &= \frac{\rho_{\rm g} v_{\rm th} r_{\rm c}}{4k_{\rm B}T\beta_\infty n_{\rm c}} \\ &= \frac{\pi \rho_{\rm p} v_{\rm th}}{3k_{\rm B}T\beta_\infty q_{\rm c}} r_{\rm c}^4, \end{aligned} \tag{2.36}$$

where $q_{\rm c} \equiv \rho_{\rm c}/\rho_{\rm g}$ is the cloud mass mixing ratio. Since $\rho_{\rm c}$ is determined by saturation vapor density at the cloud base (see Section 2.6.1), $q_{\rm c} = \rho_{\rm s}(z_{\rm b})/\rho_{\rm g}(z_{\rm b}) = m_{\rm KCl} q_{\rm KCl}/m_{\rm g}$, where $m_{\rm KCl}$ is the mass of a KCl molecule. Coagulation growth is terminated when the vertical mixing becomes more efficient, and thus the final size is determined from the condition $\tau_{\rm coag} = \tau_{\rm mix}$. Equating Equations (2.36) and (2.19), the final particle size determined by coagulation $r_{\rm coag}$ is predicted as

$$r_{\rm coag} = \left(\frac{3\beta_\infty}{\sqrt{8\pi}} \frac{m_{\rm KCl} q_{\rm KCl}}{\rho_{\rm p} K_{\rm z}(z_{\rm b})} g^{1/2} H^{5/2} \right)^{1/4} \left(\frac{P_*}{P_{\rm b}} \right)^{1/10}, \tag{2.37}$$

where $P_{\rm b}$ is the pressure of the cloud base and P_* is the pressure in which the coagulation growth is completed. Equation (2.37) implies the final particle size in this regime is almost independent of $n_{\rm CCN}$ because P_* is insensitive to the choice of $n_{\rm CCN}$ as seen in Figure 2.5. This explains why the final particle size is almost independent of $n_{\rm CCN}$ for high CCN number density in Figure 2.4. Particularly, we find that Equation (2.37) is in a good agreement with the minimum final size derived from the numerical results if we assume $P_* = 0.1 P_{\rm b}$. Then, Equation (2.37) can be rewritten as the following useful formula

$$r_{\rm coag} = 1.25\ \mu{\rm m} \left(\frac{g}{10\ {\rm m\ s^{-2}}} \right)^{1/8} \left(\frac{H}{10^2\ {\rm km}} \right)^{5/8} \left(\frac{K_{\rm z}(z_{\rm b})}{10^3\ {\rm m^2\ s^{-1}}} \right)^{-1/4} \left(\frac{q_{\rm KCl}}{10^{-5}} \right)^{1/4}. \tag{2.38}$$

Figure 2.6 shows that the final particle size asymptotically reaches that predicted from Equation (2.38) except the case of steam atmosphere. The deviation for steam atmosphere is caused by coalescence as explained in next subsection.

It should be noted that the asymptotic behavior of the final particle size is only found for compact-sphere clouds. In this collision-dominated regime, cloud particles likely grow into porous aggregates in reality. As shown in later sections, for porous-aggregate clouds, the final particle size varies with CCN number density even for high $n_{\rm CCN}$ [1]. Nevertheless, one can use Equation (2.37) as a lower limit of particle size. This is because, as shown in later sections, the sizes of cloud particle aggregates are larger than those of spherical cloud particles.

2.6.3 Coalescence Regime ($\tau_{\rm coal} < \tau_{\rm mix}$)

Coalescence is dominant only if condensing vapor is very abundant as in pure steam atmospheres as shown in the right panel of Figure 2.5. When coalescence is dominant, the final particle size becomes larger than the lower limit set by coagulation $r_{\rm coag}$ (see the bottom panel of Figure 2.6). Because larger particles have larger settling velocity, coalescence suppresses the cloud-top height in the steam atmosphere.

Here we predict the threshold abundance of condensing vapor that induces the significant growth through coalescence. Because the particle size is larger than the gas mean free path near the cloud base ~ 10 μm in most of our calculations, the terminal velocity is expressed as the Epstein's law, approximated as

$$v_{\rm t}(r_{\rm c}) \approx \frac{2\beta_\infty g \rho_{\rm p}}{3\rho_{\rm g} v_{\rm th}} r_{\rm c}. \tag{2.39}$$

Therefore the coalescence timescale can be rewritten as

$$\begin{aligned} \tau_{\rm coal} &= \frac{1}{2\pi r^2 \Delta v n} \\ &\sim \frac{2v_{\rm th}}{\beta_\infty g q_{\rm c}}. \end{aligned} \tag{2.40}$$

Because $q_{\rm c} = m_{\rm KCl} q_{\rm KCl}/m_{\rm g}$ (see Section 2.6.2), the coalescence timescale just above the cloud base is independent of $n_{\rm CCN}$, and only depends on the mixing ratio of the condensing vapor. If $\tau_{\rm coal} \ll \tau_{\rm mix}$, the cloud particles grows via coalescence in addition to condensation and coagulation. Comparing Equation (2.40) with $\tau_{\rm mix}(z_{\rm b})$, we find that coalescence occurs near the cloud base if the condensate mixing ratio is much higher than

$$\begin{aligned} q_* &\approx \frac{2v_{\rm th} K_{\rm z} m_{\rm g}}{\beta_\infty g H^2 m_{\rm KCl}} \\ &\approx 5\times10^{-7} \left(\frac{g}{10\ {\rm m\ s^{-2}}}\right)^{-1/2} \left(\frac{H}{10^2\ {\rm km}}\right)^{-3/2} \\ &\quad \times \left(\frac{K_{\rm z}(z_{\rm b})}{10^3\ {\rm m^2\ s^{-1}}}\right) \left(\frac{m_{\rm g}}{2\ {\rm amu}}\right). \end{aligned} \tag{2.41}$$

Substituting the parameters for the steam atmosphere of GJ1214 b, the mixing ratio of condensing vapor $q_{\rm KCl} = 2.61\times10^{-4}$ exceeds the $q_* \sim 2\times10^{-5}$ by an order of magnitude, and hence coalescence dominates the particle growth.

[1] In the sections focusing on the aggregate clouds, the CCN number density is replaced by the size of particles constituting a cloud particle aggregate (called monomer). Qualitatively speaking, as explained later, the higher CCN number density, the smaller monomer size is.

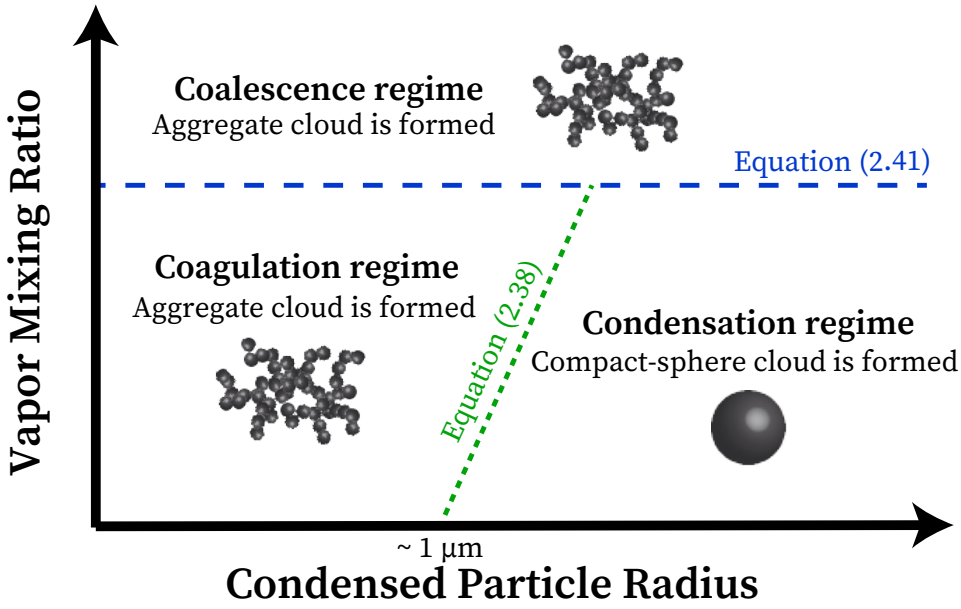


Figure 2.7: Schematic illustration of the growth regimes of cloud particles in terms of the condensed vapor abundance and the condensed particle radius (Equation 2.34). We also denote which the compact-sphere or the aggregate cloud is expected in each regime.

2.7 Summary

So far, we have investigated how the vertical profiles of mineral compact-sphere clouds vary with the atmospheric metallicity and CCN concentration. In particular, we have discussed how the particle size is determined by microphysical processes. Our main findings are summarized as follows.

1. The vertical profiles of mineral clouds significantly vary with CCN concentration and atmospheric metallicity. The particle size decreases with increasing CCN concentration and increases with increasing metallicity, though the latter dependence is relatively weak.

2. Characteristic sizes of cloud particles are mainly determined by the competition between particle growth and eddy transport near the cloud base. This stems from the fact that the particle growth timescale steeply increases with altitude because of the depletion of condensing vapor and the decrease of particle number density.

3. The cloud particle's size is always larger than the minimum size determined by coagulation growth near the cloud base (Equation 2.37). This minimum size sets the maximum vertical extent of compact-sphere clouds.

4. When the mixing ratio of condensing vapor exceeds a threshold (Equation 2.41), the cloud particles grow further through coalescence. Importantly, this processes only depends on the cloud mass mixing ratio and occurs even if the particle number density is very low, as known from the timescale of Equation (2.40).

We summarize the particle growth regime in Figure 2.7. Coagulation growth is negligible if CCN concentration is so low that condensed particle radius (Equation 2.34) is much larger

than the coagulation threshold radius (Equation 2.38). Coalescence is also negligible if the abundance of condensing vapor is much lower than the threshold abundance (Equation 2.41). Notably, threshold size between coagulation and condensation regimes (Equation 2.38) would be useful to evaluate the minimum size of cloud particles and the maximum vertical extent of mineral cloud.

Although we have approximated cloud particles as compact spheres so far, the approximation may not be valid in the coagulation and coalescence regime. Since heterogeneous growth process, such as vapor condensation, keep a spherical particle shape (Lavvas et al., 2011), the cloud particles would be compact spheres in the condensation regime. On the other hand, collision growth of solid particles produces non-spherical aggregates (e.g., Dominik & Tielens, 1997; Blum & Wurm, 2000). Therefore, mineral cloud particles likely grow into aggregates of cloud particles in the coagulation and coalescence regimes. This may be regarded as an analog of a snowflake in our Earth atmosphere. In next chapter, we investigate how the particle porosity impacts on the mineral cloud formation in exoplanetary atmospheres.

Chapter 3

Clouds of Fluffy Aggregates: How They Form in Exoplanetary Atmospheres

Modified from Ohno, Okuzumi, & Tazaki (2019), The Astrophysical Journal, in press

3.1 Abstract

Transmission spectrum surveys have suggested the ubiquity of high-altitude clouds in exoplanetary atmospheres. Theoretical studies have been investigating the formation processes of the high-altitude clouds. However, previous studies have approximated cloud particles as compact spheres, which is not always true for solid mineral particles that likely constitute exoplanetary clouds. In this chapter, we investigate how the porosity of cloud particles evolve in exoplanetary atmospheres and influence the cloud vertical profiles. We construct a porosity evolution model that takes into account the fractal aggregation and the compression of cloud particle aggregates. The internal density of a cloud particle aggregate decreases with increasing the particle mass until the compression sets in. We find that the compression caused by gas drag occurs once the size of a cloud particle aggregate exceeds a threshold, which is approximately $30\ \mu\mathrm{m}$ and insensitive to relevant parameters. We couple the porosity model to a cloud microphysical model in order to investigate the effects of the porosity evolution on cloud vertical structures. We demonstrate that the compression rarely occurs in the context of mineral cloud formation, and the particle internal density can be lower than the material density by 2–3 orders of magnitude. As a result, fluffy-aggregate clouds ascend to altitude much higher than that for compact-sphere clouds assumed so far. Our results may help to explain the formation of high-altitude clouds in exoplanetary atmospheres.

3.2 Introduction

Recent observational studies have suggested that exoplanets universally posses clouds in their atmospheres (e.g., Kreidberg et al., 2014; Sing et al., 2016; Crossfield & Kreidberg, 2017). This motivates the community to study the cloud formation processes in exoplanetary atmospheres. Because of high temperature of close-in exoplanets, it has been suggested that the clouds are made of solid minerals (e.g., Morley et al., 2012; Mbarek & Kempton, 2016; Lee et al., 2018), which we call mineral clouds. Several previous studies have attempted to figure out the mineral cloud formation using cloud microphysical models (e.g., Helling et al., 2008; Helling & Fomins, 2013; Lee et al., 2015, 2016; Gao et al., 2018; Ohno & Okuzumi, 2018; Gao & Benneke, 2018; Powell et al., 2018; Lines et al., 2018; Ormel & Min, 2019).

Previous studies have commonly assumed that mineral cloud particles are compact spheres. However, as known from snowflakes in an atmosphere on Earth, the assumption is not always true for solid condensate particles. Theoretical and experimental studies have suggested that solid particles can grow into aggregates with very low internal density (e.g., Dominik & Tielens, 1997; Blum & Wurm, 2000; Wada et al., 2008). Because the fluffy aggregate has a sedimentation velocity much lower than the compact sphere with same mass, it would drastically affect the vertical extents of mineral clouds. Moreover, the optical properties of a non-spherical aggregate are quite different from a compact sphere (e.g., Tazaki et al., 2016; Tazaki & Tanaka, 2018), which may influence the observable transmission spectra. Some previous studies pointed out that the porosity of cloud particles may drastically affect the cloud vertical distributions (Marley et al., 2013; Ohno & Okuzumi, 2018). However, there has been a no physically-based framework to handle the porosity evolution for mineral cloud formation in exoplanetary atmospheres.

In this chapter, we develop a new framework to handle the formation of mineral clouds made of non-spherical aggregates. We utilize the porosity evolution model established by planet formation community to model how the porosity of cloud particles evolve during the cloud formation. Then, we investigate how the porosity evolution affects the vertical distributions of mineral clouds using a cloud microphysical model developed in Chapter 2. The organization of this chapter is as follows. In Section 3.3, we introduce the method to calculate the porosity evolution of cloud particles in planetary atmospheres. In Section 3.4, we investigate how the porosity of cloud particles evolve in the context of KCl cloud formation in a super-Earth GJ1214b. In Section 3.5, we study how the porosity evolution affect the vertical distributions of mineral clouds using a cloud microphysical model coupled with the porosity model. In Section 3.6, we state caveats of current model and relation to a previous model used for photochemical haze formation. In Section 3.7, we summarize this chapter.

3.3 Modeling Porosity Evolution of Cloud Particles

Non-spherical aggregates form through the mutual sticking of solid particles with a low collision energy (e.g., Meakin, 1991). The smallest particles constituting an aggregate are called *monomers*. In the context of cloud formation, cloud particle aggregates (CPAs hereafter) would form when the collision growth is a dominant mechanism (the coagulation and the coalescence regimes in Chapter 2). In this thesis, we refer a cloud particle to a CPA and constituting particles to monomers.

One of the most important quantities that characterize a porous aggregate is the filling factor

ϕ defined by

$$\phi = \frac{\rho_{\rm agg}}{\rho_{\rm mon}}, \tag{3.1}$$

where $\rho_{\rm agg}$ is the mean internal density of the aggregate and $\rho_{\rm mon}$ are the bulk density of the individual monomers. For aggregates made of single-sized monomers, Equation (3.1) can also be written as

$$\phi = \frac{NV_{\rm mon}}{V_{\rm agg}}, \tag{3.2}$$

where N is the number of the constituent monomers, and $V_{\rm agg}$ and $V_{\rm mon}$ are the volumes of the aggregate and individual monomers, respectively. Here, the volume of an aggregate is defined as that of a sphere with the same gyration radius. The number of constituent monomers is another important parameter for aggregate of monodisperse monomers because it is directly related to the aggregate mass.

The set of N and ϕ defines the characteristic size, or length scale, of a porous aggregate. If we approximate an aggregate with a sphere of radius $r_{\rm agg}$, the ratio of volumes $V_{\rm mon}$ to $V_{\rm agg}$ is $V_{\rm agg}/V_{\rm mon} = (r_{\rm agg}/r_{\rm mon})^3$, where $r_{\rm mon}$ is the monomer radius. Using this expression with Equation (3.2), we obtain the relation that determines $r_{\rm agg}$ as a function of N and ϕ,

$$r_{\rm agg} = \left(\frac{N}{\phi}\right)^{1/3} r_{\rm mon}, \tag{3.3}$$

In atmospheres, the filling factor of an aggregate can change through various processes.In what follows, we introduce how the filling factor of an aggregate ϕ evolves in planetary atmospheres. For convention, we describe a filling factor determined by a specific process using a subscript ϕ; for example, $\phi_{\rm coll}$ for the collisional compression.

3.3.1 Fractal Growth

Aggregates forming through low-energy sticking collisions often have an open structure with fractal geometry (e.g., Meakin, 1991). A fractal aggregate can be characterized by the fractal dimension $D_{\rm f}$ defined by

$$N = k_0 \left(\frac{r_{\rm agg}}{r_{\rm mon}}\right)^{D_{\rm f}}, \tag{3.4}$$

where k_0 is a prefactor of order unity, $r_{\rm mon}$ is the radius of individual monomers, and $r_{\rm agg}$ is the characteristic radius of an aggregate. An aggregate with $D_{\rm f} = 1$ is "chain-like" in the sense that its length scale $r_{\rm agg}$ is proportional to its mass ($\propto N$), while an aggregate with $D_{\rm f} = 2$ is "plane-like" in the sense that its cross section $\sim r_{\rm agg}^2$ is proportional to its mass. Experimental and numerical studies show that aggregates growing by accreting similar-sized aggregates have $D_{\rm f} = 1.7$–2.2, whereas aggregates growing by accreting individual monomers tend to have $D_{\rm f} \approx 3$ (e.g., Meakin, 1991; Okuzumi et al., 2009). Non-ballistic collisions and rotation of aggregates could also reduce the fractal dimension down to $D_{\rm f} \approx 1.1$ (Paszun & Dominik, 2006). $D_{\rm f} = 2$ is often assumed in the studies of haze formation on Titan and Pluto (e.g., Lavvas et al., 2010; Gao et al., 2017a). Unless otherwise noted, we assume that aggregate-aggregate collisions dominate over aggregate-monomer collisions, adopting $D_{\rm f} \approx 2$ and $k_0 \approx 1$ (Okuzumi et al., 2009). We will discuss the validity of the assumption in Section 3.6.

Once the fractal dimension is given, the filling factor of a fractal aggregate, $\phi_{\rm frac}$, can be calculated as a function of N. Substituting $r_{\rm agg}/r_{\rm mon} = k_0^{-1/D_{\rm f}} N^{1/D_{\rm f}}$ along with $D_{\rm f} = 2$ and $k_0 = 1$ into Equation (3.3) and solving for ϕ, we obtain

$$\phi_{\rm frac} = N^{-1/2}, \tag{3.5}$$

which indicates that the filling factor decreases with increasing N, i.e., as the aggregate grows. Whenever two aggregates stick at a low velocity, the newly formed aggregate contains a large void whose volume is comparable to the volume of the collided aggregates (see Section 4 of Okuzumi et al. 2009 for more quantitative analysis). This causes the decrease of the filling factor.

3.3.2 Collisional Compression

The fractal growth described by Equation (3.5) breaks down if the impact energy is higher than needed for internal restructuring of the newly forming aggregate, for which case collisional compaction occurs (e.g., Dominik & Tielens, 1997; Blum & Wurm, 2000; Wada et al., 2007, 2008; Paszun & Dominik, 2009). For a collision between two aggregates with similar individual masses $\approx m_{\rm agg}/2$, the collisional energy can approximately be written as

$$E_{\rm imp} \approx \frac{1}{8} m_{\rm agg} \Delta v^2, \tag{3.6}$$

where Δv is the collisional velocity. Here, $m_{\rm agg}$ stands for the mass of the newly forming aggregate, and we have used that the reduced mass of the collided aggregates is $\approx (m_{\rm agg}/2)/2 = m_{\rm agg}/4$. Restructuring of the new aggregate occurs if $E_{\rm imp}$ is much higher than the energy $E_{\rm roll}$ needed to roll one monomer over another monomer in contact by 90° against rolling friction (Dominik & Tielens, 1997; Blum & Wurm, 2000). Following Dominik & Tielens (1995), we evaluate $E_{\rm roll}$ as

$$E_{\rm roll} = 6\pi^2 \gamma r_{\rm mon} \xi_{\rm crit}, \tag{3.7}$$

where γ is the surface energy of the monomers and $\xi_{\rm crit}$ is the critical rolling displacement above which inelastic rolling occurs. A realistic value of $\xi_{\rm crit}$ is somewhat uncertain: the model of Dominik & Tielens (1995) anticipates $\xi_{\rm crit} \sim 2$ Å, whereas the measurement by Heim et al. (1999) of the rolling friction force acting on silica microspheres suggests a ~ 10 times larger value. We set $\xi_{\rm crit} = 2$ Å to examine maximal impacts of the compression processes.

The filling factor of grain aggregates after collisional internal restructuring has been extensively studied by means of N-body dynamical simulations (Wada et al., 2007, 2008; Paszun & Dominik, 2009; Suyama et al., 2008, 2012). According to Wada et al. (2008), the size of an aggregate after a high-energy ($E_{\rm imp} > E_{\rm roll}$) collision between two equal-sized fractal ($D_{\rm f} = 2$) aggregates follows

$$\frac{r_{\rm agg}}{r_{\rm mon}} = N^{2/5} \left(\frac{E_{\rm imp}}{0.15 N E_{\rm roll}} \right)^{-1/10}. \tag{3.8}$$

Using Equation (3.3), Equation (3.8) translates into the filling factor after a high-energy collision,

$$\phi_{\rm coll} = N^{-1/2} \left(\frac{E_{\rm imp}}{0.15 E_{\rm roll}} \right)^{3/10}. \tag{3.9}$$

Here, the prefactor $N^{-1/2}$ corresponds to the filling factor without collisional compression (see Equation 3.5), whereas the factor $(E_{\rm imp}/0.15E_{\rm roll})^{3/10}$ represents compression occurring for $E_{\rm imp} > E_{\rm roll}$. Wada et al. (2008) derived Equation (3.8) for aggregates after a single compressive collision, but Suyama et al. (2008) later confirmed that the expression approximately holds for aggregates growing through multiple compressive collisions (see their Equation (33)).

For particles in atmospheres, the collision velocity in Equation (3.6) is calculated as the root sum square of the thermal (Brownian) relative velocity and the relative velocity $\Delta v_{\rm t}$ of gravitational settling, i.e.,

$$\Delta v = \sqrt{\frac{32 k_{\rm B} T}{\pi m_{\rm agg}} + \Delta v_{\rm t}^2}. \tag{3.10}$$

Here we write $\Delta v_{\rm t} \approx \epsilon v_{\rm t}'$, where $v_{\rm t}'$ is the terminal settling velocity of individual aggregates before collision and ϵ is a numerical factor arising from finite width of actual size distribution of the aggregates. We here adopt $\epsilon = 0.5$ following Sato et al. (2016). For the terminal velocity of aggregates, we use an expression for spheres (Ohno & Okuzumi, 2017),

$$v_{\rm t}' = \frac{2 g r_{\rm agg}'^2 \rho_{\rm agg}'}{9\eta} \beta(r_{\rm agg}') \left[1 + \left(\frac{0.45 g r_{\rm agg}'^3 \rho_{\rm g} \rho_{\rm agg}'}{54 \eta^2} \right)^{2/5} \right]^{-5/4}, \tag{3.11}$$

where $r_{\rm agg}'$ and $\rho_{\rm agg}'$ are the characteristic radius and density of aggregates before collision, respectively, η is the dynamic viscosity of ambient gas, and β is the slip correction factor accounting for the free-molecular flow regime. In Equation (3.11), we have approximated the aerodynamic radius of an aggregate with its characteristic radius $r_{\rm agg}$ defined by Equation (3.3). This approximation is invalid for very fluffy aggregates with $D_{\rm f} < 2$, for which the aerodynamic radius is generally smaller than the characteristic radius [1] (Okuzumi, 2009). We use this assumption because we only consider $D_{\rm f} \geq 2$ in this study. The slip correction factor is given by (e.g., Seinfeld & Pandis, 2012)

$$\beta(r_{\rm agg}') = 1 + \frac{l_{\rm g}}{r_{\rm agg}'} \left[1.257 + 0.4 \exp\left(-\frac{1.1 r_{\rm agg}'}{l_{\rm g}} \right) \right], \tag{3.12}$$

where $l_{\rm g}$ is the mean free path of gas molecules. The second term in the bracket in Equation (3.11) corrects for high Reynolds (turbulent) flow, although it is mostly negligible for slowly settling aggregates considered in this study.

3.3.3 Gas-drag Compression

An aggregate moving relative to the surrounding gas can experience compression when the gas drag force acting on it is strong enough to cause internal restructuring. We employ the model of Kataoka et al. (2013a) to evaluate the filling factor of an aggregate under gas-drag compression (see Kataoka et al. 2013a; Arakawa & Nakamoto 2016 for applications of the model to dust evolution in protoplanetary disks). We assume that compression occurs when the ram pressure $P_{\rm ram}$

[1] The reason can be easily understood for the special case of the free molecular regime, for which the aerodynamic cross section is approximately equal to the projected area (Blum et al., 1996). For $D_{\rm f} < 2$, the projected area increases linearly with mass (e.g., Minato et al., 2006), but the "characteristic" cross section $\pi r_{\rm agg}^2 \propto N^{2/D_{\rm f}}$ increases *faster* than mass ($\propto N$). For $D_{\rm f} \approx 2$, the characteristic cross section $\approx N \pi r_{\rm mon}^2$ is only ~ 2 times larger than the projected area (see, e.g., Figure 8 of Okuzumi et al., 2009), and therefore the characteristic radius differs from the aerodynamic radius only by $\sim 40\%$. The approximation is even better for $D_{\rm f} > 2$ (Okuzumi et al., 2009).

of the gas flow exceeds the static compressional strength $P_{\rm str}$ of the aggregate. The compression thus proceeds until $P_{\rm ram}$ becomes equal to $P_{\rm str}$. Based on the results of N-body simulations, Kataoka et al. (2013a) found that the static compressional strength can be written as

$$P_{\rm str} = \frac{E_{\rm roll}}{r_{\rm mon}^3}\phi^3, \tag{3.13}$$

where $E_{\rm roll}$ is the rolling energy already introduced in Section 3.3.2. The ram pressure can be evaluated as the drag force per cross section of the aggregate. For an aggregate setting in an atmosphere at a terminal velocity, the drag force is equal to the gravity $m_{\rm agg}g$, where g is the gravitational acceleration. Thus, $P_{\rm ram}$ is given by

$$P_{\rm ram} \approx \frac{m_{\rm agg}g}{\pi r_{\rm agg}^2} = \frac{4}{3}r_{\rm agg}g\rho_{\rm mon}\phi. \tag{3.14}$$

Solving $P_{\rm str} = P_{\rm ram}$ together with Equation (3.3) for ϕ, the equilibrium filling factor under gas-drag compression is obtained as

$$\phi_{\rm drag} = N^{1/7}\left(\frac{4g\rho_{\rm mon}r_{\rm mon}^4}{3E_{\rm roll}}\right)^{3/7}. \tag{3.15}$$

Equation (3.15) indicates that under gas-drag compression, the filling factor increases with aggregate mass. It is worth noting that $\phi_{\rm drag}$ is independent of the ambient gas density because the gas drag force balances with the gravity, which does not depend on the gas density.

3.3.4 A General Formula

For a given number of monomers, equivalent to the aggregate mass, one can calculate the equilibrium filling factor from the highest one determined by the fractal growth, gas-drag compression, and collisional compression (Kataoka et al., 2013b), i.e.,

$$\phi_{\rm eq} = \max[\phi_{\rm frac}, \phi_{\rm drag}, \phi_{\rm coll}]. \tag{3.16}$$

3.4 Application of Porosity Model to KCl Clouds in GJ1214b

We here illustrate how the filling factor of CPAs in an super-Earth atmosphere evolves as they grow. We consider the cloud of KCl solid particles in the super-Earth GJ1214b. It is assumed that the cloud has its base at $P = 100$ mbar and $T = 700$ K, where P is the atmospheric pressure. The material density and surface energy are $\rho_{\rm mon} = 2$ g cm^{-3} and $\gamma = 0.11$ J m^{-2} for KCl crystals (Westwood & Hitch, 1963). We note that one cannot calculate the filling factor for collisional compression $\phi_{\rm coll}$ without a knowledge of filling factor of the aggregates before the collision, as the terminal velocity depends on the aggregate density (see Equation 3.11). Thus, we first calculate $\phi_{\rm eq}$ only from $\phi_{\rm frac}$ and $\phi_{\rm gas}$, and then $\phi_{\rm coll}$ is calculated with the obtained $\phi_{\rm eq}$.

We find that the internal density of CPAs can be lower than the material density by several orders of magnitude. The evolution pathways of the equilibrium filling factor for $r_{\rm mon} = 0.01$, 0.1, and 1 μm are shown in Figure 3.1. Here the equilibrium filling factor is expressed as a function of the number of monomers making up the aggregates, $N = m_{\rm agg}/m_{\rm mon}$. One can see that the aggregates are highly porous, with $\phi_{\rm eq} < 0.1$, over a wide range of N. For small

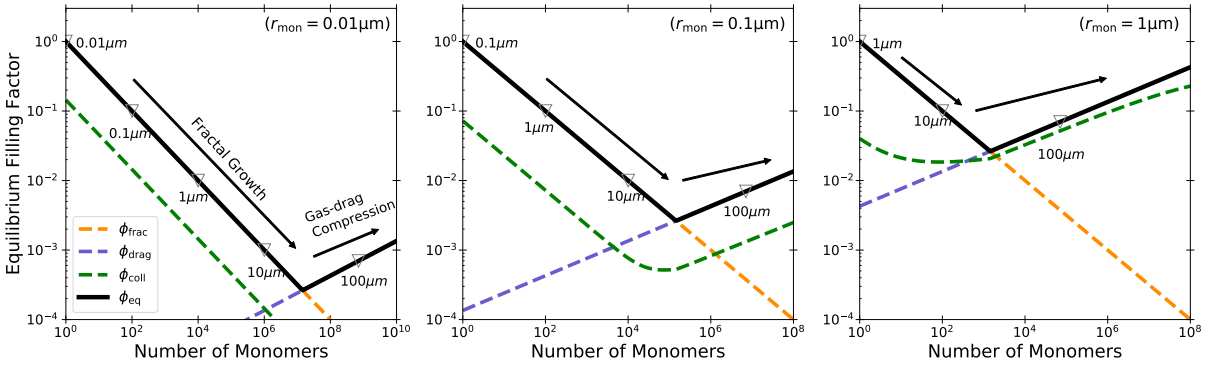


Figure 3.1: Equilibrium filling factor of KCl particle aggregates at the base of the KCl cloud in the super-Earth GJ1214b. The left, center, and right panels are for monomer radii $r_{\rm mon} = 0.01$, 0.1, and 1 μm, respectively. The orange, blue, green, and black lines show the filling factors determined by fractal growth ($\phi_{\rm frac}$; Equation 3.5), gas-drag compression ($\phi_{\rm drag}$; Equation 3.15), collisional compression ($\phi_{\rm coll}$; Equation 3.9), and all of them ($\phi_{\rm eq}$; Equation 3.16), respectively. The aggregate radius $r_{\rm agg} = 0.01$, 0.1, 1, 10, and 100 μm are denoted as the triangles.

N, both gas-drag and collisional compression are negligible and the filling factor is determined by fractal growth. Once an aggregate size exceeds a certain value, either collisional or gas-drag compression sets in. For all monomer sizes shown in Figure 3.1 ($r_{\rm mon} = 0.01$–1 μm), gas-drag compression always dominates over collision compression. Collisional compression is important for larger monomer sizes and occurs only for $r_{\rm mon} > 1$ μm around at the cloud base. No matter which compression mechanism dominates, the filling factor increases with N, and hence with aggregates mass. Nevertheless, the filling factor never exceeds 0.1 as long as the monomer mass is in the range $10^2 < N < 10^6$. The results thus demonstrate the importance of considering the porosity of mineral cloud aggregates.

3.4.1 Analytic Estimates of Compression Threshold Sizes

To further elaborate how the porosity of CPAs evolve in general cases, we here analytically estimate the threshold sizes at which the compression sets in.

Gas-drag Compression Threshold

Comparison between Equations (3.5) and (3.15) shows that $\phi_{\rm drag}$ exceeds $\phi_{\rm frac}$ when the number of monomers satisfies

$$N > \left(\frac{9\pi^2\gamma\xi_{\rm crit}}{2\rho_{\rm mon}g}\right)^{2/3} r_{\rm mon}^{-2}, \tag{3.17}$$

where we use Equation (3.7). Since $r_{\rm agg} = N^{1/2} r_{\rm mon}$ for $D_{\rm f} = 2$, we find that a $D_{\rm f} = 2$ aggregate starts to experience gas-drag compression when its characteristic radius exceeds a threshold

$$\begin{aligned} r_{\rm drag} &= \left(\frac{9\pi^2\gamma\xi_{\rm crit}}{2\rho_{\rm mon}g}\right)^{1/3} \\ &\approx 30\ \mu{\rm m} \left(\frac{g}{10\ {\rm m\ s^{-2}}}\right)^{-1/3} \left(\frac{\rho_{\rm mon}}{2\ {\rm g\ cm^{-3}}}\right)^{-1/3} \left(\frac{\gamma}{0.1\ {\rm J\ m^{-2}}}\right)^{1/3}. \end{aligned} \tag{3.18}$$

It is worth noting that $r_{\rm drag}$ is independent of the monomer size and only depends on material properties and planetary gravity. Equation (3.18) indicates that gas-drag compression is responsible to aggregates larger than tens micron, while it will be responsible to micron-sized aggregates on high-gravity objects, such as brown dwarfs.

Collisional Compression Threshold

We here estimate the threshold size at which fractal aggregates begin to be compressed by high-energy collisions. Since the thermal kinetic energy $k_{\rm B}T{\sim}10^{-20}$ J $(T/1000\ {\rm K})$ is generally several orders of magnitude smaller than the rolling energy $E_{\rm roll}{\sim}10^{-17}$ J $(\gamma/0.1\ {\rm J\ m^{-2}})(r_{\rm mon}/1\ \mu{\rm m})$, one can consider that only relative velocity from gravitational settling induces collisional compression. For small fractal aggregates, the second term in the bracket in Equation (3.11) is negligible, and thus we approximately have

$$v_{\rm t}' \approx \frac{2gr_{\rm agg}'^2\rho_{\rm agg}'}{9\eta}\beta. \tag{3.19}$$

For fractal aggregates of $D_{\rm f}=2$, we also have $\rho_{\rm agg}' \approx (r_{\rm mon}/r_{\rm agg}')\rho_{\rm mon}$, $r_{\rm agg}' = 2^{-1/2}r_{\rm agg}$, and $m_{\rm agg} = (r_{\rm agg}/r_{\rm mon})^2 m_{\rm mon}$, where $r_{\rm agg}$ is the radius of the newly formed aggregate. Substituting $\Delta v_{\rm t} \approx \epsilon v_{\rm t}'$ with these expressions into Equation (3.6), the collisional energy of a settling-induced collision is given by

$$E_{\rm imp} \approx \frac{1}{16}m_{\rm mon}\left(\frac{gr_{\rm agg}^2\rho_{\rm mon}}{9\eta}\beta\right)^2. \tag{3.20}$$

Collisional compression occurs ($\phi_{\rm coll} > \phi_{\rm frac}$) when $E_{\rm imp} > 0.15E_{\rm roll}$ (see Equations (3.5) and (3.9)). For $r_{\rm agg} \gg l_{\rm g}$ ($\beta \approx 1$), the threshold size for collisional compression is given by

$$\begin{aligned} r_{\rm coll} &= \left(\frac{9\eta}{\rho_{\rm mon}g}\sqrt{\frac{2.4E_{\rm roll}}{m_{\rm mon}}}\right)^{1/2} \\ &\approx 70\ \mu{\rm m}\left(\frac{g}{10\ {\rm m\ s^{-2}}}\right)^{-1/2}\left(\frac{\rho_{\rm mon}}{2\ {\rm g\ cm^{-3}}}\right)^{-3/4}\left(\frac{r_{\rm mon}}{1\ \mu{\rm m}}\right)^{-1/2} \\ &\quad\times\left(\frac{\gamma}{0.1\ {\rm J\ m^{-2}}}\right)^{1/4}\left(\frac{T}{1000\ {\rm K}}\right)^{1/4}, \end{aligned} \tag{3.21}$$

where we have used the dynamic viscosity for hydrogen-rich atmospheres $\eta = 5.877{\times}10^{-7}\ {\rm Pa\ s}\sqrt{T[{\rm K}]}$ (Woitke & Helling, 2003). In the opposite limit of $r_{\rm agg} \ll l_{\rm g}$, for which $\beta \approx 1.7l_{\rm g}/r_{\rm agg}' \approx 2.4l_{\rm g}/r_{\rm agg}$, we obtain the threshold size of

$$\begin{aligned} r_{\rm coll} &= \frac{10P}{\pi\rho_{\rm mon}gv_{\rm th}}\sqrt{\frac{2.4E_{\rm roll}}{m_{\rm mon}}} \\ &\approx 90\ \mu{\rm m}\left(\frac{g}{10\ {\rm m\ s^{-2}}}\right)^{-1}\left(\frac{\rho_{\rm mon}}{2\ {\rm g\ cm^{-3}}}\right)^{-3/2}\left(\frac{r_{\rm mon}}{1\ \mu{\rm m}}\right)^{-1} \\ &\quad\times\left(\frac{\gamma}{0.1\ {\rm J\ m^{-2}}}\right)^{1/2}\left(\frac{v_{\rm th}}{1\ {\rm km\ s^{-1}}}\right)^{-1}\left(\frac{P}{100\ {\rm mbar}}\right). \end{aligned} \tag{3.22}$$

Here, we have used $l_{\rm g} = 3\eta/(\rho_{\rm g}v_{\rm th})$ and $\rho_{\rm g} = (8/\pi)P/v_{\rm th}^2$, where $v_{\rm th} = \sqrt{8k_{\rm B}T/\pi m_{\rm g}}$ is the mean thermal velocity of gas molecules and $m_{\rm g}$ is the mass of a gas molecule.

3.5 Modeling Formation of Fluffy-Aggregate Clouds

We calculate the vertical structure of the fluffy-aggregate clouds using the double-moment bulk scheme described in previous sections (see also Ohno & Okuzumi, 2017, 2018). In what follows, we briefly state the difference of a model used in this section and that used in previous section.

3.5.1 Prescription of Nucleation and Condensation

Formation of the fluffy-aggregate cloud will be triggered by the formation of monomers via nucleation followed by condensation (Figure 3.2). The processes will determine the size of monomers, which predominantly controls the porosity evolution and thus the particle growth. However, microphysical processes associated to the monomer formation—especially the nucleation of initial condensates—are highly uncertain for exoplanetary atmospheres. Although the classical nucleation theory is available, as used in previous studies (e.g., Helling & Fomins, 2013; Powell et al., 2018; Gao & Benneke, 2018), one should keep in mind that the theory sometimes deviates from the nucleation rate measured by numerical and laboratory experiments by several orders of magnitudes (e.g., Ford, 1997; Tanaka et al., 2011; Lee et al., 2018).

In this study, we mimic the monomer formation by setting the size of monomers as a free parameter. For the sake of simplicity, every monomer is assumed to have the same size. We assume that the nucleation predominantly occurs at the cloud base, and the formed condensate particles instantaneously grow until all condensable vapor at the cloud base is incorporate into the particles. In other words, we calculate the growth of cloud particles in the region above which the monomer formation is completed (Figure 3.2).

3.5.2 Aggregate Growth and Transport above the Cloud Base

The formed monomers are collided each other and grow into the fluffy aggregates (Figure 3.2). The aggregates are then mixed in the vertical direction by atmospheric circulation, which we approximate as a diffusion process in the horizontal averaged sense (Parmentier et al., 2013; Charnay et al., 2015a; Zhang & Showman, 2018a,b). The upward transport is limited by the downward settling motion of the particles. We treat these processes using 1D vertical transport equations with a collisional growth term (Ohno & Okuzumi, 2018),

$$\frac{\partial n_{\rm c}}{\partial t} = \frac{\partial}{\partial z}\left[n_{\rm g} K_{\rm z} \frac{\partial}{\partial z}\left(\frac{n_{\rm c}}{n_{\rm g}}\right) + v_{\rm t} n_{\rm c}\right] - \left|\frac{\partial n_{\rm c}}{\partial t}\right|_{\rm coll}, \tag{3.23}$$

$$\frac{\partial \rho_{\rm c}}{\partial t} = \frac{\partial}{\partial z}\left[\rho_{\rm g} K_{\rm z} \frac{\partial}{\partial z}\left(\frac{\rho_{\rm c}}{\rho_{\rm g}}\right) + v_{\rm t} \rho_{\rm c}\right], \tag{3.24}$$

where $n_{\rm g}$ is the atmospheric gas number density and $|\partial n_{\rm c}/\partial t|_{\rm coll}$ is the decrease of the aggregate number density due to collisional growth. The collision rate can be calculated by the same formula as that for compact spheres, as described in Section 2.4.5, with replacing the particle radius by the characteristic radius of a CPA (e.g., Cabane et al., 1993). It should be noted that the condensation term is omitted in Equation 3.24 because we only calculate the region above which the condensation growth is terminated.

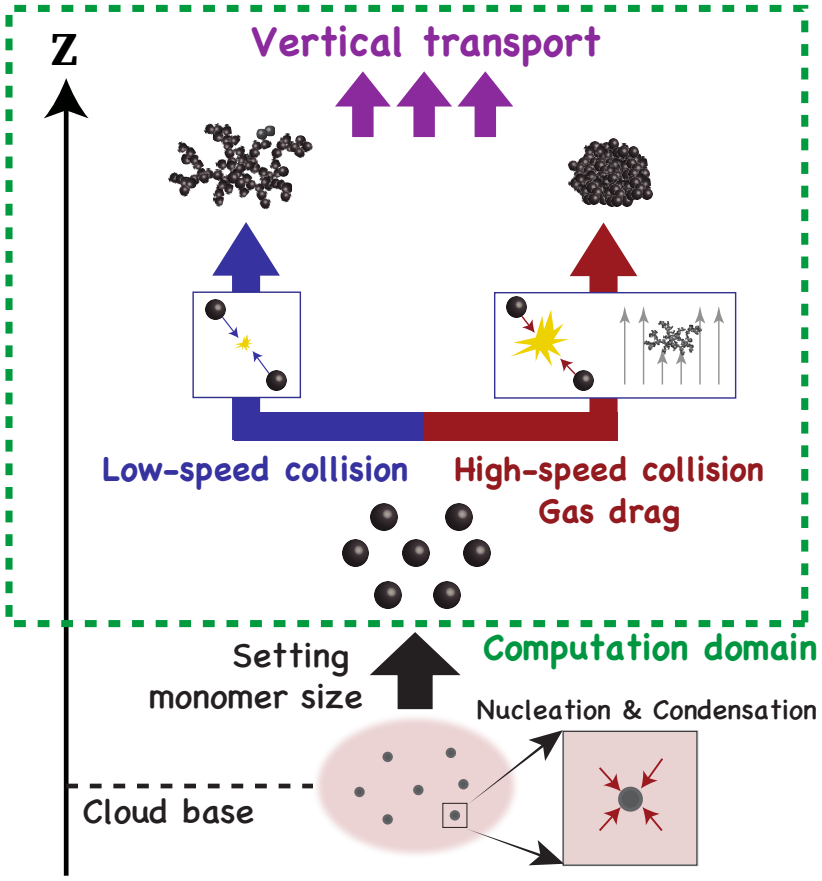


Figure 3.2: Cartoon illustrating the formation of fluffy-aggregate clouds.

3.5.3 Numerical Procedures

We consider that the cloud particles are in solid form and made of pure KCl, which is a major condensable species formed in warm ($T = 500$–1000 K) exoplanets (Morley et al., 2013; Lee et al., 2018). For super-Earths, the pressure and temperature at cloud forming region (0.1 bar and 900 K, see e.g., Gao & Benneke, 2018) are well below the triple-point pressure and temperature of KCl (140 bars and 1041 K, Rodrigues & Silva Fernandes, 2007). Thus, the KCl clouds are likely made of solid particles that could grow into an aggregate.

To obtain the vertical profiles of ρ_c and n_c, we solve Equations (3.24) and (3.23) until the system reaches a steady state. The characteristic radii of CPAs are calculated by using the equilibrium filling factor from Equation (3.16) at each time step. We note that the collisional compression should occur only when the particle collisions dominate over the vertical transport. Otherwise, the compression can occur without collision, which is clearly unrealistic. To take into account it, we switch off the collisional compression if the vertical mixing timescale $\tau_{\rm mix} \equiv H^2/K_z$ is shorter than the collisional growth timescale $|d \log n_c/dt|^{-1}$. The upper boundary condition is set to zero-flux, while the flux at the lower boundary is calculated assuming that n_c/n_g and ρ_c/ρ_g are constant at the cloud base. Since we have assumed that all condensable vapor is incorporated in the cloud particles at the cloud base as stated before, the cloud mass density at the lower boundary is given by

$$\rho_c(P_b) = \rho_s(P_b), \tag{3.25}$$

Table 3.1: Fiducial Parameters used for Calculations of Fluffy-Aggregate Cloud Formation

metallicity	$\mu_{\rm g}$	$q_{\rm v,KCl}$ (mol/mol)	K_0 ($\rm m^2\ s^{-1}$)	Δz (km)
1×solar	2.3	1.83×10^{-7}	7.0×10^2	20
10×solar	2.5	1.80×10^{-6}	2.8×10^3	20
100×solar	4.3	1.70×10^{-5}	3.0×10^3	10
1000×solar	16.7	1.20×10^{-4}	3.0×10^2	5

where $P_{\rm b}$ is the cloud-base height in pressure and $\rho_{\rm s}$ is the saturation vapor density of KCl, which is calculated by the saturation vapor pressure described in Morley et al. (2012). For a given monomer radius, the number density of cloud particles at the lower boundary is also calculated as

$$n_{\rm c}(P_{\rm b}) = \frac{3\rho_{\rm s}(P_{\rm b})}{4\pi r_{\rm mon}^3 \rho_{\rm p}}. \tag{3.26}$$

The top and bottom of the computation domain are imposed at 10^{-8} bar and the cloud-base height, which is determined by the volume mixing ratio of KCl vapor $q_{\rm v,KCl}$ listed in Table 3.1 and the saturation vapor pressure. We apply a publicly available code of thermochemical equilibrium calculations (TEA, Blecic et al., 2016) to estimate the mean molecular weight and abundance of KCl in this section. We also calculate the vertical distributions for the $1000\times$ solar atmospheric metallicity rather than the pure steam atmosphere, which is assumed in contemporaneous studies investigating the vertical distributions of clouds and hazes (e.g., Gao & Benneke, 2018; Kawashima & Ikoma, 2019).

3.5.4 Vertical Distributions of Fluffy-Aggregate Clouds

We here demonstrate how the porosity evolution affects the vertical profiles of KCl clouds. Figure 3.3 shows the vertical distribution of the size $r_{\rm agg}$, cloud mass mixing ratio $q_{\rm c} = \rho_{\rm c}/\rho_{\rm g}$, and filling factor of aggregates $\phi_{\rm eq}$ for various monomer sizes and atmospheric metallicities. We also plot the vertical profiles of compact ($D_{\rm f} = 3$) sphere clouds for comparison. The left panels of Figure 3.3 show that the cloud particles produced at the cloud base grow locally until the timescale of collisional growth becomes comparable to the vertical diffusion timescale. Well above the cloud base, no appreciable growth occurs because the growth timescale increases with height (Ohno & Okuzumi, 2018; Powell et al., 2018; Gao & Benneke, 2018). Notably, the cloud mass mixing ratio for submicron monomer cases is high even at a very high altitude of $P < 10^{-4}$ bar as compared to the case of compact-sphere clouds. The reason for this will be explained in a later part of this section.

We note that the aggregate sizes in upper atmospheres may decrease with height in reality, as seen in other studies (Gao & Benneke, 2018; Ormel & Min, 2019). The trend is not captured in our calculations where the particle sizes are constant at upper atmospheres. This is caused by the fact that our model assumes a narrowly-peaked size distribution that cannot handle the decrease of the mean size caused by the removal of the largest particles from the distribution. However, the size-decreasing effect is presumably not crucial for slowly settling CPAs. This is because the effective size becomes nearly constant in vertical, as seen in our calculations, when the particles have sufficiently small sizes and thus small settling velocity (see e.g., Figure 4 of Gao et al., 2018).

The trend of vertical size distribution is appreciably different between compact-sphere and

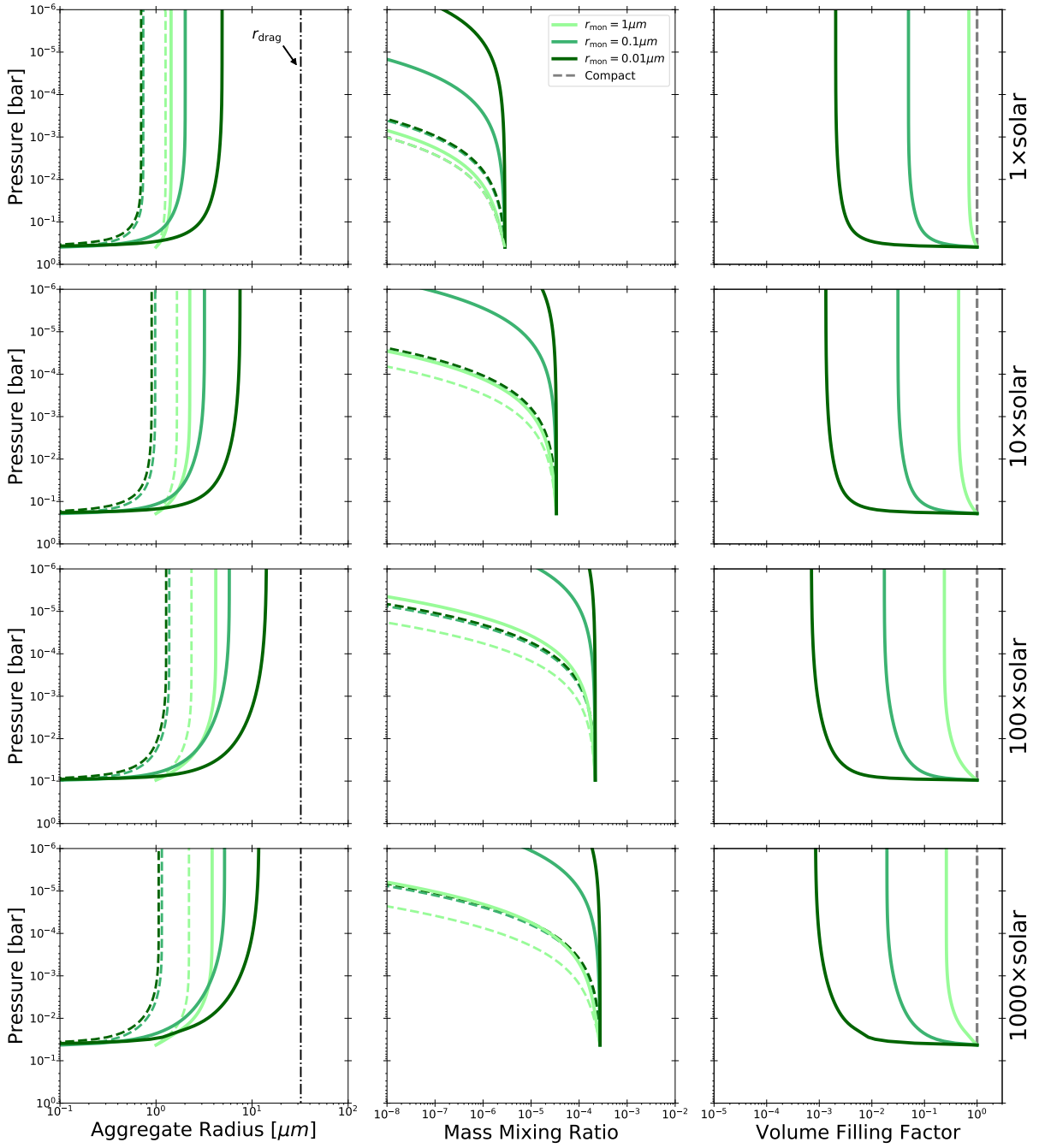


Figure 3.3: Vertical structure of a KCl cloud in GJ1214b from compact and fluffy aggregate models. The left, center, and right columns show the radius $r_{\rm agg}$, mass mixing ratio $\rho_{\rm c}/\rho_{\rm g}$, volume filling factor of CPAs, respectively. The top, middle, and bottom rows are for atmospheric metallicities of $1\times$, $10\times$, $100\times$, and $1000\times$ solar, respectively. The vertical axes are atmospheric pressure for all panels. The light-green, green, and dark-green lines show the profiles for $r_{\rm mon} = 1$, 0.1, and 0.01 μm, respectively. The dotted lines also show the profiles for compact-sphere clouds ($D_{\rm f} = 3$) for reference. The black dash-dot lines in the left column denote the compression radius $r_{\rm drag}$ given by Equation (3.18).

fluffy-aggregate cases. For compact-sphere case, the particle size well above the cloud top decreases with decreasing monomer size $r_{\rm mon}$ because a higher number density at the cloud base (which corresponds to a smaller monomer size at the base; see Equation 3.26) leads to a smaller particle size above the base (Gao et al., 2018; Ohno & Okuzumi, 2018; Ormel & Min, 2019). The trend is originated from the fact that, for a given mass mixing ratio, a total amount of condensing materials on each particle decreases with increasing a number density. The coagulation is effective for a high number density, but halted once the particle size exceeds the threshold above which the number density becomes too low to cause the collisions (see Section 3.2 of Ohno & Okuzumi, 2018). By contrast, for fluffy-aggregate clouds, the aggregate radius at high altitude *increases* with decreasing monomer radius $r_{\rm mon}$. As shown below, this is because the coagulation timescale is a function of aggregate mass and because aggregates made of smaller monomers have to grow to larger in size to obtain a certain mass. For aggregates larger than the mean free path of themselves, the timescale of coagulation growth $\tau_{\rm coag} \equiv |d \log n_{\rm c}/dt|^{-1}_{\rm coag}$ is approximately given by

$$\tau_{\rm coag} \approx \frac{3\eta}{4k_{\rm B}Tn_{\rm c}}, \tag{3.27}$$

which follows from Equation (2.24). Using the relation $q_{\rm c}\rho_{\rm g} = m_{\rm agg}n_{\rm c}$, we obtain

$$\tau_{\rm coag} \approx \frac{3\eta m_{\rm agg}}{4k_{\rm B}T\rho_{\rm g}q_{\rm c}}, \tag{3.28}$$

which indicates that the coagulation timescale is independent of aggregates properties other than $m_{\rm agg}$. Since the final size is determined by the balance between coagulation and mixing timescales ($\tau_{\rm coag} = \tau_{\rm mix}$), the final aggregate mass is given by

$$m_{\rm agg} \approx \frac{4k_{\rm B}TH^2}{3\eta K_{\rm z}}\rho_{\rm g}(P_*)q_{\rm c}, \tag{3.29}$$

where P_* is the pressure level where the growth is completed. For $D_{\rm f} = 2$, the aggregate mass scales as $m_{\rm agg} \propto r_{\rm agg}^2 r_{\rm mon}$, and hence the final aggregates radius increase with decreasing monomer size.

The aggregate size slightly increase with increasing on atmospheric metallicity. In the case of $r_{\rm mon} = 0.1$ μm, for example, the aggregate radii at high altitude are 2, 3, 5, and 5 μm for the metallicities of $1\times$, $10\times$, $100\times$, and $1000\times$ solar abundance, respectively. The increase of the aggregate size is caused by the fact that a higher atmospheric metallicity (q_c at the cloud base) leads to a higher cloud density that facilitates coagulation growth. This can also be seen from Equation (3.29), which shows $m_{\rm agg} \propto q_{\rm c}$. However, the aggregate size also depends on the mixing timescale $H^2/K_{\rm z}$ (see Equation 3.29), which decreases with increasing the atmospheric metallicity in our parameter set. This effect substantially cancels out the effects of $q_{\rm c}$, which explains the weak metallicity-dependence of the aggregate size in Figure 3.3.

The key result of this section is that the aggregates never experience compression in the cases studied here. The dot-dashed lines in the left panels of Figure 3.3 show the threshold size for the gas-drag compression $r_{\rm drag}$ (Equation 3.18) above which the aggregates leave fractal growth. Figure 3.3 shows that the particle growth is insufficient to reach the threshold size for the gas-drag compaction. Although the collisional compression can operate on micron-size aggregates in upper atmospheres ($P < 10^{-3}$ bar, see Equation 3.22), it does not take place there because the number density is too low to cause the particle collision, i.e., $\tau_{\rm coll} \gg \tau_{\rm mix}$. As a result, aggregates are fractal ($D_{\rm f} \approx 2$) even at high altitude.

The absence of the compression enables us to evaluate the vertical extent of clouds. The cloud particle aggregates can ascend to the height of $\tau_{\rm mix} \sim \tau_{\rm fall}$, where $\tau_{\rm fall} \equiv H/v_{\rm t}$ is the falling timescales (e.g., Charnay et al., 2015a). Assuming $l_{\rm g} \gg r_{\rm agg}$ for upper atmospheres, the terminal velocity can be approximated as

$$v_{\rm t} \approx \frac{\rho_{\rm mon} g}{\rho_{\rm g} v_{\rm th}} r_{\rm mon}, \tag{3.30}$$

where we use the relation $r_{\rm agg}\rho_{\rm agg} = r_{\rm mon}\rho_{\rm mon}$ for $D_{\rm f} = 2$. Solving $\tau_{\rm mix} = \tau_{\rm fall}$ about the pressure, we find the pressure level $P_{\rm top}$ to which cloud particles can ascend:

$$\begin{aligned} P_{\rm top} &\approx \frac{\rho_{\rm mon} g^2 H^2 r_{\rm mon}}{v_{\rm th} K_{\rm z}} \\ &\sim 0.03 \ {\rm mbar} \left(\frac{r_{\rm mon}}{0.1 \ \mu{\rm m}}\right) \left(\frac{\rho_{\rm mon}}{2 \ {\rm g \ cm^{-3}}}\right) \left(\frac{K_{\rm z}}{10^4 \ {\rm m^2 \ s^{-1}}}\right)^{-1} \left(\frac{v_{\rm th}}{1 \ {\rm km \ s^{-1}}}\right)^3, \end{aligned} \tag{3.31}$$

where we use $v_{\rm th} = \sqrt{(8/\pi) g H}$. Equation (3.31) indicates that $P_{\rm top}$ is independent of the size of cloud particle aggregates $r_{\rm agg}$. This explains why the cloud particle aggregates made of smaller monomers can ascend higher altitude in Figure 3.3 despite their very large sizes ($\gg 1 \ \mu$m).

3.6 Discussion

3.6.1 Model Caveats

In this study, we have adopted simplified porosity and microphysical model. The models are useful to clarify the effects of the porosity evolution, but involves some caveats because of its simplicity. In what follows, we state the caveats of our model and discuss their possible impacts on the results.

Validity of $D_{\rm f} = 2$ for Other Size Distributions

The most strong assumption of our porosity model may be the fractal dimension of 2 for the fractal growth (Section 3.3.1). We have adopted this assumption since our cloud microphysical model assumes the narrowly peaked size distribution, for which the equal-sized collision is a dominant growth process. However, the cloud particles could have different shape of size distributions (Powell et al., 2018; Gao & Benneke, 2018), and the monomer-aggregate collision might be dominant. In that case, CPAs grow into more spherical shapes (e.g., $D_{\rm f} \approx 3$), and the cloud vertical extent would be small as compared to the case of $D_{\rm f} = 2$.

Here, we test the validity of the assumption $D_{\rm f} = 2$ for various size distributions. We introduce a mass-weighted collision rate onto a particle with mass $m_{\rm t}$ ($m \leq m_{\rm t}$), defined as (Okuzumi, 2009)

$$C_{m_{\rm t}}(m) = \frac{m K(m_{\rm t}, m) f(m)}{\int_0^{m_{\rm t}} m' K(m_{\rm t}, m') f(m') dm'}, \tag{3.32}$$

where $K(m, m')$ is the collision kernel between particles with masses m and m', and $f(m)dm$ is the number density of particles with masses between m and $m + dm$. Equation (3.32) measures the contributions of aggregates with masses of m on the growth of aggregate with mass of $m_{\rm t}$.

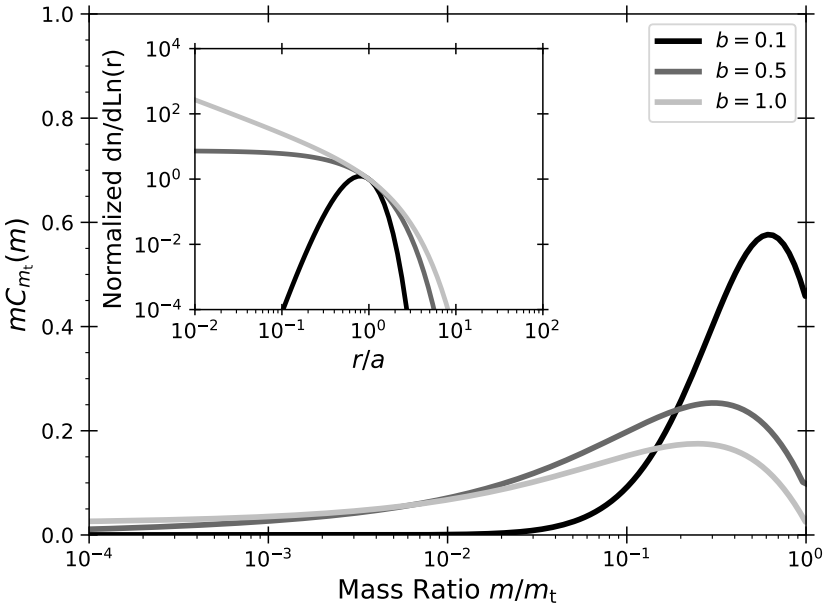


Figure 3.4: Normalized mass-weighted collision rate between particles with masses m_t and m. The black, gray, and silver lines show the collision rate for the Hansen size distributions with $b = 0.1$, 0.5, and 1.0, respectively. The corresponding size distributions normalized by $af(a)$ are also shown in the inner panel.

We assume that the cloud particles obey the Hansen size distribution (Hansen, 1971), described as

$$f(r) \equiv \frac{dn(r)}{dr} \propto r^{(1-3b)/b} \exp\left(-\frac{r}{ab}\right), \tag{3.33}$$

where a is the mean effective radius and b is the effective variance. The shape of the size distribution is controlled by the effective variance b; for example, $b < 0.5$ yields log-normal-like distributions, while $b > 0.5$ yields power-low-like distributions.

Figure 3.4 shows the mass-weighted collision rate and size distributions for $b = 0.1$, 0.5, and 1.0. We assume $a = 1$ μm and m_t calculated from the mass-weighted particle size:

$$m_\mathrm{t} = \frac{4\pi\rho_\mathrm{p}}{3}\left(\frac{\int_0^\infty rmf(r)dr}{\int_0^\infty mf(r)dr}\right)^3 = \frac{4\pi\rho_\mathrm{p}}{3}a^3(1+b)^3. \tag{3.34}$$

We use the collision kernel described in Chapter 15 of Jacobson (2005) assuming a constant particle density. Figure 3.4 demonstrates that the growth is largely contributed by the collisions of particles with masses of $m/m_\mathrm{t} \sim 0.01$–1. According to Okuzumi et al. (2009), collisions with mass ratio of 0.01–1 lead to the fractal dimension of $D_\mathrm{f} \sim 1.9$–2.1 (see their Figure 6), which is almost the same as $D_\mathrm{f} = 2$ assumed in this study. Thus, the assumption of $D_\mathrm{f} = 2$ may be reasonable for various shapes of size distributions. However, it should be noted that the size distribution of the CPAs has been unknown to date. We will examine how the size and porosity distributions of CPAs evolve in exoplanetary atmospheres in our forthcoming paper.

Limitation of the Compression Model

Here we state several limitations of a compression model adopted in Section 3.3.3. First, the relation between mass and size of the collisionally compressed aggregates (Equation 3.8) was derived for collisions between two equal-mass aggregates with $D_{\rm f} \approx 2$ (Wada et al., 2008). For different-mass collisions, the degree of compression is evaluated from the comparison of the impact energy with work done by dynamic compression strength (Suyama et al., 2012). we also note that the head-on-collision is assumed here, but offset collisions could induce the elongation of aggregates, further hinders the compression (Paszun & Dominik, 2009). Second, the static compression strength used for the gas-drag compression (Equation 3.13) was derived for an aggregate whose internal structure is characterized by $D_{\rm f} \approx 2$ (Kataoka et al., 2013a). The compression strength for different $D_{\rm f}$ was recently proposed by Arakawa et al. (2019) from a semi-analytical argument. Although the verification with numerical experiments remain to be carried out, their formula is potentially applicable to our compression model. Further numerical experiments will be helpful to extend the compression model to more universal cases.

Simplified Nucleation and Condensation

In this study, we have assumed that saturated vapor is instantaneously incorporated into the condensation nuclei at the cloud base. This assumption would be reasonable since the condensation timescale is much shorter than the vertical mixing timescale near at the cloud base (Ohno & Okuzumi, 2018; Powell et al., 2018; Gao & Benneke, 2018). Additional condensation could transform the CPAs to sphere-like particles if the surface growth rate via condensation dominates over the coagulation rate (Lavvas et al., 2011). However, the effect is presumably insignificant for KCl clouds because other condensing species, such as $\rm Na_2S$ and MnS, have the cloud bases at deeper atmospheres and are likely depleted at the KCl cloud formation region (e.g., Mbarek & Kempton, 2016). ZnS is an only species whose cloud base is placed near at the KCl cloud base (e.g., Morley et al., 2012). But, we expect that CPAs are still present as aggregates even if ZnS condensation takes place. This is because the abundance of ZnS is 2–3 times lower than KCl and likely insufficient to fill all pores.

We have also assumed that the nucleation followed by condensation, namely the monomer formation, occurs right at the cloud base. This would be true if the condensation nuclei are supplied from deep atmospheres, as argued in Lee et al. (2018). On the other hand, the monomer formation could occur above the cloud base in the context of homogeneous nucleation that needs significant supersaturation to set in (e.g., Helling & Fomins, 2013). The monomers formed in upper atmospheres might increase the $D_{\rm f}$ of CPAs through different-size collisions. We expect that the resulting $D_{\rm f}$ is still close to 2, as discussed in Section 3.6.1, though a microphysical model solving size distributions will be needed to verify it.

3.6.2 Comparison with Other Porosity Models

Some previous studies of haze microphysics adopted a porosity model different from ours (Wolf & Toon, 2010; Adams et al., 2019). The porosity model adopted in the haze models assumes that the fractal dimension approaches $D_{\rm f} \approx 2.4$ as the number of monomers increase. The assumed fractal dimension is comparative to $D_{\rm f} = 2.5$ that was observed for an aggregates with maximal compression via high-energy collisions in the numerical experiments (Wada et al., 2008; Suyama et al., 2008). However, the threshold at which compression sets in is considerably different from

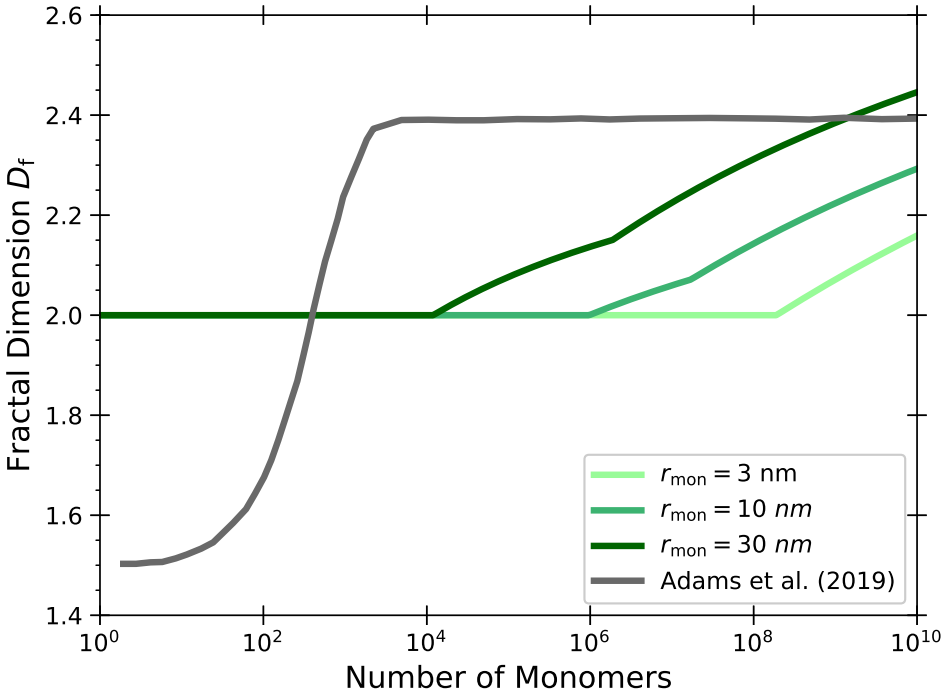


Figure 3.5: Comparison of our porosity model with that used in Adams et al. (2019). The vertical and horizontal axes show the fractal dimension $D_{\rm f}$ and number of monomers $N_{\rm mon}$. Different colored lines exhibit the evolution track of $D_{\rm f}$ for different monomer size, and the gray line shows the track assumed in Adams et al. (2019). We assume $P = 0.01$ mbar to evaluate the collision velocity.

our model. Figure 3.5 shows the fractal dimension as a function of the number of monomers in Adams et al. (2019) and our model, where we calculate $D_{\rm f}$ from Equations (3.3) and (3.4):

$$D_{\rm f} = 3\left(1 - \frac{\log \phi_{\rm eq}}{\log N_{\rm mon}}\right)^{-1}. \tag{3.35}$$

For comparisons, we use the surface energy of tholine $\gamma = 0.0709$ J m^{-2} (Yu et al., 2017) and material density $\rho_{\rm p} = 1$ g cm^{-3}. In the model of Adams et al. (2019), the fractal dimension increases to ≈ 2.4 at $N_{\rm mon} > 10^3$, while our model predicts that the compression sets in $N_{\rm mon} > 10^4$–10^8, depending on the monomer size. Thus, the aggregate hazes in previous studies were assumed to be compressed much easier than our prediction. This is a reason why aggregate hazes in Adams et al. (2019) produce flat spectra rather than those with spectral slopes.

The easily compressed aggregates in previous studies were speculated from the laboratory study of soot formation in a flame. In the experiments, it was observed that the soot-aggregates are restructured by the Coulomb interaction between oppositely charged parts (Onischuk et al., 2003). However, one should take a caution about the compression due to the Coulomb interaction because the charge states of aerosols in exoplanetary atmospheres are poorly known. Investigating the aerosol charge processes (e.g., Helling et al., 2011a,b) might help to evaluate if the restructuring due to Coulomb interaction is possible.

3.7 Summary

In this chapter, we have investigated how the porosity of cloud particle aggregates (CPAs) evolve in exoplanetary atmospheres. Based on the results of numerical experiments investigating the aggregate restructuring, we have constructed a porosity evolution model that takes into account the fractal growth, collisional compression, and the compression caused by gas drag. Using a cloud microphysical model coupled with the porosity model, we have examined how the porosity evolution influences the cloud vertical distributions. Our findings are summarized as follows.

(1) The internal density of CPAs can be much lower than the material density by 1–3 orders of magnitudes (Section 3.3), depending on the size of monomers.

(2) CPAs maintain the fractal dimension of $D_{\rm f} = 2$ until the compression sets in. The gas-drag compression sets in once the CPA becomes larger than $\approx 30\ \mu{\rm m}$ (Equation 3.18). The collisional compression is less important than the gas-drag compression in most cases.

(3) The compression of CPAs hardly occurs during the KCl cloud formation since the particle growth is not sufficient to induce the compression (Section 3.5). In other words, CPAs can maintain the fractal dimension of $D_{\rm f} = 2$.

(4) The porosity evolution in general results in the cloud vertical extent much larger than that of the compact-sphere clouds. The fluffy-aggregate clouds can ascend to the height where the monomer can ascend to (Equation 3.31).

The porosity model developed in this chapter can be universally applied to the solid particles in planetary atmospheres. In particular, it is important to properly assess the porosity of photochemical haze in order to evaluate its impacts on climate and observations (e.g., Rannou et al., 1997; Wolf & Toon, 2010; Adams et al., 2019). Our future study will investigate how the porosity of photochemical haze evolve in the atmosphere.

Chapter 4

Transmission Spectra of Cloudy Atmospheres on Super-Earths

Partly cited from Ohno, Okuzumi, & Tazaki (2019), The Astrophysical Journal, in press

4.1 Abstract

Recent observational efforts have gradually extended the catalog of transmission spectra for super-Earths. Many of them exhibit featureless spectra that may indicate the presence of cloudy atmospheres. In this chapter, we investigate the impacts of clouds on observable transmission spectra using a cloud microphysical model. In particular, we investigate how the clouds of fluffy-aggregates affect the transmission spectra for the first time. The compact-sphere cloud tends to produce the flat-like spectra, as assumed in many previous studies. On the other hand, we found that the fluffy-aggregate clouds tend to produce the spectral slope originated by the aggregate scattering properties at relatively long wavelength. We apply our cloud and spectrum models to super-Earths GJ1214b, GJ436b, GJ3470b, HD97658b, and HAT-P-11b to constrain their atmospheric compositions. We found that these super-Earths can be demarcated into two classes: GJ3470b and HAT-P-11b likely have low-metallicity atmospheres, while GJ1214b, GJ436b, and HD97658b likely have high-metallicity atmospheres. The dichotomy of atmospheric metallicity may indicate the different formation path of these super-Earths.

4.2 Introduction

Recent observational efforts have gradually extended a catalog of transmission spectra of super-Earths. The observations have been conducted for a variety of super-Earths; for example, warm ($T_{\rm eq}$ = 500–1000 K) planets (e.g., Kreidberg et al., 2014; Knutson et al., 2014a,b; Wakeford et al., 2017; Benneke et al., 2019a; Chachan et al., 2019), possible magma-ocean planets (Tsiaras et al., 2016), low-density (puffed) planets (Kreidberg et al., 2018; Libby-Roberts et al., 2019), and a planet orbiting in habitable zone (Benneke et al., 2019b; Tsiaras et al., 2019). These atmospheric observations potentially open a new window to infer the formation processes of super-Earths because the atmospheric composition likely reflects the past solid and gas accretion processes.

It has been widely accepted that exoplanetary atmospheres are probe to be covered by clouds and/or hazes (e.g., Pont et al., 2013; Kreidberg et al., 2014; Knutson et al., 2014a,b; Sing et al., 2016; Benneke et al., 2019a), making difficult to interpret the observed spectra. However, thanks to recent progresses of cloud microphysical modeling (e.g., Helling et al., 2008, 2017, 2019; Lee et al., 2015, 2016; Gao et al., 2018; Ohno & Okuzumi, 2018; Powell et al., 2018; Lines et al., 2018; Ormel & Min, 2019), it is possible to associate the cloud properties to atmospheric composition. This may enable us to derive insight on atmospheric properties of cloudy planets.

In this chapter, we investigate how mineral clouds affect the transmission spectrum. In particular, we examine the effects of particle porosity on observable transmission spectra for the first time. Then, we study the cloud vertical structures and resulting transmission spectra of super-Earths GJ1214b, GJ436b, GJ3470b, HD97658b, and HAT-P-11b, which are listed in Crossfield & Kreidberg (2017). Comparing synthetic transmission spectra with the observations, we investigate what atmospheric metallicity the super-Earths likely possess. The organization of this chapter is as follows. In Section 4.3, we introduce the method to calculate the synthetic transmission spectrum. In Section 4.4, we show the results of synthetic transmission spectrum. We also examine how the cloud particle aggregates influence the observable transmission spectrum. In Section 4.5, we apply the cloud and transmission spectrum models to several super-Earths to constrain their atmospheric composition. In Section 4.6, we discuss the implications of our results for JWST observations. In Section 4.7, we summarize this chapter.

4.3 Methodology of Synthetic Transmission Spectrum

We calculate synthetic transmission spectra as follows. What we need to do is to calculate the wavelength-dependent transit depth $D(\lambda)$ of a planet, which can be expressed as (e.g., Heng & Kitzmann, 2017)

$$D(\lambda) = \frac{\pi R_0^2 + 2\pi \int_{R_0}^{\infty} [1 - \exp(-\tau_{\rm s})] r dr}{\pi R_*^2}, \tag{4.1}$$

where R_0 is the reference transit radius and $\tau_{\rm s}$ is the optical depth for slant viewing geometry, called the slant optical depth, and r is the distance from the center of the planet. We take R_0 to be the radius at the pressure level of 10 bar following previous studies (e.g., Kreidberg et al., 2015). The slant optical depth $\tau_{\rm s}$ is calculated by integrating the extinction by gas molecules and cloud particles along the observer's line of sight (e.g., Fortney et al., 2003):

$$\tau_{\rm s}(r) = 2 \int_r^{\infty} (\alpha_{\rm g} + \alpha_{\rm c}) \frac{r' dr'}{\sqrt{r'^2 - r^2}}, \tag{4.2}$$

where $\alpha_{\rm g}$ and $\alpha_{\rm c}$ are the extinction efficiencies of gas molecules and cloud particles, respectively.

In what follows, we first assume a hypothetical planet like GJ1214b to synthesize a transmission spectrum. The stellar radius R_* and planet's semi-major axis a are taken to be $R_* = 0.216 R_{\rm sun}$ and $a = 0.014$ au, which are the values for GJ1214b from the Exoplanet eu catalog. The PT structure is calculated as stated in Chapter 2. We use the cloud vertical distributions shown in chapter 3 to calculate the cloud opacity. The methodology of the opacity calculations are described in following subsections.

4.3.1 Gas Opacity

To evaluate the gas opacity, we calculate the mixing ratio of gas molecules using the open-source Thermochemical Equilibrium Abundances (TEA) code (Blecic et al., 2016). The TEA calculates the gas mixing ratio in thermochemical equilibrium for given temperature, pressure, and elemental abundances based on Asplund et al. (2009) using the Gibbs free-energy minimization method. Following Freedman et al. (2008, 2014), we take into account the molecular absorption of H_2, H_2O, CH_4, CO, CO_2, NH_3, H_2S, and PH_3 as well as the Rayleigh scattering of the molecules. We calculate the absorption and scattering cross sections of the molecules following the method of Kawashima & Ikoma (2018) with the line list of HITRAN2016. The Voigt function is calculated by the polynomial fitting (Kuntz, 1997; Ruyten, 2004), and the total internal partition function sums are calculated by TIPS code (Gamache et al., 2017). We refer readers to the relevant literature (e.g., Rothman et al., 1998; Sharp & Burrows, 2007) for detail methodology of the gas opacity calculations. Further improvements of the line lists and the broadening coefficients (e.g., Tennyson & Yurchenko, 2018; Gharib-Nezhad & Line, 2019) remain for future studies, as our current focus is to study how the fluffy-aggregate clouds influence the transmission spectra.

4.3.2 Aggregates Opacity

The Mie theory (e.g., Bohren & Huffman, 1983) is usually used for the calculations of the opacity of spherical particles, but is no longer valid for irregular aggregates. The Mie theory coupled with the effective medium theory is one of the ways to calculate the aggregate opacity (Marley et al., 2013). However, this approach also fails to reproduce scattering properties of an aggregate when the relevant wavelength is much smaller than the aggregate (Tazaki et al., 2016; Tazaki & Tanaka, 2018). Aggregates potentially grow to 1–10 μm in size as shown in Section 3.5, while current and future observations mainly use shorter wavelengths such as 1.1–1.7 μm for HST/WFC3, 0.6–5 μm for JWST/NIRSpec (Batalha et al., 2017), and 1.25–7.8 μm for ARIEL (Tinetti et al., 2016). Therefore, the effective medium theory is still not a good approximation especially for upcoming observations.

To properly calculate the aggregate opacity, we apply the modified mean field (MMF) theory (Tazaki & Tanaka, 2018). The MMF theory is based on the Rayleigh-Gans-Debye (RGD) theory that calculates the interference of single-scattered waves from every monomer by taking the aggregate structure into account (Tazaki et al., 2016) with modifications for multiple scattering within an aggregate using the mean field assumption (Berry & Percival, 1986). The MMF theory successfully reproduces the extinction, absorption, and scattering opacities of aggregates calculated by the rigorous T-matrix method in a wide range of wavelength (Tazaki & Tanaka, 2018). For calculations, we apply the Gaussian cut-off for the two-points correlation function

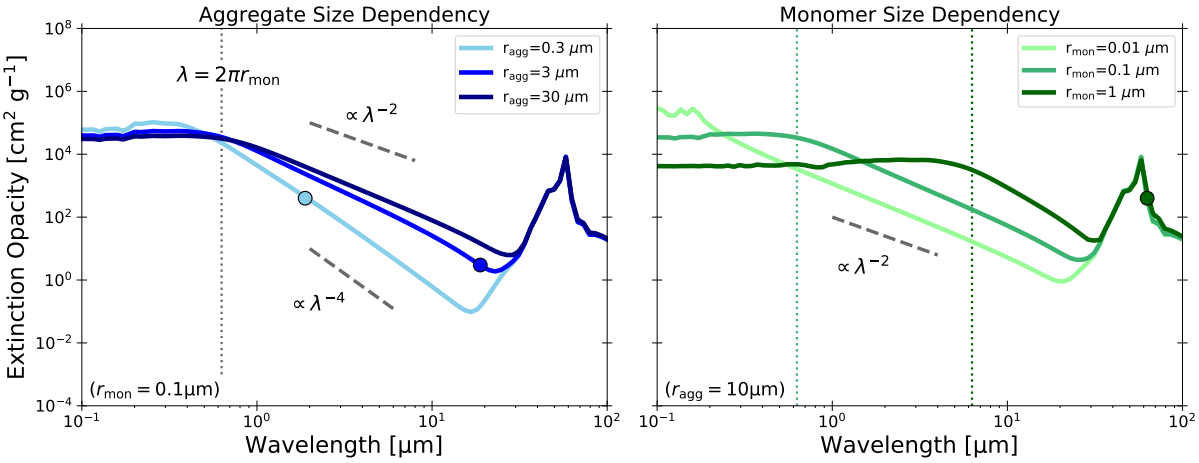


Figure 4.1: Extinction opacity of KCl aggregates with $D_{\rm f} = 2$ as a function of wavelength for different aggregate sizes $r_{\rm agg}$ and monomer sizes $r_{\rm mon}$, calculated by the MMF theory. The left panel is for aggregates of fixed $r_{\rm mon} = 0.1\ \mu m$ and different $r_{\rm agg}$, wheres the right panel is for fixed $r_{\rm agg} = 10\ \mu m$ and different $r_{\rm mon}$. The wavelength corresponding to $2\pi r_{\rm mon}$ and $2\pi r_{\rm agg}$ are denoted as dotted lines and filled circles, respectively.

that specifies the aggregate structure (Tazaki et al., 2016).

Figure 4.1 shows the extinction opacity of KCl aggregates of $D_{\rm f} = 2$ for different aggregate sizes $r_{\rm agg}$ and monomer sizes $r_{\rm mon}$. The refractive index of KCl is taken from Palik (1985) compiled by Kitzmann & Heng (2018). In the examples presented here, the extinction opacity is dominated by scattering in the wavelength range $\lambda \sim 0.2$–$10\ \mu m$. At longer wavelengths, absorption dominates over scattering, and the absorption peak of KCl appears at $\lambda \sim 50\ \mu m$. It is worth noting that the absorption feature is visible even if aggregate size is very large, as seen in the case of $r_{\rm agg} = 30\ \mu$m. This is because, unless the multiple scattering becomes dominant, the absorption cross section of an aggregate is the sum of the absorption of every monomer, and thus the wavelength dependence is the same as that of an individual monomer (Berry & Percival, 1986; Tazaki & Tanaka, 2018).

According to the MMF theory, the optical properties of an aggregate behave differently among three wavelength regimes $\lambda \ll 2\pi r_{\rm mon}$, $2\pi r_{\rm mon} \ll \lambda \ll 2\pi r_{\rm agg}$, and $\lambda \gg 2\pi r_{\rm mon}$. In the first regime, geometric optics applies to the constituent monomers, and the scattering cross section is approximately given by $\sigma_{\rm s} \sim \pi r_{\rm agg}^2$, independent of wavelength. In the opposite limit of $\lambda \gg 2\pi r_{\rm agg}$, the Rayleigh limit applies to the aggregate, and the scattering cross section obeys the well-known law $\sigma_{\rm s} \propto \lambda^{-4}$. I the left panel of Figure 4.1, this can be seen in the case of $r_{\rm agg} = 0.3\ \mu m$, at $\lambda \sim 1$–$10\ \mu m$.

The intermediate regime $2\pi r_{\rm mon} \ll \lambda \ll 2\pi r_{\rm agg}$ provides unique opacity properties for aggregates. For this regime, we find that the scattering opacity scales with wavelength dependence as $\sigma_{\rm s} \propto \lambda^{-2}$ (see Figure 4). In this intermediate regime, the scattered wave by an aggregate is a superposition of singly scattered waves from individual monomers, and the scattering cross section of a $D_{\rm f} = 2$ aggregate has following dependence. (Berry & Percival, 1986, Section 5)

$$\sigma_{\rm s} \propto r_{\rm agg}^2 r_{\rm mon}^2 \lambda^{-2} \log\left(16\pi^2 r_{\rm agg}^2 / b\lambda^2\right), \tag{4.3}$$

where b is a constant order of unity. This explains the scattering slope for $r_{\rm agg} = 3\ \mu$m and $30\ \mu$m in the left panel of Figure 4.1. The unique scattering slope is caused by interference among the

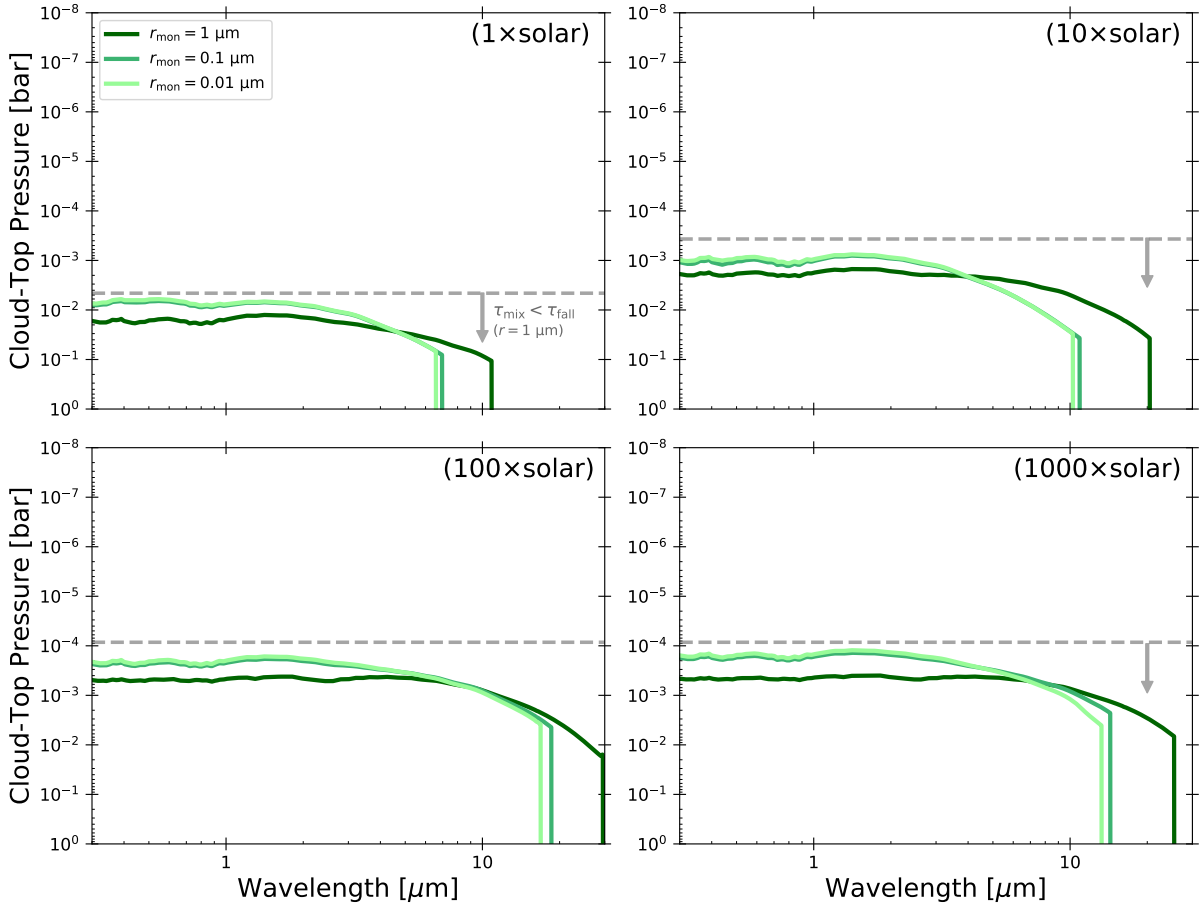


Figure 4.2: Cloud-top pressure of the compact-sphere clouds as a function of wavelength. The dark-green, green, and light-green lines are for $r_{\rm mon} = 1$, 0.1, and 0.01 μm, respectively. Note that the monomer size merely determines the number density of cloud particles at the cloud base. The dashed lines indicate the pressure level of $\tau_{\rm mix} = \tau_{\rm fall}$ for $r = 1$ μm, which is similar to the minimum size of a spherical cloud particle set by coagulation (Section 2.6.2). Each panel exhibits the result for the different atmospheric metallicities.

scattered waves from individual monomers. The scattered waves toward large scattering angles ($> \lambda/2\pi r_{\rm agg}$) cancel out because of the presence of waves with opposite phases, leading to the λ^{-2} dependence (Kataoka et al., 2014).

4.3.3 Cloud-top Pressure

Before showing the synthetic spectra, we investigate the cloud-top pressure, defined as the pressure level at which the cloud becomes optically thick along the line of sight of an observer (i.e., $\tau_{\rm s} = 1$). The cloud-top pressure clarifies the observable region of atmospheres and was examined by previous studies (Ohno & Okuzumi, 2018; Powell et al., 2018; Gao & Benneke, 2018; Helling et al., 2019). Figure 4.2 shows the cloud-top pressure of compact-sphere clouds as a function of wavelength for different monomer sizes and the atmospheric metallicities. The cloud-top pressure is largely independent of wavelength in visible to near-infrared. This is because, as argued in Chapter 2, the cloud particle always grow into the size larger than ~ 1 μm

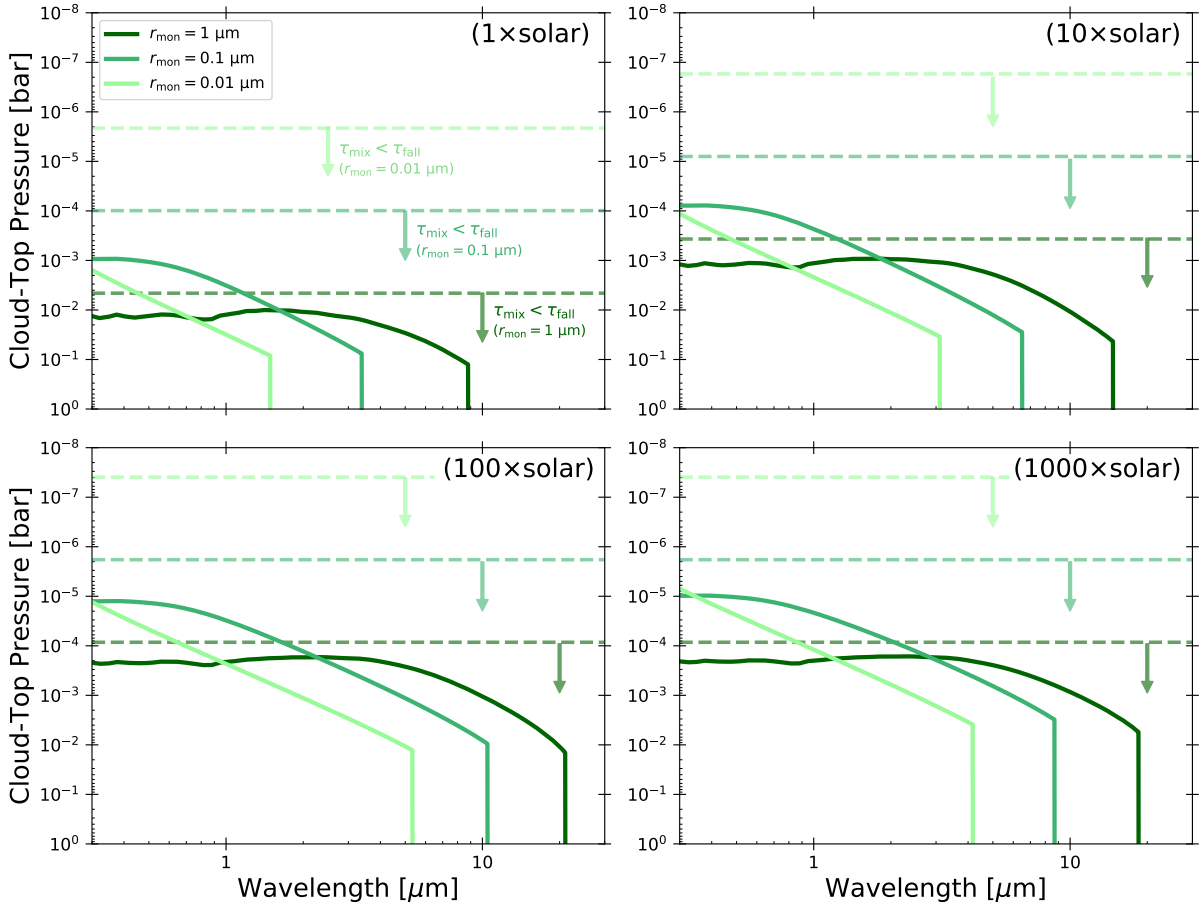


Figure 4.3: Same as Figure 4.2, but for fluffy-aggregate clouds. The dashed lines indicate the pressure level of $\tau_{\rm mix} = \tau_{\rm fall}$ for different monomer sizes.

due to coagulation for which the extinction cross section is determined by a geometric one at $\lambda \ll 2\pi r$. In the limit of the small monomer size (high CCN concentration), the cloud-top pressure converges to that for particles with the coagulation threshold size (Equation 2.38). One can also see that cloud-top height is limited by the pressure at which $\tau_{\rm mix} = \tau_{\rm fall}(r = 1\ \mu{\rm m})$. This is because the cloud mass mixing ratio steeply decreases with altitude through gravitational settling above that altitude, resulting in a low cloud opacity there.

The cloud-top pressure profiles of fluffy-aggregate clouds are quite different from those for compact-sphere clouds. Figure 4.3 shows the cloud-top pressure of fluffy-aggregate clouds, as done for compact-sphere clouds in Figure 4.2. In contrast to the compact-sphere clouds, the cloud-top pressure tends to vary with wavelength. In general, the cloud top is located at a lower atmosphere for longer wavelength and vice versa for shorter wavelength. This stem from the fact that the scattering opacity decreases with increasing wavelength for $\lambda > 2\pi r_{\rm mon}$ (see Figure 4.1). We note that the cloud top hardly exceeds the altitude of $\tau_{\rm mix} = \tau_{\rm drag}$ (dashed lines in Figure 4.3) for parameter ranges examined in this study. In near-infrared wavelength, the cloud-top height increases with decreasing monomer size as long as $r_{\rm mon} > 0.1\ \mu{\rm m}$, as CPAs constituted by smaller monomers ascend to higher altitude. On the other hand, the cloud-top height decreases with decreasing monomer size for $r_{\rm mon} < 0.1\ \mu{\rm m}$. This opposite trend is caused by the monomer size dependence of aggregate scattering opacity. Using Equation (4.3) and an aggregate mass

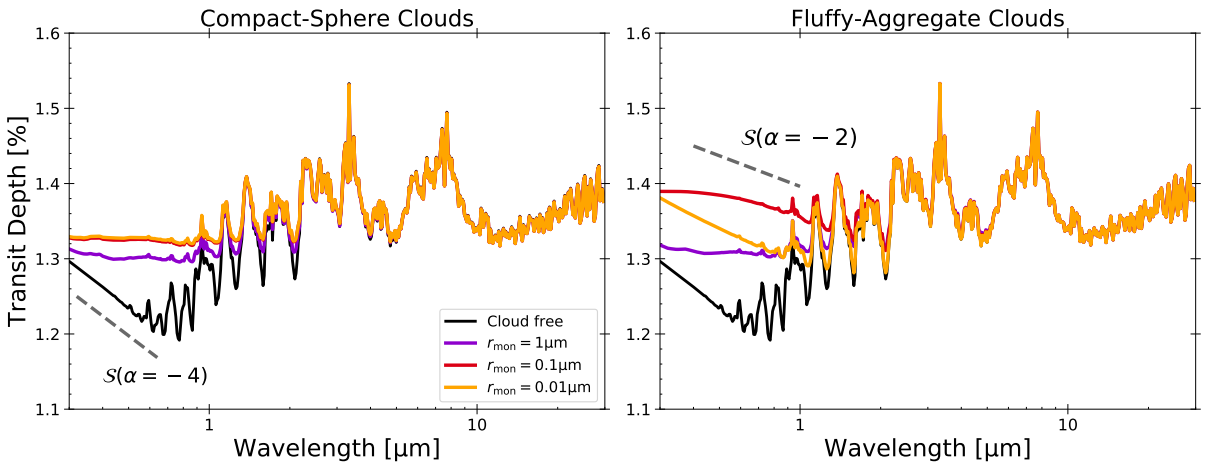


Figure 4.4: Synthetic transmission spectra of GJ1214b with a solar-metalicity atmosphere, from compact-sphere and fluffy-aggregate models (left and right panels, respectively) presented in Section 3.5. The purple, red, and orange lines are from the models assuming the monomer radii of $r_{\rm mon} = 1\ \mu$m, $0.1\ \mu$m, and $0.01\ \mu$m, respectively. In the compact-sphere models, the monomer size merely determines the number density of cloud particles at the cloud base (see Equation 3.26). For comparison, the spectrum for a cloud-free atmosphere is also shown by the black line. The gray dashed lines denote the spectral slopes corresponding to $\alpha \propto \lambda^{-4}$ for the left panel, and $\propto \lambda^{-2}$ for the right panel (see Equation 4.5). For clarity, the spectral resolution is binned down to $\lambda/\Delta\lambda \approx 100$, corresponding to the resolution of HST/WFC3.

$m_{\rm agg} \propto r_{\rm agg}^2 r_{\rm mon}$, one can see that the scattering mass opacity follows

$$\kappa_{\rm s} \equiv \frac{\sigma_{\rm s}}{m_{\rm agg}} \propto r_{\rm mon}\lambda^{-2} \log\left(16\pi^2 r_{\rm agg}^2/b\lambda^2\right). \tag{4.4}$$

Thus, the scattering mass opacity decreases with decreasing monomer size. On the other hand, in the limit of small monomer size (i.e., $\tau_{\rm mix} \ll \tau_{\rm fall}$), the cloud mass mixing ratio $q_{\rm c}$ is vertically constant and independent of monomer size (see Figure 3.3). Therefore, the scattering efficiency ($\alpha_{\rm c} = \rho_{\rm g} q_{\rm c} \kappa_{\rm s}$) and thus the cloud-top height decrease with decreasing monomer size for very small $r_{\rm mon}$.

We also find that the cloud-top pressure tends to be smaller for higher atmospheric metallicities. This is because the cloud mass mixing ratio increases with increasing the metallicity. Specifically, the cloud-top pressure for the atmospheric metallicity of 100 and $1000\times$ solar reach $P < 10^{-5}$ bar at near-infrared wavelength if the monomer is smaller than $1\ \mu$m.

4.4 Results of Synthetic Transmission Spectra

We begin by studying how the compact-sphere and fluffy-aggregate clouds affect transmission spectra. For later convenience, we introduce a metric characterizing the spectral slope, given by (e.g., Line & Parmentier, 2016)

$$\mathcal{S} \equiv \frac{dD(\lambda)}{d\log\lambda} = \frac{2\pi R_{\rm p} H}{\pi R_*^2}\alpha, \tag{4.5}$$

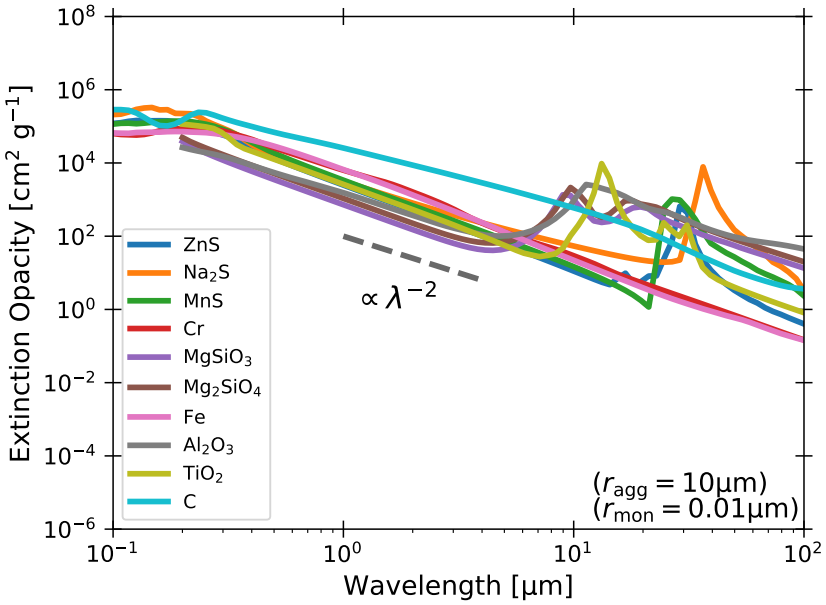


Figure 4.5: Extinction mass opacity of aggregates with $D_f = 2$ for a variety of condensable materials. The refractive index of each mineral is taken from Kitzmann & Heng (2018).

where α is the power-law index of the extinction efficiency of atmosphere, i.e., $(\alpha_g + \alpha_c) \propto \lambda^\alpha$. For example, $\alpha = -4$ for the Rayleigh scattering particles, and $\alpha = 0$ for gray cloud particles. Here, we have naively used the pressure scale height H instead of the cloud scale height. Strictly speaking, the the could scale height is equal to H only when the particle settling timescale is much longer than the mixing timescale (see e.g., Equation (33) of Ohno & Okuzumi, 2018). The cluod scale height is smaller than H at high altitude where the cloud mass mixing ratio decreases with increasing height, implying $\tau_{\rm fall} < \tau_{\rm mix}$. However, cloud particles at such very high altitude are usually so depleted that their contribution to transmission spectra is small. In fact, as shown in previous section, the cloud top hardly exceeds the the pressure level of $\tau_{\rm mix} = \tau_{\rm fall}$ for the parameter space examined in this study. Therefore, Equation (4.5) offers a reasonable diagnosis of the spectral slope.

Figure 4.4 shows the synthetic transmission spectra of GJ1214b with a solar-metallicity atmosphere and with a KCl cloud obtained from compact-sphere and fluffy-aggregate models (see the top rows of Figure 3.3 for the cloud vertical structure). We set the reference radius to $R_0 = 2.25 R_{\rm Earth}$ so that the cloud-free solar-composition atmosphere produces the planet-to-star radius ratio of $R_p/R_* \sim 0.115$ (i.e., $D \sim 1.3\%$) in near-infrared (e.g., Narita et al., 2013a). We calculate the optical properties of compact spheres using the Mie theory (e.g., Bohren & Huffman, 1983). For comparison, we also plot the transmission spectrum for the cloud-free atmosphere, which exhibits molecular absorption signatures of mainly H_2O molecules and the spectral slope in $\lambda < 0.5$ μm caused by the Rayleigh scattering of H_2 molecules. In the left panel of Figure 4.4, the compact-sphere clouds produce a floor of the transit depth at $\lambda < 2$ μm. In the compact-sphere model, a cloud deck that is gray in visible is produced no matter how small the monomers at the cloud base are, because they always grow to > 1 μm in size through coagulation as shown in Section 3.5 (see also Ohno & Okuzumi 2018).

The transmission spectrum for fluffy-aggregate clouds exhibit a considerably different shape from that for compact-sphere clouds. Since the fluffy-aggregate cloud is lofted to much higher

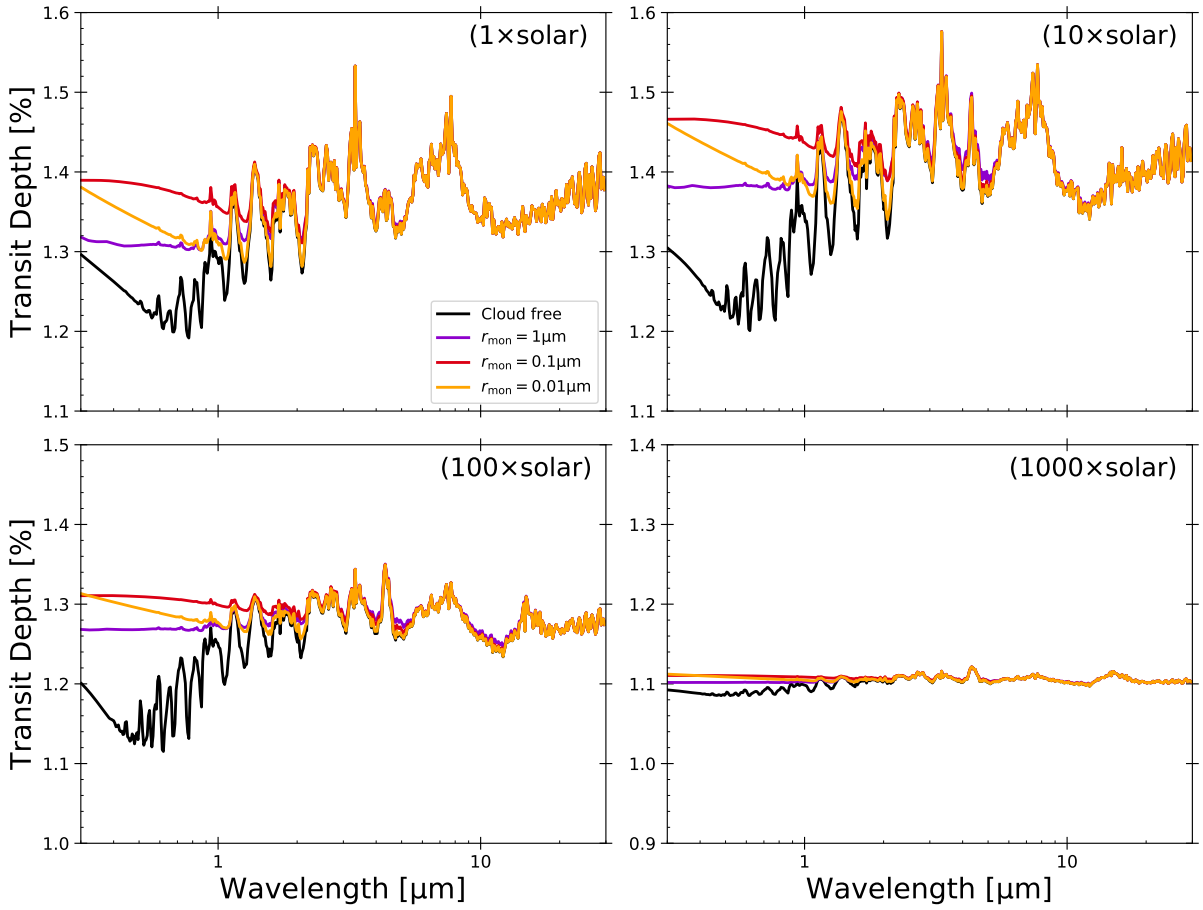


Figure 4.6: Synthetic transmission spectra of GJ1214b with a cloud of fluffy KCl aggregates for various atmospheric metallicities.

altitude, the absorption features in the spectra are largely obscured as compared to the cases of the compact-sphere clouds except for the case of $r_{\rm mon} = 0.01$ μm in which the effect that decreases the cloud extinction efficiency is important (Section 4.3.3). Furthermore, the fluffy-aggregate clouds produce a spectral slope at $\lambda < 2$ μm, in particular when the monomers are small. The spectrum for $r_{\rm mon} = 1$ μm is nearly identical between the fluffy-aggregate and compact-sphere models because the monomers satisfy $\lambda < 2\pi r_{\rm mon}$ at near-infrared wavelengths. The spectral slope for $r_{\rm mon} = 0.1$ and 0.01 μm is well characterized by $\mathcal{S}(\alpha = -2)$, originated by the wavelength dependence of the scattering opacity for $2\pi r_{\rm mon} < \lambda < 2\pi r_{\rm agg}$ (see Section 4.3.2).

Since the spectral slope with $\mathcal{S}(\alpha = -2)$ originates from the scattering property of aggregates, it could potentially be used as an observational signature for CPAs when the atmospheric scale height H is well constrained. To test whether the slope with $\mathcal{S}(\alpha = -2)$ appears for minerals other than KCl, we calculate the optical properties of various minerals that may build up exoplanetary clouds, shown in Figure 4.5. We find that the slope with $\mathcal{S}(\alpha = -2)$ also emerges for many other materials, except for graphite, C, whose extinction is dominated by absorption at entire wavelength. However, caution should be taken regarding this interpretation because $\mathcal{S}(\alpha = -2)$ may also be caused by the combination of small and large compact spheres.

Although the fluffy aggregates can largely obscure the molecular features in visible to near-infrared, they are optically too thin to hide the features at longer wavelengths ($\lambda > 2$ μm), as

Table 4.1: System parameters and model setting for each planet

	$M_{\rm p}$ $[M_{\rm Earth}]$	$R_{\rm p}$ $[R_{\rm Earth}]$	g $[{\rm m\ s^{-1}}]$	$T_{\rm eq}$ [K]	H [km]
GJ1214b	6.46	2.67	8.93	530	215
GJ3470b	12.58	4.10	6.76	620	332
GJ436b	22.25	4.3	12.79	650	184
HD97658b	7.55	2.25	14.45	690	173
HAT-P-11b	23.39	4.37	11.47	810	255

can be seen in Figure 4.6. This implies that future transmission spectroscopy at $\lambda > 2\ \mu m$ with JWST and ARIEL could detect molecular features in super-Earths that look cloudy in visible and near-infrared.

The transmission spectrum from the fluffy-aggregate model also substantially depends on the atmospheric metallicity. Figure 4.6 shows the transmission spectra from the fluffy-aggregate model for various atmospheric metallicities, where $R_0 = 2.25 R_{\rm Earth}$ is assumed for every case. One can see that the higher the atmospheric metallicity is, the flatter the spectral slope is. This is because the gradient of spectral slope is proportional to the pressure scale height H (see Equation 4.5), which decreases with increasing the atmospheric metallicity. The effect is notable for $100\times$ solar metallicity, and the spectral slope is almost flat for $> 1000\times$ solar metallicity.

4.5 Model Applications to Super-Earths

In this section, we compare the synthetic transmission spectra with observations of several super-Earths, namely GJ1214b, GJ436b, GJ3470b, HD97658b, and HAT-P-11b, to constrain their atmospheric compositions. We perform a series of cloud formation and spectrum calculation for each planet. The difference of physical properties among these planets are summarized in Table 4.1.

4.5.1 Overview of Cloud Profile on Each Planet

In this subsection, we briefly review the cloud structures on planets other than GJ1214b. To apply a cloud model, we construct a vertical PT profile of each planet using an analytical model of Guillot (2010). For GJ436b and GJ3470b, we choose the ratio of thermal to visible opacity ($\gamma = \kappa_{\rm vis}/\kappa_{\rm th}$) and thermal opacity ($\kappa_{\rm th}$) so that PT profiles match the PT profiles retrieved from their emission spectra (Morley et al., 2017; Benneke et al., 2019a). For HD97658b and HAT-P-11b, we use an analytical fit of the Rosseland mean opacity described in Freedman et al. (2014). For HD97658b and HAT-P-11b, we use an analytical fit of the Rosseland mean opacity of Freedman et al. (2014) and set the opacity ratio to $\gamma = 0.05$, which reasonably reproduces the retrieved PT profiles of the similar super-Earth GJ436b. The obtained PT profiles are summarized in Figure 4.7. It should be noted that our current model does not take into account the feedback of cloud opacity on PT profiles, which is a subject of future studies.

We calculate the cloud profiles using a microphysical model used in Chapter 3. For some planets (HD97658b, HAT-P-11b), the atmospheric temperature becomes higher than the condensation temperature at high altitude (see Figure 4.7), implying that particle evaporation sets

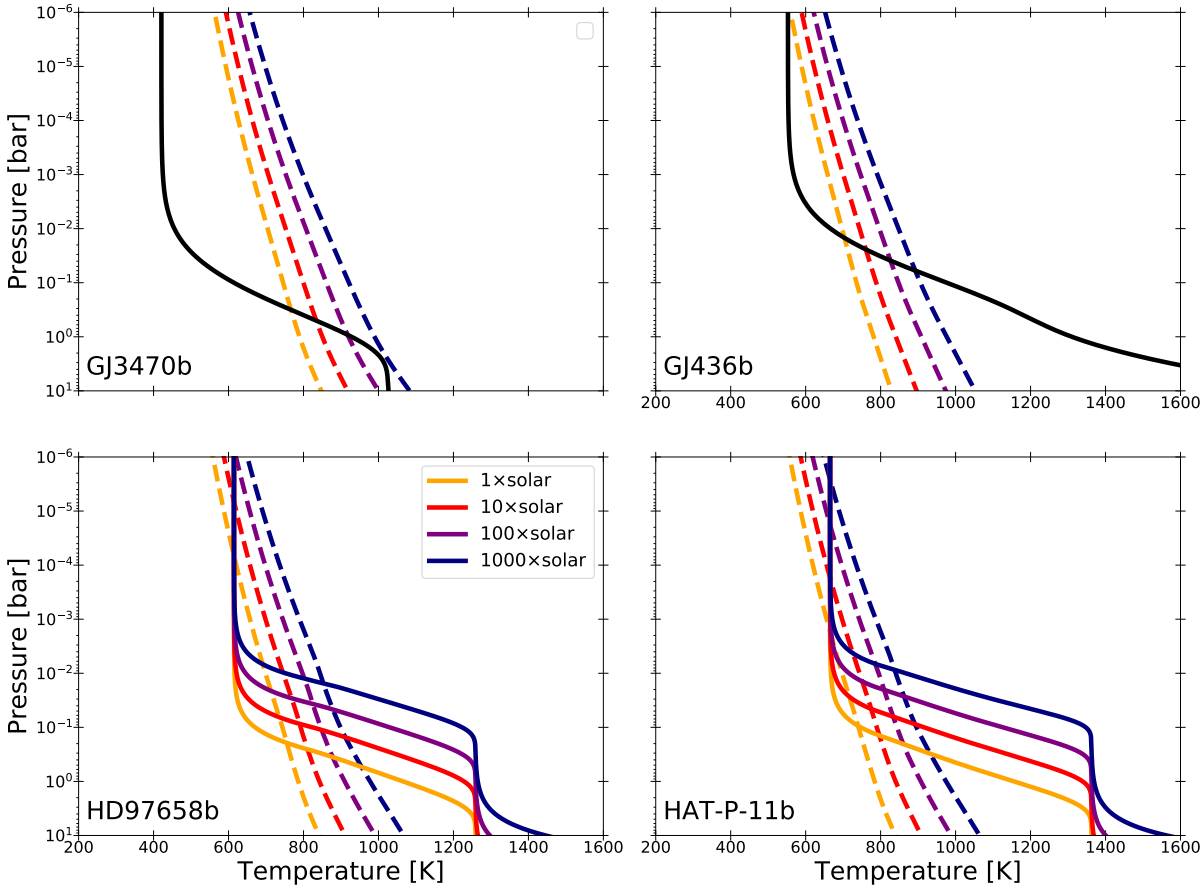


Figure 4.7: PT profiles assumed in this chapter. Each panel exhibits PT profiles (solid lines) and condensation temperature of KCl clouds (dashed lines) for different planets. The orange, red, purple, and navy lines indicate the profiles for the atmospheric metallicity of $1\times$, $10\times$, $100\times$, and $1000\times$ solar abundance, respectively.

in. To take into account the evaporation, we prescribe the condensation/evaporation term as

$$\left(\frac{\partial \rho_{\rm c}}{\partial t}\right)_{\rm cond/evap} = \min\left[4\pi r_{\rm agg}^2 C_{\rm s} n_{\rm c}(q_{\rm i} m_{\rm i} P/m_{\rm g} - \rho_{\rm s}), 0\right], \tag{4.6}$$

where $C_{\rm s} = \sqrt{k_{\rm B}T/2\pi m_{\rm i}}$ is the mean relative velocity of vapor molecules, $q_{\rm i}$ is the volume mixing ratio of i-th condensable vapor, $m_{\rm i}$ and $m_{\rm g}$ are the mass of the vapor and atmospheric molecules, respectively, and $\rho_{\rm s}$ is the saturation vapor mass density. Although one needs to solve another continuity equation of condensing vapors to evaluate the vapor density, the maximum vapor density should be set by the mixing ratio below the cloud base because of the nature of the diffusion equation. For the eddy diffusion coefficient $K_{\rm z}$, we assume a power-law function as used for GJ1214b,

$$K_{\rm z} = K_{\rm 1bar}\left(\frac{P}{1\ {\rm bar}}\right)^{-2/5}. \tag{4.7}$$

We set $K_{\rm 1bar} = 2.5 \times 10^3\ {\rm m^2\ s^{-2}}$ as a fiducial value for planets other than GJ1214b. The assumed value is comparable to that obtained by Charnay et al. (2015a) for GJ1214b and close to that obtained by a recent study of Komacek et al. (2019) for $T_{\rm eq} \sim 500$ K.

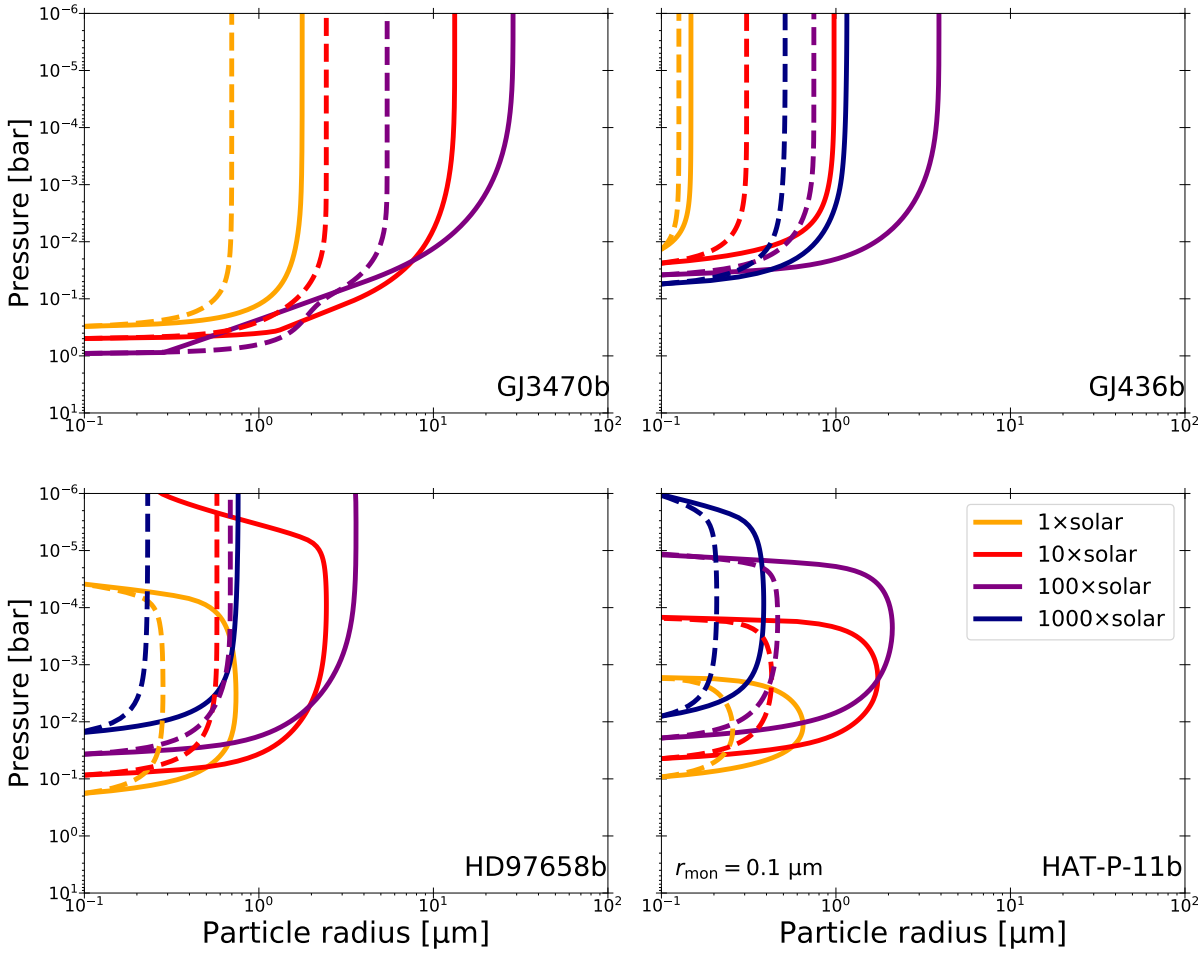


Figure 4.8: Vertical distributions of the mean particle size. Each panel exhibit the distributions for different planets. The solid and dashed lines show the distributions for the aggregate and compact-sphere clouds. The yellow, red, purple, and navy lines show the distributions for the atmospheric metallicity of $1\times$, $10\times$, $100\times$, and $1000\times$ solar abundance, respectively. The monomer size is assumed to be 0.1 μm for all cases.

Here, we show the results of the cloud formation calculations to clarify potential differences of the cloud structure among each super-Earths. Figure 4.8 exhibit vertical distributions of mean particle sizes in each super-Earth for different atmospheric metallicity. Cloud particle aggregates rapidly grow near the cloud base and plateau at the upper altitude, as found in Chapter 2 and 3. In general, the cloud particle aggregates (solid lines in Figure 4.8) grow into the sizes larger than those of compact-sphere clouds (dashed lines in Figure 4.8). We also confirm that the cloud particle aggregates rarely grow into so large size that the compression sets in, in agreement with the results of Chapter 3. Figure 4.9 also shows the vertical distributions of cloud mass mixing ratio. As found in Chapter 3, in general, the fluffy-aggregate clouds ascend to the altitude higher than those for compact-sphere clouds when the same monomer size is assumed.

The cloud particle size is somewhat different for different planets: for example, the cloud particle aggregates grow into 2–30 μm in GJ3470b, while only grow into 0.5–5 μm in HD97658b. This is caused by the difference of the atmospheric scale height (see Table 4.1). Since $\tau_{\rm mix} \propto H^2$, an atmosphere with smaller H more efficiently hinders the particle growth. Indeed, we can see

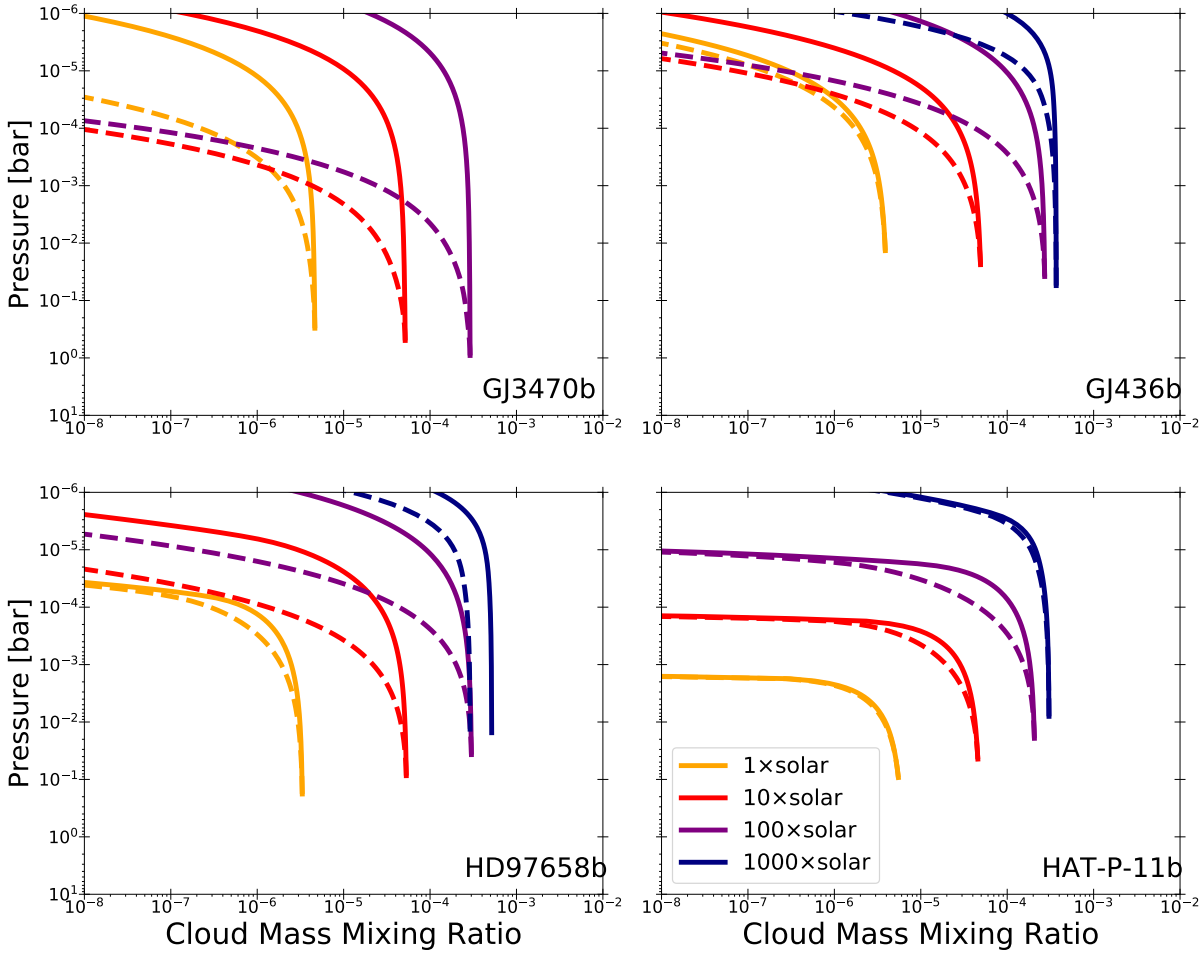


Figure 4.9: The same as Figure 4.8, but for Vertical distributions of cloud mass mixing ratio.

that a particle size ranking roughly follows the ranking of the scale height: the particle growth is less efficient for HD97658b and GJ436b, while more efficient for GJ3470b. The same explanation can be applied to the distributions for the $1000\times$ solar metallicity, in which the particle size is inefficient due to the small atmospheric scale height. However, it should be noted that current calculations assume the same value of K_z for all planets. To conclusively assess which planet is favored for the particle growth, one needs to know an exact value of K_z for each planet.

We find that KCl clouds undergo the evaporation in HD97658b and HAT-P-11b at the upper atmospheres. For HD97658b, the particle size rapidly decreases via evaporation at $P < 10^{-4}$ bar for $1\times$ solar and $P < 10^{-5}$ bar for $10\times$ solar metallicity. The evaporation does not take place for $> 100\times$ solar metallicity, as the condensing vapor is sufficiently abundant. For HAT-P-11b, the evaporation occurs for all atmospheric metallicities examined here, and the size rapidly decreases at $P < 2 \times 10^{-3}$, 10^{-4}, 10^{-5} and 10^{-6} bar for $1\times$, $10\times$, $100\times$, and $1000\times$ solar metallicity, respectively. These results are in agreement with what can be predicted from PT profiles in Figure 4.7. As seen in Figure 4.9, the evaporation leads to the depletion of the clouds at the upper atmospheres on HD97658b and HAT-P-11b, especially when the atmospheric metallicity is low. Interestingly, this is qualitatively in agreement with the finding of Crossfield & Kreidberg (2017): the hotter atmosphere is, the more cloudless atmosphere is.

4.5.2 Comparisons with Observations of Super-Earths

Here, we compare our synthetic transmission spectra with the observed transmission spectra of super-Earths to constrain their atmospheric metallicities. We calculate the cloud profiles as well as the synthetic spectra for the atmospheric metallicities of 1–1000$\times$ solar abundances and monomer sizes of 0.01–1 μm. We also vary the reference radius R_0 so that matches the observed planet radius. For planets other than GJ1214b, we use a look-up table of molecular abundance in thermochemical equilibrium calculated by an open-source code GGchem (Woitke et al., 2018) to accelerate the calculations. The relative goodness-of-fit for each model is quantified by the reduced chi-square $\chi^2_{\rm red}$. The model freedom is the number of data points minus three, the number of the fitting parameters (atmospheric metallicity, monomer size, and reference radius).

Case Study for GJ1214b

GJ1214b is presumably the most studied super-Earth. Numerous previous studies have observed the transmision spectrum of this planet (Bean et al., 2011; Croll et al., 2011; Désert et al., 2011; de Mooij et al., 2012; Berta et al., 2012; Murgas et al., 2012; Colón & Gaidos, 2013; Narita et al., 2013a,b; Fraine et al., 2013; Gillon et al., 2014; Kreidberg et al., 2014; Rackham et al., 2017). Remarkably, GJ1214b exhibits extremely flat transmission spectrum that cannot be explained by cloud-free atmospheres (Kreidberg et al., 2014). It has been suggested that the flat spectrum could be explained if the high-altitude clouds is placed at $P < 0.01$ mbar in pressure. Although there are numerous observational data, observations in visible wavelength are seriously scattered, which may stem from the stellar activity (Rackham et al., 2017). Moreover, different literature uses different orbital parameters to determine the transit depth, which yields non-physical offsets in the spectra (e.g., Lothringer et al., 2018). To avoid these effects, we only use the latest data of HST-WFC3 to calculate the reduced chi-squared value for each model.

Figure 4.10 shows the best-fit transmission spectra for the metallicity of 1, 10, 100, and 1000$\times$ solar abundance. For compact-sphere clouds (top row of Figure 4.10), we obtain the minimum reduced chi-squared values of $\chi^2_{\rm red} = 70.9$,51.9, 16.7, and 1.66 for atmospheric metallicities of 1, 10, 100, and 1000$\times$ solar abundance, respectively. For fluffy-aggregate clouds (bottom row), we obtain the minimum reduced chi-squared values of $\chi^2_{\rm red} = 60.23$, 36.50, 6.78, and 1.16 for atmospheric metallicities of 1, 10, 100, and 1000$\times$ solar abundance, respectively [1]. It should be noted that each best-fit model adopts a different monomer size: the adopted monomer size is typically $r_{\rm mon} = 0.01$ μm for compact-sphere clouds and $r_{\rm mon} = 0.3$ μm for fluffy-aggregate clouds. The presence of the cloud appreciably improves the goodness-of-fit of the model as compared to the cloud-free case. For example, a cloud-free atmosphere with 1000$\times$ solar metallicity yields $\chi^2_{\rm red} = 5.44$ (the gray line in the right panel), whereas the models with the compact-sphere and fluffy-aggregate clouds yields $\chi^2_{\rm red} = 1.66$ and 1.16. Overall, a higher atmospheric metallicity better explains the observed transmission spectrum of GJ1214b. This is mainly due to the fact that the mixing ratio of KCl in the low-metallicity atmosphere is too low to produce sufficiently opaque clouds. We also note that the best-fit spectra reasonably match the transit depth observed by Spitzer-IRAC as well (Désert et al., 2011; Fraine et al., 2013; Gillon

[1] We note that the qualitatively same results were obtained when used other observational data. For example, using all observational data, the smallest reduced chi-square for the atmospheric metallicities of 1, 10, 100, and 1000$\times$ solar abundance are $\chi^2_{\rm red} = 12.33$, 9.04, 3.28, and 2.41, respectively. For the comparison with the latest HST-WFC3 (Kreidberg et al., 2014) and Spitzer-IRAC data (Gillon et al., 2014), we obtain the reduced chi-squared of $\chi^2_{\rm red} = 57.13$, 37.13, 6.62, and 2.03 for the metallicities of 1, 10, 100, and 1000$\times$ solar abundance, respectively.

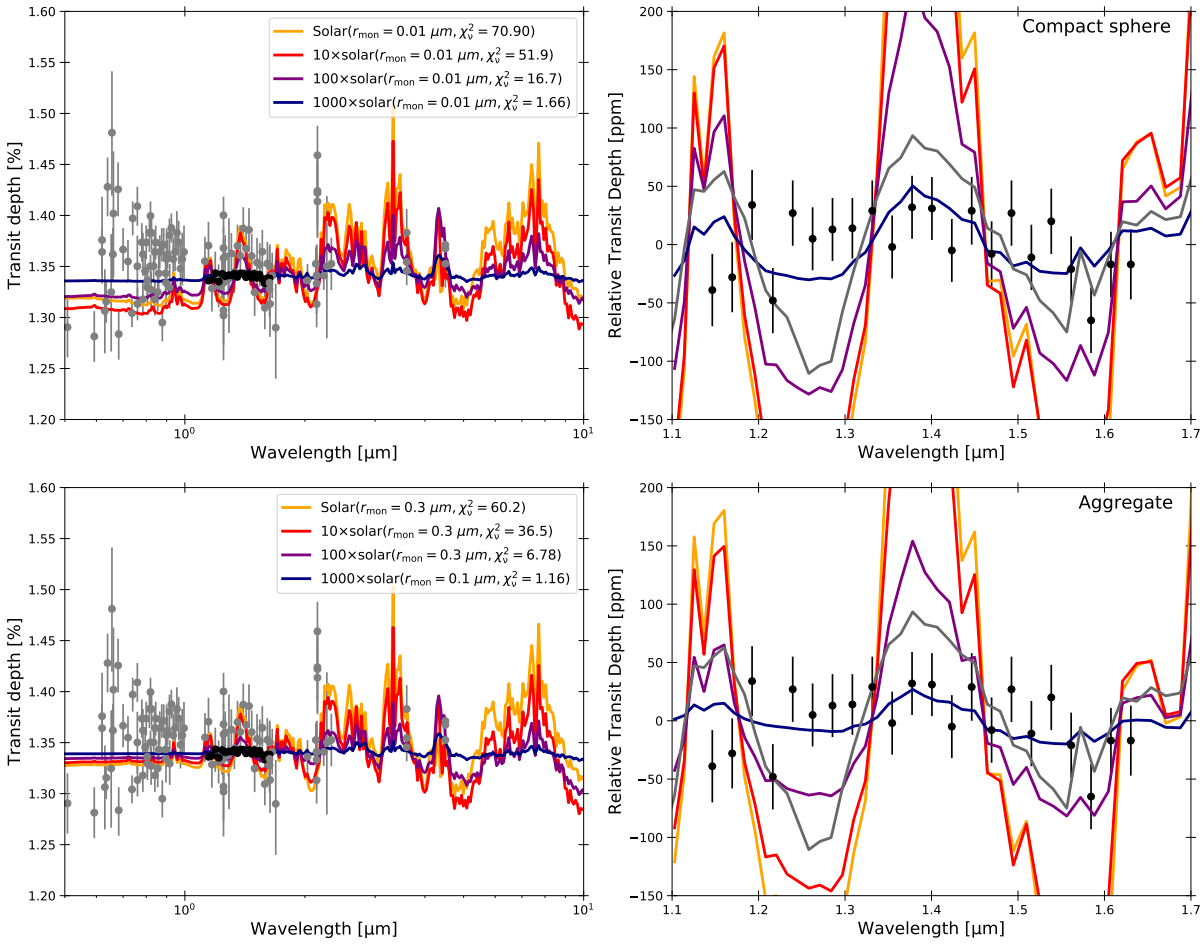


Figure 4.10: Best-fit transmission spectra of GJ1214 b compared with the observed spectrum. Top and bottom rows show the best-fit spectra for the compact-sphere and the fluffy-aggregate cloud models. The different colored lines show the best-fit spectra for the different atmospheric metallicity. The gray line in the right panel denotes the best-fit spectrum of a cloud-free atmosphere with the $1000\times$ solar metallicity. The left panel shows the comparisons with all observational data (gray dots, Bean et al., 2011; Croll et al., 2011; Désert et al., 2011; de Mooij et al., 2012; Berta et al., 2012; Murgas et al., 2012; Colón & Gaidos, 2013; Narita et al., 2013a,b; Fraine et al., 2013; Gillon et al., 2014; Rackham et al., 2017), while the right panel shows the comparisons with the data points of only HST-WFC3 (black dots, Kreidberg et al., 2014). The spectral resolution is binned down to $\lambda/\Delta\lambda \approx 100$ for clarity.

et al., 2014).

We find that the compact-sphere and the aggregate cloud models yield the similar best-fit spectra. For the atmospheric metallicity of $1000\times$ solar abundance, the compact-sphere cloud model yields the minimum chi-squared value of $\chi_{\rm red} = 1.66$ at $r_{\rm mon} = 0.01$ μm, whereas the fluffy-aggregate cloud model yields $\chi_{\rm red} = 1.16$ at $r_{\rm mon} = 0.1$ μm. Since the compact-sphere clouds produce the amplitude of H_2O absorption at $\lambda = 1.4$ μm slightly larger than that for fluffy-aggregate clouds, the aggregate model yields a better match to the observations. Why does the difference look so small? In principle, the best-fit spectrum for compact-sphere clouds is found for the smallest monomer size ($r_{\rm mon} = 0.01$ μm). In the limit of small monomer sizes, the particle size of compact-sphere cloud approach ≤ 1 μm (Figure 3.3, see also Chapter 2). At the visible to near-infrared wavelength in which the cloud opacity falls into the geometric limit, the clouds of submicron compact spheres are indistinguishable from the clouds of aggregates constituted by submicron monomers. We will revisit this topic in Section 4.5.3.

Our results for compact-sphere clouds may seem incompatible to the study of Gao & Benneke (2018) who suggests that the flat spectrum of GJ1214b can be explained only when the eddy diffusion coefficient is higher than that predicted by 3D GCM (Charnay et al., 2015a) by orders of magnitude. The difference is originated by the treatment of condensation nuclei. We vary the concentration of condensation nuclei as a free parameter, whereas Gao & Benneke (2018) calculates the nucleation rate in first principle using a classical nucleation theory. The effective particle size in Gao & Benneke (2018) is as large as $\sim$10 μm, which is quite larger than the particle size in our calculations for small monomer sizes. Since cloud particles with large sizes are subject to gravitational settling, their simulation needs a high $K_{\rm z}$ to loft the large cloud particles. Therefore, our results complement the study of Gao & Benneke (2018): the flat spectrum could be explained without assuming extremely high $K_{\rm z}$ if the amount of condensation nuclei (or nucleation rate) is much higher than that predicted by classical nucleation theory. Indeed, the nucleation rate predicted by classical nucleation theory tends to deviate from the the rate measured by experiments by several orders of magnitude (Ford, 1997). Lee et al. (2018) also reports that classical nucleation theory underestimates the nucleation rate of TiO_2 condensates that act as condensation nuclei in hot-Jupiters (e.g., Helling et al., 2019). Further observational and laboratory studies would be needed to verify the accuracy of nucleation theory.

Case Study for GJ436b

GJ436b is a Neptune-sized exoplanet, and a number of studies observed not only the transmission spectrum (Gillon et al., 2007a,b; Alonso et al., 2008; Pont et al., 2009; Shporer et al., 2009; Cáceres et al., 2009; Beaulieu et al., 2011; Knutson et al., 2011, 2014a; Lanotte et al., 2014; Morello et al., 2015; Lothringer et al., 2018) but also the emission spectrum (Deming et al., 2007; Demory et al., 2007; Stevenson et al., 2010; Knutson et al., 2011; Lanotte et al., 2014; Morley et al., 2017). Specifically, relatively flat transmission spectra observed by the HST-WFC3 (Knutson et al., 2014a) indicates the presence of high-altitude clouds at $P < 1$ mbar or an extremely metal-rich atmosphere with $> 1000\times$ solar abundance. Although there are a number of observational data, we calculate the reduced chi-squared value only using the latest data of HST-WFC3 (Knutson et al., 2014a). This is because different literature uses different orbital parameters to determine the transit depth, which yields non-physical offsets in the spectra (e.g., Lothringer et al., 2018).

Figure 4.11 shows the best-fit synthetic transmission spectrum for each atmospheric metal-

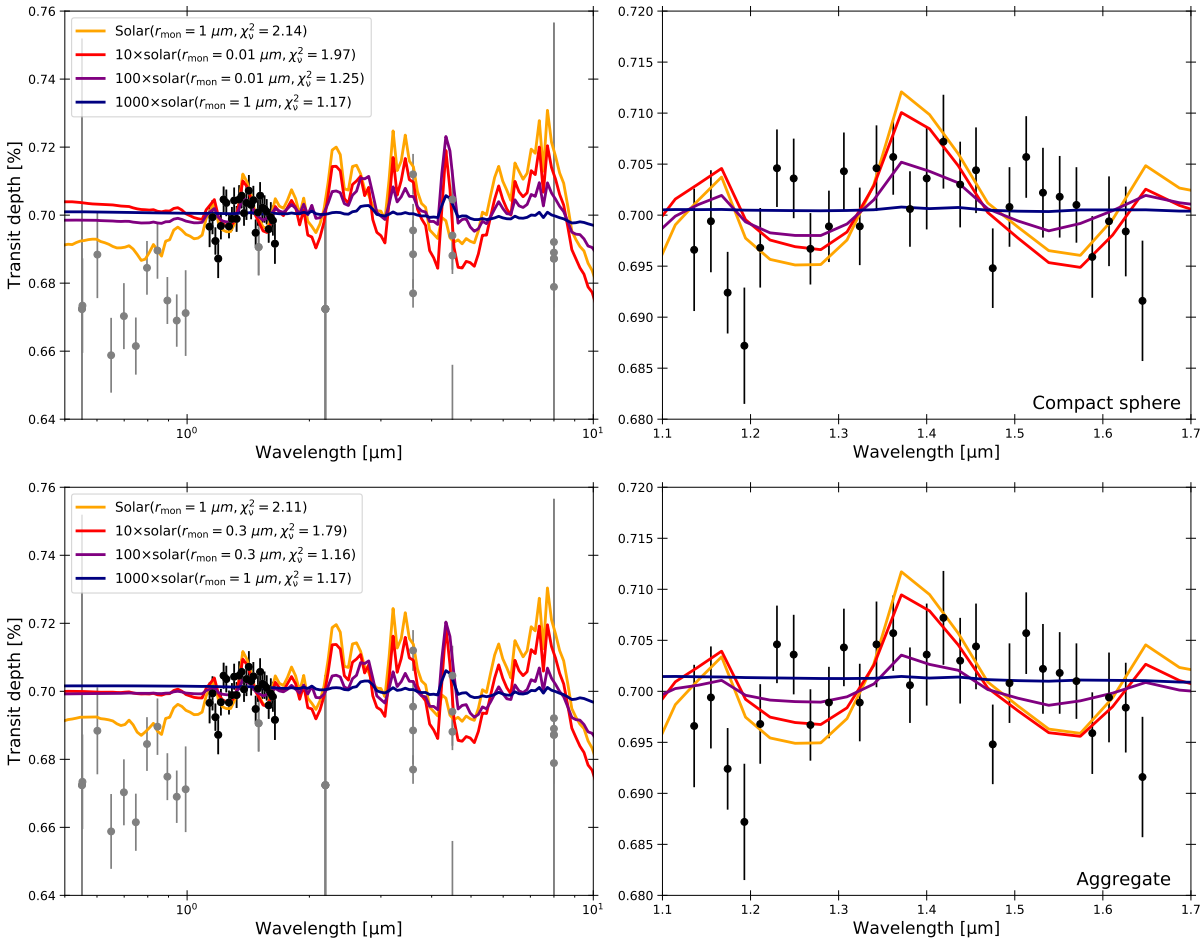


Figure 4.11: Same as Figure 4.10, but for GJ436b. The gray dots exhibit all available observational data (Gillon et al., 2007a,b; Alonso et al., 2008; Pont et al., 2009; Shporer et al., 2009; Cáceres et al., 2009; Beaulieu et al., 2011; Knutson et al., 2011; Lanotte et al., 2014; Morello et al., 2015; Lothringer et al., 2018). The black dots indicate the latest observational data of HST-WFC3 (Knutson et al., 2014a).

licity. In principle, cloud opacity makes the spectra featureless in visible to near infrared wavelength ($\lambda < 2\ \mu$m), while many absorption features (mainly caused by H_2O, CH_4, and CO) appear in the longer wavelength. This is due to the fact that clouds become optically thin at such long wavelength. For the compact-sphere cloud, the obtained reduced chi-squared value is $\chi^2_{\rm red} = 2.14$ for $1\times$ solar, 1.97 for $10\times$ solar, 1.25 for $100\times$ solar, and 1.17 for $1000\times$ solar abundance. On the other hand, for the aggregate cloud, we obtain $\chi^2_{\rm red} = 2.11$ for $1\times$ solar, 1.79 for $10\times$ solar, 1.16 for $100\times$ solar, and 1.17 for $1000\times$ solar abundance. Both sphere and aggregate models yields similar results of χ_ν, as similar to the case study for GJ1214b. This is due to the fact that the aggregate opacity falls in the geometric regime in visible to near-infrared, while the shape of longer wavelength is determined solely by the gas opacity. We will discuss this topic later (Section 4.5.3).

In both sphere and aggregate models, we find that the model with higher metallicity atmospheres ($\geq 100\times$ solar) better explains the observation of HST-WFC3. This is due to the fact that the higher atmospheric metallicity is, the more massive cloud is. Indeed, we can see that the

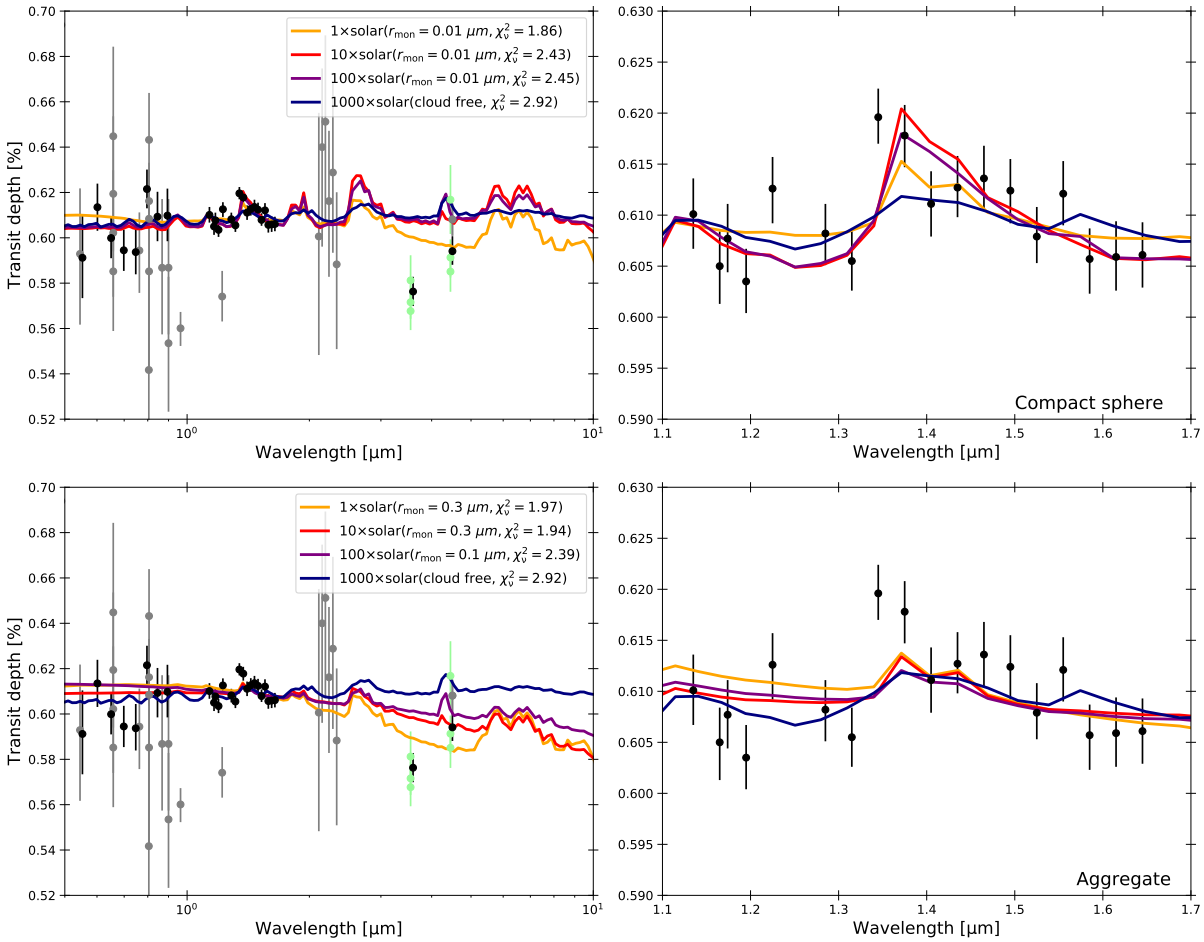


Figure 4.12: Best-fit synthetic transmission spectra for GJ3470b. The gray dots exhibit all available observational data (Demory et al., 2013b; Fukui et al., 2013; Crossfield et al., 2013; Nascimbeni et al., 2013; Biddle et al., 2014; Dragomir et al., 2015; Awiphan et al., 2016; Chen et al., 2017). The latest observational data of HST and Spitzer (Benneke et al., 2019a) are denoted by the black dots. The green dots indicate the transit depth observed by Spitzer-IRAC at individual transits. The old HST data of Ehrenreich et al. (2014) are not shown here for the sake of clarify. We note that CH_4 is omitted as suggested by Benneke et al. (2019a).

amplitude of the absorption feature at $\lambda = 1.4\,\mu$m, caused by H_2O, decreases with increasing the metallicity. The current observation is better explained by flat-like spectra, which is produced by high metallicity atmospheres. Future improvements of the observation precision would verify whether GJ436b indeed has flat-like spectra.

Case Study for GJ3470b

GJ3470b is a Uranus-sized exoplanet and a number of observations have been carried out for this planet (Demory et al., 2013b; Fukui et al., 2013; Crossfield et al., 2013; Nascimbeni et al., 2013; Ehrenreich et al., 2014; Biddle et al., 2014; Dragomir et al., 2015; Awiphan et al., 2016; Cheng et al., 2017; Benneke et al., 2019a). To avoid the offsets caused by different analysis procedures, we compare the synthetic spectra with observational data of Benneke et al. (2019a) who performed a comprehensive analysis of transmission spectra from visible to infrared wave-

length. Benneke et al. (2019a) found that the atmosphere of GJ3470b is significantly depleted in CH_4, which may stem from the effects of disequilibrium chemistry (e.g., Tsai et al., 2018). Since our current model does not take into account the effects of disequilibrium chemistry, we simply omit the contribution of CH_4 on atmospheric opacity to mimic the effects of CH_4 deficit.

Figure 4.12 shows the best-fit transmission spectrum computed by our model. For the compact-sphere cloud, we obtain the minimum reduced chi-squared value of $\chi^2_{\rm red} = 1.86$ for $1\times$ solar, 2.43 for $10\times$ solar, 2.45 for $100\times$ solar, and 2.92 for $1000\times$ solar abundance. On the other hand, for the aggregate cloud, the obtained chi-squared value is $\chi^2_{\rm red} = 1.97$ for $1\times$ solar, 1.94 for $10\times$ solar, 2.39 for $100\times$ solar, and 2.92 for $1000\times$ solar abundance. The model of compact-sphere cloud yields slightly better match to the observations. This is because the compact-sphere cloud model better explains the H_2O absorption feature at $\lambda = 1.4\,|\mu{\rm m}$. The aggregate cloud model tends to yield the weak absorption feature as compared to the observed amplitude. Some previous studies suggested the presence of steep spectral slope in visible wavelength (e.g., Dragomir et al., 2015; Chen et al., 2017). Our both compact-sphere and aggregate models do not show such slopes, which is in agreement with the latest observation of Benneke et al. (2019a). For both compact-sphere and aggregate cloud models, the models of low metallicity atmospheres ($< 100\times$ solar) are favored to explain the observation, especially the H_2O feature at $\lambda = 1.4\,\mu$m, as compared to the models of high metallicity atmospheres.

One of the remarkable feature of GJ3470b is that the transit depth observed by the Spitzer at $\lambda = 3.6$ and $4.5\,\mu$m are apparently smaller than those observed at near-infrared wavelength. The observations were conducted by three individual transits, and all transit events yield the transit depth smaller than those at near-infrared (Benneke et al., 2019a, see also green dots in Figure 4.12). Therefore, repeatability has been ensured for the Spitzer's observations. Another concern is the effects of stellar spots occulted by a transiting planet that results in the transit depth smaller than the true value [2] (e.g., Pont et al., 2008; McCullough et al., 2014; Rackham et al., 2018). However, Benneke et al. (2019a) discussed that the effects of stellar spot could change the transit depth only by a few ppm at the Spitzer's band, which is too small to reconcile the transit depth between Spitzer's band and near-infrared. Therefore, the steep drop of the transit depth from near-infrared to Spitzer's bands is presumably a real phenomena. Benneke et al. (2019a) suggested that the Spitzer's observations can be explained by the Mie scattering of cloud particles.

Interestingly, with focusing on the Spitzer's observation, the aggregate cloud model can explain the drop of transit depth better than the compact-sphere cloud model. This is because, for the compact-sphere cloud, the cloud particles grow into so large size that falls into the nearly geometric opacity regime. As a result, compact-sphere cloud tends to yield flat-like spectra in the Spitzer's band, which fail to explain the drop of transit depth from near-infrared ($\lambda = 1.1$–$1.7\,\mu$m) to Spitzer's band ($\lambda = 3.6\,\mu$m). By contrast, cloud particle aggregates with small monomer size parameter ($2\pi r_{\rm mon}/\lambda < 1$) can yield the spectral slope even if the size of a cloud particle aggregate is size (Ohno et al., 2019).

If the slope is indeed caused by the aggregate cloud, the monomer size could be constrained as $r_{\rm mon} \leq 0.6\,\mu$m, where we use the fact that the aggregate opacity falls into geometric limit for $r_{\rm mon} > \lambda/2\pi$ (Berry & Percival, 1986). Although current observations for the wavelength of $> 2\,\mu$m are sparse, near-future observations, such as JWST and Twinkle, would help to verify

[2] For example, occulted star spots and/or faculae effectively make unocculted stellar disk bright during the planet transit as compared to the stellar disk before the transit. This results in the estimated planetary radius smaller than the true radius.

which compact-sphere or aggregate cloud model can explain the overall shape of transmission spectrum. We will discuss the feasibility of JWST to distinguish the aggregate clouds from the compact-sphere clouds in Section 4.6.

Although we suggest that the current Spitzer's observation may be better explained by the aggregate cloud model, the compact-sphere model may be able to explain the observation as well if atmospheric circulation is more vigorous than that assumed here. Strong atmospheric circulation (or $K_{\rm z}$) can inhibit the growth of cloud particles and maintain a small particle size that causes the Rayleigh scattering, as originally suggested by Benneke et al. (2019a). Ohno & Okuzumi (2018) analytically estimated a lower limit of mean particle size (Equation (2.38)) which cloud particles inevitably grow into via coagulation. Inserting $r = 0.6$ μm into Equation (2.38), which is suggested by Benneke et al. (2019a), we can estimate the minimum eddy diffusion coefficient near the cloud base as

$$K_{\rm z,min} \approx 3 \times 10^3 \ {\rm m^2 \ s^{-1}} \left(\frac{q_{\rm c}}{10^{-7}} \right). \tag{4.8}$$

Equation (4.8) yields $K_{\rm z,min} \approx 6 \times 10^3$ m^2 s^{-1} for solar composition atmosphere. The higher eddy diffusion coefficient is needed for higher atmospheric metallicity because of the dependence of $q_{\rm c}$. Therefore, if future observations identify that the slope is caused by compact-sphere cloud, one might be able to derive the insight on the atmospheric circulation on this planet.

Case Study for HD97658b

HD97658b is a super-Earth similar to GJ1214b, but the densest planet in super-Earths listed in Crossfield & Kreidberg (2017). Previous studies have observed the transit of this planet at several wavelength (Dragomir et al., 2013; Knutson et al., 2014b; Van Grootel et al., 2014). In particular, observation of HST-WFC3 found relatively featureless spectrum at near-infrared and suggested the presence of clouds and/or high-metallicity atmospheres (Knutson et al., 2014b). For HD97658b, we use the all observational data to calculate the reduced chi-squared value because all of them assumed the same system parameter to derived the transit depth (Dragomir et al., 2013; Van Grootel et al., 2014; Knutson et al., 2014b).

Figure 4.13 shows the best-fit synthetic transmission spectrum for different atmospheric metallicities. For the compact-sphere clouds, we obtain the minimum reduced chi-squared value of $\chi^2_{\rm red} = 2.47$ for $1\times$ solar, 2.86 for $10\times$ solar, 2.73 for $100\times$ solar, and 2.29 for $1000\times$ solar metallicity. For the fluffy-aggregate clouds, we obtain the minimum reduced chi-squared value of $\chi^2_{\rm red} = 2.32$ for $1\times$ solar, 2.68 for $10\times$ solar, 2.65 for $100\times$ solar, and 2.26 for $1000\times$ solar metallicity. As similar to the previous case studies, compact-sphere and aggregate cloud models yield the similar reduced chi-squared value. The highest metallicity model ($1000\times$solar) matches the observations slightly better than lower metallicity models. However, the difference of $\chi^2_{\rm red}$ is not so significant among different model, and thus further observations would be needed to draw a more robust conclusion.

One of the notable feature in the observed spectrum of this planet is the transit depth observed by Spitzer at $\lambda = 4.5$ μm that is much smaller than those at visible to near-infrared. This steep drop of transit depth is reminiscent of the spectral slope seen in GJ3470b. Here, we estimate what wavelength dependence of cloud opacity can explain the Spitzer's observation. The wavelength dependence of transit depth is given by (Equation (1.12)),

$$\frac{dD}{d\log\lambda} = \frac{2R_0 H}{R_{\rm s}^2}\alpha, \tag{4.9}$$

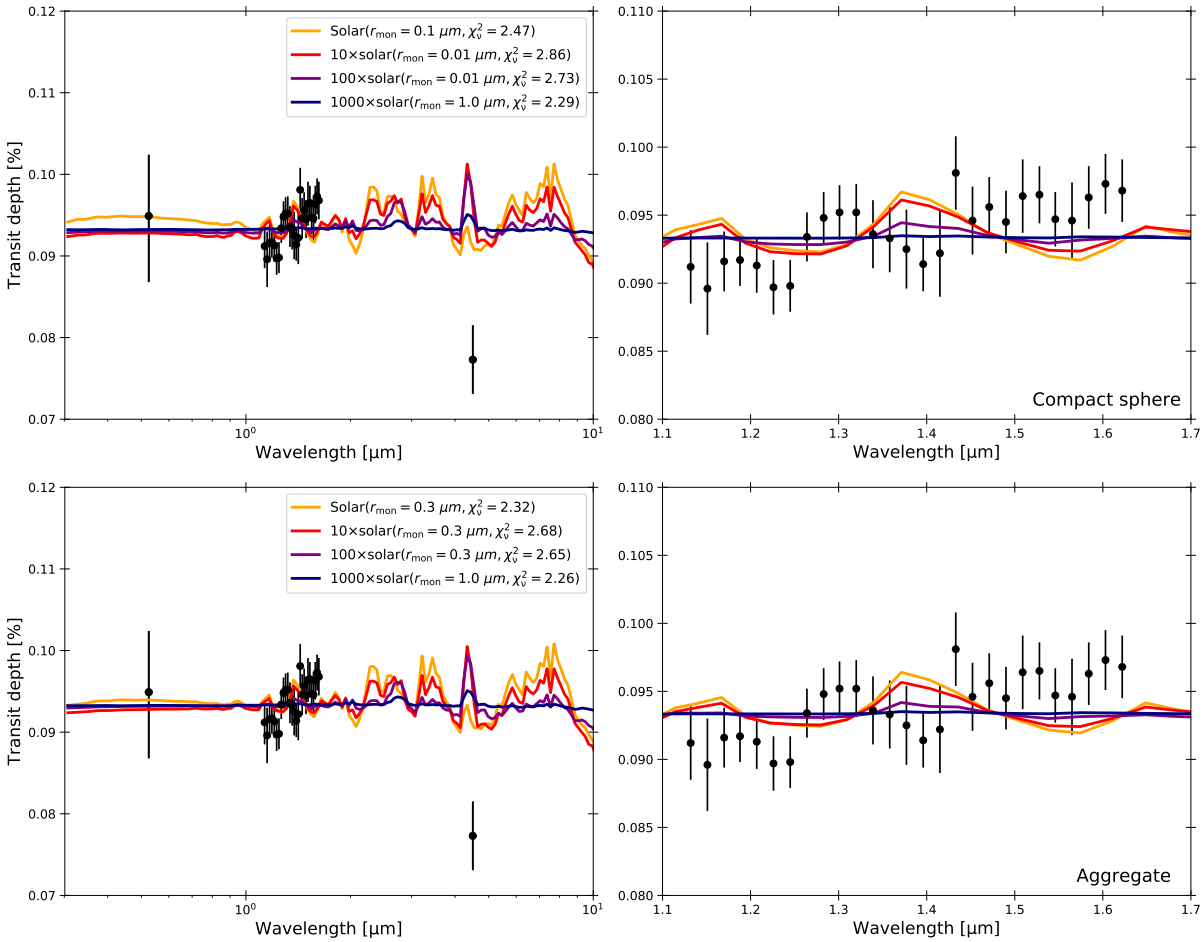


Figure 4.13: Best-fit synthetic transmission spectra for HD97658b. The black dots exhibit all available observational data (Dragomir et al., 2013; Knutson et al., 2014b; Van Grootel et al., 2014).

where we assume that the cloud opacity follows $\kappa \propto \lambda^\alpha$. Since $D \sim (R_0/R_\mathrm{s})^2$, the required wavelength dependence is given by

$$\alpha \approx \frac{R_\mathrm{s}}{2H\sqrt{D}} \frac{dD}{d\log\lambda} \tag{4.10}$$

If one attempts to explain the observed drop of transit depth from $D = 950$ ppm at $\lambda = 1.5\,\mu$m to $D = 800$ ppm at $\lambda = 4.5\,\mu$m assuming solar composition atmosphere, the required wavelength dependence is $\alpha \approx -7$. This is quite steeper than the dependence for the Rayleigh scattering, $\alpha = -4$. Therefore, from current observational data, it is difficult to claim that the Spitzer's observation stem from the scattering of cloud particles. Future precise observations will be needed to shed light on the nature of HD97658b's atmosphere in more detail.

Case Study for HAT-P-11b

HAT-P-11b is a Neptune-sized exoplanet whose mass and radius are similar to GJ436b. Several studies have observed the transmission spectra of this planet from visible to infrared (Fraine et al., 2014; Mansfield et al., 2018; Chachan et al., 2019). Specifically, Chachan et al. (2019) performed

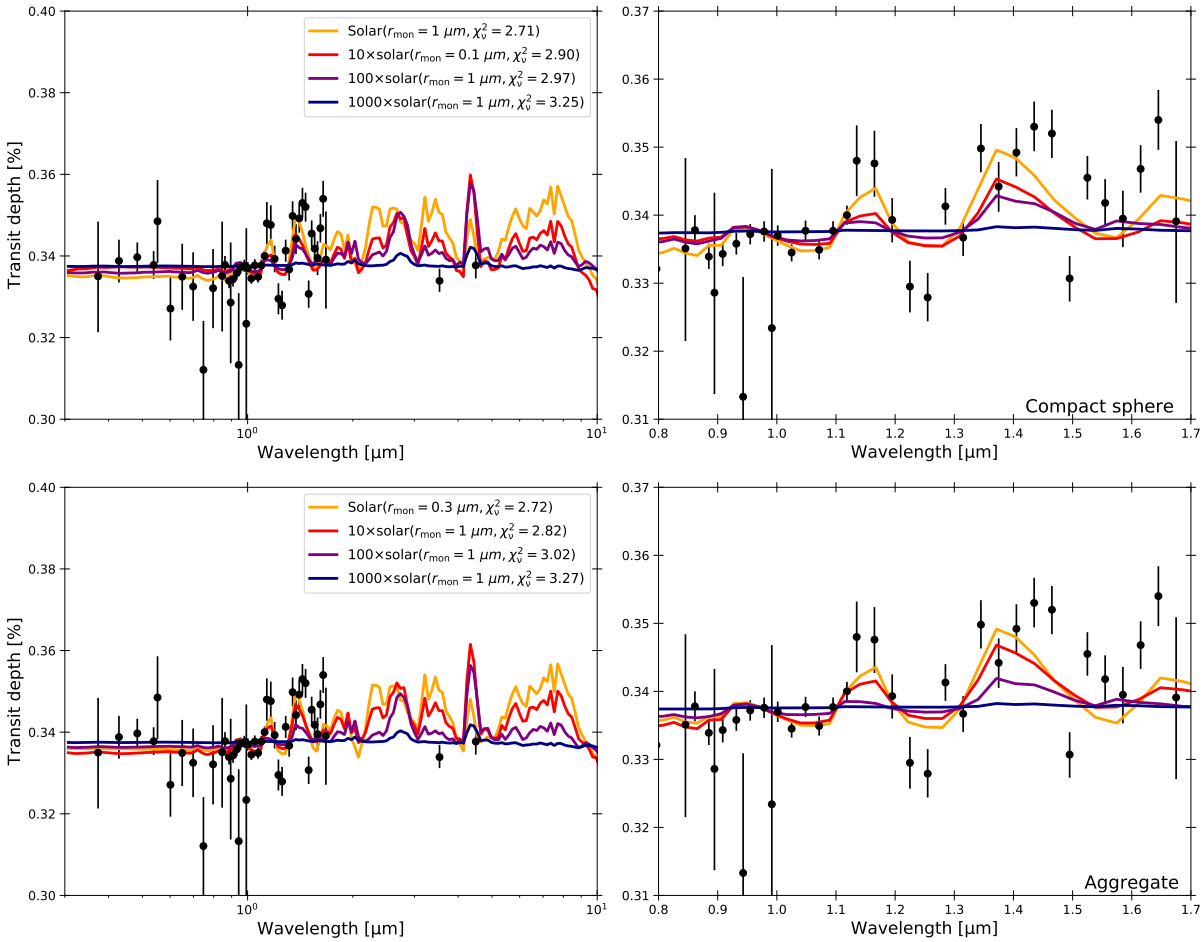


Figure 4.14: Best-fit synthetic transmission spectra for HAT-P-11b. The black dots exhibit the observational data of Chachan et al. (2019).

a comprehensive analysis of transmission spectra from visible to infrared wavelength. To avoid the effects of offsets caused by different observational analyses, we compare the synthetic spectra with transit depth listed in Chachan et al. (2019).

Figure 4.14 shows the best-fit transmission spectra for different atmospheric metallicities. For compact-sphere cloud, we obtain the minimum chi-squared value of $\chi^2_{\rm red} = 2.71$ for $1\times$ solar, 2.90 for $10\times$ solar, 2.97 for $100\times$ solar, and 3.25 for $1000\times$ solar metallicity. On the other hand, for the aggregate cloud, the chi-squared value is $\chi^2_{\rm red} = 2.72$ for $1\times$ solar, 2.82 for $10\times$ solar, 3.02 for $100\times$ solar, and 3.27 for $1000\times$ solar metallicity. Both compact-sphere and aggregate cloud models yield the similar results again, as seen in the previous case studies. For both compact-sphere and aggregate cloud models, the lower metallicity models better match to the observations. This is because HAT-P-11b shows noticeable H_2O feature at $\lambda = 1.4$ μm, which is hardly explained by flat-like spectra produced by the high-metallicity ($> 100\times$ solar) models. This is similar to GJ3470b for which the low-metallicity models better match the observed spectra. In particular, for solar metallicity, clouds disappear at upper atmosphere ($P < 1$ mbar in pressure) due to the evaporation (see Figure 4.9), leading to a relatively strong H_2O feature.

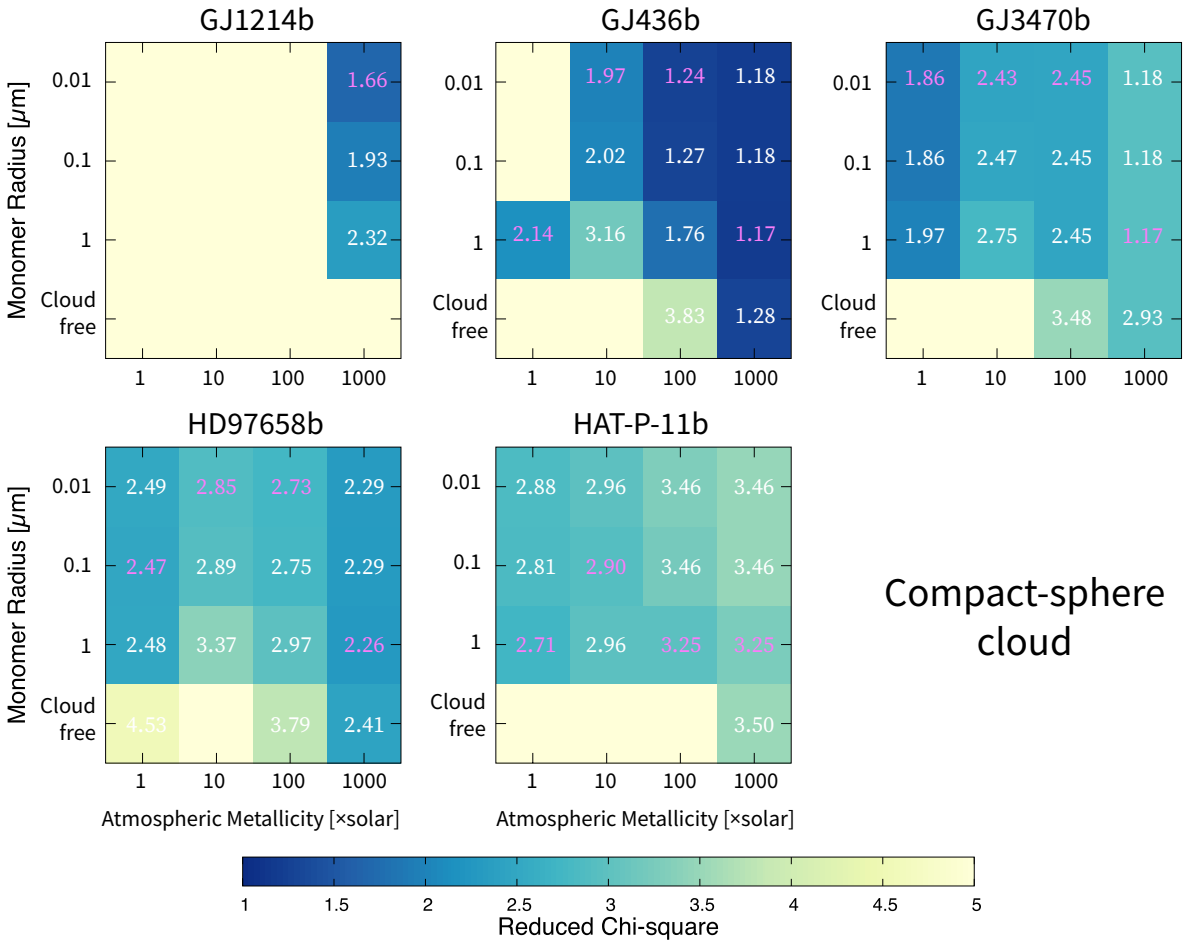


Figure 4.15: Reduced chi-squared value of parameters of the compact-sphere cloud models for each planet. Each figure show the reduced chi-squared value for each parameter set. The magenta text denotes the minimum $\chi^2_{\rm red}$ for given atmospheric metallicity.

Summary of Inferred Metallicity

We summarize obtained reduced chi-squared value of each parameter set for compact-sphere clouds in Figure 4.15 and the fluffy-aggregate clouds in Figure 4.16. As stated so far, the minimum reduced chi-squared value is qualitatively similar between the compact-sphere and the aggregate cloud models. For the compact-sphere clouds, the small monomer size preferentially yields the good match to the observations. This is because the smaller monomer size (i.e., high CCN concentration) is, the smaller the particle size at an upper atmosphere is (Chapter 2). Some exception also exists, such as the $r_{\rm mon} = 1\ \mu$m for solar metallicity atmosphere of GJ436b. This exception is originated when the particle growth is inefficient. In the case of GJ436b, the particle size at upper atmosphere is too small to flatten the near-infrared spectrum when the monomer size is small. Therefore, if one attempts to explain the observations of GJ436b by compact-sphere clouds, our results implies that the initial monomer, which is formed via nucleation followed by condensation, should be larger than $\approx 1\ \mu$m. In contrast to compact-sphere clouds, the aggregate cloud models preferentially adopt the monomer size of $r_{\rm mon} \sim 0.3$–$1\ \mu$m. This is because, as argued in Section 4.4, the aggregate clouds become too transparent to obscure the spectral feature if the monomer size is too small, say $r_{\rm mon} \ll 0.1\ \mu$m. Our results imply that the nucleated cloud

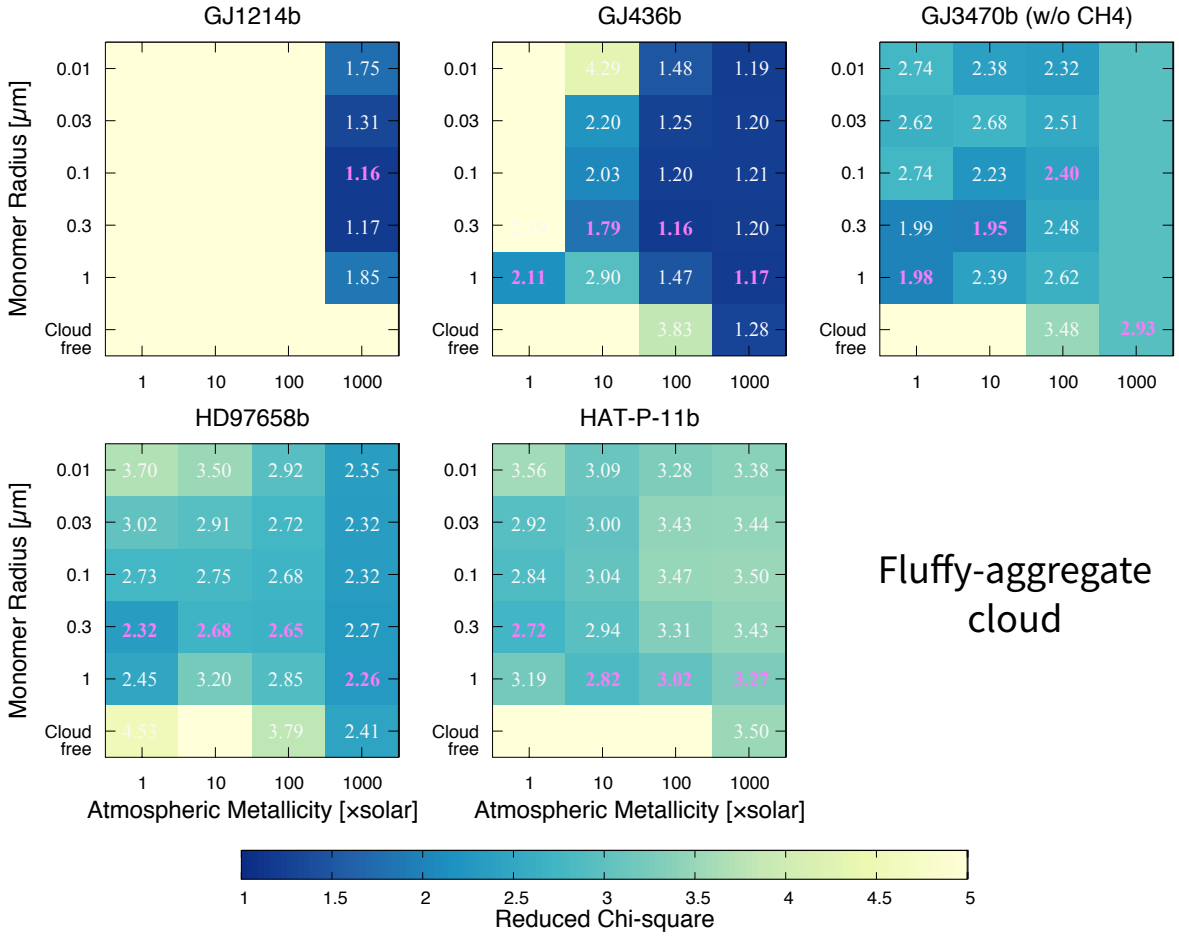


Figure 4.16: Same as Figure 4.15, but for the fluffy-aggregate cloud models.

particles should grow into submicron size via condensation if the featureless spectrum is caused by the aggregate clouds. Therefore, although the obtained reduced chi-squared value is similar, the compact-sphere and the aggregate cloud models potentially have different implications for initial monomer formation via some nucleation processes.

We find that super-Earths examined here can be demarcated into at least two categories. The first is the planets for which high-metallicity atmospheres ($\geq 100\times$ solar abundance) are preferred to explain the transmission spectra. GJ1214b, GJ436b, and HD97658b can be classified into this category. The second category is the planets for which low-metallicity atmospheres ($\leq 10\times$ solar abundance) are preferred to explain the transmission spectra. GJ3470b and HAT-P-11b may be classified into this category.

We state the containment on the atmospheric metallicity for each planet in detail. For GJ1214b, only models with $> 100\times$ solar metallicities can explain the observations within $\chi^2_{\rm red} < 5$ regardless of the monomer sizes. The extremely high-metallicity models ($\sim 1000\times$ solar) can explain the observations pretty well. For GJ436b,the high-metallicity models ($\geq 100\times$ solar) produce pretty good matches ($\chi^2_{\rm red} \sim 1$) to the observations, and hence this planet likely possess the high-metallicity atmosphere. However, low atmospheric metallicity with fine-tuned monomer sizes ($r_{\rm mon} \sim 0.3\ \mu$m) also produces moderate matches to the observations ($\chi^2_{\rm red} \sim 2$) and may not be ruled out yet. Since the spectra at the infrared ($\lambda > 2\ \mu$m) behave qualitatively

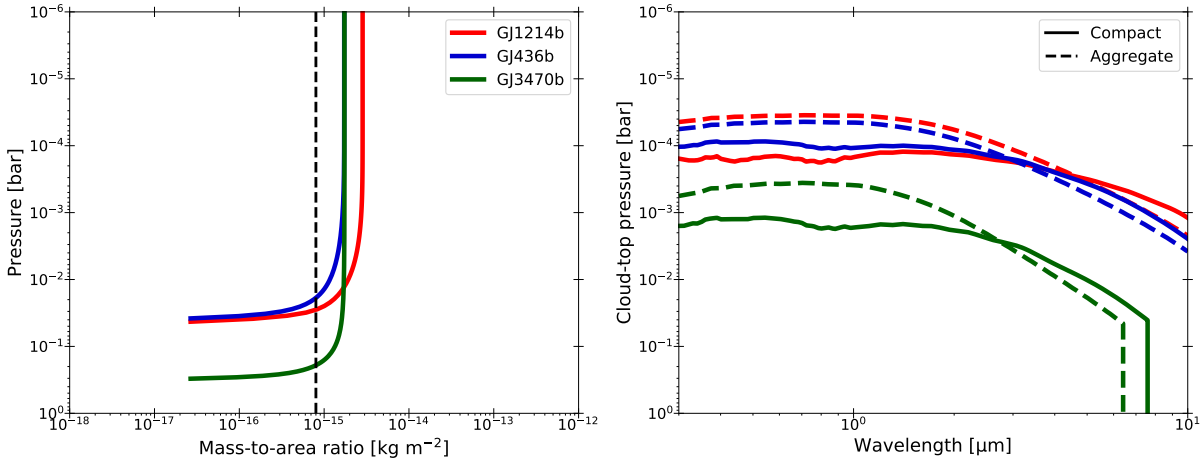


Figure 4.17: (Left): Vertical distributions of mass-to-area ratio of cloud particles in compact-sphere cloud models for GJ1214b (red), GJ436b (blue), and GJ3470b (green). The monomer sizes and atmospheric metallicity are selected so that produce the best-fit transmission spectra. The black dashed line denotes the mass-to-area ratio of cloud particle aggregates of $r_{\rm mon} = 0.3$ μm. (Right): Cloud-top pressure in the best-fit models of GJ1214b (red), GJ436b (blue), and GJ3470b (green) as a function of wavelength. The solid and dashed lines show the cloud-top pressure for the best-fit models compact-sphere cloud models and aggregate cloud model.

different between low and high metallicity atmospheres (Figure 4.11), future observations will be helpful to derive more robust conclusion. For HD97658b, an extremely high-metallicity atmosphere ($\sim 1000\times$ solar) can match the observations within $\chi^2_{\rm red} < 2$ regardless of the monomer size. However, low metallicity atmospheres with $r_{\rm mon} \approx 0.3$ μm yield the moderate matches to the observations as well($\chi^2_{\rm red} \sim 2$), and thus further observations are needed to better constrain the atmospheric metallicity.

4.5.3 Degeneracy between Compact-Sphere and Aggregate Clouds

So far, we have seen that compact-sphere and aggregate cloud models tend to yield the similar best-fit spectra. This may look inconsistent with the finding of Section 4.4 in which the aggregate cloud tends to produce different spectral shapes from those for compact-sphere clouds. The similarity stems from the fact that the best-fit spectra preferentially adopt the monomer size of $r_{\rm mon} = 0.3$–1 μm. As shown in Section 4.4, the cloud particle aggregate yields the gray opacity in the wavelength shorter than $\lambda \sim 2\pi r_{\rm mon}$, corresponding to $\lambda < 1.8$ μm for $r_{\rm mon} = 0.3$ μm. Therefore, in visible to near-infrared wavelength, both compact-sphere and aggregate clouds produce the similar flat-like spectra. On the other hand, at longer wavelength $\lambda > 2$ μm, the spectral shape is insensitive to cloud properties because gas opacity tends to dominate over the cloud opacity. This is a one of the reason why the compact-sphere and the aggregate cloud models yield similar best-fit spectra.

Another reason is that, in the geometric limit, the opacity of a spherical particles is degenerated with that for an aggregate constituted by the same-sized monomers. In the geometric limit, the aggregate mass opacity is given by

$$\kappa_{\rm geo} \sim \frac{\pi r_{\rm agg}^2}{m_{\rm agg}} = \frac{3}{4\rho_{\rm p} r_{\rm mon}}, \tag{4.11}$$

where we assume $D_{\rm f} = 2$. One can see that the opacity is identical to that for a compact sphere with a radius of r. Moreover, the sedimentation velocity of a spherical particle is also identical to that of an aggregate constituted by the same-sized monomers, implying that the vertical mass distribution is also the same.

Above explanation means that the vertical opacity distributions are determined by the mass-to-area ratio of cloud particles at the short wavelength. We show the particle mass-to-area ratio in the compact-sphere cloud models producing the best-fit transmission spectra in the left panel of Figure 4.17. One can see that the the mass-to-area ratio for compact-sphere clouds is indeed similar to that of a cloud particle aggregate with $r_{\rm mon} = 0.3$ μm within a factor of 2–3. As a result, at the short wavelength (< 2 μm), the difference of cloud-top pressure between compact-sphere and aggregate clouds is only a factor of 2–3 as well (right panel of Figure 4.17). Using Equation (1.11), we estimate the difference of transit depth at the short wavelength between compact-sphere and aggregate cloud models as

$$D_{\rm agg} - D_{\rm com} \approx 2 \left(\frac{R_{\rm p}}{R_{\rm s}} \right)^2 \left(\frac{H}{R_{\rm p}} \right) \log \left(\frac{P_{\rm top,agg}}{P_{\rm top,com}} \right) \sim 25 \text{ ppm} \left(\frac{D}{0.5\%} \right) \left(\frac{H}{100 \text{ km}} \right) \left(\frac{R_{\rm p}}{3 R_{\rm E}} \right). \tag{4.12}$$

The difference is comparable to the smallest observational noise derived by HST-WFC3, such as $\sim$ 40 ppm for GJ436b (Knutson et al., 2014a) and $\sim$ 30 ppm for GJ3470b (Benneke et al., 2019a). The spectral behavior is also the same at such short wavelength. Therefore, it is currently hard to distinguish both models from the observations[3].

Although it is difficult to distinguish the aggregate cloud from the compact-sphere clouds in current observations, the difference would be found by future observations that can probe long wavelength. This is because, out of the geometric limit, the spectral behavior of a cloud particle aggregate is different from that of a spherical cloud particle. This can be seen in Figure 4.17: the cloud-top pressure of cloud particle aggregates increases with increasing wavelength at > 2 μm more steeply than that of compact-sphere clouds. Although the cloud opacity tends to be obscured by gas opacity, it may be able to see the spectral behavior of the cloud opacity if CH_4 is depleted. This is actually demonstrated in the case study for GJ3470b in which the aggregate model better explains the spectral slope. Since the CH_4 deficit is suggested for other sub-Neptunes, such as GJ436b (Stevenson et al., 2010) and WASP-107b (Kreidberg, 2018), future observations may find the spectral slope in the long wavelength as well. It is also worth noting that the drop of transit depth from near-infrared to Spitzer's band was observed for some hot-Jupiters (e.g., Nikolov et al., 2015; Sing et al., 2015) where the carbon chemistry is dominated by CO rather than CH_4.

4.6 Implications for Observations of JWST

Future observations, such as JWST, will probe the transmission spectrum at wavelength much longer than that probed by current instruments. For example, JWST-NIRSpec can probe the wavelength span of $\lambda = 0.7$–5 μm with spectral resolution of $R \sim 1000$. At such long wavelength, the cloud opacity tends to be out of the geometric limit, leading to distinct spectral behav-

[3]Note that the difference can be larger for planets with larger transit depth D. This is why the reduced chi-squared value is somewhat different between the two cloud models for GJ1214b.

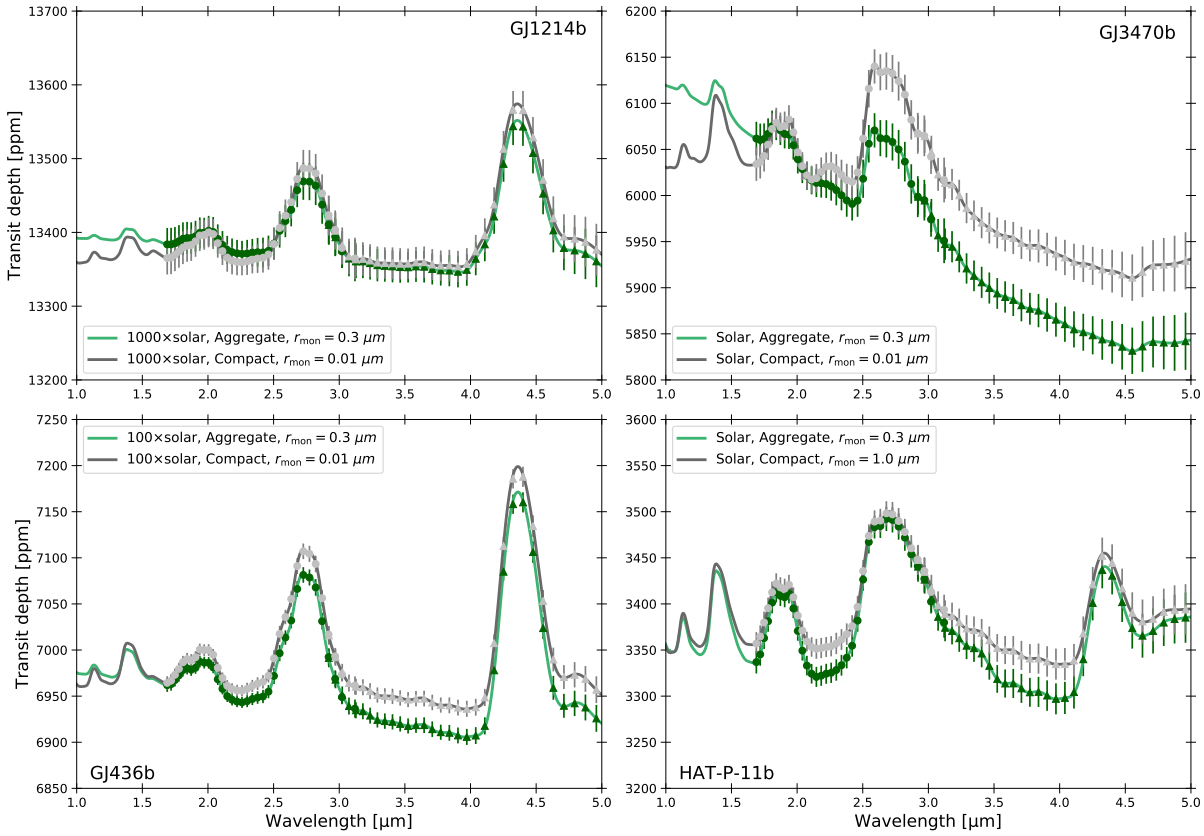


Figure 4.18: Observational noises for JWST-NIRSpec calculated by PandExo (Batalha et al., 2017). Each panel shows the results for different super-Earth. The gray and green lines show the best-fit synthetic spectra without CH_4 for compact-sphere and aggregate cloud models, which are binned down to $R = 30$. The green and gray symbols show the expected observational noises with 1σ error bars, where the circles and triangles denote NIRSpec G235M/H and G395M/H. Here, we assume the observational time of 5 transits and spectral resolution of $R = 30$. Stellar parameters and transit duration are taken from exoplanets.org.

ior for compact-sphere and aggregate clouds[4]. It is worth investigating how future observations are influenced by whether the cloud is made of compact-spheres or fluffy-aggregates.

Here, we investigate the feasibility of JWST to distinguish the aggregate clouds from compact-sphere clouds. We examine the feasibility for planets with CH_4, as the CH_4 deficit has been suggested for some warm super-Earths (Stevenson et al., 2010; Kreidberg, 2018; Benneke et al., 2019a). We calculate the synthetic observations of JWST-NIRSpec using an open-source noise simulator, PandExo (Batalha et al., 2017). The model takes into account the photon noise, background noise, and read noise. To evaluate potential dispersion of observed spectra, we utilize the best-fit synthetic spectra for compact-sphere and fluffy-aggregate cloud models as true atmospheric spectra. Stellar SED models are taken from Phoenix Stellar Atlas (Husser et al., 2013). We do not include noise floors in our simulated observations, although it may limit the capability of JWST (Greene et al., 2016).

[4]We note that this is valid for relatively scattering clouds. If the extinction is dominated by absorption, the spectral behavior is invariant with particle internal structure as long as $D_f = 2$ (Lavvas et al., 2019). However, as shown in Figure 4.5, the opacity of mineral cloud is prone to be dominated by scattering.

We show the observational 1σ noises simulated for 5 transits with spectral resolution of $R = 30$ in Figure 4.18. The evaluated noise is typically 20–30 ppm for GJ1214b, 15–20 ppm for GJ3470b, and 5–10 ppm for GJ436b, and 10–20 ppm for HAT-P-11b. Figure 4.18 shows that several gas molecules, such as H_2O ($\lambda \approx 1.8, 2.8\ \mu$m) and CO_2 ($\lambda \approx 2.8, 4.3\ \mu$m), produce the spectral feature much larger than observational noise. This results demonstrate the capability of JWST for detecting atmospheric molecules.

We also find that the compact-sphere and aggregate cloud models potentially produce noticeable difference in transmission spectra observed by JWST-NIRSpec. The difference is quite small in the short wavelength ($< 3\ \mu$m) because the cloud opacity is obscured by the gas opacity. On the other hand, at long wavelength ($> 3\ \mu$m), the aggregate cloud models systematically produce the transit depth smaller than that of compact-sphere clouds, since the aggregate scattering opacity decreases with increasing wavelength (Equation 4.3). The difference of transit depth is as large as $\approx$ 30 ppm for GJ436b and HAT-P-11b and $>$ 50 ppm for GJ3470b. Since the difference is quite larger than the expected observational noise, it would be able to distinguish whether the cloud is made of compact-spheres or fluffy-aggregates.

We note that it is hard to identify the difference of the two cloud models for GJ1214b. This is because the extremely high atmospheric metallicity leads to a small atmospheric scale height and thus small model differences. In other words, planets with large atmospheric scale height are favored to search the fluffy-aggregate clouds. A super-Neptune WASP-107b would be a good target to test the idea because this planet has low surface gravity, featureless near-infrared spectrum, and possibly a CH_4-depleted atmosphere (Kreidberg, 2018).

4.7 Summary

We have studied the impacts of cloud on the transmission spectrum of exoplanetary atmospheres using a cloud microphysical model. We investigated how the cloud particle aggregates affect the observable spectra for the first time. We have also applied the cloud and spectrum models to super-Earths GJ1214b, GJ436b, GJ3470b, HD97658b, and HAT-P-11b to constrain their atmospheric compositions from the observed spectra. Our findings are summarized as follows.

(1) The fluffy-aggregate clouds largely obscure the absorption signatures of gas molecules in transmission spectra at visible to near-infrared (Section 4.4).

(2) The aggregate clouds also produce the spectral slope originated by the scattering properties of aggregates when the monomer size parameter is lower than unity ($2\pi r_{\rm mon}/\lambda < 1$, Section 4.3.2). The slope reflects the wavelength dependence of the aggregate scattering opacity, $\alpha_{\rm c} \propto \lambda^{-2}$ (Section 4.4). Since the compact-sphere clouds produce either the flat spectrum or the Rayleigh scattering slope corresponding to $\alpha_{\rm c} \propto \lambda^{-4}$, the slope measurement could help to identify the aggregate clouds in observations.

(3) Recent study of Crossfield & Kreidberg (2017) suggests that hotter planets tend to be cloudless. This trend might be explained by the fact that KCl clouds disappear at environments hotter than $\sim$ 700 K, although one needs to assess the impacts of sodium clouds to draw a more robust conclusion.

(4) Our results might suggest the dichotomy of super-Earths in terms of the atmospheric metallicity. GJ1214b and GJ436b, which exhibit the featureless spectra, likely possess high-metallicity atmosphere, such as $\geq 100\times$ solar abundance. By contrast, GJ3470b and HAT-P-11b, which exhibit clear H_2O absorption in near-infrared, likely possess low-metallicity atmospheres, such as $< 100\times$ solar abundance. The atmospheric metallicity of HD97658b was not

well constrained from current observations.

(5) We found that the compact-sphere and fluffy-aggregate clouds can similarly match the current observations. This is because sub-micron compact spheres and aggregates constituted by sub-micron monomers have the same aerodynamical and optical properties at visible to near-infrared wavelength, which predominantly determines the goodness of model fits.

(6) The degeneracy between the compact-sphere and the aggregate clouds is potentially solved by the observations at long wavelength. This is partially demonstrated for the case study of GJ3470b, in which the aggregate clouds better explain the Spitzer's observation as compared to the compact-sphere clouds. The simulated observational noise of JWST suggests that it may be able to distinguish between the compact-sphere and the aggregate clouds for GJ3470b, GJ436b, and HAT-P-11b using the JWST-NIRSpec if their atmospheres are depleted in CH_4.

In this chapter, we have suggested that super-Earths might be demarcated into two subdivisions: planets with low-metallicity atmospheres and high-metallicity atmospheres. The difference of atmospheric metallicity likely indicates the distinct formation path for these planets. The atmospheric metallicity is also associated to planet internal structure because planetary radius is sensitive to the properties of atmospheres (e.g., Adams et al., 2008a; Valencia et al., 2013). Therefore, the atmospheric metallicity inferred in this chapter potentially has a implications on their internal structure. In next chapter, we will discuss what we can learn about the internal structure and formation process of super-Earths studied so far.

Chapter 5

Inferring Interior Structure and Formation Process of Super-Earths

5.1 Abstract

The origin of super-Earths—the most common exoplanets in this universe—is a fundamental question in current planetary sciences. Planetary interior structure is one of the key to infer the formation process. The interior structure is speculated from the planetary mass-radius relation; however, the interiors of large super-Earths ($R_{\rm p} > 1.6 R_{\rm E}$) have been poorly understood because the planetary radius is sensitive to the unknown atmospheric properties. In this chapter, we examine the interior structure of super-Earths studied in Chapter 4 utilizing the atmospheric metallicity and opaque pressure level constrained from the observations of transmission spectra. The planetary mass-radius relation appreviably depends on both the metallicity and the opaque pressure level. We find that the super-Earths have approximately 1–30% of planetary mass in their atmospheres, depending on the ice mass fraction of the core. Estimating the lower limit of atmospheric mass from the atmospheric mass loss timescale, we suggest that the cores of GJ3470b and HAT-P-11b are largely made of rock. Using a adiabatic model of protoatmosphere, we also showed that the protoatmospheres on GJ1214b and GJ436b, for which the high atmospheric metallicity have been suggested, become too massive to explain the current atmospheric masses if the planets were formed in-situ. Based on the results, we discuss the formation scenario of these super-Earths.

5.2 Introduction

Observational efforts in the last decade have revealed the prevalence of exoplanets with sizes between Earth and Neptune, called super-Earths (e.g., Mayor et al., 2011; Fressin et al., 2013; Fulton et al., 2017). Motivated by this finding, there are numerous studies of super-Earth formation. The scenarios are roughly classified into in-situ formation (e.g., Hansen & Murray, 2012; Lee et al., 2014; Chatterjee & Tan, 2014; Ogihara et al., 2015, 2018; Lee & Chiang, 2016; Jankovic et al., 2019) and migration scenario (e.g., Alibert et al., 2006; Terquem & Papaloizou, 2007; Cossou et al., 2014; Izidoro et al., 2017, 2019; Bitsch et al., 2019; Lambrechts et al., 2019; Liu et al., 2019). It is still under active debate which is a predominant mechanism.

One of the key diagnosis of the formation process is planetary interior structure. For example, the amount of ices involved in a planetary core can be used to infer the birth place of the planet, as the presence of ice likely indicates that the planet was formed outside the snow line. In addition, the amount of planetary atmosphere is also useful to infer the past gas accretion on protoplanetary core and the birth place as well (e.g,, Lee et al., 2014; Lee & Chiang, 2016).

The planetary interior structure can be inferred from the planetary mass-radius relation. Previous studies showed that the relation of small, high-density super-Earths with radii of $< 1.6 R_{\rm Earth}$ can be well explained by Earth-like rocky cores (e.g., Weiss & Marcy, 2014; Rogers, 2015; Otegi et al., 2019). By contrast, the interior structure of large, low-density super-Earths with radii of $> 1.6 R_{\rm Earth}$, which occupy the majority of super-Earth population (Fulton & Petigura, 2018), have been largely uncertain to date. This is mainly due to the presence of atmosphere that inflates the planetary radius and causes the degeneracy of interior structure (e.g., Adams et al., 2008a; Rogers & Seager, 2010; Valencia et al., 2013). Since the mass-radius relation is sensitive to atmosphere, one needs to know atmospheric properties, such as the composition, to better constrain the interior structure of large super-Earths.

In this chapter, we investigate the interior structure of super-Earths GJ1214b, GJ436b, GJ3470b, HD97658b, and HAT-P-11b utilizing the atmospheric properties constrained by the transmission spectra of their atmospheres (Chapter 4). We aim to constrain the atmospheric mass fraction and ice mass fraction in the core. Then, we discuss what we can learn about the formation process of these super-Earths from the atmospheric composition and interior structure. The organization of this chapter is as follows. In Section 5.3, we introduce an interior structure model adopted in this chapter. In Section 5.4, we show how the mass-radius relation of exoplanets depends on atmospheric properties. In Section 5.5, we investigate the atmospheric and ice mass fraction of super-Earths. In Section 5.6, we discuss the formation process of super-Earths based on their atmospheric composition and interior structure. In Section 5.7, we summarize this chapter.

5.3 Method

In this chapter, we construct a model to investigate the planetary mass-radius relation for a given planetary interior structure. The model has been extensively applied for solar-system planets (e.g., Hubbard & Macfarlane, 1980; Fortney & Hubbard, 2003, 2004; Guillot, 2005; Kurosaki et al., 2014; Vazan et al., 2015, 2016, 2018a; Miguel et al., 2016; Kurosaki & Ikoma, 2017) as well as for exoplanets (e.g., Valencia et al., 2007a,b, 2010, 2013; Seager et al., 2007; Adams et al., 2008a; Fortney et al., 2008; Rogers & Seager, 2010; Rogers et al., 2011; Thomas & Madhusudhan, 2016; Thorngren et al., 2016; Vazan et al., 2018b). The interior structure is described by a set of stellar structure equations, namely, mass conservation, hydrostatic balance, and ther-

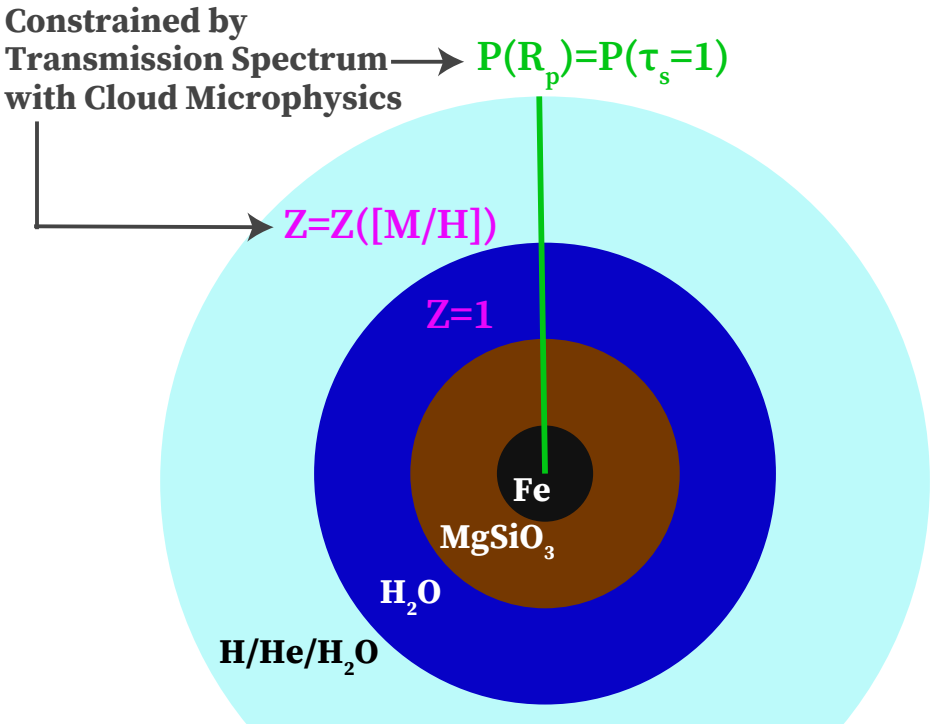


Figure 5.1: Cartoon illustrating the interior structure model used in this chapter. We assume a differentiated planet composed of four layers: homogeneous atmosphere, ice shell, rock shell, and iron core. The rock/iron core is assumed to be made of 67.5% $MgSiO_3$ and 32.5% Fe by masses, which is similar to Earth composition (Seager et al., 2007). We assume the atmosphere made of H/He/H_2O mixture whose metal mass fraction, Z, varies with the atmospheric metallicity. We utilize the results of the synthetic transmission spectra compared with the observations to set the atmospheric metallicity and an upper boundary of atmospheric pressure.

modynamic equations (e.g., Guillot, 2005):

$$\frac{\partial r}{\partial M_{\rm r}} = \frac{1}{4\pi r^2 \rho}, \tag{5.1}$$

$$\frac{\partial P}{\partial M_{\rm r}} = \frac{G M_{\rm r}}{4\pi r^4}, \tag{5.2}$$

$$\frac{\partial T}{\partial M_{\rm r}} = -\frac{G M_{\rm r}}{4\pi r^4}\frac{T}{P}\nabla, \tag{5.3}$$

where $M_{\rm r}$ is the mass enclosed in a sphere with radius r. In this chapter, we simply assume a homogeneously mixed atmosphere. The assumption enables us to evaluate the temperature gradient $\nabla \equiv d\log T/d\log P$ from the Schwarzschild criterion [1],

$$\nabla = \min\left(\nabla_{\rm ad}, \nabla_{\rm rad}\right), \tag{5.4}$$

[1] If composition gradient is present in the atmosphere, one has to adopt different criterion, such as the Ledoux's criterion (for more detail, see e.g., Vazan et al., 2015; Kurokawa & Inutsuka, 2015).

where $\nabla_{\rm ad}$ and $\nabla_{\rm rad}$ are the adiabatic and radiative temperature gradient. Differentiating Equation (2.11), we obtain the radiative gradient,

$$\nabla_{\rm rad} = -\frac{3\kappa L_{\rm int}}{64\pi\sigma_{\rm SB} G M}\frac{P}{T^4}\left[1+\left(\frac{T_{\rm irr}}{T_{\rm int}}\right)^4 f(1-\gamma^2)\exp\left(-\gamma\sqrt{3}\tau\right)\right], \tag{5.5}$$

where $L_{\rm int} = 4\pi r^2 \sigma_{\rm SB} T_{\rm int}^4$ is the planetary intrinsic luminosity, κ is the thermal opacity, and τ is the thermal optical depth calculated by

$$\frac{\partial \tau}{\partial M_{\rm r}} = -\frac{\kappa}{4\pi r^2}. \tag{5.6}$$

Equation (5.5) is applicable to both optically thick and thin region: for example, the equation returns to widely-used diffusion approximation equation in the limit of $\tau \gg 1/\sqrt{3}\gamma$. Equations (5.1), (5.2), and (5.3) involve four variables (r,P,T,ρ), and thus another equation is needed to close the system, which is given by the equation of state (EOS). For hydrogen/helium, we apply the EOS of Chabrier et al. (2019) that extends the widely-used EOS of Saumon et al. (1995) by combining the results of first principle molecular dynamics simulations. For water, we apply Mazevet et al. (2019) that also extends the EOS derived by experimental data (IAPWS, Wagner & Pruß, 2002) using the molecular dynamics simulations. For rock and iron, we use the modified polytropic equation of state of Seager et al. (2007) because the density is relatively insensitive to temperature (Valencia et al., 2006). We calculate physical properties of a hydrogen/helium/water mixture invoking the additive-volume rule (Saumon et al., 1995). In this context, the density is given by

$$\frac{1}{\rho} = \frac{X}{\rho_{\rm H}} + \frac{Y}{\rho_{\rm He}} + \frac{Z}{\rho_{\rm H_2O}}, \tag{5.7}$$

where X, Y, and Z are the mass mixing ratio of hydrogen, helium, and water, respectively. The adiabatic temperature gradient is calculated from the definition of

$$\nabla_{\rm ad} \equiv \left(\frac{d\log T}{d\log P}\right)_{\rm S} = -\left(\frac{d\log S}{d\log P}\right)_{\rm T} \Big/ \left(\frac{d\log S}{d\log T}\right)_{\rm P}, \tag{5.8}$$

where S is the entropy, given by

$$S = X S_{\rm H} + Y S_{\rm He} + Z S_{\rm H_2O}. \tag{5.9}$$

We integrate Equations (5.1), (5.2), (5.3), and (5.6) inward from the outer boundary, $M_{\rm r} = M_{\rm p}$, to the planetary center, $M_{\rm r} = 0$, with the fourth-order Runge-Kutta method. The outer boundary condition is set to $r(M_{\rm r}) = R_{\rm p}$, $T(M_{\rm r}) = T_{\tau=0}$, $P(M_{\rm r}) = P_{\tau_{\rm s}=1}$, and $\tau(M_{\rm r}) = 0$, where $T_{\tau=0}$ is the temperature in the limit of $\tau = 0$, given by (Guillot, 2010)

$$T_{\tau=0} = \left[\frac{1}{2}T_{\rm int}^4 + \frac{1}{8}T_{\rm irr}^4\left(1+\frac{\sqrt{3}\gamma}{2}\right)\right]^{1/4}. \tag{5.10}$$

$P_{\tau_{\rm s}=1}$ is the pressure at which the slant optical depth exceeds unity. We perform the inward integration in an iterative fashion with changing the planetary radius, $R_{\rm p}$, so that the planetary radius satisfies $r(0) = 0$.

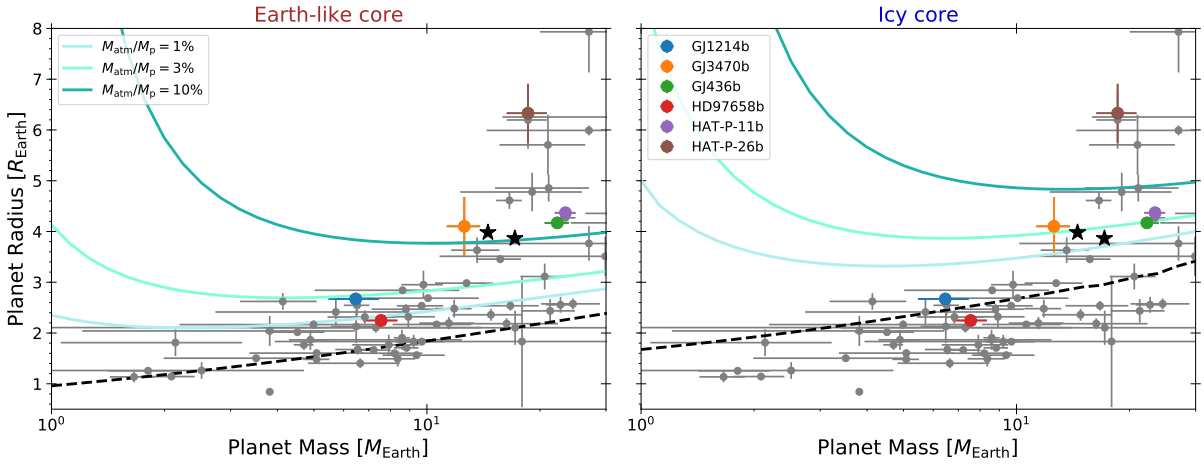


Figure 5.2: Mass-radius relation of rocky and icy planets with solar compsotion atmospheres. The different colored lines show the relations for different gas-to-core mass ratio. The left and right column show the M-R diagram for Earth-like core and pure icy core. The dashed black lines denote the MR diagram of core without atmospheres. M-R relations of observed exoplanets, taken from Exoplanet.eu catalog, are also plotted, where we only exhibit exoplanets whose mass and radius are constrained by radial velocity and transit observations. We assume $T_{\rm eq} = 500$ K, $T_{\rm int} = 50$ K, and $P_{\tau=1} = 100$ mbar. The black symbols denote the mass-radius relation of Uranus and Neptune.

We leave $P_{\tau_{\rm s}=1}$ as a free parameter in calculations for unspecific planets. It should be noted that the pressure $P_{\tau_{\rm s}=1}$ is largely lowered by cloud opacity and could be much smaller than the traditionally assumed value, $P(M_{\rm p}) \sim 1$ bar. This "cloud-top effect" is potentially important, as it substantially puffs the planet radius. A recent study of Gao & Zhang (2019) suggests that this effect may explain the presence of planets with extremely low density (called super-puffs), such as Kepler-51b (Masuda, 2014). To properly select the pressure at the upper boundary, we determine $P_{\tau_{\rm s}=1}$ from the best-fit transmission spectra shown in Section 4.5.2.

5.4 Mass-Radius Relation of Exoplanets

Here, we show the results of interior structure calculations. Figure 5.3 exhibit the radius of as a function of planetary mass, which we call a mass-radius relation, for pure rocky and icy core planets with solar composition atmospheres. Icy planets have larger radii than those of rocky planets for given mass simply because its low core density. For large planets, say $< 10 M_{\rm Earth}$, planetary radius increases with increasing its mass. On the other hand, for small planets, planetary radius increases with *decreasing* its mass. This behavior is in agreement with previous studies (Rogers et al., 2011; Valencia et al., 2013) and caused by the fact that gravitational energy decreases with decreasing the mass, leading to weak bounding of the atmosphere. We elaborate the parameter dependence of the mass-radius relation in later.

The planet radius is sensitive to atmospheric mass. Figure 5.3 shows that the higher atmospheric mass is, the larger planetary radius is. This behavior is also in agreement with previous studies (e.g., Adams et al., 2008a; Valencia et al., 2013). It has been known that the radius inflation due to an atmosphere leads to the degeneracy of planetary interior structure. For example, as

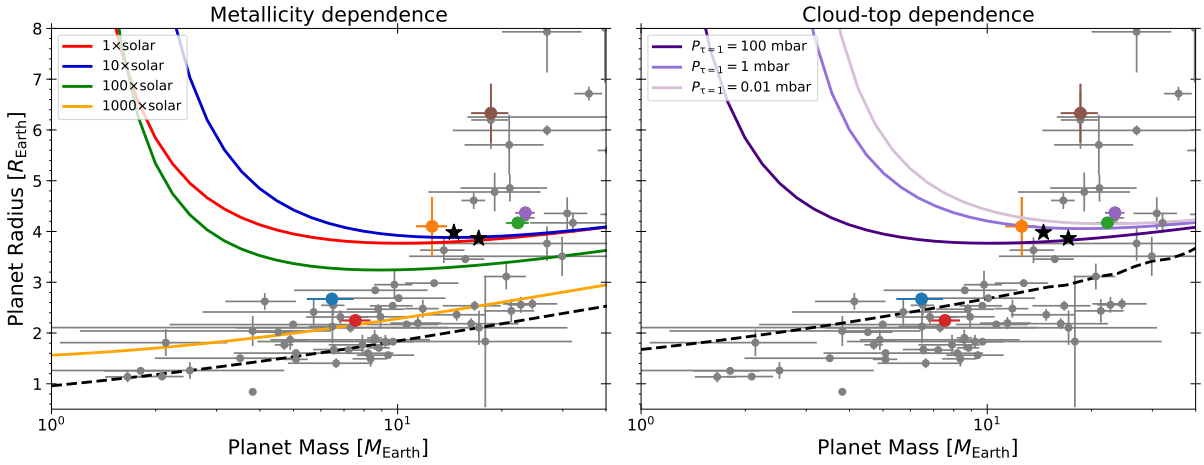


Figure 5.3: Same as Figure 5.3, but for different atmospheric metallicity (left panel) and cloud-top pressure (right panel). We have assumed Earth-like core and $M_{\rm atm}/M_{\rm p} = 10\%$ in each panel.

seen in Figure 5.3, the mass and radius of GJ1214b can be explained by both a pure icy planet and a Earth-like core surrounded by the solar composition atmosphere with $M_{\rm atm}/M_{\rm p} = 3\%$. This demonstrates that it is impossible to constrain planetary interior structure without information on the atmospheric properties.

The mass-radius relation also depends on atmospheric metallicity. The left panel of Figure 5.2 shows the mass-radius relation for different atmospheric metallicity. The dependence is somewhat complicated. Planetary radius initially increases with increasing the metallicity until the metallicity reaches $\sim$100$\times$ solar abundance. For the higher metallicity, by contrast, the radius decreases with increasing the metallicity. The latter trend is simply because higher metallicity results in smaller atmospheric scale height that shrinks the radius. The former trend stems from the fact that, because of higher atmospheric opacity, the higher metallicity produces the radiative-convective boundary at higher altitude that leads to hotter interior. Since the mean molecular mass is nearly invariant until $\sim$ 100$\times$ solar metallicity, higher metallicity merely heats the interior and puffs the planet. Therefore, planetary radius is maximized at $\sim$ 10$\times$ solar metallicity.

The mass-radius relation is affected by the pressure level where becomes optically thick, i.e., $P_{\tau=1}$. The right panel of Figure 5.2 shows that transiting planetary radius increases with decreasing the opaque pressure level. The effect is more noticeable for smaller planets. For super-Earths studied in this chapter, this radius inflation due to high-altitude photosphere, which may stem from the presence of clouds, substantially affects the radius of GJ1214b and HD97658b.

We now construct a simple analytical model to better figure out aforementioned parameter dependence of the mass-radius relation. Assuming a fully-convective adiabatic atmosphere, the atmospheric mass is approximately given by (e.g., Ginzburg et al., 2016)

$$M_{\rm atm} \sim \rho_{\rm g,p} R_{\rm p}^3 \left(\frac{R'_{\rm B}}{R_{\rm p}}\right)^{\frac{1}{\gamma-1}}, \tag{5.11}$$

where $\rho_{\rm g,p}$ is the atmospheric density at the planetary radius, γ is the adiabatic index, $R'_{\rm B}$ is

defined as $R'_{\rm B} = R_{\rm B}(1-\gamma^{-1})$, and $R_{\rm B}$ is the Bondi radius given by,

$$R_{\rm B} \equiv \frac{GM_{\rm c}}{c_{\rm s}^2} = \frac{GM_{\rm c}}{dP/d\rho}, \tag{5.12}$$

where $M_{\rm c}$ is the core mass. We have assumed that core radius is much smaller than planetary radius, i.e., $R_{\rm cp}$. Solving Equation (5.11) about $R_{\rm p}$, we obtain

$$\begin{aligned} R_{\rm p} &= \left(\frac{M_{\rm atm}}{\rho_{\rm g,p}}\right)^{\frac{\gamma-1}{3\gamma-4}} R_{\rm B}^{(4-3\gamma)} \\ &\approx \left[\frac{\gamma}{\gamma-1}\frac{k_{\rm B}T}{Gm_{\rm g}}\left(\frac{f_{\rm atm}}{\rho_0}\right)^{(\gamma-1)} M_{\rm p}^{(\gamma-2)}\right]^{1/(3\gamma-4)}, \end{aligned} \tag{5.13}$$

where we define the gas-to-core mass ratio, $f_{\rm atm} = M_{\rm atm}/M_{\rm p}$, and use the relation of $dP/d\rho \approx k_{\rm B}T/m_{\rm g}$ and $M_{\rm c} \approx M_{\rm p}$. Since the adiabatic index takes $7/5$ for diatomic molecules, planetary radius increases with increasing T and $f_{\rm atm}$, while decreases with increasing $m_{\rm g}$, ρ_0, and $M_{\rm p}$ according to Equation (5.13). This well explains the parameter dependence seen in the mass-radius relation of low-mass planets for which the assumption of $R_{\rm c} \ll R_{\rm p}$ is valid. Qualitatively speaking, the radius inflation found for low-mass planets is caused by a weak gravitational bounding of the atmosphere.

5.5 Atmospheric Mass Fraction of Super-Earths

We now focus on the super-Earths for which synthetic transmission spectra are compared with the observations (Section 4.5.2). One of the great interest is how much an atmosphere and icy materials each planet possesses. To calculate the interior structure of these super-Earths, we use the equilibrium temperature, intrinsic temperature, and opacity ratio used for the calculations of cloud formation and synthetic transmission spectra in previous sections. The opaque pressure level, $P_{\tau=1}$, is provided by the best-fit synthetic transmission spectra in Chapter 4. We vary the atmospheric mass and ice mass fraction of the core so that explains the observed mass-radius relation for each planet.

Figure 5.4 shows the atmospheric mass fraction required to match the observed radius as a function of ice mass fraction of the core. In general, the required atmospheric mass decreases with increasing the ice mass fraction of the core. Atmospheric metallicity has little impacts on the atmospheric mass for $< 100\times$ solar, but significantly increases it for $> 100\times$ solar. For GJ3470b and HAT-P-11b for which low-metallicity atmospheres ($\leq 100\times$ solar) are favored to explain the observations (Section 4.5.2), the required atmospheric mass is $M_{\rm p}/M_{\rm atm} \approx 0.1$–$0.01$, depending on how much ice is included in the core. We note that the derived atmospheric mass for pure rocky core ($M_{\rm atm} \sim 0.1$) is in agreement with Lopez & Fortney (2014) who derived the H/He atmospheric mass fraction for various super-Earths assuming pure rocky core. The atmospheric mass is less changed even if the atmospheric metallicity increases up to $100\times$ solar. Although it is impossible to assess whether GJ3470b and HAT-P-11b are rocky or icy planets solely from Figure 5.4, we can infer that they acquired the atmospheres with mass of $> 0.01M_{\rm p}$ during the protoplanetary disks existed.

The results are qualitatively different for GJ1214b, GJ436b, and HD97658b, for which high-metallicity atmospheres ($\geq 100\times$ solar) are favored to explain the observations. If the metallicity

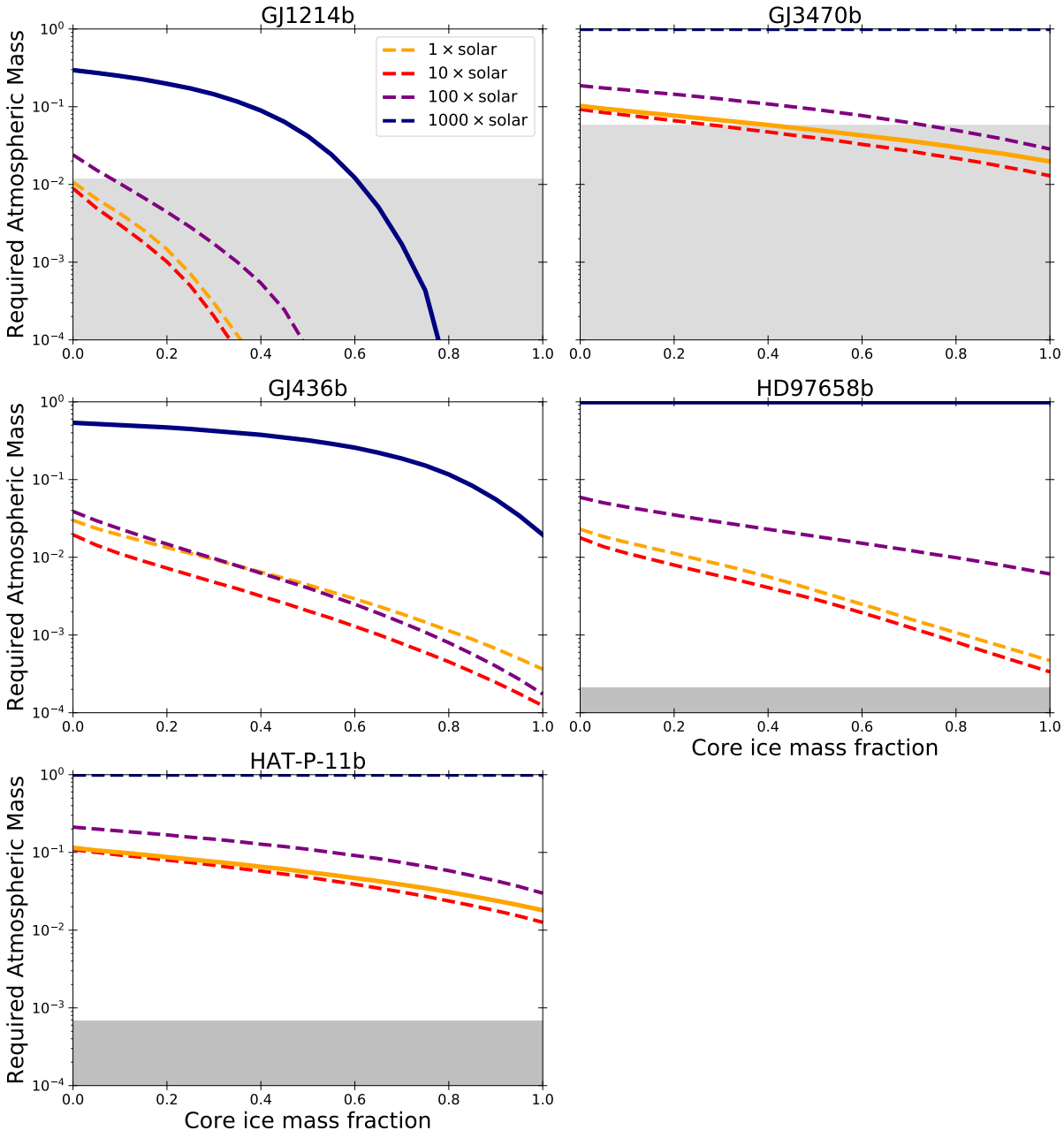


Figure 5.4: Atmospheric mass fraction of super-Earths for which transmission spectrum has been observed (Section 4.5.2). Each panel shows the atmospheric mass fraction, $M_{\rm atm}/M_{\rm p}$, required to match observed planetary radius as a function of ice mass fraction of core. Different panel exhibits the results for different planets. The different colored lines show the required atmospheric mass for different atmospheric metallicity. The gray shaded regions indicate the atmospheric mass that is too small to be kept against to atmospheric evaporation during 3 Gyr, where the mass loss rate is constrained by observations (Ehrenreich et al., 2015; Bourrier et al., 2017; Mansfield et al., 2018). For GJ1214b and GJ3470b, the mass loss rate are determined by a theoretical model (Salz et al., 2016).

is extremely high ($1000\times$ solar), as suggested from the argument in Section 4.5.2, these planets retain substantial amount of atmosphere, $M_{\rm atm}/M_{\rm p} \approx 0.5$–$0.1$. Notably, the atmospheric mass is comparable to the core mass if these planets have pure rocky core. It has been known that a planetary core embedded in a protoplanetary disk gravitationally attracts surrounding gasses in a runnaway fashion once the atmospheric mass is comparable to the core mass (e.g., Pollack et al., 1996; Ikoma et al., 2000). We will further discuss possible formation process of these super-Earths in Section 5.6. It should be noted that the required atmospheric mass is sensitive to actual atmospheric metallicity. For example, if the atmospheric metallicity is $100\times$ solar, the atmospheric mass is greatly reduced to $< 0.03 M_{\rm p}$. Precise determination of the atmospheric metallicity with future observations would be helpful to better constrain the interior structure of super-Earths.

5.5.1 Minimum Atmospheric Mass Constrained by Atmospheric Escape

We attempt to give a constrain on total atmospheric mass, which can be useful to constrain how much ice is included in planetary core. The lower limit may be set by the atmospheric mass loss since the close-in exoplanets are subject to atmospheric escape driven by high-energy photons from central stars. The atmospheric mass loss timescale can be defined as

$$\tau_{\rm loss} = \frac{f_{\rm atm} M_{\rm p}}{\dot{M}_{\rm loss}}, \tag{5.14}$$

where $f_{\rm atm} = M_{\rm atm}/M_{\rm p}$ and $\dot{M}_{\rm loss}$ is the mass loss rate. Since the timescale must be longer than the system age, $\tau_{\rm age}$, in order to retain the atmosphere, the minimum atmospheric mass is evaluated as

$$\begin{aligned} f_{\rm atm} &\sim \frac{\dot{M}_{\rm loss}}{M_{\rm p}} \tau_{\rm age} \\ &= 0.005 \times \left(\frac{\dot{M}_{\rm loss}}{10^9 \ {\rm g \ s^{-1}}} \right) \left(\frac{M_{\rm p}}{M_{\rm Earth}} \right)^{-1} \left(\frac{\tau_{\rm age}}{1 \ {\rm Gyr}} \right). \end{aligned} \tag{5.15}$$

The mass loss rate is estimated for some exoplanets using the transit observations at ultraviolet wavelength (e.g., Ehrenreich et al., 2015; Bourrier et al., 2016) and absorption band of helium (e.g., Spake et al., 2018). Previous observational studies have measured the mass loss rate of 10^8–10^9 g s^{-1} for GJ436b (Ehrenreich et al., 2015), $< 10^8$ g s^{-1} for HD97658b (Bourrier et al., 2017), and 10^9–10^{11} g s^{-1} for HAT-P-11b (Mansfield et al., 2018). To evaluate the minimum atmospheric mass, we assume the mass loss rate of $\dot{M}_{\rm loss} = 10^8$ g s^{-1} for GJ436b and HD97658b and $\dot{M}_{\rm loss} = 10^9$ g s^{-1} for HAT-P-11b. For GJ1214b and GJ3470b, there is no observational constrain on the mass loss rate. Therefore, we assume $\dot{M}_{\rm loss} = 10^{9.68}$ g s^{-1} and $10^{10.66}$ g s^{-1} for GJ1214b and GJ3470b, respectively, taken from Salz et al. (2016) who performed first principle simulations of XUV-driven atmospheric escape. System age is somewhat uncertain, especially for GJ1214b and HD97658b. Therefore, we assume a conservative value of $\tau_{\rm age} = 3$ Gyr for all planets, which falls into the age estimated for GJ436b, GJ3470b, and HAT-P-11b [2].

The gray shaded region in Figure 5.4 denotes the atmospheric mass whose mass loss timescale is shorter than 3 Gyr. Therefore, if the required atmospheric mass falls into this region, such

[2]The system ages of these planets are taken from NASA Eoplanet Arxive.

atmosphere is not stable against to the atmospheric escape, and corresponding core composition could be ruled out. We find that the atmospheres of GJ436b, HD97658b, and HAT-P-11b tend to be stable against to the atmospheric escape. The atmosphere on GJ436b is stable for almost any core composition as long as the atmospheric metallicity is very high ($\sim 1000\times$ solar), as suggested by transmission spectrum (Section 4.5.2). The core ice mass fraction is also not constrained for HD97658b even if we assume the upper limit of mass loss rate suggested by the observation (10^8 g s^{-1}, Bourrier et al., 2017). For HAT-P-11b, the interpretation varies within the uncertainty of the observations. If the mass loss rate takes the smallest observed value (10^9 g s^{-1}, Mansfield et al., 2018), the atmosphere is stable against to the evaporation for any core composition. By contrast, if the mass loss rate takes the highest observed value (10^{11} g s^{-1}, Mansfield et al., 2018), atmosphere could be stable only when the core is mostly made of rocky (the ice mass fraction of < 0.1). Thus, further observational constrain on the mass loss rate is needed to better constrain the core composition.

In contrast to the former planets, the core composition of GJ1214b and GJ3470b are constrained relatively better than former planets. For GJ3470b, the atmosphere is not stable against to atmospheric escape once its mass becomes lower than $\sim 0.05 M_{\rm p}$. This can rule out a relatively ice-rich (> 0.2) core of GJ3470b because such ice-rich core needs a tiny amount of atmosphere to match observed radius, while such tiny amount of atmosphere is easily evaporated. The high-metallicity atmosphere can be stable even for pure ice core, but not supported by the transmission spectra (Section 4.5.2). Therefore, we suggest that the core of GJ3470b is largely made of rocky materials rather than icy materials. By contrast, GJ1214b could possess the moderate amount of ice (< 0.4) if one assumes high-metallicity atmosphere ($1000\times$ solar), as suggested by the transmission spectra (Chapter 4). If the atmosphere is moderately hydrogen-rich ($\leq 100\times$solar), it can imply that the planetary core is largely made of rocky materials (ice mass fraction is < 0.1). Therefore, we suggest that GJ1214b is either a rocky/icy planet surrounded by a massive high-metallicity atmosphere or a rocky planet surrounded by a hydrogen-rich atmosphere. Future observations would be able to derive more conclusive interpretations.

5.6 Implications for High-Metallicity Atmospheres on Planet Formation

We now return to a fundamental question of planet formation theory: how were super-Earths formed? The series of our investigations offer some hints to discuss it, namely the atmospheric metallicity and total atmospheric mass. In particular, super-Earths with high-metallicity atmospheres are interesting because the metallicity is associated to both past solid accretion process and the onset of runnaway gas accretion. We now examine the past gas accretion process with a simple timescale argument. Let us estimate the atmospheric mass assuming a fully convective protoatmosphere. This is corresponding to the situation in which the atmosphere is intensely heated by the planetesimal and/or pebble accretion. In this context, the atmospheric density profile is given by (Rafikov, 2006; Ginzburg et al., 2016)

$$\rho(r) = \rho_{\rm out}\left[1+\nabla_{\rm ad}\frac{R_{\rm B}}{r}-\nabla_{\rm ad}\frac{R_{\rm B}}{r_{\rm out}}\right]^{1/(\gamma-1)} \tag{5.16}$$

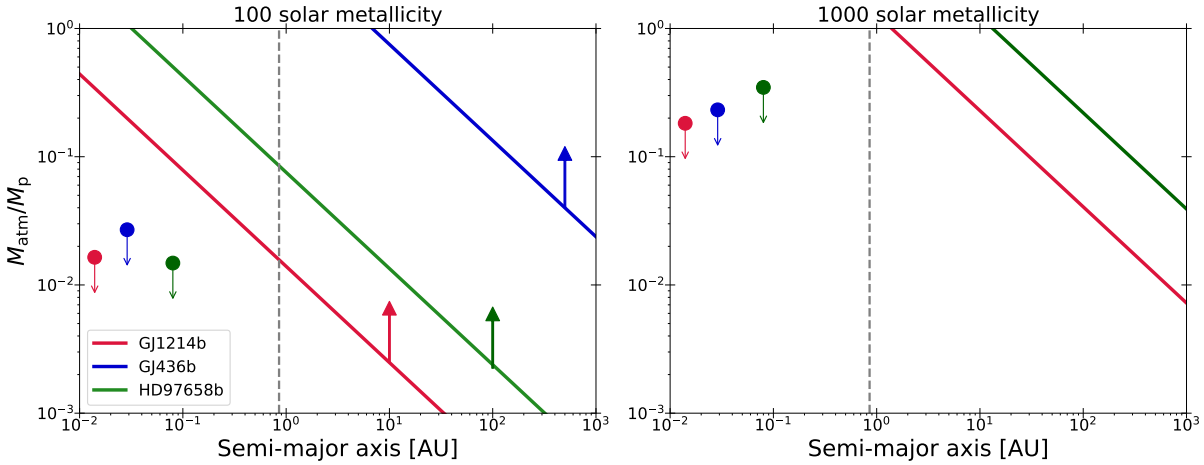


Figure 5.5: Mass of fully-convective protoatmosphere as a function of orbital distance. The left and right panel show $M_{\rm atm}/M_{\rm p}$ for $100\times$ and $1000\times$ solar metallicities, respectively. The red, blue, and green shaded regions show the results for GJ1214b, GJ436b, and HD97658b, respectively, assuming $f_{\rm disk} = (M_{\rm s}/M_{\rm sun})^{1.69}$ (Sanchis et al., 2019). The colored dots denote the current orbital distance and the maximum atmospheric mass inferred from the interior model for each planet. The gray dashed line indicate the orbital distance of H_2O snow line ($T = 170$ K) for $L_{\rm s} = 0.1L_{\rm sun}$. Here, Earth-like core density ($\rho_{\rm core} = 6$ g cm^{-3}) and MMSN are assumed to evaluate the atmospheric mass.

where $\rho_{\rm out}$ is the density of disk gas and $r_{\rm out}$ is the outer boundary of the protoatmosphere. The atmospheric mass is calculated as

$$M_{\rm atm} = \int_{\rm R_{core}}^{R_{\rm B}} 4\pi r^2 \rho(r) dr$$

The outcome of integration significantly depends on the adiabatic constant. The atmospheric mass is concentrated in the outermost convective layer for $\gamma > 4/3$, while near the core for $\gamma < 4/3$. Here, we assume $\gamma < 4/3$ since high-metallicity atmospheres are largely composed of polyatomic molecules, such as H_2O, that have large number of degree of freedom. In this circumstance, the atmospheric mass is evaluated as (Lee & Chiang, 2015)

$$\begin{aligned} M_{\rm atm} &\approx 4\pi\rho_{\rm out} R_{\rm core}^3 (\nabla_{\rm ad} R_{\rm B}/R_{\rm core})^{1/(\gamma-1)}. \qquad (5.17) \\ \frac{M_{\rm atm}}{M_{\rm p}} &= 3\rho_{\rm out}\nabla_{\rm at}^{1/(\gamma-1)} \left(\frac{4\pi}{3}\right)^{1/3(\gamma-1)} \left(\frac{Gm_{\rm g}}{k_{\rm B}T}\right)^{1/(\gamma-1)} M_{\rm p}^{2/3(\gamma-1)} \rho_{\rm core}^{1/3(\gamma-1)-1} \\ &\approx 0.03 \left(\frac{\rho_{\rm out}}{10^{-9}\ {\rm g\ cm^{-3}}}\right) \left(\frac{T}{300\ {\rm K}}\right)^{-4} \left(\frac{\mu_{\rm g}}{18\ {\rm amu}}\right)^4 \left(\frac{\rho_{\rm core}}{1\ {\rm g\ cm^{-3}}}\right)^{1/3} \left(\frac{M_{\rm p}}{M_{\rm Earth}}\right)^{8/3}, \end{aligned}$$

where we have assumed $\gamma = 1.3$ for the transformation from second to third line. One can evaluate the atmospheric mass for given formation location through Equation (5.17) once a specific disk model is assumed. For example, let us assume the minimum mass solar nebula whose temperature, gas surface density, and midplane density are given by (Hayashi, 1981)

$$T = 280\ {\rm K} \left(\frac{a}{1\ {\rm AU}}\right)^{-1/2} \left(\frac{L_{\rm s}}{L_{\rm sun}}\right)^{1/4}, \qquad (5.18)$$

$$\Sigma_{\rm g} = 1.7 \times 10^3 \ {\rm g \ cm^{-2}} \left(\frac{a}{1 \ {\rm AU}} \right)^{-3/2} \tag{5.19}$$

$$\rho_{\rm out} = 7.8 \times 10^{-10} \ {\rm g \ cm^{-3}} \left(\frac{a}{1 \ {\rm AU}} \right)^{-11/4} \left(\frac{M_{\rm s}}{M_{\rm sun}} \right)^{1/2} \left(\frac{L_{\rm s}}{L_{\rm sun}} \right)^{-1/8}, \tag{5.20}$$

where $\Sigma_{\rm g}$ is the disk gas surface density. Since planetary Bondi radius is much smaller than the scale height of protplanetary disk, we can approximate the nebula density by the density at the midplane. Inserting Equation (5.18) and (5.20) into (5.17), we obtain

$$\begin{aligned} \frac{M_{\rm atm}}{M_{\rm p}} \approx 0.03 f_{\rm disk} \ &\times \ \left(\frac{a}{1 \ {\rm AU}} \right)^{-3/4} \left(\frac{M_{\rm s}}{M_{\rm sun}} \right)^{1/2} \left(\frac{L_{\rm s}}{L_{\rm sun}} \right)^{-9/8} \\ &\times \ \left(\frac{\mu_{\rm g}}{18 \ {\rm amu}} \right)^{10/3} \left(\frac{\rho_{\rm core}}{1 \ {\rm g \ cm^{-3}}} \right)^{1/3} \left(\frac{M_{\rm p}}{M_{\rm Earth}} \right)^{8/3}, \end{aligned} \tag{5.21}$$

where we introduce the scaling factor $f_{\rm disk}$ accounting for the fact that smaller stars have smaller disk mass (e.g., Pascucci et al., 2016; Sanchis et al., 2019). We note that Equation (5.21) is different from the similar derivation of Rafikov (2006) since the author assumed $\gamma = 7/5$. Equation (5.21) indicates that the mass of protoatmosphere is a sensitive function of atmospheric mean molecular weight and planetary mass. It should be noted that Equation (5.21) provides a lower-limit of accreted atmospheric mass because of the adiabatic assumption. The assumption is violated once the exterior heat sources become insignificant. In that case, the disk gasses continuously accrete onto the planetary core until the atmospheric contraction (cooling) timescale becomes sufficiently long, resulting in massive atmospheres (Lee et al., 2014; Lee & Chiang, 2015).

The mass of adiabatic atmosphere is likely the minimum mass of a protoatmosphere because further cooling of atmosphere triggers additional gas accretion. Figure 5.5 shows the mass of fully-convective protoatmosphere (Equation 5.21) compared with the current atmospheric mass inferred from the interior model (Section 5.5). In the figure, the stellar luminosity is assumed to be $0.1 L_{\rm sun}$ for M-dwarfs GJ1214 and GJ436, similar to the past luminosity of low-mass stars predicted by a stellar evolution model (Baraffe et al., 2002). We find that the planetary core acquires the atmospheric mass much higher than the current mass by orders of magnitude if the in-situ formation is assumed. For the moderately hydrogen-rich case ($100\times$ solar), the atmospheric mass is comparable or higher than the core mass (i.e., $M_{\rm atm}/M_{\rm p} \geq 0.5$), suggesting that the runnaway gas accretion sets in. This is more apparent in very metal-rich atmosphere cases ($1000\times$ solar) in which the mass of protoatmosphere is always higher than core mass. This result is qualitatively in agreement with previous studies who found that high-metallicity atmospheres preferentially results in runnwary gas accretion onto a planetary core (Stevenson, 1982; Hori & Ikoma, 2011; Venturini et al., 2015).

There are several possibilities to reconcile the mass of protoatmosphere and current atmospheric mass. The atmospheric escape after the dissipation of a protoplanetary disk may reconcile the current atmospheric mass and a massive protoatmosphere suggested by Figure 5.5. Close-in planets are subject to the atmospheric escape, and several mechanisms have been proposed so far (e.g., Ikoma & Hori, 2012; Owen & Wu, 2016, 2017; Ginzburg et al., 2018). However, Owen & Wu (2013) suggests that XUV-driven mass loss have minor impacts on gas giant (for different suggestion, see Kurokawa & Nakamoto, 2014). Another concertn is that the atmospheric metallicity is diluted to solar-like value once the planet grow into a gas giant via runnaway gas accretion (Venturini et al., 2016). This is opposite to the current atmospheric

metallicity suggested by the transmission spectra (Section 4.5.2). Therefore, in order to explain both the atmospheric mass and the atmospheric metallicity, the runnaway gas accretion must be halted somehow.

Simply, these planets may be formed in the late stage of protoplanetary disks. The protoplanetary disk is dissipated with the timescale of 1–3 Myr (Ribas et al., 2015), and the disk mass density accordingly decreases with time. The mass of fully-convective protoatmosphere is proportional to the disk mass density (Equation 5.17). Therefore, the atmospheric mass can be comparable to the current mass if the final assembly of the planetary core occurs at a proper timing. This scenario seems a fine-tuning problem but may be a natural consequence because the orbital crossing of protoplanet is triggered by the decrease of ambient gas density (Lee et al., 2014; Lee & Chiang, 2016). One of the concern is that it is unclear whether the high-metallicity atmosphere can be achieved in this scenario. Fortney et al. (2013) suggested that larger planetesimals ($\geq 100\,\mathrm{km}$) less increase the atmospheric metallicity because of an inefficient ablation in protoatmospheres. In addition, hydrodynamic simulations suggest that a protoatmosphere is continuously interchanged by surrounding disk gasses (e.g., Ormel et al., 2015; Lambrechts & Lega, 2017; Kurokawa & Tanigawa, 2018; Kuwahara et al., 2019), which may inhibit the increase of atmospheric metallicity. Assuming the incoming mass flux of gas flow is dominated by the shear flow at the Bondi radius, the recycling timescale is estimated as (Ormel et al., 2015)

$$\tau_{\mathrm{recycle}} \sim \frac{M_{\mathrm{atm}}}{R_{\mathrm{B}}^2(\rho_{\mathrm{disk}} R_{\mathrm{B}} \sqrt{GM_{\mathrm{s}}/a^3})} \sim 10^{-1}\,\mathrm{yr} \left(\frac{M_{\mathrm{atm}}}{M_{\mathrm{p}}}\right) \left(\frac{M_{\mathrm{p}}}{10 M_{\mathrm{Earth}}}\right)^{-2} \left(\frac{a}{0.1\,\mathrm{AU}}\right)^{11/4} \tag{5.22}$$

Equation (5.22) suggests that the atmospheric recycling is extremely fast at the current position of super-Earths. In other words, Equation (5.22) indicates that protoatmosphere polluted by heavy element is immediately interchanged by the surrounding low-metallicity disk gasses. Therefore, we suggest that "late-formation" scenario is favored to explain the formation of super-Earths with *low*-metallicity atmospheres rather than high-metallicity atmospheres [3].

Another attractive idea that may overcome aforementioned obstacles is the formation at outer region of the protoplanetary disk followed by the orbital migration. Figure 5.5 indicates that the atmospheric mass decreases with increasing the orbital distance because of low disk density. For example, the minimum atmospheric mass of protoatmosphere can be smaller than the current atmospheric mass of GJ1214b at $a \geq 1\,\mathrm{AU}$, beyond the snow line. Although this trend is violated if the accretion heating is inefficient, in the context of the pebble accretion, outer planets tend to undergo accretion heating as compared to inner planet (Lambrechts et al., 2014; Bitsch et al., 2018). This is due to the fact that the pebble accretion is halted for planetary mass larger than a threshold, which is so-called a pebble isolation mass given by (Lambrechts et al., 2014)

$$M_{\mathrm{iso}} \approx 20 \left(\frac{a}{5\,\mathrm{AU}}\right)^{3/4} M_{\mathrm{Earth}}. \tag{5.23}$$

Lambrechts et al. (2014) suggests that Uranus and Neptune can avoid the runnaway gas accretion thanks to an intense heating caused by the pebble accretion and the large isolation mass at wide orbital distances. It is worth noting that this "outside pebble accretion" scenario can naturally explain the origin of high-metallicity atmosphere as well. Owing to its small size, pebbles are

[3] However, recent studies of non-isothermal simulations suggest that the recycling operates only on relatively outer protoatmosphere (Lambrechts & Lega, 2017; Kurokawa & Tanigawa, 2018). The isolated inner atmosphere may be able to retain substantial heavy elements. Further work of hydrodynamical simulations with envelope pollution is warranted.

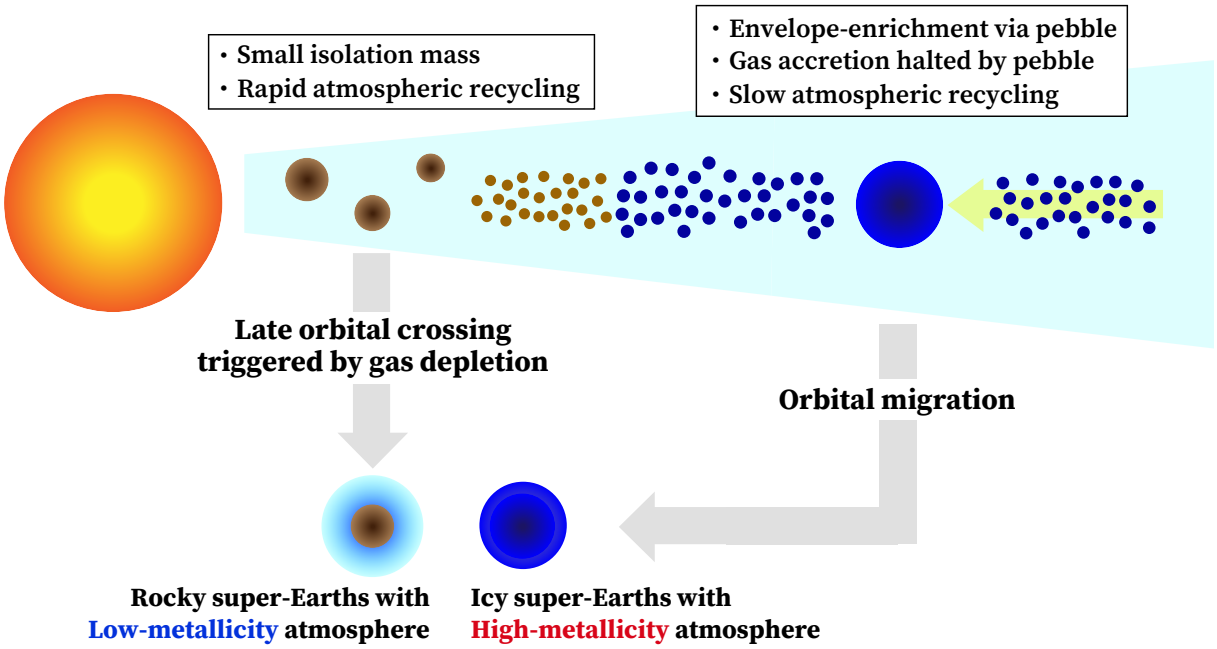


Figure 5.6: Cartoon illustrating the potential origin of the dichotomy of atmospheric metallicity in super-Earths.

easily ablated in a protoatmosphere and enhance the atmospheric metallicity. The dilution of the metallicity due to the atmospheric recycling can also be diminished because the recycling timescale steeply increases with increasing orbital distance (Equation 5.22). Therefore, we suggest that super-Earths with high-metallicity atmospheres may be analog of icy planets in our solar system. It is worth noting that the orbital plane of GJ436b is nearly perpendicular to the stellar equator (Bourrier et al., 2018). This potentially suggests the past orbital migration, in agreement with the "outside pebble accretion" scenario.

Finally, we state several caveats and prospects for suture studies. In this section, we discuss the formation scenario based on the planetary orbital distance and disk properties at a snapshot of certain time. In reality, however, both of which evolves with time. The solid accretion rate also varies with time, which may lead to violate the assumption of adiabatic protoatmosphere. Since the planet formation is intrinsically time-dependent phenomena, one need to trace the time evolution of all above factors to assess the formation scenario proposed here. Furthermore, atmospheric mass and maybe composition evolves with time even after the disk dissipation through relevant physical processes, such as atmospheric escape. End-to-end studies would be needed to connect the past formation process to current exoplanetary atmospheres, which we will work on in future studies.

5.7 Summary

In this chapter, we have investigated the interior structure of super-Earths GJ1214b, GJ436b, GJ3470b, HD97658b, and HAT-P-11b to explore their formation process. Using an interior structure model, we have examined the atmospheric mass fraction and ice mass fraction of planetary core, where the atmospheric metallicity and cloud-top pressure are constrained by transmission spectra in Chapter 4. We have discussed the potential origin of these super-Earths from

the stand point of atmospheric metallicity and interior structure. Our findings are summarized as follows.

(1) The atmospheric masses of the super-Earths are ranging from $\sim$ 1–30 $\mathrm{wt}\%$, depending atmospheric metallicity and ice mass fraction of core. Estimating the lower limit of atmospheric mass from the timescale of atmospheric escape, we found that the core of GJ3470b is largely made of rock (core ice mass fraction is < 0.3). HAT-P-11b may also have rocky core, but small observational uncertainty is needed to verify it.

(2) Under the assumption of high atmospheric metallicity, the atmospheric masses of GJ1214b, GJ436b, and HD97658b are significantly smaller than the minimum mass of protoatmosphere if in-situ formation and MMSN are assumed. We suggest that the atmospheric mass and high atmospheric metallicity might be reconciled if these planets were formed at outer protoplanetary disks followed by inward migration.

(3) Based on the atmospheric metallicity and the interior structure, we suggest that super-Earths with low-metallicity atmospheres may be formed at current positions, while the planets with high-metallicity atmospheres may be formed at outer parts of protoplanetary disks followed by inward migration. Further study of detailed planet formation theory will be able to test the scenario presented here.

Chapter 6

Summary of this Thesis

The goal of this thesis has been to better understand formation process of mineral clouds on warm super-Earths and what can we learn from the transmission spectra of cloudy atmospheres. To conclude this thesis, we summarize our finding and prospects for future studies.

6.1 Microphysical modeling of mineral cloud formation

In chapter 2, we established a cloud microphysical model that fully takes the vertical transport and growth of cloud particles into account. It was confirmed that the model successfully reproduces the observed properties of water clouds on Earth and ammonia clouds on Jupiter. Then, we applied the microphysical model for the first time to mineral clouds on super-Earths. We found that the particle growth controls the vertical extent of clouds, but only occurs near at the cloud base. The particle size and vertical cloud structure are substantially depending on the amount of cloud condensation nuclei and the atmospheric metallicity. Although the amount of the condensation nuclei is highly uncertain for exoplanets, it is possible to estimate the minimum particle size, say $\sim 1\ \mu\mathrm{m}$, which cloud particles inevitably grow into via coagulation.

6.2 Modeling porosity evolution of cloud particles

In chapter 3, we investigated how the porosity of cloud particles influences cloud vertical structure. According to the results of Chapter 2, mineral cloud particles likely grow into cloud particle aggregates in the collision-dominated growth regimes, as seen in snowflakes in Earth atmospheres. Using the porosity evolution model based on direct N-body simulations, we quantitatively modeled how the porosity of cloud particles evolves in exoplanetary atmospheres for the first time. The cloud particle aggregates initially grow without significant compression, and thus the particle density decreases with increasing the size. Once the particle size exceeds the threshold for the compression, the particle density increases with increasing the size via compression caused by ram pressure from surrounding gas flows. We find that the density can decrease by 2–3 orders of magnitude from material density until the compression sets in. We also analytically demonstrate that the threshold compression radius is $\approx 30\ \mu\mathrm{m}$ and insensitive to relevant parameters, such as gravity and material surface energy.

We combine the porosity model with cloud microphysical model developed in Chapter 2 in order to investigate the vertical structure of fluffy-aggregate clouds. Because of large particle

cross-sections that leads to efficient coagulation, cloud particle aggregates grow into relatively large particles as compared to the case for compact-sphere clouds. However, the particle size rarely exceeds aforementioned compression threshold, and thus cloud particle aggregates can keep low particle densities during the cloud formation. We found that the fluffy-aggregate clouds can ascend to altitude much higher than that for classically assumed compact-sphere clouds.

6.3 Transmission spectrum of the aggregate clouds

In Chapter 4, we investigate how the fluffy-aggregate clouds affect observable transmission spectra of exoplanetary atmospheres. Since previous studies about the transmission spectrum assumed a compact sphere to model the cloud opacity, our study is the first attempt to figure out how the particle microstructure affects observable spectra. Since the fluffy-aggregate clouds are prone to ascend high altitude, they can largely obscure molecular features in observed spectra, unless cloud particle aggregates are constituted by extremely small monomers that reduce the scattering opacity. In addition to the effects obscuring the molecular feature, we found that the aggregate clouds can produce a characteristic spectral slope originated by the scattering properties of aggregates. Because the aggregate scattering follows $\kappa \propto \lambda^{-2}$, which is different from $\kappa \propto \lambda^{-4}$ for the Rayleigh scattering, the spectral slope measurement may offer observable signatures to identify the aggregate clouds.

We further apply the cloud and spectrum models to a number of super-Earths, for which the transmission spectra suggest the presence of high-altitude clouds. According to recent observations of HST, for a temperature range of $T_{\rm eq} = 500$–1000 K, hotter planets tend to be cloudless, which may imply the temperature dependence of the degree of cloudiness. We found the qualitatively same trend in calculated cloud structures. This temperature dependence stems from the disappearance of salt (KCl) clouds at hotter environments (> 700 K) and potentially explains the observed trend. We compared the synthetic transmission spectra with observed spectra of GJ436b, GJ3470b, HD97658b, and HAT-P-11b. Comparing the synthetic spectra with the observed spectra, we found that GJ1214b, GJ436b, and HD97658b likely high-metallicity atmosphere, whereas GJ3470b and HAT-P-11b likely possess low-metallicity atmospheres. This result may suggests that super-Earths can be classified into further subdivisions in terms of the atmospheric metallicity.

6.4 Atmospheres and interior structures of cloudy super-Earths

In Chapter 5, we examine the atmospheric mass of these super-Earths using an interior structure model. The results of Chapter 4 enables us to set atmospheric metallicity and pressure level at the transit radius, both of which substantially affect the planet mass-radius relation. We found that these super-Earths have their masses up to $\sim 30\%$ in the atmospheres, depending on the atmospheric metallicity and ice mass fraction in the core. In particular, for planets with high atmospheric metallicity ($\geq 100\times$ solar), the atmospheric mass is much smaller than the minimum mass of protoatmosphere during the planet formation if in-situ formation at MMSN is assumed. This potentially suggests that super-Earths with high-metallicity atmospheres were formed at outer parts of protoplanetary disks followed by orbital migration.

Chapter 7

Future prospect

7.1 Implication for Future Observations

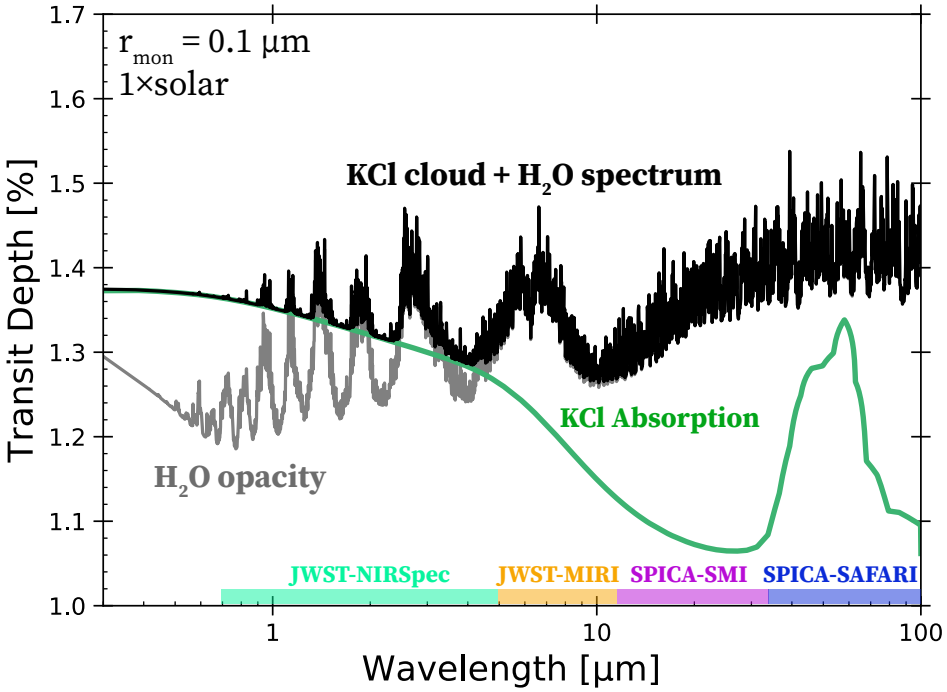


Figure 7.1: Preliminary result assessing whether the absorption feature of salt (e.g., KCl, Na_2S) clouds can be detected by next generation space telescope, SPICA. The calculation method is similar to Section 3. The parameter of GJ1214b is assumed in this figure. The gray and green lines show the transmission spectrum originated by H_2O vapor and KCl clouds, respectively. The black line shows the total transmission spectrum. One can see that absorption feature of KCl is obscured by the absorption feature of H_2O vapor in this case.

Although we discussed the atmospheric metallicity of several super-Earths in Chapter 4.5.2, more observations will be needed to verify it. Our calculations in Chapter 3 and 4 suggest that clouds tend to be optically thin at longer wavelength ($> 2\ \mu$m). As a result, the shape of transmission spectrum could significantly vary with the metallicity at such long wavelength

even if the spectrum looks featureless at near-infrared wavelength. The transmission spectrum at such long wavelength will be observed by future instruments, such as JWST ($\lambda = 0.6$–$14\ \mu$m, Batalha et al., 2017), Twinkle ($\lambda = 0.4$–$4.5\ \mu$m, Edwards et al., 2019), and ARIEL ($\lambda = 1.25$–$7.8\ \mu$m, Tinetti et al., 2018). Crudely assessing, for example, Figure 4.11 shows the difference of transit depth between spectrum with the solar-composition atmosphere and the high-metallicity atmosphere is an order of ~ 200 ppm at $\lambda \sim 3$–$4\ \mu$m. The noise floor of JWST is conservatively 20–50 ppm (Greene et al., 2016; Batalha et al., 2017), and thus it would be possible to distinguish low and high metallicity atmospheres.

Another interesting prospect is detecting the absorption feature of mineral cloud itself. Since the absorption feature of mineral clouds are prone to emerge at $\lambda > 5\ \mu$m. This wavelength region is covered by JWST and SPICA, and thus the cloud feature may be detectable. Detecting cloud feature would help to distinguish whether cloudy atmosphere is originated by mineral clouds or photochemical hazes. In addition, detecting the cloud feature may open a new window to constrain atmospheric C/O because the cloud composition can be quite different between carbon-rich and oxygen-rich atmospheres (Helling et al., 2017). We are now assessing the feasibility that detects the absorption feature of salt clouds in warm super-Earths by SPICA, as shown in Figure 7.1. Our preliminary calculation suggest that absorption feature of salt clouds tend to be obscured by absorption feature of water vapor. We are planning to further investigate what condition enables us to detect the feature of the mineral clouds in near future.

7.2 Further Model Improvements

7.2.1 Radiative feedback of clouds on PT profiles

In this thesis, we have neglected the effects of cloud opacity on atmospheric PT profiles. However, in reality, it is expected that the cloud opacity affects the PT profiles. Cloud have the both effects of heating and cooling the atmosphere, depending on its optical properties (Heng et al., 2012). For example, if cloud is made of scattering materials, the cloud enhances the bond albedo and cools the atmosphere (e.g., Roman & Rauscher, 2019). By contrast, for clouds made of absorbing materials, the cloud absorbs the stellar illumination and heat the upper atmosphere (Lines et al., 2019). For salt clouds (e.g., KCl) focused in this thesis, Charnay et al. (2015b) reported that the the temperature at lower atmosphere, say > 1 mbar in pressure, is substantially cooled by the scattering of KCl clouds. This results in the cloud base at deeper atmospheres. Since the particle growth mainly occurs near the cloud base, the radiative feedback potentially affect resulting cloud structure.

To test the effects of the radiative feedback, we calculate the cloud structures in PT structure of different bond albedo (top panel of Figure 7.2). In principle, the higher bond albedo is, the deeper cloud base is. The cloud base at the deep atmospheres tend to cause the efficient particle growth because of small eddy diffusion coefficient and high number density of cloud particles. The different albedo less affects the cloud vertical distributions as long as the cloud base is placed at ~ 0.1–1 bar (cases of albedo of 0 and 0.3 in Figure 7.2), while it significantly affects the distributions once the cloud base is placed at deep convective atmospheres (case of albedo 0.6 in Figure 7.2). In such deep atmosphere, the cloud particles grow into relatively large size. Furthermore, at the high density deep atmospheres, the gas-drag law falls into not the Epstein's regime but the Stokes's regime, leading to efficient gravitational settling. For example, the terminal velocity of a cloud particle aggregate with $D_{\rm f} = 2$ in the Stokes's regime is given

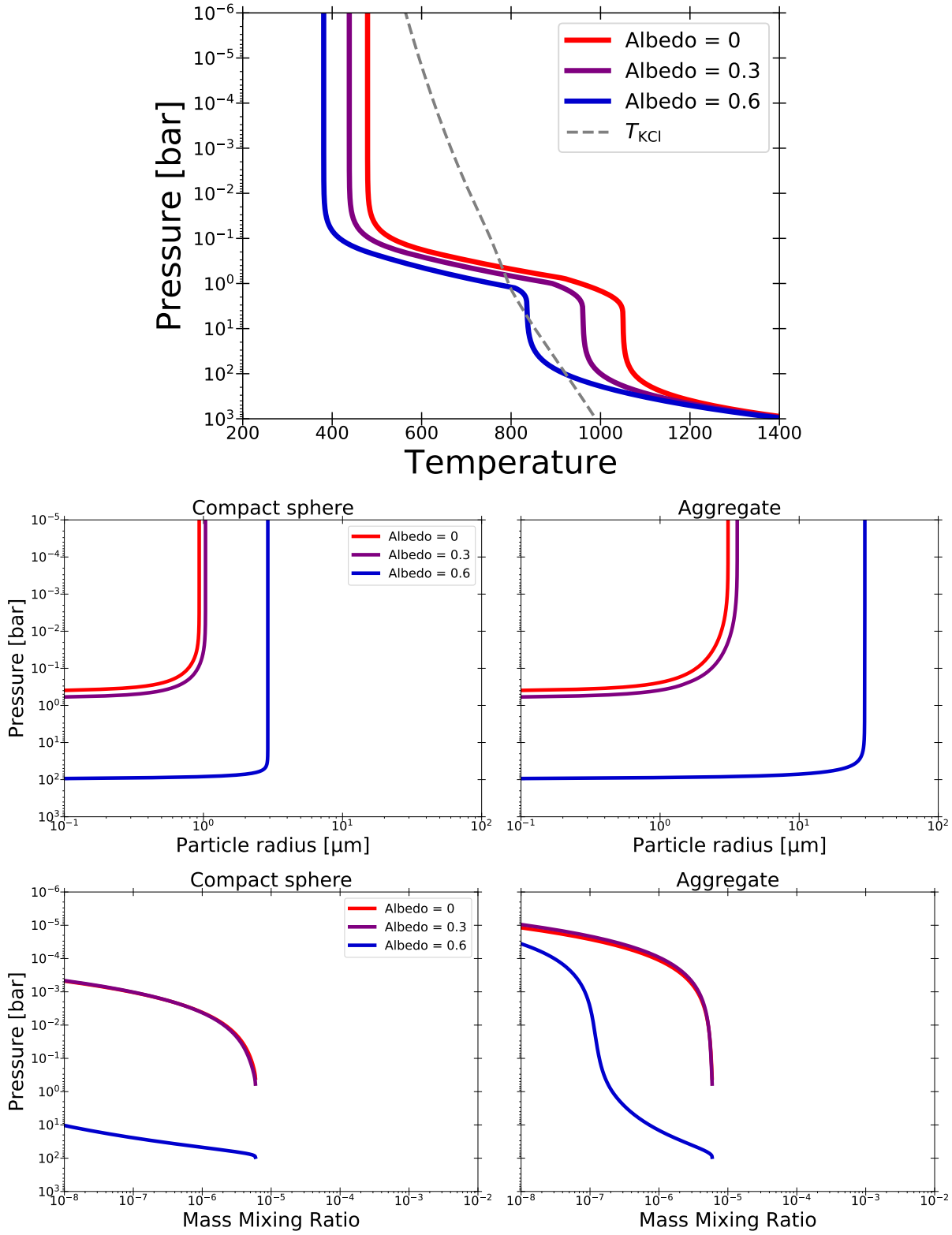


Figure 7.2: Vertical cloud distributions for different bond albedo of planets. The top panel shows the PT structure of solar metallicity atmospheres of GJ1214b for different bond albedo, where the condensation temperature of KCl is denoted by a gray dashed line. The middle and bottom rows exhibit the vertical distributions of particle radius and mass mixing ratio. The left and right column show the results for compact-sphere and aggregate clouds, where the monomer size of $r_{\rm mon} = 0.1\ \mu$m is assumed.

by

$$v_{\rm t} \approx \frac{2g\rho_{\rm p}}{9\eta} r_{\rm mon} r_{\rm agg}. \tag{7.1}$$

In contrast to the Epstein's regime in which the terminal velocity is independent of aggregate radius, the velocity is proportional to the aggregate radius in the Stokes regime. This is why the mass mixing ratio steeply decreases at the deep atmospheres even for the aggregate clouds.

Although the clouds potentially inhibit their ascending when the albedo becomes very high, the inhibition also yields the cloudless atmosphere. Therefore, when the radiative feedback is significant, time variability of cloud structure is expected. In order to capture the time variability, one needs to simulate the evolution of PT profiles simultaneously. One of the sophisticated way is to simulate the cloud microphysics and full radiative transfer (Lee et al., 2016; Lines et al., 2018). Alternatively, one may simplify either the cloud microphysics or radiative transfer schemes. For the purpose of investigating the cloud formation, we suggest that the analytical treatment of PT profiles (e.g., Heng et al., 2012) would be useful to be implemented in cloud models. Our future study would address the effects of clouds on PT profiles in more detail.

7.2.2 Improvements of Nucleation Treatment

In this thesis, we have assumed that cloud condensation nuclei (CCNs) are continuously supplied from the cloud base. The fixed concentration of CCNs at the lower boundary was also adopted by cloud models for Earth (Turco et al., 1979). The assumption would be reasonable if the preexisted CCNs are supplied from deep atmospheres (heterogeneous nucleation) or CCNs are newly formed near at the cloud base via homogeneous nucleation. We discuss the validity of our assumption for each case below.

For the heterogeneous nucleation scenario, it is highly uncertain whether CCNs are predominantly supplied from upper atmospheres or deep atmospheres for exoplanets. For the former case, the possible candidates of CCNs are photochemical hazes formed in upper atmospheres (e.g., Lavvas et al., 2019) and/or dust grains injected from meteorites (Plane, 2012), which is known to act as condensation nuclei for noctilucent clouds on Earth (e.g., Turco et al., 1982). Our assumption is invalid for these top-down CCNs supply, and thus we should instead introduce the source term of CCNs at upper atmosphere. For the later case, one of the candidate of CCNs supplied from deep atmospheres is the mineral cloud made of high-temperature refractory condensates, such as Cr, Fe, and TiO_2, formed in deep atmospheres (Lee et al., 2018). For this scenario, our assumption would reasonably express the supply of CCNs. The calculations of cloud formation including the deep cloud formation might be able to test this scenario.

For the homogeneous nucleation scenario, Gao et al. (2018); Gao & Benneke (2018) showed that the homogeneous nucleation of KCl nuclei takes place near the cloud base. Our calculations produce the vertical cloud distributions similar to their simulations: cloud mass mixing ratio and particle radius remains nearly constant until the gravitational settling dominates over the eddy diffusion (see Figure 4 of Gao et al., 2018). Therefore, our prescription for CCNs is capable of handling the case in which the homogeneous nucleation takes place near the cloud base. However, Helling et al. (2008) and subsequent studies have suggested that the nucleation of TiO_2 nuclei predominantly occurs apart from the cloud base for brown dwarfs and hot Jupiters. The difference may stem from the difference of cooling temperature required to maximize the homogeneous nucleation rate, which depends on the material surface energy (Yamamoto & Hasegawa,

1977). We should check how the assumption of CCNs affects the cloud structure in future investigations on mineral clouds in hot Jupiters.

We acknowledge that the current treatment for CCNs likely has some limitations to capture the real phenomena. For example, we fix the concentration of CCNs through the simulations, while the concentration may vary with time. In the context of homogeneous nucleation, the cloud particles settled from upper atmospheres decreases the super saturation of vapors and terminates the nucleation, while the termination of nucleation increases the super saturation again to drive the nucleation. Such periodic behavior was indeed seen in previous studies assuming homogeneous nucleation (e.g., Barth & Toon, 2003; Gao & Benneke, 2018) and unable to be captured by our prescription for CCNs. However, we note that it is unclear whether such time variability occurs in real atmospheres because the atmospheres are not 1D but 3D. In real atmospheres, the nucleation would occur only at upwelling regions[1], while the cloud particles may be rained out at regions apart from there. A multi-dimensional model of cloud formation would be needed to address the topic of time variability.

To conclude this subsection, we suggest the possible future studies to improve the treatment of CCNs. Since the cloud structure is sensitive to the concentration of CCNs, the parameterization of the CCN concentration diminishes the model predictivity. The nucleation theory (Pruppacher & Klett, 1996; Seinfeld & Pandis, 2012; Gail & Sedlmayr, 2013) enables us to determine the CCN concentraion in first principle, but the theory tends to deviate from the actual nucleation rate by several orders of magnitude (e.g., Ford, 1997; Tanaka et al., 2011; Lee et al., 2018). The assumption of homogeneous nucleation might also cause serious errors if heterogeneous nucleation is a predominant mechanism. There are two directions at least. The first is to validate the classical nucleation theory for mineral condensates formed in exoplanets. In addition to laboratory studies (e.g., Kimura et al., 2012), numerical experiments of molecular dynamics simulations (Tanaka et al., 2011) would be useful to verify the nucleation theory. The another direction is to calibrate the nucleation properties from observations. Ormel & Min (2019) proposed a framework to constrain the nucleation profiles through retrieval models, which would be helpful to establish a reliable cloud model from future observations.

7.2.3 Multiple Mineral Clouds

In this thesis, we have only investigated the formation of KCl clouds. This is because KCl cloud is the most abundant species that forms in all super-Earths studied in this thesis. However, in reality, multiple species may build up the mineral clouds, depending on the atmospheric temperature structure. The top panel of Figure 7.3 shows the condensation temperature of several mineral clouds. For the fiducial parameter of $T_{\rm int} = 50$ K, which is supported by thermal evolution calculations (Rogers & Seager, 2010; Valencia et al., 2013), the condensation temperature of KCl, NaCl, and ZnS intersect the curve of atmospheric PT profiles, implying that these species are potentially condensed into solid phases there. Although the abundance of ZnS is relatively small as compared to KCl, NaCl might seem to form more massive clouds than KCl because Na is more abundant than K. However, it should be noted that the abundance of NaCl is regulated by the abundance of Cl, which is an order of magnitude lower than Na (Cl/Na=0.18, Asplund et al., 2009). We also recall that abundance of KCl is also limited by depleted one of either K or Cl. This implies that the abundance of KCl + NaCl is regulated by the abundance of Cl. It is

[1]However, because of the presence of strong horizontal jets in exoplanetary atmospheres (e.g., Showman & Guillot, 2002), the cooling of vapors driven by day-to-night horizontal flow may also cause the nucleation as well.

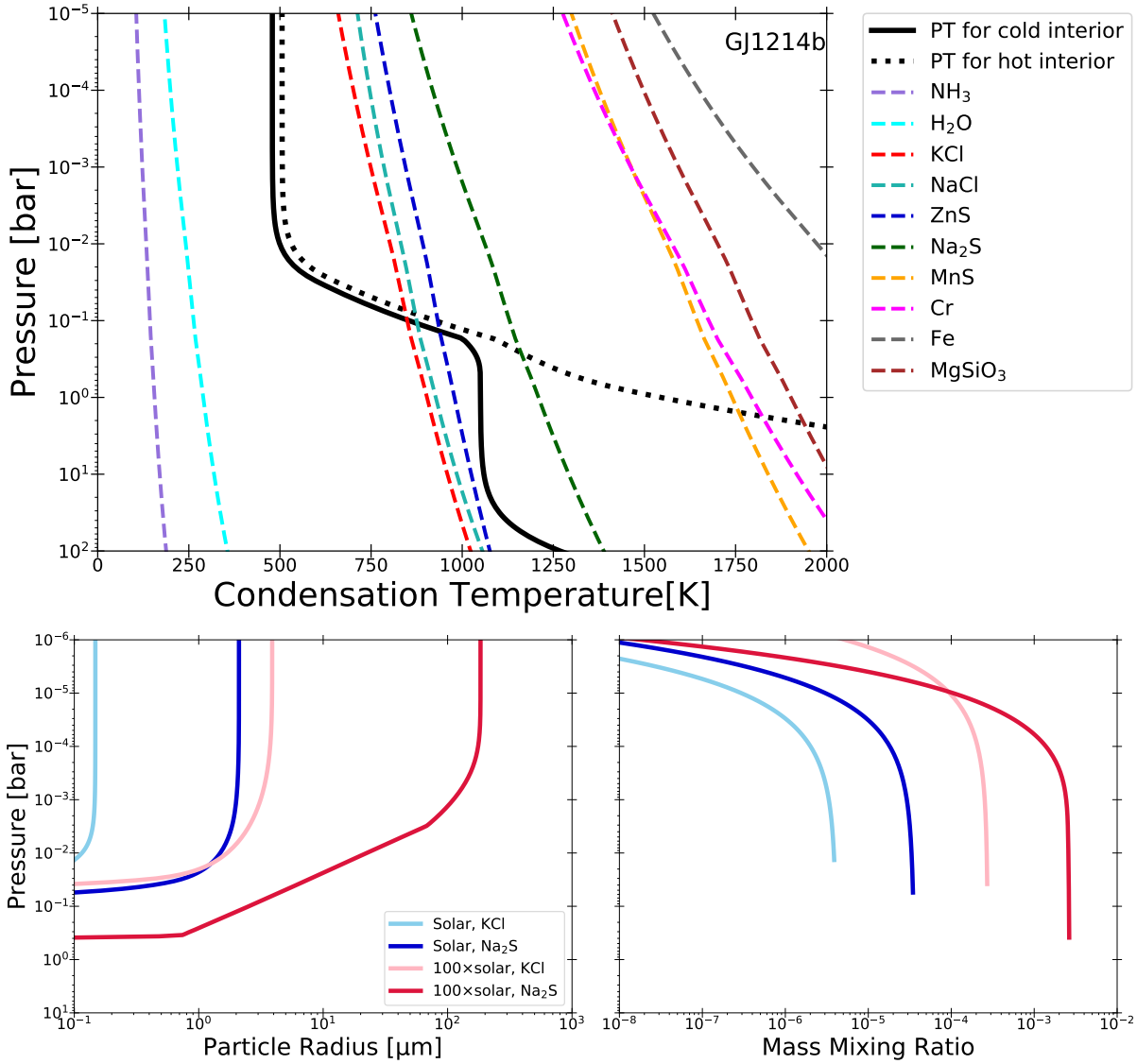


Figure 7.3: (Top):Condensation temperature of several mineral species (dashed colored lines). The PT profile of GJ1214b is also shown for reference. The black solid and dotted lines show the profiles for intrinsic temperature of $T_{\rm int} = 50$ K (cold) and 400 K (hot). The atmospheric metallicity of $100\times$ solar abundance is assumed. (Bottom):Vertical distributions of KCl clouds and Na_2S clouds in GJ436b with a solar metallicity atmosphere, where the aggregate clouds of $r_{\rm mon} = 0.1$ μm is assumed.

also worth noting that NaCl and KCl have the very similar optical properties (Wakeford & Sing, 2015) and (homogeneous) nucleation trends (Lee et al., 2018). Therefore, our result would be less affected by the formation of NaCl clouds.

We note that the Na_2S may play an important role to build the mineral clouds because the abundance of Na_2S can be higher than KCl by an order of magnitude. In Figure 7.3, the condensation temperature intersects the PT curves at deep atmospheres, say > 100 bar. Although it may be expected that such deep mineral cloud do not ascend to upper atmospheres, detail investigations would be needed to verify the assumption. Rather, Na_2S cloud could be dominant clouds for planets quite hotter than GJ1214b, such as HAT-P-11b. Furthermore, if the intrinsic temperature ($T_{\rm int}$) is quite higher than that predicted by thermal evolution models ($T_{\rm int} \sim 50$ K, Rogers & Seager, 2010; Valencia et al., 2013), the Na_2S cloud can form relatively upper atmospheres (see dotted line in Figure 7.3). Such high intrinsic temperature is suggested for hot Jupiters (Thorngren et al., 2019) and may also apper for super-Earths (Millholland, 2019).

To examine the potential impacts of Na_2S cloud formation, we calculate the vertical distributions of Na_2S clouds in the bottom panels of Figure 7.3. In the calculation, we assume the PT profiles of GJ436b (Figure 4.7) because high intrinsic temperature ($T_{\rm int} = 400$ K) is suggested for this planet (Morley et al., 2017). The vertical distributions of fluffy-aggregate clouds are only examined here. In principle, Na_2S cloud particles grow into the size quite larger than KCl because of the high abundance of Na_2S. This results in the cloud mass mixing ratio higher than KCl clouds. Therefore, in general, it is expected that Na_2S clouds efficiently make upper atmospheres opaque as compared to the case of KCl clouds. On the other hand, when the metallicity is high (case of $100\times$ solar in Figure 7.3), the particle grow so large size that causes gas-drag compression of cloud particle aggregates. This results in the gravitational settling more efficient than KCl clouds for which the aggregate is not compressed. Therefore, the impacts of Na_2S cloud may not be simply determined by the abundance of condensing gasses. We plan to perform a comprehensive investigations on the impacts of Na_2S cloud in near-future.

7.2.4 Better understanding of tracer transport

The vertical transport of cloud particles has been conventionally prescribed by the eddy diffusion coefficient, $K_{\rm z}$ (e.g., Ackerman & Marley, 2001; Ohno & Okuzumi, 2018; Gao & Benneke, 2018; Powell et al., 2018; Ormel & Min, 2019; Ohno et al., 2019). Several studies have examined how $K_{\rm z}$ varies with relevant parameters, such as equilibrium temperature, atmospheric metallicity, and particle size (Parmentier et al., 2013; Charnay et al., 2015a; Zhang & Showman, 2018a,b; Komacek et al., 2019). However, it is still somewhat difficult to evaluate the exact value of $K_{\rm z}$. In particular, the eddy diffusion coefficient on non-synchronized exoplanets have never examined in detail. Although close-in planets are likely tidally locked, it has been known that some close-in planets have non-zero eccentricity; for example, $e = 0.16$ for GJ436b (Bourrier et al., 2018) and $e = 0.22$ for HAT-P-11b (Yee et al., 2018). Non-zero eccentricity causes a periodic intense heating near at the periapse, substantially affects the atmospheric circulation (Langton & Laughlin, 2008; Kataria et al., 2013; Lewis et al., 2017; Ohno & Zhang, 2019a). It would be important to investigate how the eddy diffusion coefficient depends on planetary eccentricity.

Another potentially important factor is a planetary obliquity—the angle between planetary rotation axis and orbital normal. Recent study of Millholland & Laughlin (2019) suggests that orbital configurations of super-Earths, in which many planets are lying just wide of the first-

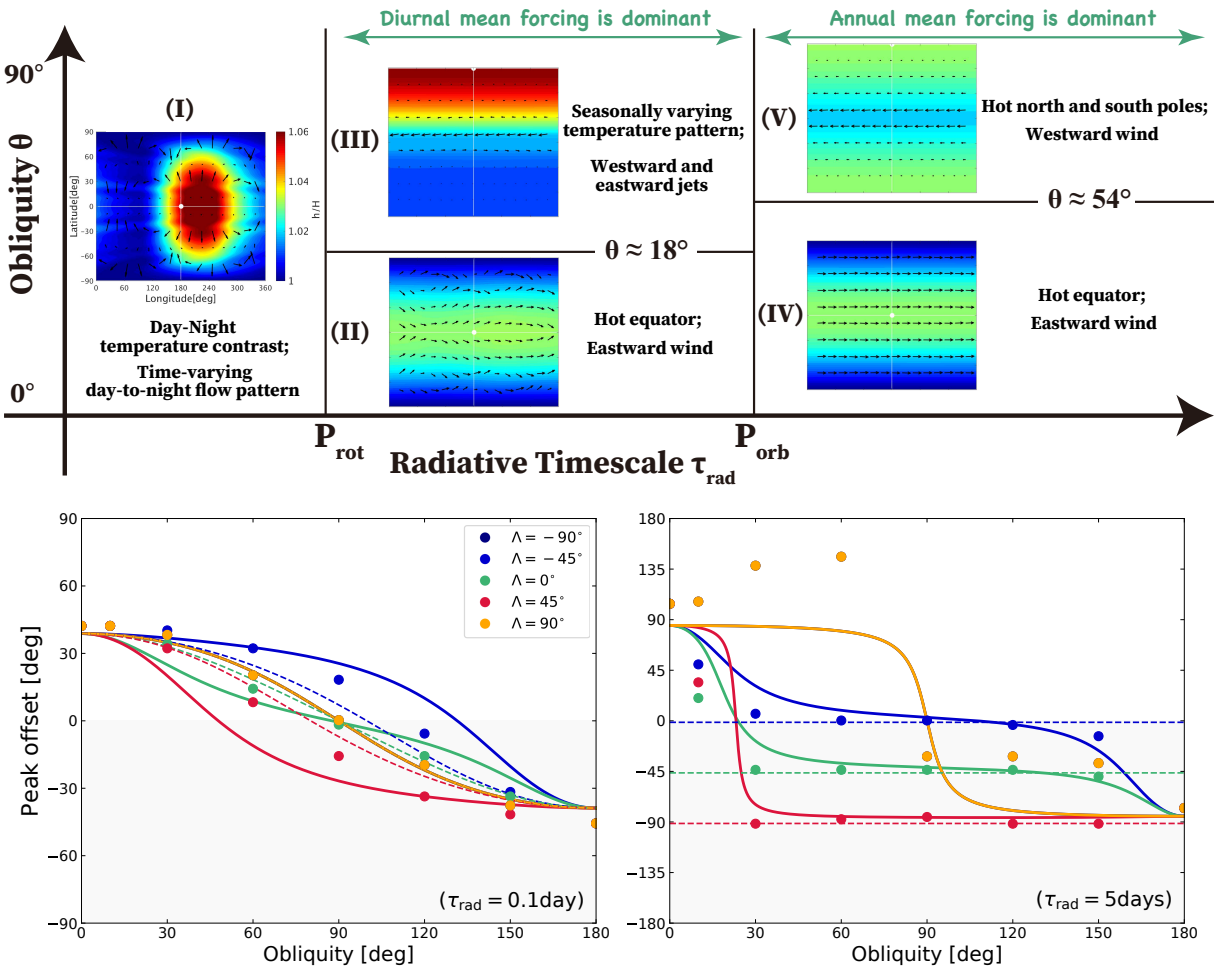


Figure 7.4: Top: Atmospheric circulation regime of planets with non-zero obliquities, taken from Ohno & Zhang (2019a). The circulation regime can be demarcated into five regimes in terms of obliquity, rotation period, orbital period, and atmospheric radiative timescales. Each panel shows atmospheric flow patterns and atmospheric height fields (diagnosing temperature distributions) simulated by a shallow water model. Bottom: Peak-offset of thermal light curves of tilted exoplanets as a function of obliquity, taken from Ohno & Zhang (2019b). Peak offset is defined as the orbital phase of thermal flux peak subtracted by orbital phase of the secondary eclipse (for review, see Parmentier & Crossfield, 2018). Different colored symbols indicate the offset for different orbital configuration [3]. The colored dots show the offset of thermal light curves calculated by the shallow water model of Ohno & Zhang (2019a). The solid lines show the offset predicted by analytical light curves presented in Ohno & Zhang (2019b). The dotted lines show the asymptotic behavior of analytical prediction.

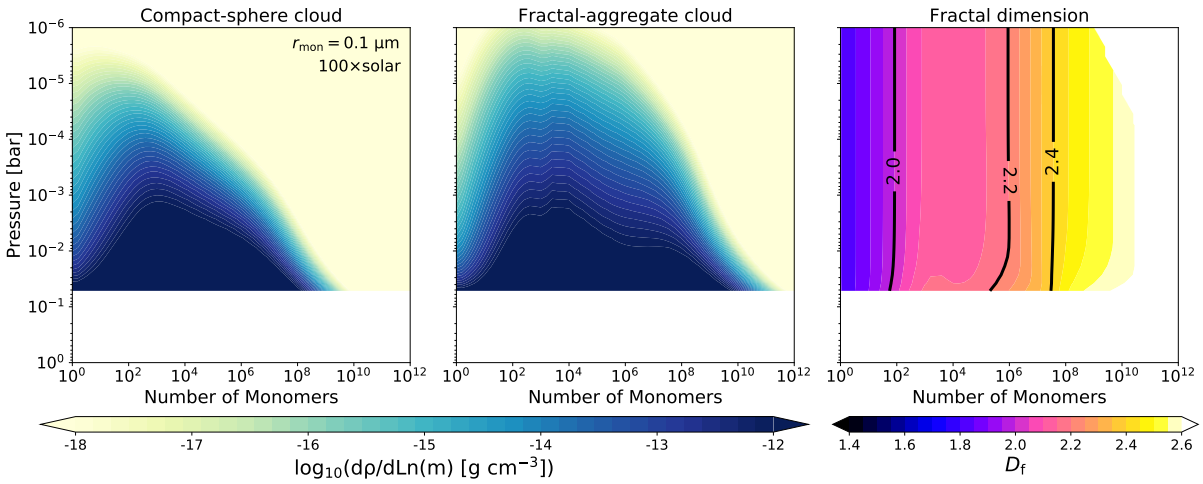


Figure 7.5: Preliminary results of the co-evolution of size and porosity distributions of cloud particle aggregates. The left and middle panels exhibit the cloud mass density contained in each vertical and mass grid for compact-sphere and fluffy-aggregate clouds, respectively. The right panel shows the fractal dimension distribution in the simulation of middle panel.

order mean motion resonance, may stem from the orbital energy dissipation via obliquity tide. They also suggest that these planets may retain substantially large obliquity. If this is true, the obliquity potentially affects the atmospheric circulation and possibly K_z. We performed a comprehensive study on atmospheric circulation on planets with non-zero obliquity using a shallow water model (Ohno & Zhang, 2019a) and found that the circulations indeed vary with obliquities drastically (top panel of Figure 7.4). Thus, the eddy diffusion coefficient is likely affected by the obliquity as well. Although observation methods constraining exoplanetary obliquity have been not established yet, we found that the observations of thermal light curve may help to constrain exoplanetary obliquities (Ohno & Zhang, 2019b). In short, we revealed that non-tilted planets inevitably yield the thermal flux peak before the secondary eclipse, while tilted planets are prone to produce the flux peak after the secondary eclipse (Ohno & Zhang, 2019b). As a next step, we will examine how the particle transport varies with planetary obliquity and resulting observations in future.

7.2.5 Co-evolution of Size and Porosity Distributions of Cloud Particles

In reality, the porosity evolution of cloud particles should be influenced by the size distributions because particle morphology depends on the size ratio of collided aggregates (Okuzumi et al., 2009). We have assumed that cloud particle aggregates retain $D_f = 2$ until the compression sets in. Although we showed that the $D_f = 2$ can be a reasonable approximation not only for monodisperse but also for various shapes of the size distributions (Section 3.6), a microphysical model solving a full size distribution is needed to verify it. We are now developing a new code to calculate the evolution of both size and porosity distributions in a self-consistent manner. Figure 7.5 shows the preliminary results of cloud distributions on GJ1214b for atmosphere with $100\times$ solar metallicity. We found that the cloud particles largely retain the fractal dimension of $D_f = 1.9$–2.2 as expected in section 3.6, but some large cloud particles grow into relatively compact aggregates ($D_f \geq 2.4$) and cannot ascend to very high altitude. Our near-future studies

will examine the co-evolution process of size and porosity distributions in more detail to better understand the mineral cloud formation.

7.2.6 Beyond 1D model

Real cloud formation occurs in 3D atmospheres. We have assumed that the cloud distribution is horizontally uniform and approximated by the horizontally-averaged profile. Since close-in exoplanets have vigorous atmospheric circulation that homogenizes the cloud distributions, approximation of the horizontal average are partially justified by 3D GCM with passive tracers (Parmentier et al., 2013; Charnay et al., 2015a; Komacek et al., 2019). However, these GCM studies did not take into account the cloud microphysics, and it is unclear how it affects the cloud spatial distributions. In particular, the condensation/evaporation rate of cloud particles is sensitive to atmospheric temperature that varies significantly at place to place. Therefore, spatial cloud distributions may be substantially inhomogeneous, especially for very hot planets where spatial temperature variation is significant.

There are several possible approaches to examine the cloud formation processes in 3D atmospheres. One of the straightforward way is to combine the cloud microphysical model with 3D GCM to calculate cloud properties at each vertical, longitudinal, and latitudinal grid. A few studies investigated the 3D cloud profiles by combining 3D GCM with the cloud model based on moment bulk scheme (Lee et al., 2016; Lines et al., 2018). Although this is the most sophisticated way, this method is computationally demanding and difficult to perform parameter survey. Another approach is to apply a 1D cloud model to vertical column at each longitude and latitude grid, where the temperature profile is postprocessed from the 3D GCM (e.g., Lee et al., 2015; Helling et al., 2019). For example, Helling et al. (2019, including K.O.) calculated a 3D cloud structure on HAT-P-7b using a pre-calculated temperature structure taken from a 3D GCM. They showed that night side ($\phi = 90$–270 deg) is relatively cool, and cloud is preferentially formed in the night side. Since HAT-P-7b is very hot planets ($T_{\rm eq} \approx 2100$ K), temperature contrast between dayside and nightside is quite large, resulting in significantly inhomogensous clouds. Although this method can predict the 3D cloud structures determined by local thermal conditions, the shortcoming is the ignored horizontal transport that presumably smears out the cloud distributions determined by the local conditions.

As an intermediate approach, we propose that pseudo 2D model could be useful to figure out the 3D cloud formation process. The pseudo 2D model simulates the vertical profiles of column rotating along the equator and was previously used to study the effects of disequilibrium chemistry (Agúndez et al., 2014). Since the model is computationally cheap, it is possible to perform the parameter survey to figure out how the relevant parameters, such as equilibrium temperature, atmospheric composition, dynamical timescale, affect the cloud profiles. We are planing to construct such simplified model to perform the comprehensive investigations on 3D cloud formation in future.

7.3 Applications of Porosity Model to Photochemical Hazes

The porosity evolution is also a critical factor in the context of photochemical haze formation. It has been widely accepted that photochemical hazes in upper atmospheres of Titan are fractal aggregates with $D_{\rm f} \approx 2$ (e.g., West & Smith, 1991; Rannou et al., 1997; Lavvas et al., 2010). In the context of exoplanetary atmospheres, the photochemical haze is the another candidate

causing the featureless transmission spectra (e.g., Morley et al., 2015; Kawashima & Ikoma, 2018, 2019). In particular, recent studies suggest that the effects of photochemical hazes on transmission spectra highly depend on assumed particle porosity (Adams et al., 2019; Lavvas et al., 2019). Since the haze could alter the inferred atmospheric composition, it is important to figure out how the haze formation takes place in exoplanetary atmospheres. As a first stepping stone to work on the hazes formation, we are now applying the porosity model to the hazes formation on a solar system objects, such as Pluto and Triton (Zhang et al., 2019, Ohno, Zhang, et al. in prep). In short, as shown in Figure 7.6, our aggregate haze model successfully explains the solar occultation observations of Voyager2 (Herbert & Sandel, 1991; Krasnopolsky et al., 1992) and suggests that the haze production rate is lower than that suggested for Pluto (Gao et al., 2017b) by an order of magnitude. We are planning to apply the model to exoplanetary hazes to figure out the haze formation processes on exoplanets in future.

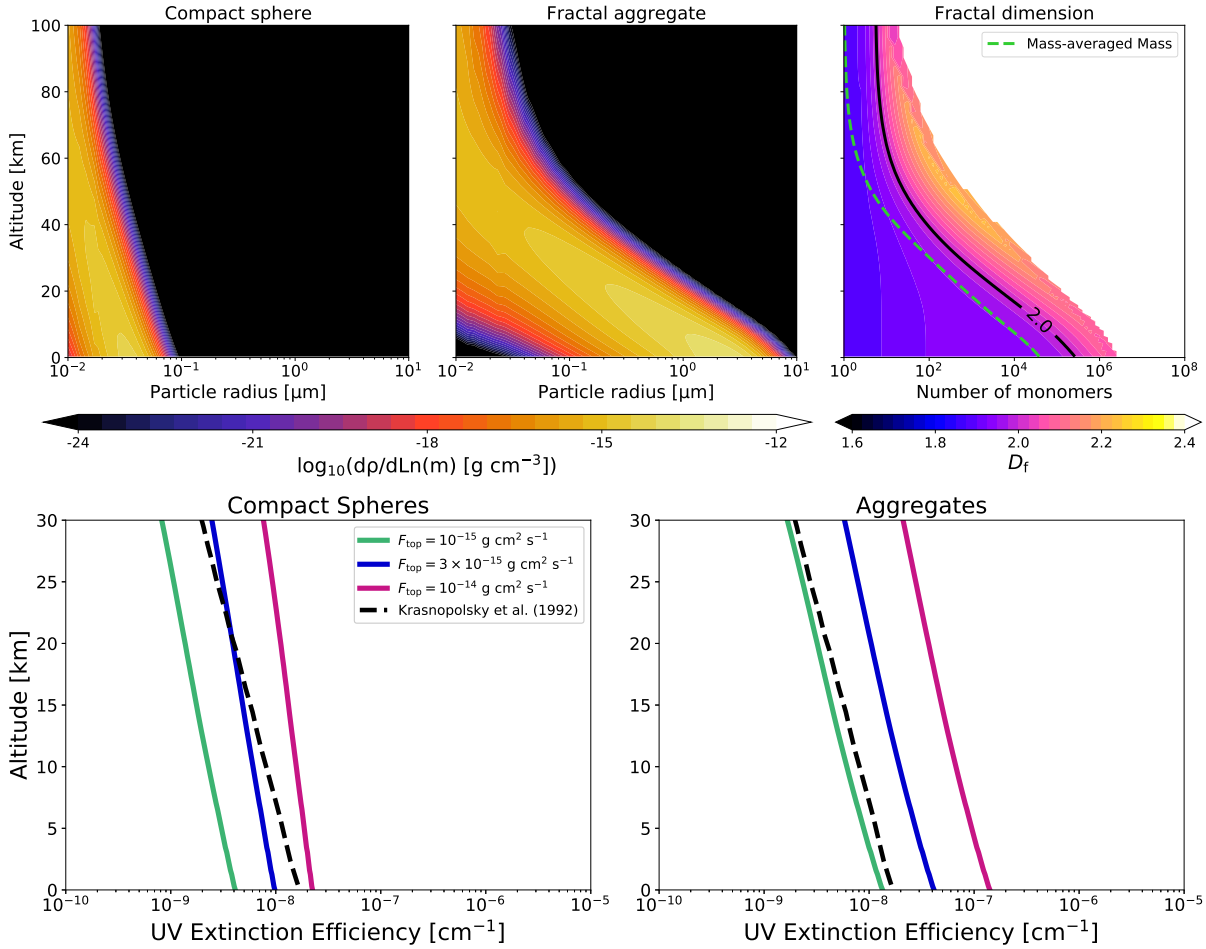


Figure 7.6: Top: Same as Figure 7.5, but for preliminary results of the calculations of haze formation on Triton. Bottom: Vertical distributions of extinction efficiency of Triton's haze at UV wavelength ($\lambda = 0.15\ \mu$m). Left and right panels show the results for compact-sphere and aggregate hazes, respectively. The different colored lines show the results for different haze downward mass flux. It is suggested that the haze mass flux takes $\approx 1.2 \times 10^{-14}$ g cm^{-2} s^{-1} for Pluto (Gao et al., 2017b). The black dashed lines denote the extinction efficiency retrieved by the solar occultation observations of Voyager 2 (Herbert & Sandel, 1991; Krasnopolsky et al., 1992)

Appendix A

Full derivation of transmission spectrum

One of the most well-used way may be the transmission spectroscopy that observes the primary transit of an exoplanet in multi wavelength (e.g., Seager & Sasselov, 2000; Brown, 2001). The basic idea of this method is that transit depth, the area-ratio of a transiting planet to a stellar disk (see Figure 1.3), varies with observed wavelength because of the wavelength dependence of atmospheric opacity. Several previous studies have stated the theoretical basis of transmission spectroscopy with analytical argument (Lecavelier Des Etangs et al., 2008; de Wit & Seager, 2013; Bétrémieux & Swain, 2017; Heng & Kitzmann, 2017; Jordán & Espinoza, 2018). Here, I also briefly review the theoretical basis of transmission spectroscopy as well. The transit depth D can be calculated by

$$D = \frac{\pi R_0^2 + \int_{\mathrm{R_0}}^{\infty} 2\pi r(1 - e^{-\tau_\mathrm{s}})dr}{\pi R_\mathrm{s}^2}, \tag{A.1}$$

where R_s is the stellar radius, R_0 is the solid radius of transiting planet, and τ_s is the optical depth along the line of sight of observer, called slant optical depth or chord optical depth (e.g., Fortney et al., 2003). The slant optical depth is calculated by

$$\tau_\mathrm{s}(r) = 2\int_\mathrm{r}^{\infty} \frac{\rho_\mathrm{g}\kappa r' dr'}{\sqrt{r'^2 - r^2}}, \tag{A.2}$$

where ρ_g is the atmospheric mass density and κ is the atmospheric mass opacity. The solution of Equation (A.2) cannot be expressed explicitly without utilising special function, but one can know the basic trend by invoking some approximations. Assuming isothermal atmosphere and vertically constant opacity and gravity, the equation is rewritten by

$$\tau_\mathrm{s}(r) = 2\rho_\mathrm{g}(r)\kappa \int_\mathrm{r}^{\infty} \frac{r\exp\left[-(r'-r)/H\right]}{\sqrt{r'^2 - r^2}} dr', \tag{A.3}$$

where $H = k_\mathrm{B}T/m_\mathrm{g}g$ is the pressure scale height, k_B is the Boltzmann constant, T is the temperature, m_g is the mean mass of atmospheric molecules, and g is the surface gravity. For typical close in exoplanets, the pressure scale height is

$$H = \frac{k_\mathrm{B}T}{m_\mathrm{g}g} \sim 360\ \mathrm{km} \left(\frac{T}{1000\ \mathrm{K}}\right) \left(\frac{m_\mathrm{g}}{2.3\ \mathrm{amu}}\right)^{-1} \left(\frac{g}{10\ \mathrm{m\ s^{-1}}}\right)^{-1}. \tag{A.4}$$

Introducing the variable $r'/r = x$, Equation (A.3) is rewritten by

$$\tau_\mathrm{s}(r) = 2\rho_\mathrm{g}(r)\kappa r \exp\left(\frac{r}{H}\right) \int_1^{\infty} \frac{x\exp\left(-\frac{r}{H}x\right)}{\sqrt{x^2 - 1}} dx. \tag{A.5}$$

$$\tau_{\rm s}(r) = 2\rho_{\rm g}(r)\kappa r \exp\left(\frac{r}{H}\right)\int_1^\infty \frac{x\exp\left(-\frac{r}{H}x\right)}{\sqrt{x^2-1}}dx. \tag{A.6}$$

The integral part can be expressed by the modified Bessel function of the first kind, $K_1(r/H)$ (Bétrémieux & Kaltenegger, 2015). Therefore, the slant optical depth is explicitly written by

$$\tau_{\rm s}(r) = 2\rho_{\rm g}(r)\kappa r \exp\left(\frac{r}{H}\right)K_1\left(\frac{r}{H}\right). \tag{A.7}$$

According to Bétrémieux & Kaltenegger (2015), the Bessel function multiplied by the exponetial term can be expressed in a power series,

$$\exp(x)K_{\rm t}(x) = \sqrt{\frac{\pi}{2y}}\left[1+\frac{(4t^2-1)}{8y}+\frac{(4t^2-1)(4t^2-9)}{128y^2}+\dots\right]. \tag{A.8}$$

Since planet radius is much larger than scale height in general ($r/H \gg 1$), high-order terms in Equation (A.8) are negligible. Therefore, to zeroth order, the slant optical depth in Equation (A.7) can be approximated by

$$\tau_{\rm s}(r) \approx \rho_{\rm g}(r)\kappa H\sqrt{\frac{2\pi r}{H}} = \tau_{\rm v}(r)\sqrt{\frac{2\pi r}{H}}, \tag{A.9}$$

where $\tau_{\rm v}$ is the vertical optical depth. Since $r \approx R_{\rm p}$, Equation (A.9) is equivalent to Equation (1.5) presented in Section 1.3. Equation (A.9) demonstrates that the slant optical depth is much larger than the vertical optical depth by a factor of $\sqrt{2\pi r/H}$. For example, the ratio is $\sim$75 for Earth and $\sim$128 for Jupiter (Fortney, 2005). Since one cannot observe optically too thick region ($\tau_{\rm s} \gg 1$), the transmission spectrum probes relatively upper atmospheres. Let us evaluate transit depth variation caused by the atmospheric extinction. Since the atmosphere is much smaller than planetary radius, we can further approximate Equation (A.9) as

$$\tau_{\rm s} \approx \rho_{\rm g}(r)\kappa H\sqrt{\frac{2\pi R_0}{H}} = \tau_0 \exp\left(-\frac{r-R_0}{H}\right)\sqrt{\frac{2\pi R_0}{H}}, \tag{A.10}$$

where I define $\tau_0 = \tau_{\rm s}(R_0)$. The equation yields the relation of

$$\frac{d\tau_{\rm s}}{\tau_{\rm s}} = -\frac{dr}{H} \tag{A.11}$$

Inserting Equations (A.10) and (A.11) into (A.1), we obtain

$$D = \left(\frac{R_0}{R_{\rm s}}\right)^2\left\{1+\frac{2H}{R_0}\int_0^{\tau_0}(1-e^{-\tau})\left[1+\frac{H}{R_0}\log\frac{\tau}{\tau_0}\right]\frac{d\tau}{\tau}\right\}. \tag{A.12}$$

Since $H \ll R_0$, the term of $(H/R_0)\log\tau/\tau_0$ can be neglected (Heng & Kitzmann, 2017). Using the relation of Equation (9) of Heng & Kitzmann (2017), Equation (A.13) is solved as

$$D = \left(\frac{R_0}{R_{\rm s}}\right)^2\left[1+\frac{2H}{R_0}(E_1(\tau_0)+\gamma+\log\tau_0)\right], \tag{A.13}$$

where $E_1(x)$ is the first order exponential integral and $\gamma \approx 0.577$ is the Euler-Mascheroni constant. The asymptotic behavior of the exponential integral for $x \gg 1$ is given by (Gray, 2005)

$$E_{\rm n}(x) = \frac{1}{x\exp(x)}\left[1-\frac{n}{x}+\frac{n(n+1)}{x^2}-\dots\right]. \tag{A.14}$$

It is usually assumed that the solid radius R_0 is corresponding to the radius at which $\tau_0 \gg 1$, and thus one can crudely approximate $E_1(\tau_0) \approx 0$. Therefore, one can write the transit depth as

$$D \approx \left(\frac{R_0}{R_\mathrm{s}}\right)^2 \left[1 + \left(\frac{2H}{R_0}\right)(\gamma + \log\tau_0)\right] = \left(\frac{R_0}{R_\mathrm{s}}\right)^2 \left[1 + \left(\frac{2H}{R_0}\right)\left(\gamma + \log\left(\rho_{\mathrm{g}0}\kappa\sqrt{2\pi R_0 H}\right)\right)\right], \tag{A.15}$$

where $\rho_{\mathrm{g}0} = \rho_\mathrm{g}(R_0)$, and the second term in the bracket stands for the contribution of atmospheric extinction. Since the most terms are independent of observed wavelength, wavelength dependence of transit depth directly provides information on atmospheric opacity. Equation (A.15) demonstrates that the variation of transit depth due to the atmospheric extinction is an order of $R_0 H / R_{\mathrm{s\,p}}^2 H / R_\mathrm{s}^2 \approx$. One can also find that the variation logarithmically increases with increasing the atmospheric opacity.

Acknowledgements

First, I would like to show the deepest gratitude to my supervisor, Prof. Satoshi Okuzumi. He gave all what I need for scientific activity, such as how to face to physics, how to give a presentation, how to write a paper. I could not carry out the research projects of this thesis without his continuous supports for 6 years. He generously advised not only on scientific activity but also on my daily life and mentality. I cannot thank you enough for his throughout supports. I am also grateful to Prof. Xi Zhang, who is effectively a second supervisor in my PhD course. His picky supervision and numerous advises greatly impact on my philosophy to scientific activity. He also kindly helped my visit to UC Santa Cruz, which were very beneficial to me.

I have been supported by many people during the PhD course. I am grateful to Ryo Tazaki for giving insightful comments on the optical properties of aggregates, Tristan Guillot and Kenji Kurosaki for giving helpful comments on interior structure modeling. I thank Shigeru Ida, Taishi Nakamoto, Hideko Nomura, Teruyuki Hirano, Hiroyuki Kurokawa, Yuka Fujii, Keiko Hamano, Takahiro Ueda, Yuhito Shibaike, Seongjoong Kim, Chen-en Wei, Ayano Nakajima, Ayaka Okuya, and Ayumu Kuwahara for enlightening comments at the planetary seminar, student seminar, and others. In particular, I would like to appreciate Sota Arakawa who always had an insightful idea and inspired me. I could not work so hard without him. I also have to thank Shigeru Ida whose lecture determined my direction to this field when I was an undergrad student. I thank Yui Kawashima, Peter Gao, Chuhong Mai, Ehsan Gharib-Nezhad, Yuki Tanaka, Tetsuo Taki for encouragements. I am also greatful to Shoji Mori, Haruka Sakuraba, Kazuaki Homma, Kosuke Seki, Takayuki Matsuura, and Yuto Nara for fantastic daily life at the Okuzumi laboratory, I would like to thank all of you again.

Most importantly, I would like to thank my parents for their continuous supports since I was born in this planet.

REFERENCES

Ackerman, A. S., & Marley, M. S. 2001, ApJ, 556, 872, doi: 10.1086/321540
Adachi, I., Hayashi, C., & Nakazawa, K. 1976, Progress of Theoretical Physics, 56, 1756, doi: 10.1143/PTP.56.1756
Adams, D., Gao, P., de Pater, I., & Morley, C. V. 2019, ApJ, 874, 61, doi: 10.3847/1538-4357/ab074c
Adams, E. R., Seager, S., & Elkins-Tanton, L. 2008a, ApJ, 673, 1160, doi: 10.1086/524925
Adams, F. C., Laughlin, G., & Bloch, A. M. 2008b, ApJ, 683, 1117, doi: 10.1086/589986
Agúndez, M., Parmentier, V., Venot, O., Hersant, F., & Selsis, F. 2014, A&A, 564, A73, doi: 10.1051/0004-6361/201322895
Alibert, Y., Baraffe, I., Benz, W., et al. 2006, A&A, 455, L25, doi: 10.1051/0004-6361:20065697
Alonso, R., Barbieri, M., Rabus, M., et al. 2008, A&A, 487, L5, doi: 10.1051/0004-6361:200810007
Andrews, S. M., Wilner, D. J., Hughes, A. M., Qi, C., & Dullemond, C. P. 2009, ApJ, 700, 1502, doi: 10.1088/0004-637X/700/2/1502
Angerhausen, D., DeLarme, E., & Morse, J. A. 2015, PASP, 127, 1113, doi: 10.1086/683797
Ansdell, M., Williams, J. P., van der Marel, N., et al. 2016, ApJ, 828, 46, doi: 10.3847/0004-637X/828/1/46
Arakawa, S., & Nakamoto, T. 2016, ApJ, 832, L19, doi: 10.3847/2041-8205/832/2/L19
Arakawa, S., Takemoto, M., & Nakamoto, T. 2019, arXiv e-prints, arXiv:1908.03125. https://arxiv.org/abs/1908.03125
Armstrong, D. J., de Mooij, E., Barstow, J., et al. 2016, Nature Astronomy, 1, 0004, doi: 10.1038/s41550-016-0004
Asplund, M., Grevesse, N., Sauval, A. J., & Scott, P. 2009, ARA&A, 47, 481, doi: 10.1146/annurev.astro.46.060407.145222
Awiphan, S., Kerins, E., Pichadee, S., et al. 2016, MNRAS, 463, 2574, doi: 10.1093/mnras/stw2148
Baraffe, I., Chabrier, G., Allard, F., & Hauschildt, P. H. 2002, A&A, 382, 563, doi: 10.1051/0004-6361:20011638
Barstow, J. K., Aigrain, S., Irwin, P. G. J., & Sing, D. K. 2017, ApJ, 834, 50, doi: 10.3847/1538-4357/834/1/50
Barth, E. L., & Toon, O. B. 2003, Icarus, 162, 94, doi: 10.1016/S0019-1035(02)00067-2
Batalha, N. E., Mandell, A., Pontoppidan, K., et al. 2017, PASP, 129, 064501, doi: 10.1088/1538-3873/aa65b0
Bean, J. L., Miller-Ricci Kempton, E., & Homeier, D. 2010, Nature, 468, 669, doi: 10.1038/nature09596
Bean, J. L., Désert, J.-M., Kabath, P., et al. 2011, ApJ, 743, 92, doi: 10.1088/0004-637X/743/1/92
Beaulieu, J. P., Kipping, D. M., Batista, V., et al. 2010, MNRAS, 409, 963, doi: 10.1111/j.1365-2966.2010.16516.x
Beaulieu, J. P., Tinetti, G., Kipping, D. M., et al. 2011, ApJ, 731, 16, doi: 10.1088/0004-637X/731/1/16
Benneke, B., & Seager, S. 2013, ApJ, 778, 153, doi: 10.1088/0004-637X/778/2/153
Benneke, B., Knutson, H. A., Lothringer, J., et al. 2019a, Nature Astronomy, 361, doi: 10.1038/s41550-019-0800-5
Benneke, B., Wong, I., Piaulet, C., et al. 2019b, arXiv e-prints, arXiv:1909.04642. https://arxiv.org/abs/1909.04642
Berry, M. V., & Percival, I. C. 1986, Optica Acta, 33, 577, doi: 10.1080/713821987
Berta, Z. K., Charbonneau, D., Désert, J.-M., et al. 2012, ApJ, 747, 35, doi: 10.1088/0004-637X/747/1/35
Bétrémieux, Y., & Kaltenegger, L. 2015, MNRAS, 451, 1268, doi: 10.1093/mnras/stv1078
Bétrémieux, Y., & Swain, M. R. 2017, MNRAS, 467, 2834, doi: 10.1093/mnras/stx257

Biddle, L. I., Pearson, K. A., Crossfield, I. J. M., et al. 2014, MNRAS, 443, 1810, doi: 10.1093/mnras/stu1199
Birnstiel, T., Klahr, H., & Ercolano, B. 2012, A&A, 539, A148, doi: 10.1051/0004-6361/201118136
Bitsch, B., Morbidelli, A., Johansen, A., et al. 2018, A&A, 612, A30, doi: 10.1051/0004-6361/201731931
Bitsch, B., Raymond, S. N., & Izidoro, A. 2019, A&A, 624, A109, doi: 10.1051/0004-6361/201935007
Blecic, J., Harrington, J., & Bowman, M. O. 2016, ApJS, 225, 4, doi: 10.3847/0067-0049/225/1/4
Blum, J., & Münch, M. 1993, Icarus, 106, 151, doi: 10.1006/icar.1993.1163
Blum, J., & Wurm, G. 2000, Icarus, 143, 138, doi: 10.1006/icar.1999.6234
Blum, J., Wurm, G., Kempf, S., & Henning, T. 1996, Icarus, 124, 441, doi: 10.1006/icar.1996.0221
Bohren, C. F., & Huffman, D. R. 1983, Absorption and scattering of light by small particles
Bourrier, V., Ehrenreich, D., King, G., et al. 2017, A&A, 597, A26, doi: 10.1051/0004-6361/201629253
Bourrier, V., Lecavelier des Etangs, A., Ehrenreich, D., Tanaka, Y. A., & Vidotto, A. A. 2016, A&A, 591, A121, doi: 10.1051/0004-6361/201628362
Bourrier, V., Lovis, C., Beust, H., et al. 2018, Nature, 553, 477, doi: 10.1038/nature24677
Brauer, F., Dullemond, C. P., & Henning, T. 2008, A&A, 480, 859, doi: 10.1051/0004-6361:20077759
Brown, T. M. 2001, ApJ, 553, 1006, doi: 10.1086/320950
Burgasser, A. J., Marley, M. S., Ackerman, A. S., et al. 2002, ApJ, 571, L151, doi: 10.1086/341343
Cabane, M., Rannou, P., Chassefiere, E., & Israel, G. 1993, Planet. Space Sci., 41, 257, doi: 10.1016/0032-0633(93)90021-S
Cáceres, C., Ivanov, V. D., Minniti, D., et al. 2009, A&A, 507, 481, doi: 10.1051/0004-6361/200810908
Chabrier, G., Mazevet, S., & Soubiran, F. 2019, ApJ, 872, 51, doi: 10.3847/1538-4357/aaf99f
Chachan, Y., Knutson, H. A., Gao, P., et al. 2019, arXiv e-prints, arXiv:1910.07523. https://arxiv.org/abs/1910.07523
Charbonneau, D., Brown, T. M., Noyes, R. W., & Gilliland, R. L. 2002, ApJ, 568, 377, doi: 10.1086/338770
Charnay, B., Meadows, V., & Leconte, J. 2015a, ApJ, 813, 15, doi: 10.1088/0004-637X/813/1/15
Charnay, B., Meadows, V., Misra, A., Leconte, J., & Arney, G. 2015b, ApJ, 813, L1, doi: 10.1088/2041-8205/813/1/L1
Chatterjee, S., & Ford, E. B. 2015, ApJ, 803, 33, doi: 10.1088/0004-637X/803/1/33
Chatterjee, S., & Tan, J. C. 2014, ApJ, 780, 53, doi: 10.1088/0004-637X/780/1/53
—. 2015, ApJ, 798, L32, doi: 10.1088/2041-8205/798/2/L32
Chen, G., Guenther, E. W., Pallé, E., et al. 2017, A&A, 600, A138, doi: 10.1051/0004-6361/201630228
Cheng, A. F., Summers, M. E., Gladstone, G. R., et al. 2017, Icarus, 290, 112, doi: 10.1016/j.icarus.2017.02.024
Chiang, E., & Laughlin, G. 2013, MNRAS, 431, 3444, doi: 10.1093/mnras/stt424
Chokshi, A., Tielens, A. G. G. M., & Hollenbach, D. 1993, ApJ, 407, 806, doi: 10.1086/172562
Cloutier, R., & Menou, K. 2019, arXiv e-prints, arXiv:1912.02170. https://arxiv.org/abs/1912.02170
Colón, K. D., & Gaidos, E. 2013, ApJ, 776, 49, doi: 10.1088/0004-637X/776/1/49
Cossou, C., Raymond, S. N., Hersant, F., & Pierens, A. 2014, A&A, 569, A56, doi: 10.1051/0004-6361/201424157
Cridland, A. J., Eistrup, C., & van Dishoeck, E. F. 2019a, A&A, 627, A127, doi: 10.1051/0004-6361/201834378
Cridland, A. J., Pudritz, R. E., Birnstiel, T., Cleeves, L. I., & Bergin, E. A. 2017, MNRAS, 469, 3910, doi: 10.1093/mnras/stx1069

Cridland, A. J., van Dishoeck, E. F., Alessi, M., & Pudritz, R. E. 2019b, A&A, 632, A63, doi: 10.1051/0004-6361/201936105
Croll, B., Albert, L., Jayawardhana, R., et al. 2011, ApJ, 736, 78, doi: 10.1088/0004-637X/736/2/78
Crossfield, I. J. M., Barman, T., Hansen, B. M. S., & Howard, A. W. 2013, A&A, 559, A33, doi: 10.1051/0004-6361/201322278
Crossfield, I. J. M., & Kreidberg, L. 2017, AJ, 154, 261, doi: 10.3847/1538-3881/aa9279
Davies, C. N. 1945, Proceedings of the Physical Society, 57, 259, doi: 10.1088/0959-5309/57/4/301
de Mooij, E. J. W., Brogi, M., de Kok, R. J., et al. 2012, A&A, 538, A46, doi: 10.1051/0004-6361/201117205
de Wit, J., & Seager, S. 2013, Science, 342, 1473, doi: 10.1126/science.1245450
Deming, D., Harrington, J., Laughlin, G., et al. 2007, ApJ, 667, L199, doi: 10.1086/522496
Demory, B. O., Gillon, M., Barman, T., et al. 2007, A&A, 475, 1125, doi: 10.1051/0004-6361:20078354
Demory, B.-O., de Wit, J., Lewis, N., et al. 2013a, ApJ, 776, L25, doi: 10.1088/2041-8205/776/2/L25
Demory, B.-O., Torres, G., Neves, V., et al. 2013b, ApJ, 768, 154, doi: 10.1088/0004-637X/768/2/154
Désert, J.-M., Bean, J., Miller-Ricci Kempton, E., et al. 2011, ApJ, 731, L40, doi: 10.1088/2041-8205/731/2/L40
Dominik, C., & Tielens, A. G. G. M. 1995, Philosophical Magazine, Part A, 72, 783, doi: 10.1080/01418619508243800
—. 1997, ApJ, 480, 647, doi: 10.1086/303996
Dragomir, D., Benneke, B., Pearson, K. A., et al. 2015, ApJ, 814, 102, doi: 10.1088/0004-637X/814/2/102
Dragomir, D., Matthews, J. M., Eastman, J. D., et al. 2013, ApJ, 772, L2, doi: 10.1088/2041-8205/772/1/L2
Dressing, C. D., & Charbonneau, D. 2015, ApJ, 807, 45, doi: 10.1088/0004-637X/807/1/45
Edwards, B., Rice, M., Zingales, T., et al. 2019, Experimental Astronomy, 47, 29, doi: 10.1007/s10686-018-9611-4
Ehrenreich, D., Bonfils, X., Lovis, C., et al. 2014, A&A, 570, A89, doi: 10.1051/0004-6361/201423809
Ehrenreich, D., Bourrier, V., Wheatley, P. J., et al. 2015, Nature, 522, 459, doi: 10.1038/nature14501
Elkins-Tanton, L. T., & Seager, S. 2008, ApJ, 685, 1237, doi: 10.1086/591433
Espinoza, N., Rackham, B. V., Jordán, A., et al. 2019, MNRAS, 482, 2065, doi: 10.1093/mnras/sty2691
Estrada, P. R., & Cuzzi, J. N. 2008, ApJ, 682, 515, doi: 10.1086/589685
Ewing, C. T., & Stern, K. H. 1974, The Journal of Physical Chemistry, 78, 1998
Ford, I. J. 1997, Phys. Rev. E, 56, 5615, doi: 10.1103/PhysRevE.56.5615
Fortney, J. J. 2005, MNRAS, 364, 649, doi: 10.1111/j.1365-2966.2005.09587.x
Fortney, J. J., & Hubbard, W. B. 2003, Icarus, 164, 228, doi: 10.1016/S0019-1035(03)00130-1
—. 2004, ApJ, 608, 1039, doi: 10.1086/420765
Fortney, J. J., Lodders, K., Marley, M. S., & Freedman, R. S. 2008, ApJ, 678, 1419, doi: 10.1086/528370
Fortney, J. J., Mordasini, C., Nettelmann, N., et al. 2013, ApJ, 775, 80, doi: 10.1088/0004-637X/775/1/80
Fortney, J. J., Sudarsky, D., Hubeny, I., et al. 2003, ApJ, 589, 615, doi: 10.1086/374387
Fraine, J., Deming, D., Benneke, B., et al. 2014, Nature, 513, 526, doi: 10.1038/nature13785
Fraine, J. D., Deming, D., Gillon, M., et al. 2013, ApJ, 765, 127, doi: 10.1088/0004-637X/765/2/127
Freedman, R. S., Lustig-Yaeger, J., Fortney, J. J., et al. 2014, ApJS, 214, 25, doi: 10.1088/0067-0049/214/2/25

Freedman, R. S., Marley, M. S., & Lodders, K. 2008, ApJS, 174, 504, doi: 10.1086/521793
Fressin, F., Torres, G., Charbonneau, D., et al. 2013, ApJ, 766, 81,
doi: 10.1088/0004-637X/766/2/81
Fukui, A., Narita, N., Kurosaki, K., et al. 2013, ApJ, 770, 95, doi: 10.1088/0004-637X/770/2/95
Fulton, B. J., & Petigura, E. A. 2018, AJ, 156, 264, doi: 10.3847/1538-3881/aae828
Fulton, B. J., Petigura, E. A., Howard, A. W., et al. 2017, AJ, 154, 109,
doi: 10.3847/1538-3881/aa80eb
Gail, H.-P., & Sedlmayr, E. 2013, Physics and Chemistry of Circumstellar Dust Shells
Gamache, R. R., Roller, C., Lopes, E., et al. 2017, Journal of Quantitative Spectroscopy and Radiative
Transfer, 203, 70
Gao, P., & Benneke, B. 2018, ApJ, 863, 165, doi: 10.3847/1538-4357/aad461
Gao, P., Marley, M. S., & Ackerman, A. S. 2018, ApJ, 855, 86, doi: 10.3847/1538-4357/aab0a1
Gao, P., & Zhang, X. 2019, arXiv e-prints, arXiv:2001.00055.
https://arxiv.org/abs/2001.00055
Gao, P., Fan, S., Wong, M. L., et al. 2017a, Icarus, 287, 116, doi: 10.1016/j.icarus.2016.09.030
—. 2017b, Icarus, 287, 116, doi: 10.1016/j.icarus.2016.09.030
Gharib-Nezhad, E., & Line, M. R. 2019, ApJ, 872, 27, doi: 10.3847/1538-4357/aafb7b
Gillon, M., Pont, F., Demory, B. O., et al. 2007a, A&A, 472, L13,
doi: 10.1051/0004-6361:20077799
Gillon, M., Demory, B. O., Barman, T., et al. 2007b, A&A, 471, L51,
doi: 10.1051/0004-6361:20078283
Gillon, M., Demory, B.-O., Madhusudhan, N., et al. 2014, A&A, 563, A21,
doi: 10.1051/0004-6361/201322362
Ginzburg, S., & Sari, R. 2017, MNRAS, 464, 3937, doi: 10.1093/mnras/stw2637
—. 2018, MNRAS, 479, 1986, doi: 10.1093/mnras/sty1466
Ginzburg, S., Schlichting, H. E., & Sari, R. 2016, ApJ, 825, 29, doi: 10.3847/0004-637X/825/1/29
—. 2018, MNRAS, 476, 759, doi: 10.1093/mnras/sty290
Goldreich, P., & Ward, W. R. 1973, ApJ, 183, 1051, doi: 10.1086/152291
Gray, D. F. 2005, The Observation and Analysis of Stellar Photospheres
Greene, T. P., Line, M. R., Montero, C., et al. 2016, ApJ, 817, 17, doi: 10.3847/0004-637X/817/1/17
Guillot, T. 2005, Annual Review of Earth and Planetary Sciences, 33, 493,
doi: 10.1146/annurev.earth.32.101802.120325
—. 2010, A&A, 520, A27, doi: 10.1051/0004-6361/200913396
Guillot, T., Ida, S., & Ormel, C. W. 2014, A&A, 572, A72, doi: 10.1051/0004-6361/201323021
Gupta, A., & Schlichting, H. E. 2019, MNRAS, 487, 24, doi: 10.1093/mnras/stz1230
Hansen, B. M. S., & Murray, N. 2012, ApJ, 751, 158, doi: 10.1088/0004-637X/751/2/158
Hansen, J. E. 1971, Journal of Atmospheric Sciences, 28, 1400,
doi: 10.1175/1520-0469(1971)028<1400:MSOPLI>2.0.CO;2
Hayashi, C. 1981, Progress of Theoretical Physics Supplement, 70, 35, doi: 10.1143/PTPS.70.35
Heim, L.-O., Blum, J., Preuss, M., & Butt, H.-J. 1999, Physical Review Letters, 83, 3328,
doi: 10.1103/PhysRevLett.83.3328
Helling, C., & Fomins, A. 2013, Philosophical Transactions of the Royal Society of London Series A,
371, 20110581, doi: 10.1098/rsta.2011.0581
Helling, C., Jardine, M., & Mokler, F. 2011a, ApJ, 737, 38, doi: 10.1088/0004-637X/737/1/38
Helling, C., Jardine, M., Witte, S., & Diver, D. A. 2011b, ApJ, 727, 4,
doi: 10.1088/0004-637X/727/1/4
Helling, C., Tootill, D., Woitke, P., & Lee, G. 2017, A&A, 603, A123,
doi: 10.1051/0004-6361/201629696
Helling, C., Woitke, P., Rimmer, P. B., et al. 2014, Life, 4, 142, doi: 10.3390/life4020142
Helling, C., Woitke, P., & Thi, W.-F. 2008, A&A, 485, 547, doi: 10.1051/0004-6361:20078220

Helling, C., Iro, N., Corrales, L., et al. 2019, arXiv e-prints, arXiv:1906.08127. https://arxiv.org/abs/1906.08127
Heng, K., Hayek, W., Pont, F., & Sing, D. K. 2012, MNRAS, 420, 20, doi: 10.1111/j.1365-2966.2011.19943.x
Heng, K., & Kitzmann, D. 2017, MNRAS, 470, 2972, doi: 10.1093/mnras/stx1453
Herbert, F., & Sandel, B. R. 1991, J. Geophys. Res., 96, 19, doi: 10.1029/91JA01821
Homma, K. A., Okuzumi, S., Nakamoto, T., & Ueda, Y. 2019, ApJ, 877, 128, doi: 10.3847/1538-4357/ab1de0
Hori, Y., & Ikoma, M. 2010, ApJ, 714, 1343, doi: 10.1088/0004-637X/714/2/1343
—. 2011, MNRAS, 416, 1419, doi: 10.1111/j.1365-2966.2011.19140.x
Howard, A. W., Marcy, G. W., Bryson, S. T., et al. 2012, ApJS, 201, 15, doi: 10.1088/0067-0049/201/2/15
Howe, A. R., & Burrows, A. S. 2012, ApJ, 756, 176, doi: 10.1088/0004-637X/756/2/176
Hubbard, W. B., & Macfarlane, J. J. 1980, J. Geophys. Res., 85, 225, doi: 10.1029/JB085iB01p00225
Husser, T. O., Wende-von Berg, S., Dreizler, S., et al. 2013, A&A, 553, A6, doi: 10.1051/0004-6361/201219058
Hyodo, R., Ida, S., & Charnoz, S. 2019, A&A, 629, A90, doi: 10.1051/0004-6361/201935935
Ida, S., & Lin, D. N. C. 2004, ApJ, 604, 388, doi: 10.1086/381724
Ida, S., Yamamura, T., & Okuzumi, S. 2019, A&A, 624, A28, doi: 10.1051/0004-6361/201834556
Ikoma, M., & Hori, Y. 2012, ApJ, 753, 66, doi: 10.1088/0004-637X/753/1/66
Ikoma, M., Nakazawa, K., & Emori, H. 2000, ApJ, 537, 1013, doi: 10.1086/309050
Izidoro, A., Bitsch, B., Raymond, S. N., et al. 2019, arXiv e-prints, arXiv:1902.08772. https://arxiv.org/abs/1902.08772
Izidoro, A., Ogihara, M., Raymond, S. N., et al. 2017, MNRAS, 470, 1750, doi: 10.1093/mnras/stx1232
Jacobson, M. Z. 2005, Fundamentals of Atmospheric Modeling, 828
Jankovic, M. R., Owen, J. E., & Mohanty, S. 2019, MNRAS, 484, 2296, doi: 10.1093/mnras/stz004
Johansen, A., & Lambrechts, M. 2017, Annual Review of Earth and Planetary Sciences, 45, 359, doi: 10.1146/annurev-earth-063016-020226
Johansen, A., Oishi, J. S., Mac Low, M.-M., et al. 2007, Nature, 448, 1022, doi: 10.1038/nature06086
Jordán, A., & Espinoza, N. 2018, Research Notes of the American Astronomical Society, 2, 149, doi: 10.3847/2515-5172/aada13
Kataoka, A., Okuzumi, S., Tanaka, H., & Nomura, H. 2014, A&A, 568, A42, doi: 10.1051/0004-6361/201323199
Kataoka, A., Tanaka, H., Okuzumi, S., & Wada, K. 2013a, A&A, 554, A4, doi: 10.1051/0004-6361/201321325
—. 2013b, A&A, 557, L4, doi: 10.1051/0004-6361/201322151
Kataria, T., Showman, A. P., Lewis, N. K., et al. 2013, ApJ, 767, 76, doi: 10.1088/0004-637X/767/1/76
Kawashima, Y., & Ikoma, M. 2018, ApJ, 853, 7, doi: 10.3847/1538-4357/aaa0c5
—. 2019, ApJ, 877, 109, doi: 10.3847/1538-4357/ab1b1d
Kimura, Y., Tanaka, K. K., Miura, H., & Tsukamoto, K. 2012, Crystal Growth & Design, 12, 3278
Kitzmann, D., & Heng, K. 2018, MNRAS, 475, 94, doi: 10.1093/mnras/stx3141
Knutson, H. A., Benneke, B., Deming, D., & Homeier, D. 2014a, Nature, 505, 66, doi: 10.1038/nature12887
Knutson, H. A., Madhusudhan, N., Cowan, N. B., et al. 2011, ApJ, 735, 27, doi: 10.1088/0004-637X/735/1/27
Knutson, H. A., Dragomir, D., Kreidberg, L., et al. 2014b, ApJ, 794, 155, doi: 10.1088/0004-637X/794/2/155
Kokubo, E., & Ida, S. 1996, Icarus, 123, 180, doi: 10.1006/icar.1996.0148

—. 1998, Icarus, 131, 171, doi: 10.1006/icar.1997.5840
—. 2000, Icarus, 143, 15, doi: 10.1006/icar.1999.6237
Komacek, T. D., Showman, A. P., & Parmentier, V. 2019, arXiv e-prints. https://arxiv.org/abs/1904.09676
Kominami, J., & Ida, S. 2002, Icarus, 157, 43, doi: 10.1006/icar.2001.6811
Krasnopolsky, V. A., Sandel, B. R., & Herbert, F. 1992, J. Geophys. Res., 97, 11, doi: 10.1029/92JE00945
Kreidberg, L. 2018, Exoplanet Atmosphere Measurements from Transmission Spectroscopy and Other Planet Star Combined Light Observations, 100
Kreidberg, L., Line, M. R., Thorngren, D., Morley, C. V., & Stevenson, K. B. 2018, ApJ, 858, L6, doi: 10.3847/2041-8213/aabfce
Kreidberg, L., Bean, J. L., Désert, J.-M., et al. 2014, Nature, 505, 69, doi: 10.1038/nature12888
Kreidberg, L., Line, M. R., Bean, J. L., et al. 2015, ApJ, 814, 66, doi: 10.1088/0004-637X/814/1/66
Krijt, S., Ciesla, F. J., & Bergin, E. A. 2016, ApJ, 833, 285, doi: 10.3847/1538-4357/833/2/285
Kuntz, M. 1997, J. Quant. Spec. Radiat. Transf., 57, 819, doi: 10.1016/S0022-4073(96)00162-8
Kurokawa, H., & Inutsuka, S.-i. 2015, ApJ, 815, 78, doi: 10.1088/0004-637X/815/1/78
Kurokawa, H., & Nakamoto, T. 2014, ApJ, 783, 54, doi: 10.1088/0004-637X/783/1/54
Kurokawa, H., & Tanigawa, T. 2018, MNRAS, 479, 635, doi: 10.1093/mnras/sty1498
Kurosaki, K., & Ikoma, M. 2017, AJ, 153, 260, doi: 10.3847/1538-3881/aa6faf
Kurosaki, K., Ikoma, M., & Hori, Y. 2014, A&A, 562, A80, doi: 10.1051/0004-6361/201322258
Kuwahara, A., Kurokawa, H., & Ida, S. 2019, A&A, 623, A179, doi: 10.1051/0004-6361/201833997
Lambrechts, M., & Johansen, A. 2012, A&A, 544, A32, doi: 10.1051/0004-6361/201219127
—. 2014, A&A, 572, A107, doi: 10.1051/0004-6361/201424343
Lambrechts, M., Johansen, A., & Morbidelli, A. 2014, A&A, 572, A35, doi: 10.1051/0004-6361/201423814
Lambrechts, M., & Lega, E. 2017, A&A, 606, A146, doi: 10.1051/0004-6361/201731014
Lambrechts, M., Morbidelli, A., Jacobson, S. A., et al. 2019, A&A, 627, A83, doi: 10.1051/0004-6361/201834229
Langton, J., & Laughlin, G. 2008, ApJ, 674, 1106, doi: 10.1086/523957
Lanotte, A. A., Gillon, M., Demory, B. O., et al. 2014, A&A, 572, A73, doi: 10.1051/0004-6361/201424373
Lavvas, P., Koskinen, T., Steinrueck, M., García Muñoz, A., & Showman, A. P. 2019, arXiv e-prints. https://arxiv.org/abs/1905.02976
Lavvas, P., Sander, M., Kraft, M., & Imanaka, H. 2011, ApJ, 728, 80, doi: 10.1088/0004-637X/728/2/80
Lavvas, P., Yelle, R. V., & Griffith, C. A. 2010, Icarus, 210, 832, doi: 10.1016/j.icarus.2010.07.025
Lecavelier Des Etangs, A., Pont, F., Vidal-Madjar, A., & Sing, D. 2008, A&A, 481, L83, doi: 10.1051/0004-6361:200809388
Lee, E. J. 2019, ApJ, 878, 36, doi: 10.3847/1538-4357/ab1b40
Lee, E. J., & Chiang, E. 2015, ApJ, 811, 41, doi: 10.1088/0004-637X/811/1/41
—. 2016, ApJ, 817, 90, doi: 10.3847/0004-637X/817/2/90
Lee, E. J., Chiang, E., & Ormel, C. W. 2014, ApJ, 797, 95, doi: 10.1088/0004-637X/797/2/95
Lee, G., Dobbs-Dixon, I., Helling, C., Bognar, K., & Woitke, P. 2016, A&A, 594, A48, doi: 10.1051/0004-6361/201628606
Lee, G., Helling, C., Giles, H., & Bromley, S. T. 2015, A&A, 575, A11, doi: 10.1051/0004-6361/201424621
Lee, G. K. H., Blecic, J., & Helling, C. 2018, A&A, 614, A126, doi: 10.1051/0004-6361/201731977
Lewis, N. K., Parmentier, V., Kataria, T., et al. 2017, arXiv e-prints, arXiv:1706.00466. https://arxiv.org/abs/1706.00466

Libby-Roberts, J. E., Berta-Thompson, Z. K., Desert, J.-M., et al. 2019, arXiv e-prints, arXiv:1910.12988. https://arxiv.org/abs/1910.12988
Line, M. R., & Parmentier, V. 2016, ApJ, 820, 78, doi: 10.3847/0004-637X/820/1/78
Line, M. R., Wolf, A. S., Zhang, X., et al. 2013, ApJ, 775, 137, doi: 10.1088/0004-637X/775/2/137
Lines, S., Mayne, N. J., Manners, J., et al. 2019, MNRAS, 488, 1332, doi: 10.1093/mnras/stz1788
Lines, S., Mayne, N. J., Boutle, I. A., et al. 2018, A&A, 615, A97, doi: 10.1051/0004-6361/201732278
Liou, K. 2002, An Introduction to Atmospheric Radiation, ISSN (Elsevier Science). https://books.google.co.jp/books?id=mQ1DiDpX34UC
Lissauer, J. J., Ragozzine, D., Fabrycky, D. C., et al. 2011, ApJS, 197, 8, doi: 10.1088/0067-0049/197/1/8
Liu, B., Lambrechts, M., Johansen, A., & Liu, F. 2019, A&A, 632, A7, doi: 10.1051/0004-6361/201936309
Lodders, K. 2003, ApJ, 591, 1220, doi: 10.1086/375492
Lopez, E. D., & Fortney, J. J. 2014, ApJ, 792, 1, doi: 10.1088/0004-637X/792/1/1
Lothringer, J. D., Benneke, B., Crossfield, I. J. M., et al. 2018, AJ, 155, 66, doi: 10.3847/1538-3881/aaa008
MacDonald, R. J., & Madhusudhan, N. 2017, MNRAS, 469, 1979, doi: 10.1093/mnras/stx804
MacDonald, R. J., Marley, M. S., Fortney, J. J., & Lewis, N. K. 2018, ApJ, 858, 69, doi: 10.3847/1538-4357/aabb05
Madhusudhan, N., Amin, M. A., & Kennedy, G. M. 2014, ApJ, 794, L12, doi: 10.1088/2041-8205/794/1/L12
Madhusudhan, N., Bitsch, B., Johansen, A., & Eriksson, L. 2017, MNRAS, 469, 4102, doi: 10.1093/mnras/stx1139
Mai, C., & Line, M. R. 2019, ApJ, 883, 144, doi: 10.3847/1538-4357/ab3e6d
Manara, C. F., Morbidelli, A., & Guillot, T. 2018, A&A, 618, L3, doi: 10.1051/0004-6361/201834076
Mansfield, M., Bean, J. L., Oklopčić, A., et al. 2018, ApJ, 868, L34, doi: 10.3847/2041-8213/aaf166
Marley, M. S., Ackerman, A. S., Cuzzi, J. N., & Kitzmann, D. 2013, Clouds and Hazes in Exoplanet Atmospheres, ed. S. J. Mackwell, A. A. Simon-Miller, J. W. Harder, & M. A. Bullock, 367–391
Masuda, K. 2014, ApJ, 783, 53, doi: 10.1088/0004-637X/783/1/53
Mayor, M., & Queloz, D. 1995, Nature, 378, 355, doi: 10.1038/378355a0
Mayor, M., Marmier, M., Lovis, C., et al. 2011, arXiv e-prints, arXiv:1109.2497. https://arxiv.org/abs/1109.2497
Mazevet, S., Licari, A., Chabrier, G., & Potekhin, A. Y. 2019, A&A, 621, A128, doi: 10.1051/0004-6361/201833963
Mbarek, R., & Kempton, E. M. R. 2016, ApJ, 827, 121, doi: 10.3847/0004-637X/827/2/121
McCullough, P. R., Crouzet, N., Deming, D., & Madhusudhan, N. 2014, ApJ, 791, 55, doi: 10.1088/0004-637X/791/1/55
Meakin, P. 1991, Reviews of Geophysics, 29, 317, doi: 10.1029/91RG00688
Miguel, Y., Guillot, T., & Fayon, L. 2016, A&A, 596, A114, doi: 10.1051/0004-6361/201629732
Miller-Ricci, E., & Fortney, J. J. 2010, ApJ, 716, L74, doi: 10.1088/2041-8205/716/1/L74
Miller-Ricci, E., Seager, S., & Sasselov, D. 2009, ApJ, 690, 1056, doi: 10.1088/0004-637X/690/2/1056
Miller-Ricci Kempton, E., Zahnle, K., & Fortney, J. J. 2012, ApJ, 745, 3, doi: 10.1088/0004-637X/745/1/3
Millholland, S. 2019, ApJ, 886, 72, doi: 10.3847/1538-4357/ab4c3f
Millholland, S., & Laughlin, G. 2019, Nature Astronomy, 3, 424, doi: 10.1038/s41550-019-0701-7
Minato, T., Köhler, M., Kimura, H., Mann, I., & Yamamoto, T. 2006, A&A, 452, 701, doi: 10.1051/0004-6361:20054774
Mizuno, H. 1980, Progress of Theoretical Physics, 64, 544, doi: 10.1143/PTP.64.544

Mollière, P., Wardenier, J. P., van Boekel, R., et al. 2019, A&A, 627, A67, doi: 10.1051/0004-6361/201935470
Morbidelli, A., & Raymond, S. N. 2016, Journal of Geophysical Research (Planets), 121, 1962, doi: 10.1002/2016JE005088
Mordasini, C., van Boekel, R., Mollière, P., Henning, T., & Benneke, B. 2016, ApJ, 832, 41, doi: 10.3847/0004-637X/832/1/41
Morello, G., Waldmann, I. P., Tinetti, G., et al. 2015, ApJ, 802, 117, doi: 10.1088/0004-637X/802/2/117
Moriarty, J., & Fischer, D. 2015, ApJ, 809, 94, doi: 10.1088/0004-637X/809/1/94
Morley, C. V., Fortney, J. J., Kempton, E. M.-R., et al. 2013, ApJ, 775, 33, doi: 10.1088/0004-637X/775/1/33
Morley, C. V., Fortney, J. J., Marley, M. S., et al. 2012, ApJ, 756, 172, doi: 10.1088/0004-637X/756/2/172
—. 2015, ApJ, 815, 110, doi: 10.1088/0004-637X/815/2/110
Morley, C. V., Knutson, H., Line, M., et al. 2017, AJ, 153, 86, doi: 10.3847/1538-3881/153/2/86
Movshovitz, N., Bodenheimer, P., Podolak, M., & Lissauer, J. J. 2010, Icarus, 209, 616, doi: 10.1016/j.icarus.2010.06.009
Murgas, F., Pallé, E., Cabrera-Lavers, A., et al. 2012, A&A, 544, A41, doi: 10.1051/0004-6361/201219380
Narita, N., Nagayama, T., Suenaga, T., et al. 2013a, PASJ, 65, 27, doi: 10.1093/pasj/65.2.27
Narita, N., Fukui, A., Ikoma, M., et al. 2013b, ApJ, 773, 144, doi: 10.1088/0004-637X/773/2/144
Nascimbeni, V., Piotto, G., Pagano, I., et al. 2013, A&A, 559, A32, doi: 10.1051/0004-6361/201321971
Nikolov, N., Sing, D. K., Pont, F., et al. 2014, MNRAS, 437, 46, doi: 10.1093/mnras/stt1859
Nikolov, N., Sing, D. K., Burrows, A. S., et al. 2015, MNRAS, 447, 463, doi: 10.1093/mnras/stu2433
Öberg, K. I., Murray-Clay, R., & Bergin, E. A. 2011, ApJ, 743, L16, doi: 10.1088/2041-8205/743/1/L16
Ogihara, M., & Hori, Y. 2018, ApJ, 867, 127, doi: 10.3847/1538-4357/aae534
Ogihara, M., Kokubo, E., Suzuki, T. K., & Morbidelli, A. 2018, A&A, 615, A63, doi: 10.1051/0004-6361/201832720
Ogihara, M., Morbidelli, A., & Guillot, T. 2015, A&A, 578, A36, doi: 10.1051/0004-6361/201525884
Ohno, K., & Okuzumi, S. 2017, ApJ, 835, 261, doi: 10.3847/1538-4357/835/2/261
—. 2018, ApJ, 859, 34, doi: 10.3847/1538-4357/aabee3
Ohno, K., Okuzumi, S., & Tazaki, R. 2019, arXiv e-prints, arXiv:1908.02201. https://arxiv.org/abs/1908.02201
Ohno, K., & Zhang, X. 2019a, ApJ, 874, 1, doi: 10.3847/1538-4357/ab06cc
—. 2019b, ApJ, 874, 2, doi: 10.3847/1538-4357/ab06ca
Oka, A., Nakamoto, T., & Ida, S. 2011, ApJ, 738, 141, doi: 10.1088/0004-637X/738/2/141
Okuzumi, S. 2009, ApJ, 698, 1122, doi: 10.1088/0004-637X/698/2/1122
Okuzumi, S., Momose, M., Sirono, S.-i., Kobayashi, H., & Tanaka, H. 2016, ApJ, 821, 82, doi: 10.3847/0004-637X/821/2/82
Okuzumi, S., Tanaka, H., Kobayashi, H., & Wada, K. 2012, ApJ, 752, 106, doi: 10.1088/0004-637X/752/2/106
Okuzumi, S., Tanaka, H., & Sakagami, M.-a. 2009, ApJ, 707, 1247, doi: 10.1088/0004-637X/707/2/1247
Okuzumi, S., & Tazaki, R. 2019, ApJ, 878, 132, doi: 10.3847/1538-4357/ab204d
Onischuk, A., di Stasio, S., Karasev, V., et al. 2003, Journal of Aerosol Science, 34, 383 , doi: https://doi.org/10.1016/S0021-8502(02)00215-X
Ormel, C. W. 2014, ApJ, 789, L18, doi: 10.1088/2041-8205/789/1/L18

Ormel, C. W., & Klahr, H. H. 2010, A&A, 520, A43, doi: 10.1051/0004-6361/201014903
Ormel, C. W., & Min, M. 2019, A&A, 622, A121, doi: 10.1051/0004-6361/201833678
Ormel, C. W., Shi, J.-M., & Kuiper, R. 2015, MNRAS, 447, 3512, doi: 10.1093/mnras/stu2704
Ormel, C. W., & Spaans, M. 2008, ApJ, 684, 1291, doi: 10.1086/590052
Otegi, J. F., Bouchy, F., & Helled, R. 2019, arXiv e-prints, arXiv:1911.04745. https://arxiv.org/abs/1911.04745
Owen, J. E., & Adams, F. C. 2019, MNRAS, 490, 15, doi: 10.1093/mnras/stz2601
Owen, J. E., & Wu, Y. 2013, ApJ, 775, 105, doi: 10.1088/0004-637X/775/2/105
—. 2016, ApJ, 817, 107, doi: 10.3847/0004-637X/817/2/107
—. 2017, ApJ, 847, 29, doi: 10.3847/1538-4357/aa890a
Paardekooper, S. J., Baruteau, C., Crida, A., & Kley, W. 2010, MNRAS, 401, 1950, doi: 10.1111/j.1365-2966.2009.15782.x
Palik, E. D. 1985, Handbook of optical constants of solids
Parmentier, V., & Crossfield, I. J. M. 2018, Exoplanet Phase Curves: Observations and Theory, 116
Parmentier, V., Showman, A. P., & Lian, Y. 2013, A&A, 558, A91, doi: 10.1051/0004-6361/201321132
Pascucci, I., Testi, L., Herczeg, G. J., et al. 2016, ApJ, 831, 125, doi: 10.3847/0004-637X/831/2/125
Paszun, D., & Dominik, C. 2006, Icarus, 182, 274, doi: 10.1016/j.icarus.2005.12.018
—. 2009, A&A, 507, 1023, doi: 10.1051/0004-6361/200810682
Petigura, E. A., Howard, A. W., & Marcy, G. W. 2013, Proceedings of the National Academy of Science, 110, 19273, doi: 10.1073/pnas.1319909110
Petigura, E. A., Howard, A. W., Marcy, G. W., et al. 2017, AJ, 154, 107, doi: 10.3847/1538-3881/aa80de
Plane, J. M. C. 2012, Chem. Soc. Rev., 41, 6507
Pollack, J. B., Hubickyj, O., Bodenheimer, P., et al. 1996, Icarus, 124, 62, doi: 10.1006/icar.1996.0190
Pont, F., Gilliland, R. L., Knutson, H., Holman, M., & Charbonneau, D. 2009, MNRAS, 393, L6, doi: 10.1111/j.1745-3933.2008.00582.x
Pont, F., Knutson, H., Gilliland, R. L., Moutou, C., & Charbonneau, D. 2008, MNRAS, 385, 109, doi: 10.1111/j.1365-2966.2008.12852.x
Pont, F., Sing, D. K., Gibson, N. P., et al. 2013, MNRAS, 432, 2917, doi: 10.1093/mnras/stt651
Powell, D., Zhang, X., Gao, P., & Parmentier, V. 2018, ApJ, 860, 18, doi: 10.3847/1538-4357/aac215
Pruppacher, H., & Klett, J. 1996, Microphysics of Clouds and Precipitation, Atmospheric and Oceanographic Sciences Library (Springer Netherlands). https://books.google.co.jp/books?id=1mXN_qZ5sNUC
Rackham, B., Espinoza, N., Apai, D., et al. 2017, ApJ, 834, 151, doi: 10.3847/1538-4357/aa4f6c
Rackham, B. V., Apai, D., & Giampapa, M. S. 2018, ApJ, 853, 122, doi: 10.3847/1538-4357/aaa08c
Rafikov, R. R. 2006, ApJ, 648, 666, doi: 10.1086/505695
Rannou, P., Cabane, M., Botet, R., & Chassefière, E. 1997, J. Geophys. Res., 102, 10997, doi: 10.1029/97JE00719
Redfield, S., Endl, M., Cochran, W. D., & Koesterke, L. 2008, ApJ, 673, L87, doi: 10.1086/527475
Rein, H. 2012, MNRAS, 427, L21, doi: 10.1111/j.1745-3933.2012.01337.x
Ribas, Á., Bouy, H., & Merín, B. 2015, A&A, 576, A52, doi: 10.1051/0004-6361/201424846
Rodrigues, P. C. R., & Silva Fernandes, F. M. S. 2007, The Journal of Chemical Physics, 126, 024503
Rogers, L. A. 2015, ApJ, 801, 41, doi: 10.1088/0004-637X/801/1/41
Rogers, L. A., Bodenheimer, P., Lissauer, J. J., & Seager, S. 2011, ApJ, 738, 59, doi: 10.1088/0004-637X/738/1/59
Rogers, L. A., & Seager, S. 2010, ApJ, 716, 1208, doi: 10.1088/0004-637X/716/2/1208
Roman, M., & Rauscher, E. 2019, ApJ, 872, 1, doi: 10.3847/1538-4357/aafdb5
Rossow, W. B. 1978, Icarus, 36, 1, doi: 10.1016/0019-1035(78)90072-6

Rothman, L. S., Rinsland, C. P., Goldman, A., et al. 1998, J. Quant. Spec. Radiat. Transf., 60, 665, doi: 10.1016/S0022-4073(98)00078-8
Ruyten, W. 2004, J. Quant. Spec. Radiat. Transf., 86, 231, doi: 10.1016/j.jqsrt.2003.12.027
Salz, M., Schneider, P. C., Czesla, S., & Schmitt, J. H. M. M. 2016, A&A, 585, L2, doi: 10.1051/0004-6361/201527042
Sánchez-Lavega, A., Pérez-Hoyos, S., & Hueso, R. 2004, American Journal of Physics, 72, 767
Sanchis, E., Testi, L., Natta, A., et al. 2019, arXiv e-prints, arXiv:1911.06005. https://arxiv.org/abs/1911.06005
Sato, T., Okuzumi, S., & Ida, S. 2016, A&A, 589, A15, doi: 10.1051/0004-6361/201527069
Saumon, D., Chabrier, G., & van Horn, H. M. 1995, ApJS, 99, 713, doi: 10.1086/192204
Saumon, D., & Marley, M. S. 2008, ApJ, 689, 1327, doi: 10.1086/592734
Schoenberg Ferrier, B. 1994, Journal of Atmospheric Sciences, 51, 249, doi: 10.1175/1520-0469(1994)051<0249:ADMMPF>2.0.CO;2
Schoonenberg, D., & Ormel, C. W. 2017, A&A, 602, A21, doi: 10.1051/0004-6361/201630013
Seager, S., Kuchner, M., Hier-Majumder, C. A., & Militzer, B. 2007, ApJ, 669, 1279, doi: 10.1086/521346
Seager, S., & Sasselov, D. D. 2000, ApJ, 537, 916, doi: 10.1086/309088
Sedaghati, E., Boffin, H. M. J., MacDonald, R. J., et al. 2017, Nature, 549, 238, doi: 10.1038/nature23651
Seinfeld, J., & Pandis, S. 2012, Atmospheric Chemistry and Physics: From Air Pollution to Climate Change (Wiley). https://books.google.co.jp/books?id=YH2K9eWsZOcC
Sharp, C. M., & Burrows, A. 2007, ApJS, 168, 140, doi: 10.1086/508708
Showman, A. P., & Guillot, T. 2002, A&A, 385, 166, doi: 10.1051/0004-6361:20020101
Shporer, A., & Hu, R. 2015, AJ, 150, 112, doi: 10.1088/0004-6256/150/4/112
Shporer, A., Mazeh, T., Pont, F., et al. 2009, ApJ, 694, 1559, doi: 10.1088/0004-637X/694/2/1559
Sing, D. K., Vidal-Madjar, A., Désert, J. M., Lecavelier des Etangs, A., & Ballester, G. 2008, ApJ, 686, 658, doi: 10.1086/590075
Sing, D. K., Wakeford, H. R., Showman, A. P., et al. 2015, MNRAS, 446, 2428, doi: 10.1093/mnras/stu2279
Sing, D. K., Fortney, J. J., Nikolov, N., et al. 2016, Nature, 529, 59, doi: 10.1038/nature16068
Spake, J. J., Sing, D. K., Evans, T. M., et al. 2018, Nature, 557, 68, doi: 10.1038/s41586-018-0067-5
Spake, J. J., Sing, D. K., Wakeford, H. R., et al. 2019, arXiv e-prints, arXiv:1911.08859. https://arxiv.org/abs/1911.08859
Stevenson, D. J. 1982, Planet. Space Sci., 30, 755, doi: 10.1016/0032-0633(82)90108-8
Stevenson, K. B., Harrington, J., Nymeyer, S., et al. 2010, Nature, 464, 1161, doi: 10.1038/nature09013
Straka, J. M., & Mansell, E. R. 2005, Journal of Applied Meteorology, 44, 445
Suyama, T., Wada, K., & Tanaka, H. 2008, ApJ, 684, 1310, doi: 10.1086/590143
Suyama, T., Wada, K., Tanaka, H., & Okuzumi, S. 2012, ApJ, 753, 115, doi: 10.1088/0004-637X/753/2/115
Suzuki, T. K., Ogihara, M., Morbidelli, A. r., Crida, A., & Guillot, T. 2016, A&A, 596, A74, doi: 10.1051/0004-6361/201628955
Swain, M. R., Vasisht, G., & Tinetti, G. 2008, Nature, 452, 329, doi: 10.1038/nature06823
Tanaka, H., & Ida, S. 1999, Icarus, 139, 350, doi: 10.1006/icar.1999.6107
Tanaka, K. K., Tanaka, H., Yamamoto, T., & Kawamura, K. 2011, J. Chem. Phys., 134, 204313, doi: 10.1063/1.3593459
Tazaki, R., & Tanaka, H. 2018, ApJ, 860, 79, doi: 10.3847/1538-4357/aac32d
Tazaki, R., Tanaka, H., Okuzumi, S., Kataoka, A., & Nomura, H. 2016, ApJ, 823, 70, doi: 10.3847/0004-637X/823/2/70
Tennyson, J., & Yurchenko, S. 2018, Atoms, 6, 26, doi: 10.3390/atoms6020026
Terquem, C., & Papaloizou, J. C. B. 2007, ApJ, 654, 1110, doi: 10.1086/509497

Thomas, S. W., & Madhusudhan, N. 2016, MNRAS, 458, 1330, doi: 10.1093/mnras/stw321
Thorngren, D., Gao, P., & Fortney, J. J. 2019, ApJ, 884, L6, doi: 10.3847/2041-8213/ab43d0
Thorngren, D. P., Fortney, J. J., Murray-Clay, R. A., & Lopez, E. D. 2016, ApJ, 831, 64, doi: 10.3847/0004-637X/831/1/64
Tinetti, G., Vidal-Madjar, A., Liang, M.-C., et al. 2007, Nature, 448, 169, doi: 10.1038/nature06002
Tinetti, G., Drossart, P., Eccleston, P., et al. 2016, in Proc. SPIE, Vol. 9904, Space Telescopes and Instrumentation 2016: Optical, Infrared, and Millimeter Wave, 99041X
Tinetti, G., Drossart, P., Eccleston, P., et al. 2018, Experimental Astronomy, 46, 135, doi: 10.1007/s10686-018-9598-x
Tsai, S.-M., Kitzmann, D., Lyons, J. R., et al. 2018, ApJ, 862, 31, doi: 10.3847/1538-4357/aac834
Tsiaras, A., Waldmann, I. P., Tinetti, G., Tennyson, J., & Yurchenko, S. N. 2019, Nature Astronomy, 451, doi: 10.1038/s41550-019-0878-9
Tsiaras, A., Rocchetto, M., Waldmann, I. P., et al. 2016, ApJ, 820, 99, doi: 10.3847/0004-637X/820/2/99
Turco, R. P., Hamill, P., Toon, O. B., Whitten, R. C., & Kiang, C. S. 1979, Journal of Atmospheric Sciences, 36, 699, doi: 10.1175/1520-0469(1979)036<0699:AODMDA>2.0.CO;2
Turco, R. P., Toon, O. B., Whitten, R. C., Keesee, R. G., & Hollenbach, D. 1982, Planet. Space Sci., 30, 1147, doi: 10.1016/0032-0633(82)90126-X
Valencia, D., Guillot, T., Parmentier, V., & Freedman, R. S. 2013, ApJ, 775, 10, doi: 10.1088/0004-637X/775/1/10
Valencia, D., Ikoma, M., Guillot, T., & Nettelmann, N. 2010, A&A, 516, A20, doi: 10.1051/0004-6361/200912839
Valencia, D., O'Connell, R. J., & Sasselov, D. 2006, Icarus, 181, 545, doi: 10.1016/j.icarus.2005.11.021
Valencia, D., Sasselov, D. D., & O'Connell, R. J. 2007a, ApJ, 665, 1413, doi: 10.1086/519554
—. 2007b, ApJ, 656, 545, doi: 10.1086/509800
Van Grootel, V., Gillon, M., Valencia, D., et al. 2014, ApJ, 786, 2, doi: 10.1088/0004-637X/786/1/2
vanZanten, M. C., Stevens, B., Nuijens, L., et al. 2011, Journal of Advances in Modeling Earth Systems, 3
Vazan, A., Helled, R., & Guillot, T. 2018a, A&A, 610, L14, doi: 10.1051/0004-6361/201732522
Vazan, A., Helled, R., Kovetz, A., & Podolak, M. 2015, ApJ, 803, 32, doi: 10.1088/0004-637X/803/1/32
Vazan, A., Helled, R., Podolak, M., & Kovetz, A. 2016, ApJ, 829, 118, doi: 10.3847/0004-637X/829/2/118
Vazan, A., Ormel, C. W., Noack, L., & Dominik, C. 2018b, ApJ, 869, 163, doi: 10.3847/1538-4357/aaef33
Venturini, J., Alibert, Y., & Benz, W. 2016, A&A, 596, A90, doi: 10.1051/0004-6361/201628828
Venturini, J., Alibert, Y., Benz, W., & Ikoma, M. 2015, A&A, 576, A114, doi: 10.1051/0004-6361/201424008
Venturini, J., & Helled, R. 2017, ApJ, 848, 95, doi: 10.3847/1538-4357/aa8cd0
Wada, K., Tanaka, H., Okuzumi, S., et al. 2013, A&A, 559, A62, doi: 10.1051/0004-6361/201322259
Wada, K., Tanaka, H., Suyama, T., Kimura, H., & Yamamoto, T. 2007, ApJ, 661, 320, doi: 10.1086/514332
—. 2008, ApJ, 677, 1296, doi: 10.1086/529511
Wagner, W., & Pruß, A. 2002, Journal of Physical and Chemical Reference Data, 31, 387, doi: 10.1063/1.1461829
Wakeford, H. R., & Sing, D. K. 2015, A&A, 573, A122, doi: 10.1051/0004-6361/201424207
Wakeford, H. R., Sing, D. K., Deming, D., et al. 2013, MNRAS, 435, 3481, doi: 10.1093/mnras/stt1536

Wakeford, H. R., Sing, D. K., Kataria, T., et al. 2017, Science, 356, 628, doi: 10.1126/science.aah4668
Wakeford, H. R., Sing, D. K., Deming, D., et al. 2018, AJ, 155, 29, doi: 10.3847/1538-3881/aa9e4e
Weidenschilling, S. J. 1977, Ap&SS, 51, 153, doi: 10.1007/BF00642464
Weiss, L. M., & Marcy, G. W. 2014, ApJ, 783, L6, doi: 10.1088/2041-8205/783/1/L6
West, R. A., & Smith, P. H. 1991, Icarus, 90, 330, doi: 10.1016/0019-1035(91)90113-8
Westwood, A. R. C., & Hitch, T. T. 1963, Journal of Applied Physics, 34, 3085, doi: 10.1063/1.1729125
Woitke, P., & Helling, C. 2003, A&A, 399, 297, doi: 10.1051/0004-6361:20021734
—. 2004, A&A, 414, 335, doi: 10.1051/0004-6361:20031605
Woitke, P., Helling, C., & Gunn, O. 2019, arXiv e-prints, arXiv:1911.03777. https://arxiv.org/abs/1911.03777
Woitke, P., Helling, C., Hunter, G. H., et al. 2018, A&A, 614, A1, doi: 10.1051/0004-6361/201732193
Wolf, E. T., & Toon, O. B. 2010, Science, 328, 1266, doi: 10.1126/science.1183260
Yamamoto, T., & Hasegawa, H. 1977, Progress of Theoretical Physics, 58, 816, doi: 10.1143/PTP.58.816
Yau, M., & Rogers, R. 1989, A Short Course in Cloud Physics (Elsevier Science). https://books.google.co.jp/books?id=yxduPwAACAAJ
Yee, S. W., Petigura, E. A., Fulton, B. J., et al. 2018, AJ, 155, 255, doi: 10.3847/1538-3881/aabfec
Yu, X., Hörst, S. M., He, C., McGuiggan, P., & Bridges, N. T. 2017, Journal of Geophysical Research (Planets), 122, 2610, doi: 10.1002/2017JE005437
Zeng, L., Jacobsen, S. B., Sasselov, D. D., et al. 2019, Proceedings of the National Academy of Science, 116, 9723, doi: 10.1073/pnas.1812905116
Zhang, X., Ohno, K., Strobel, D., Tazaki, R., & Okuzumi, S. 2019, in EPSC-DPS Joint Meeting 2019, Vol. 2019, EPSC–DPS2019–332
Zhang, X., & Showman, A. P. 2018a, The Astrophysical Journal, 866, 1, doi: 10.3847/1538-4357/aada85
—. 2018b, The Astrophysical Journal, 866, 2, doi: 10.3847/1538-4357/aada7c
Ziegler, C. L. 1985, Journal of the Atmospheric Sciences, 42, 1487, doi: 10.1175/1520-0469(1985)042<1487:ROTAMV>2.0.CO;2